UNIVERSITY OF CAPE TOWN

DEPARTMENT OF MECHANICAL ENGINEERING

NUMERICAL INVESTIGATION OF FLUID DYNAMICS IN REGIONS OF SIDE BRANCHES

AUTHOR: MALEBOGO NGOEPE

STUDENT NUMBER: NGPMAL001

SUPERVISORS: DR C.J. MEYER

DEPARTMENT OF MECHANICAL ENGINEERING

UNIVERSITY OF CAPE TOWN

DR T. FRANZ

CARDIOVASCULAR RESEARCH UNIT

UNIVERSITY OF CAPE TOWN

SUBMISSION DATE: 27 OCTOBER 2009

PROJECT NO. 78:

IN PRE-CLINICAL STUDIES AT THE UNIVERSITY OF CAPE TOWN'S CARDIOVASCULAR RESEARCH UNIT, LOCALISED INTIMAL THICKENING OF THE VEIN LUMEN HAS BEEN OBSERVED IN NATIVE VEINS OPPOSITE SIDE BRANCHES. THE LOCATION OF THE INTIMAL CUSHIONS SUGGESTS A CONNECTION TO THE LOCAL FLOW MECHANICS. THE AIM OF THE PROJECT IS TO CARRY OUT A CFD INVESTIGATION OF FLUID DYNAMICS IN THE REGION OF SIDE BRANCHES SO AS TO DETERMINE THE FACTORS WHICH CONTRIBUTE TO THE DEVELOPMENT OF THESE INTIMAL CUSHIONS.

Abstract

During analysis of saphenous veins routinely harvested for bypass surgery from 200 patients at the University of Cape Town's (UCT) Division for Cardiothoracic Surgery with its Cardiovascular Research Unit (CVRU), localised thickening of the vein lumen was observed in side branch (smaller vessels joining onto the main vein) regions. Intimal thickening in the side branch region suggests that the condition is related to the local flow dynamics.

The aim of this study was to determine the factors which contributed to the development of intimal cushions. A numerical investigation of the fluid dynamics of side branch regions was conducted. Intimal hyperplasia is often associated with low shear stress and low flow velocity regions thus the investigation involved looking at flow patterns, shear stress and pressure results.

Twenty four models of veins were developed using Computational Fluid Dynamics (CFD). These were based on the data collected at the CVRU and information found in literature. Three dimensional meshes using a combination of hexahedral and tetrahedral elements were developed. The three factors under investigation were the side branch diameter to main vein diameter ratio, number of side branches attached to the main vein and the angle at which the side branch was attached to the main vein. The models developed had different combinations of these variables.

The side branch diameter to main vein diameter ratio was found to have the most significant effect on the shear stress and velocity results. An increase in the ratio led to a decrease in the velocity and shear stress values. The number of side branches was also found to have an effect on the results. The effect of the side branch angle on the flow dynamics could not be determined.

From the results, it was concluded that the side branch diameter to main vein diameter ratio had a significant effect on local flow dynamics. As a result, it was suggested that this parameter plays a rather significant role in the development of intimal hyperplasia. It was also established that the number of side branches had an effect on local flow dynamics but more research would need to be carried out in order to establish the link between this variable and intimal hyperplasia development. More work would need to be done before the effect of the side branch angle was established.

From the study, it was recommended that more research be conducted and that the focus be on model geometry and side branch angle. More studies examining the effect of the number of side branched could also be conducted. Finally, the assumptions made during the model development could also be re-examined.

Plagiarism Declaration

1. I know that plagiarism is wrong. Plagiarism is to use another's work and pretend it is one's own.
2. Each contribution to, and quotation in, this report from the work, or works, of other people has been attributed, and has been cited and referenced in the Harvard style.
3. This report is my own work.
4. I have not allowed, and will not allow, anyone to copy my work with the intention of passing it off as his or her own work.

Signature

_____

Name: Malebogo N. Ngoepe

Student number: NGPMAL001

Date: 27 October 2009

Acknowledgements

Dr Chris Meyer, Department of Mechanical Engineering, UCT and **Dr Thomas Franz**, Cardiovascular Research Unit, UCT

For the fascinating thesis topic, supervision of my thesis and their guidance and support.

Everyone at **CERECAM**

For their support, willingness to help and words of encouragement.

My fellow undergraduate students at CERECAM, **Wayne van der Merwe and Kate Louw**

For encouraging me to work hard and keep going.

My family

For their unwavering support, encouragement and love.

My friends

For helping me maintain a balance during this period, their encouragement and their support. Thank you to **Vuyo Soldati** for his medical expertise and willingness to help when I needed medical insight.

Table of contents

Abstract i

Plagiarism declaration iii

Acknowledgements iv

List of figures ix

List of tables xiii

Glossary of terms xiv

Nomenclature xvi

1. Introduction 1

1.1 Background to the project 1

1.2 Aim of the project 2

1.2 Outline of this report 2

2. Literature Review 4

2.1 The circulatory system 4

2.1.1 Systemic and pulmonary circulation 5

2.1.2 Structure of the heart 5

2.1.3 Mechanical events of the cardiac cycle 6

2.2 Veins 7

2.2.1 Structure of veins 8

2.2.2 Mechanisms of blood transport through the veins 9

2.3 Human saphenous veins 12

2.3.1 Tributaries and valves 13

2.4 Dimensional analysis of human saphenous veins 13

2.5 Blood and its properties 16

2.5.1 Blood composition 16

2.5.2 Blood density 17

2.5.3 Blood viscosity 17

2.6 Blood flow 19

2.6.1 Flow rate and velocity of flow 19

2.6.2 Factors that govern blood flow through vessels 20

2.6.3 Pressure in blood vessels 21

2.6.4 Dimensionless numbers for steady and pulsatile flow 22

2.6.5 Laminar versus turbulent flow 22

2.6.6. Boundary layers and flow models 23

2.7 Intimal thickening in human blood vessels 24

2.7.1 Overview of intimal hyperplasia 24

2.7.2 The relationship between fluid dynamics and intimal hyperplasia 25

2.7.3 Shear stress and intimal thickening 25

3. Computational Fluid Dynamics 27

3.1 Overview of Computational Fluid Dynamics 27

3.2 The functioning of a CFD code 27

3.2.1 Pre-processor 28

3.2.2 Solver 28

3.2.3 Post-processor 28

3.3 The finite volume method 29

3.4 Pressure-velocity coupling 29

3.4.1 SIMPLE algorithm 30

3.4.2 SIMPLER algorithm 31

3.4.3 SIMPLEC algorithm 33

3.4.4 PISO algorithm 33

4. Governing Equations **35**

4.1 Conservation laws 35

4.2 Navier-Stokes equations for a Newtonian fluid 36

4.3 Hagen-Poiseulle flow 36

5. Design of Experiment **39**

5.1 Overview of the factors to be considered 39

5.2 Number of side branches 39

5.3 Ratio of side branch diameter to main vein diameter 40

5.4 Geometry 40

5.5 Summary of simulations carried out 41

5.6 Control configuration 42

6. Model Development **43**

6.1 Assumptions made when developing the model 43

6.2 Geometry used for the models 44

6.3 Mesh 48

6.4 Model symmetry 49

6.5 Model regions and naming convention 49

6.6 FLUENT inputs 50

7. Results **52**

7.1 Criteria used when assessing results 52

7.1.1 Flow pattern and velocity magnitude results 52

7.1.2 Shear stress results 52

7.1.3 Pressure 53

7.2 Flow pattern and velocity magnitude results 53

7.3 Shear stress results 62

7.4 Pressure results 69

7.5 Results from all the models 76

8. Discussion of Results 82

8.1 Effect of varying the side branch diameter to main vein diameter ratio 82

8.2 Effect of varying the number of side branches 86

8.3 Effect of varying the geometry 89

9. Scope for Further Investigation 92

9.1 Model geometry 92

9.1.1 Intermediate side branch angles 92

9.1.2 General geometry of the model 96

9.2 Flow assumptions 100

9.3 Number of side branches 104

10. Conclusions and Recommendation 108

10.1 Introduction 108

10.2 Conclusions 108

10.3 Limitations 109

10.4 Validity of results 110

10.5 Recommendations 110

References 112

Appendix A: User Defined Functions A1

Appendix B: UDF Velocity Profile Calculations B1

Appendix C: Complete Set of Results C1

Appendix D: Risk Assessment D1

Appendix E: Assessment of Ethics in a Research Project E1

Appendix F: Impact of Technology on Society F1

List of figures

2.1 The overall structure of the circulatory system (Sherwood, 2004) 4

2.2 Diagram of the heart, its valves and the vessels attached to it (Sherwood, 2004) 6

2.3 Mechanical events of the cardiac cycle (Sherwood, 2004) 7

2.4 Structure of a vein (Vascular-Web) 8

2.5 The skeletal muscle pump which is responsible for enhancing venous return (Iaizzo, 2006) 10

2.6 Venous valves ensure that blood flows in one direction only (Bayer Schering Pharma AG, 2008) 11

2.7 Diagram of the great saphenous vein and the associated branches (Cleveland Clinic, 2009) 12

2.8 Graph illustrating the number of side branches along the vein length (Human et al., 2009) 14

2.9 Graph illustrating the number of small side branches along the vein length (Human et al., 2009) 15

2.10 Graph illustrating the number of medium side branched along the vein length (Human et al., 2009) 15

2.11 Graph illustrating the number of large side branches along the vein length (Human et al., 2009) 16

2.12 Flow rate and velocity of flow through the systemic circulatory circuit (Sherwood, 2004) 19

2.13 Pressure fluctuations through the systemic circulation (Sherwood, 2004) 21

2.14 An image of intimal cushions on a saphenous vein wall (Human et al., 2009) 24

3.1 The SIMPLE algorithm (Versteeg & Malalasekera, 2007) 31

3.2 The SIMPLER algorithm (Versteeg & Malalasekera, 2007) 32

3.3 The PISO algorithm (Versteeg & Malalasekera, 2007) 34

4.1 Parabolic velocity profile for Newtonian blood flow (Fung, 1993) 38

5.1 Diagram illustrating what is meant by ‘in the direction of flow’. 41

6.1 Geometric model for the control simulation 44

6.2 Geometric model for the single branch 45^{o} model 45

6.3 Geometric model for the double branch 45^{o} model 45

6.4 Geometric model for the triple branch 45^{o} model 46

6.5 Geometric model for the single branch 90^{o} model 46

6.6 Geometric model for the double branch 90^{o} model 47

6.7 Geometric model for the triple side branch 90^{o} model 47

6.8 Diagram illustrating the mesh used for the first stage of simulations 48

6.9 Diagram illustrating the gradual change in slope of a parabolic velocity profile 49

6.10 Diagram illustrating the different zones on the model 50

7.1 Velocity contour plot and velocity magnitude graph for the control configuration 54

7.2 Velocity contour plot and velocity magnitude graph for 1_45_0.2 55

7.3 Velocity contour plot and velocity magnitude graph for 1_45_0.5 56

7.4 Velocity contour plot and velocity magnitude graph for 1_90_0.2 57

7.5 Velocity contour plot and velocity magnitude graph for 2_45_0.5 59

7.6 Velocity contour plot and velocity magnitude graph for 3_45_0.5 60

7.7 Velocity contour plot and velocity magnitude graph for 3_90_0.5 61

7.8 Shear stress contour plot and wall shear stress graph for the control configuration 62

7.9 Shear stress contour plot and wall shear stress graph for 1_45_0.2 63

7.10 Shear stress contour plot and wall shear stress graph for 1_45_0.5 64

7.11 Shear stress contour plot and wall shear stress graph for 1_90_0.2 65

7.12 Shear stress contour plot and wall shear stress graph for 2_45_0.5 66

7.13 Shear stress contour plot and wall shear stress graph for 3_45_0.5 67

7.14 Shear stress contour plot and wall shear stress graph for 3_90_0.5 68

7.15 Pressure contour plot and pressure graph for the control configuration 69

7.16 Pressure contour plot and pressure graph for 1_45_0.2 70

7.17 Pressure contour plot and pressure graph for 1_45_0.5 71

7.18 Pressure contour plot and pressure graph for 1_90_0.2 72
7.19 Pressure contour plot and pressure graph for 2_45_0.5 73
7.20 Pressure contour plot and pressure graph for 3_45_0.5 74
7.21 Pressure contour plot and pressure graph for 3_90_0.5 75
7.22 Graph illustrating the relationship between side branch diameter to main branch diameter ratio and the minimum shear stress along the main vein wall 78
7.23 Graph illustrating the relationship between side branch diameter to main branch diameter ratio and the minimum velocity along the main vein 79
7.24 Graph illustrating the relationship between side branch diameter to main branch diameter ratio and the maximum pressure at the side branch joint 79
7.25 Graph illustrating the relationship between the number of side branches and the minimum shear stress along the main vein wall 80
7.26 Graph illustrating the relationship between the number of side branches and the minimum velocity along the main vein 81
7.27 Graph illustrating the relationship between the number of side branches and the maximum pressure at the side branch joint 81
8.1 Diagram illustrating the minimum and maximum shear stress regions 84
9.1 Velocity contour plot and velocity magnitude graph for 1_68_0.5 93
9.2 Shear stress contour plot and wall shear stress graph for 1_68_0.5 94
9.3 Pressure contour plot and pressure graph for 1_68_0.5 95
9.4 Mesh for the 120^{o} model 96
9.5 Velocity contour plot and velocity magnitude graph for the 120^{o} model 97
9.6 Shear stress contour plot and wall shear stress graph for the 120^{o} model 98
9.7 Pressure contour plot and pressure graph for 120^{o} model 99
9.8 Velocity contour plot and velocity magnitude graph for the constant flow model 101
9.9 Shear stress contour plot and wall shear stress graph for the constant flow model 102
9.10 Pressure contour plot and pressure graph for the constant flow model 103
9.11 Velocity contour plot and velocity magnitude graph for the 4 branch model 105

9.12 Shear stress contour plot and wall shear stress graph for the 4 branch model 106

9.13 Pressure contour plot and pressure graph for the 4 branch model 107

List of tables

5.1 Table illustrating the simulations carried out for the investigation 42

6.1 Table illustrating the general input for the FLUENT simulations 51

7.1 Table illustrating the results from all the models 77

Glossary of terms

Cardiac infarct	Heart attack
Computational Fluid Dynamics (CFD)	Computational technique used to solve problems involving flow
FLUENT	CFD software used to run simulations
GAMBIT	Software used to for mesh development
Hagen-Poiseulle flow	Fully developed flow of a Newtonian fluid through a pipe of constant circular cross-section
Intimal cushions/thickening/hyperplasia	The thickening of the inner vein wall such that the lumen diameter is reduced
Lumen	Cavity of the vein through which blood flows
Non-communicable diseases	Diseases which is not infectious
Parabolic velocity profile	Velocity profile where the velocity is at its maximum at the centre of the flow and zero at the walls. The gradient of the profile is constant

Pulsatile flow	Flow which is propagated through a series of recurring pulses
Saphenous vein	A superficial vein of the leg
Side branch	A smaller blood vessel attaching onto the main vein
Steady flow	Flow which is propagated in a smooth, non-pulsatile manner
User Defined Functions (UDFs)	FLUENT functions developed by the user so as to enhance standard FLUENT features
Vein	A blood vessel through which blood is transported back to the heart

Nomenclature

α = Womersley number (dimensionless)
$\dot{\gamma}$ = shear rate (s^{-1})
μ = coefficient of dynamic viscosity (kg/ms)
ν = kinematic viscosity (m^2/s)
ω = frequency of the pulse wave (rad/s)
ρ = density (kg/m^3)
τ = shear stress (Pa)
τ_w = maximum shear stress (shear stress at the wall) (Pa)
τ_y = yield shear stress (Pa)

a = maximum radius (m)
a_c = core radius (m)
d = diameter (m)
E = energy (J)
k = thermal conductivity (W/m.K)
K_c = Casson viscosity coefficient (dimensionless)
L = length (m)
p = pressure (Pa)
ΔP, $\frac{dp}{dx}$ = pressure gradient (Pa)
Q = flow rate (m^3/s)
r = radius (m)
R = vascular resistance ($Pa.s/m^3$)
Re = Reynold's number (dimensionless)
$\dot{x}$ = velocity (m/s)
$\dot{x}_c$ = core velocity (m/s)
t = time (s)
T = temperature (K)
u = velocity vector (m/s)
u = x-component of velocity vector (m/s)
v = y-component of velocity vector (m/s)
w = z-component of velocity vector (m/s)

CHAPTER 1: INTRODUCTION

1.1 Background to the project

Non-communicable diseases continue to affect more and more people both in the developing and developed worlds. Cardiovascular diseases fall into this category and cover a wide range of diseases from coronary heart disease to cardiac infarct (heart attack). Several strategies have been developed in an effort to try and reduce the incidence of these diseases.

Saphenous veins are often used as grafts in coronary artery bypass surgery. During analysis of saphenous veins routinely harvested for bypass surgery from 200 patients at the University of Cape Town's (UCT) Division of Cardiothoracic Surgery with its Cardiovascular Research Unit (CVRU), localised thickening of the vein lumen was noticed. At times, the lumen of vein grafts thickens to a point where the vein luminal diameter becomes significantly reduced, thus resulting in disruptions in the normal pattern of blood flow. In some cases, the reduction in diameter results in a significant reduction in the amount of blood being pumped around the body. This reduces the amount of oxygen available to cells in the body. This generally has a severe impact on the body and can sometimes result in cardiac infarct and other such fatal conditions.

The development of intimal cushions or intimal thickening has been observed and widely studied in vein grafts but few studies relating to intimal thickening in native veins have been carried out. It has been noted that in these native veins, the thickening often occurs in side branch regions. It is thought that the presence of these side branches results in a change in local flow dynamics and that this has an effect on the development of intimal cushions.

1.2 Aim of the project

The aim of this project was to carry out a numerical investigation of fluid dynamics in native veins in the regions of side branches. In the project, various computational fluid dynamics (CFD) models of native veins and their surrounding side branches were developed. The fluid behaviour in these models was then studied. It was thought that there were several factors which would have a major effect on the fluid behaviour, including the ratio of the diameter of the side branch to that of the main vein, the geometric configuration and the number of side branches attaching to the main vein. Several models which investigated these factors were developed.

In order to understand the effects of the factors mentioned in the previous paragraph, the pressure, shear stress and localised flow pattern results of each model were studied. The models were compared against data found in literature, each other and a control experiment. An effort was then made to try and establish the relationship between the results and the development of intimal cushions in the native veins. Part of this exercise included verifying whether or not the position of these intimal cushions was related to the pressure, shear stress and velocity results.

1.3 Outline of this report

This report contains the knowledge and information on which the numerical investigation was based and also includes the details of the investigation itself. Chapter 2 is a literature review which explains most of the biological aspects of the investigation. Chapter 3 gives an overview of computational fluid dynamics, the method used for the investigation. The equations on which the investigation is based are given in chapter 4 while chapter 5 details the reasoning behind the design of the experiments. Chapter 6 details the actual model development while chapter 7 shows the results. This is followed by a discussion of these

results in chapter 8. Chapter 9 discusses some of the developments which could take place from this study. The study is concluded in chapter 10 and recommendations are given in the same chapter. Finally, the references and appendices are included at the end.

CHAPTER 2: LITERATURE REVIEW

2.1 The circulatory system

The circulatory system is the transport system of the body. It ensures that essential nutrients are delivered to all the cells in the body and that waste is removed from the cells. The three main components of the system are the heart, the blood vessels and the blood. The heart is a pump which imparts a pressure to the blood thus setting up a pressure gradient in the body. The flow of blood through the body is a result of this gradient. The blood vessels (arteries, veins and capillaries) are the network along which the blood travels from the heart to the rest of the body and back again. The blood is the actual transport medium in which substances needing to be transported are dissolved or suspended (Sherwood, 2004). This overall structure is illustrated in Fig. 2.1 below.

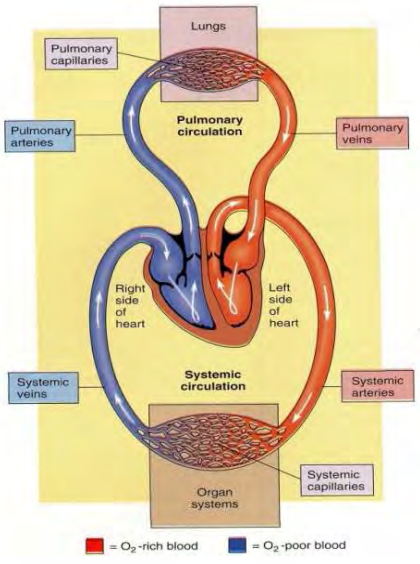

Figure 2.1: The overall structure of the circulatory system (Sherwood, 2004)

2.1.1 Systemic and pulmonary circulation

As is seen in Fig. 2.1, there are two circuits within the circulatory system. The pulmonary circuit transports blood between the heart and the lungs while the systemic circuit transports blood between the heart and the rest of the body. The main function of the pulmonary circuit is to transport deoxygenated blood from the heart to the lungs and to transport oxygenated blood from the lungs to the heart. This process of removing carbon dioxide from the blood and replenishing oxygen occurs through gaseous exchange. The systemic circuit transports oxygen and essential nutrients from the heart to the rest of the cells in the body and transports waste products from the body back to the heart (Sherwood, 2004).

2.1.2 Structure of the heart

The heart is a single, hollow and muscular organ. It is subdivided into a left and right half and has four chambers. The two upper chambers are known as the atria and are responsible for receiving blood returned to the heart. They transfer this blood to the two lower chambers known as the ventricles. These are responsible for pumping blood away from the heart. The septum, a muscular partition which prevents the mixing of blood separates the left and right halves of the heart. This is important as the right half receives and pumps oxygen-poor blood while the left half receives and pumps oxygen-rich blood. The left and right atrioventricular valves ensure that blood flows from the respective atrium to the ventricle, preventing backflow as seen in Fig. 2.2 (Sherwood, 2004).

The arteries are the vessels which carry blood away from the heart while the veins carry blood back to the heart. The aorta transports blood from the left ventricle to the rest of the body while the vena cavae returns blood from the body to the right atrium. The pulmonary artery carries blood from the right ventricle to the lungs while the pulmonary vein transports blood from the lungs to the left atrium. There are two semilunar valves between the ventricles and major arteries. The aortic and pulmonary valves ensure that the blood

flows away from the heart and prevent backflow and can be seen in Fig. 2.2 (Sherwood, 2004).

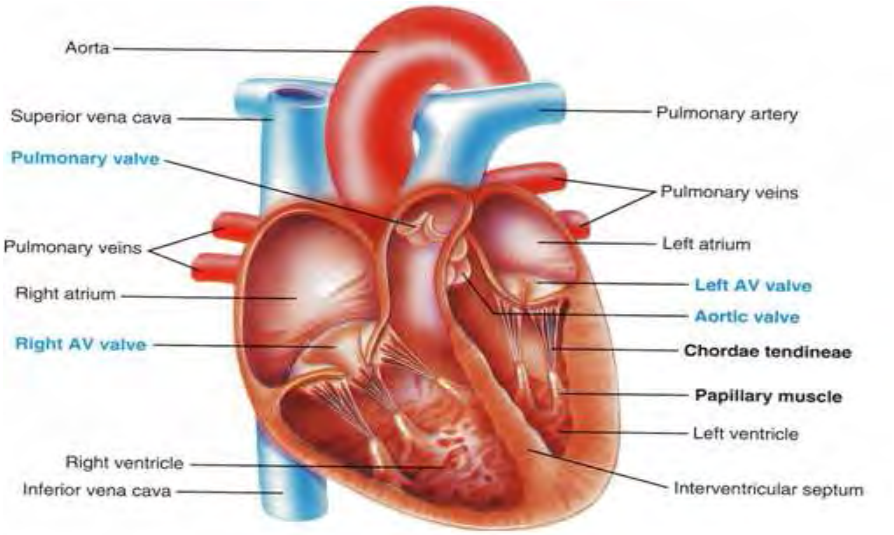

Figure 2.2: Diagram of the heart, its valves and the vessels attached to it (Sherwood, 2004)

2.1.3 Mechanical events of the cardiac cycle

During the cardiac cycle, several processes occur concurrently as is seen in Fig. 2.3. The cycle is characterised by alternating periods of systole and diastole. The heart contracts and empties during systole and then relaxes and fills during diastole. The activities are brought about by rhythmic changes in electric activity of the heart and the atria and ventricles undergo separate systole and diastole. The mechanical activity also results pressure changes which govern the opening and closing of the heart valves (Sherwood, 2004).

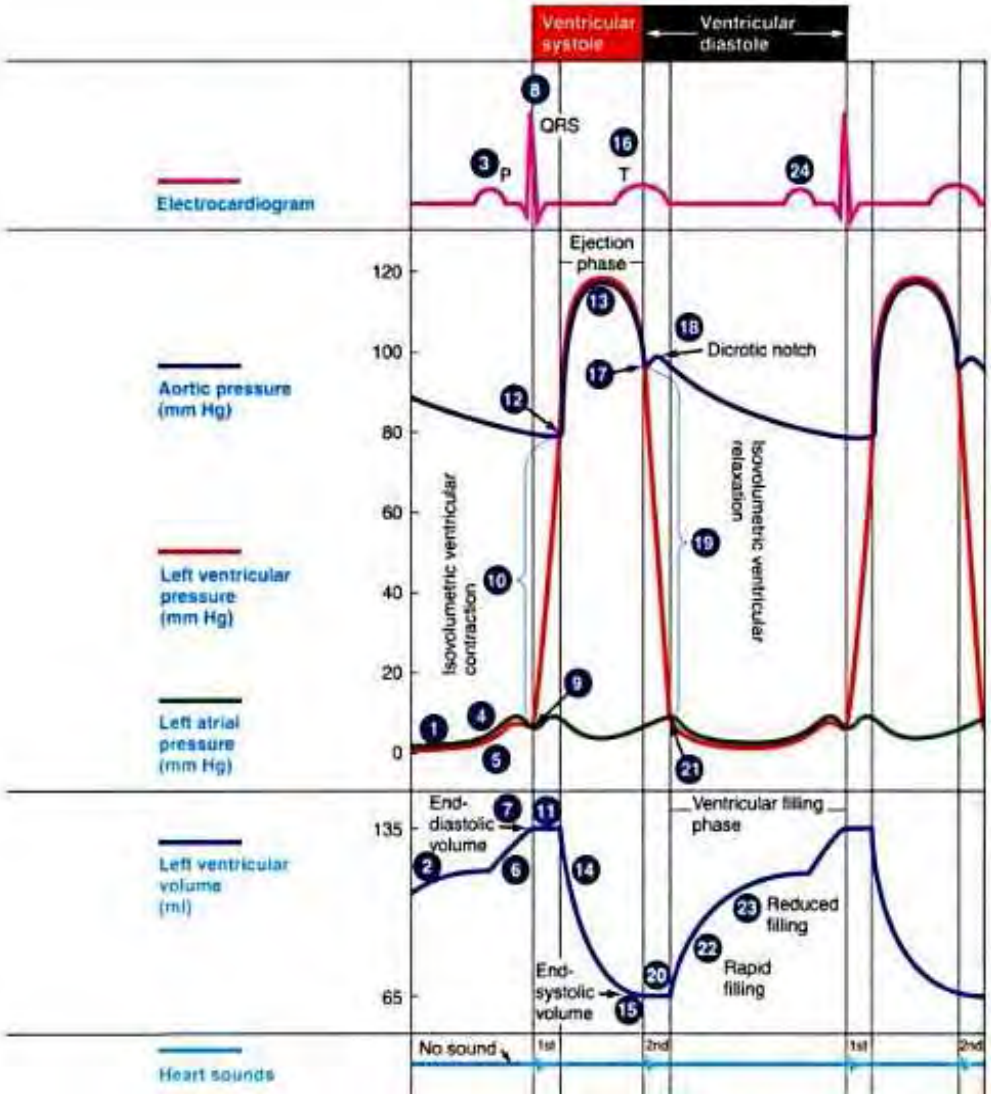

Figure 2.3: Mechanical events of the cardiac cycle (Sherwood, 2004)

2.2 Veins

Blood flows from smaller venules to larger veins, resulting in a decrease in total cross-sectional area and an increase in blood flow velocity. They offer a path along which blood can travel back to the heart and also have capacity to store blood (Sherwood, 2004).

2.2.1 Structure of veins

Relative to other blood vessels, the vein lumen has a rather large diameter, offering less resistance to blood flow. As a result of their high collagen to elastin fibre ratio, they are highly stretchable but have little elastic recoil (Sherwood, 2004).

The vein wall is made up of three layers. The intima is the innermost layer and is made up of a single layer of endothelial cells on a bed of connective tissue. The media is the middle layer and consists of smooth muscle cells and connective tissue. The relative proportion of the smooth muscle cells to the connective tissue is determined by the size and function of the vein. The adventitia is the outermost layer and is made up of connective tissue with nerve fibres, lymphatics and vessels. A diagram of the veins can be seen in Fig. 2.4 (American Venous Forum: Edited Gloviczki, P. and Yao, J., 2001).

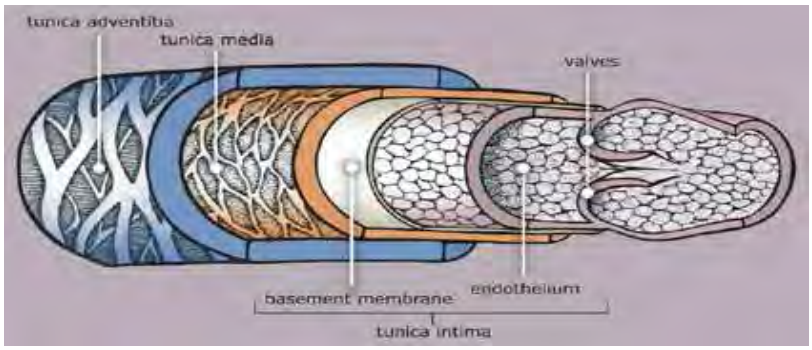

Figure 2.4: Structure of a vein (Vascular-Web, 2003)

Large veins of the lower extremities are equipped with one-way valves which are positioned every two to four centimetres. In general, there are more valves in the thigh than in the lower leg. According to the American Venous Forum, “Venous valves are bicuspid infoldings of the intima covered by endothelium on both sides with an intervening connective tissue skeleton.” The valves can be seen in Fig. 2.4 (American Venous Forum: Edited Gloviczki, P. and Yao, J., 2001).

2.2.2 Mechanisms of blood transport through the veins

There are five main mechanisms which enhance venous return. These are sympathetic activity, skeletal muscle activity, venous valves, respiratory activity and cardiac suction. These are explored in the paragraphs that follow (Sherwood, 2004).

Sympathetic activity

Venous smooth muscle is attached to a large number of sympathetic nerve fibres. Despite the low muscle tone of this smooth muscle, the sympathetic stimulation results in vascular vasoconstriction. This causes a slight rise in venous pressure, increasing the pressure gradient to drive more of the blood stored in the veins to the right atrium. In addition to this, the vasoconstriction results in a decrease in the capacity of the veins thus increasing flow through the vessels (as the veins narrow, more of the blood stored in the vein is squeezed out thus increasing blood flow through the vessels). Owing to the large diameter of the veins, however, moderate vasoconstriction caused by the sympathetic activity has little effect on the resistance to flow (Sherwood, 2004).

Skeletal muscle activity

Most large veins in the peripheral region are found between the skeletal muscles. As the muscles contract, the veins are compressed. This compression results in a reduction in the vein size and an increase in venous pressure thus squeezing the blood present in the veins towards the heart as seen in Fig. 2.5 (Sherwood, 2004).

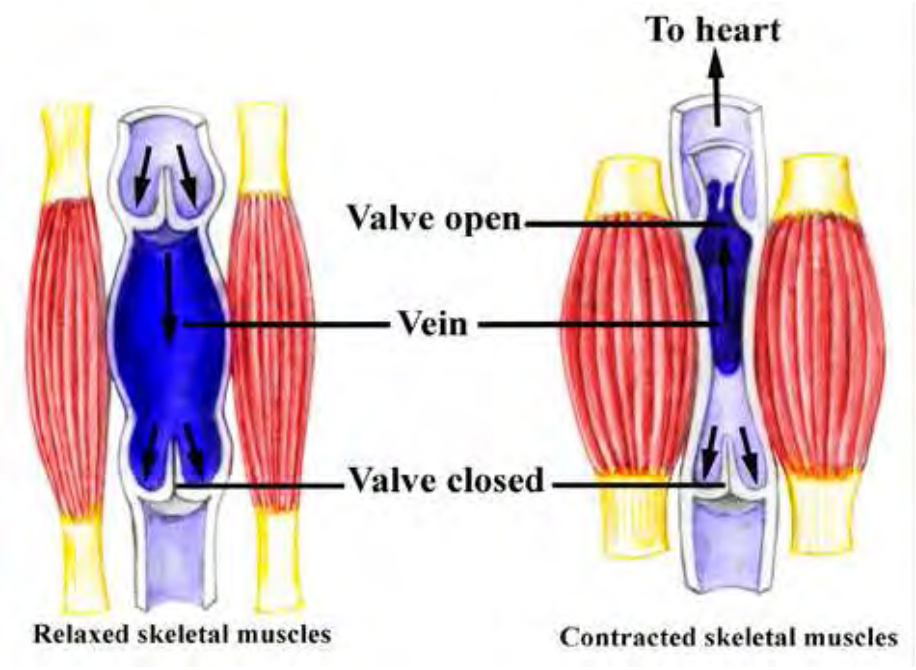

Figure 2.5: The skeletal muscle pump which is responsible for enhancing venous return (Iaizzo, 2006)

Venous valves

Both venous vasoconstriction and skeletal muscle contraction result in blood being driven to the heart. The challenge, however, arises when a tube is squeezed in the middle: the result is that blood flows in both directions away from the point of application of the force (squeezing action). The presence of venous valves ensures that blood is driven in one direction only (towards the heart) as is seen in Fig. 2.6 (Sherwood, 2004).

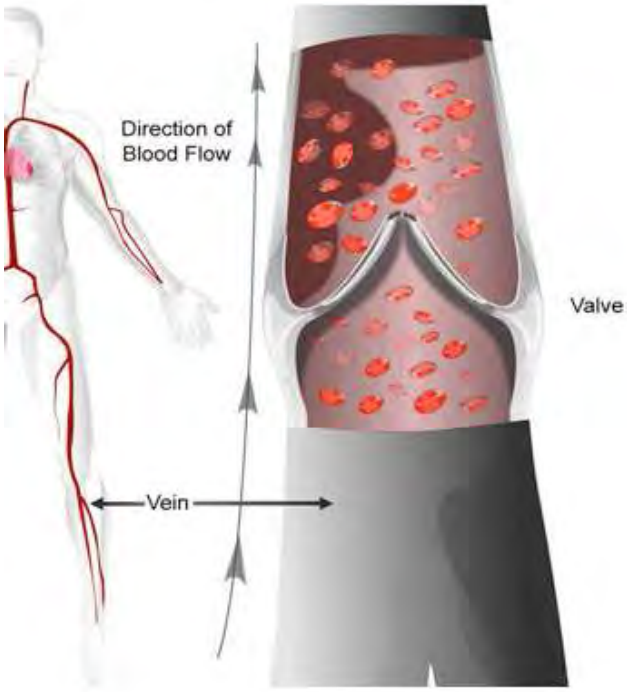

Figure 2.6: Venous valves ensure that blood flows in one direction only (Bayer Schering Pharma AG, 2008)

Respiratory activity

Respiratory activity results in subatmospheric chest pressure while the rest of the limbs are at atmospheric pressure. This results in an externally applied pressure gradient which causes blood to be squeezed from the lower extremities towards the heart, increasing venous return. This venous return mechanism is known as the respiratory pump and increases with increased respiratory activity (Sherwood, 2004).

Cardiac suction

When the heart ventricles contract, the atrioventricular valves are opened, resulting in an increase in the size of the atrial cavities. This causes a pressure drop thus setting up a pressure gradient between the heart and the lower extremities of the body. This results in an increase in venous return, with more blood being drawn towards the heart (Sherwood, 2004).

2.3 Human saphenous veins

According to the American Venous Forum (2001), “Few veins in the body have more variability in their gross anatomy than the superficial veins of the leg.” The lesser and greater saphenous veins are considered superficial veins and can be seen in Fig. 2.7. They lie mainly in the subcutaneous fat and provide a blood drainage path from the skin and subcutaneous fat layers (American Venous Forum: Edited Gloviczki, P. and Yao, J., 2001).

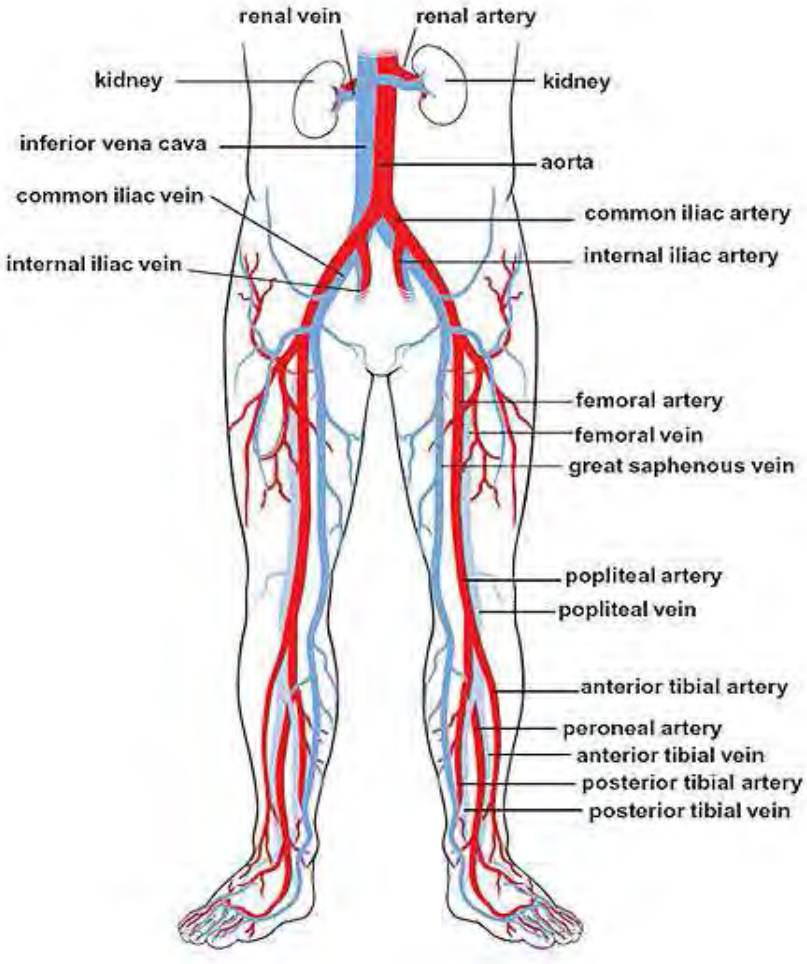

Figure 2.7: Diagram of the great saphenous vein and the associated branches (Cleveland Clinic, 2009)

2.3.1 Tributaries and valves

The greater saphenous vein runs from the ankle right up to the pelvic region. It can be found along the inner side of the leg while the lesser saphenous vein runs along posterior of the leg. Various tributaries join onto this vein along the way. In the calf, the vein has an anterior and posterior tributary, with the latter known as the posterior arch vein. It also has two major tributaries in the thigh known as the lateral and medial accessory saphenous veins as seen in Fig. 2.7 (Gray, 1858).

The presence of valves in the saphenous veins ensures that blood flows in one direction only (towards the heart). In most cases, saphenous veins contain at least six valves and have a maximum of between fourteen and twenty-five valves. There are more valves above than below the knee and there is generally one at each two to three centimetre interval (American Venous Forum: Edited Gloviczki, P. and Yao, J., 2001).

2.4 Dimensional analysis of human saphenous veins

According to Human et al. (2009), saphenous veins were harvested from two hundred patients. The outer vein diameter of the vein distended at a pressure of 120mmHg was found to range between 4 and 6mm. The side branches, which were also distended at a pressure of 120mmHg were found to have diameters ranging between 1 and 2mm. The wall thickness of the veins was found to be 398.7 ± 123.2µm. The ratios of main vein to side vein diameter ranged from 1:0.182 to 1:0.5 (Human et al., 2009).

In the same study, the side branches attached to the main vein were arbitrarily classified as small, medium and large. Their location and frequency was also recorded. As is seen in Fig. 2.8, the most common figure for the maximum number of side branches attached to the main vein at two centimetre intervals is three. Figure 2.9 reveals that at most, three small

side branches are attached to the main vein at two centimetre intervals with the number reducing to two as one moved further away from the angle. For most veins, there is a maximum of two medium side branches at two centimetre intervals with the number occasionally rising to three. As one moves closer to the pelvic region, the number drops to one as seen in Fig. 2.10. Finally, for large side branches, a pattern similar to that of medium side branches was noticed as is seen in Fig. 2.11 (Human et al., 2009).

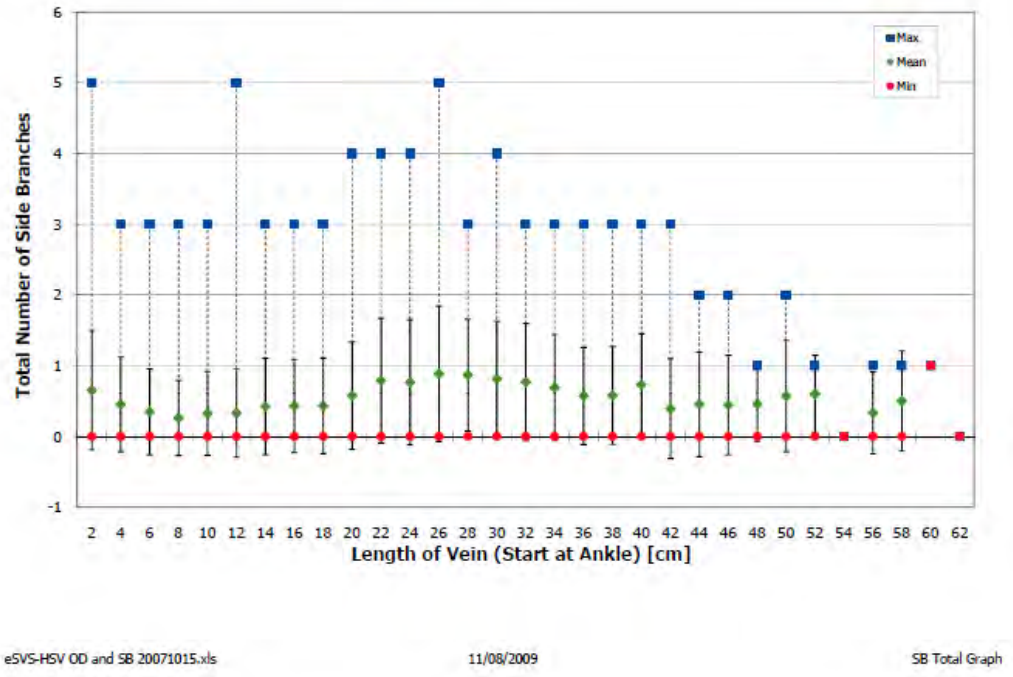

Figure 2.8: Graph illustrating the number of side branches along the vein length (Human et al., 2009)

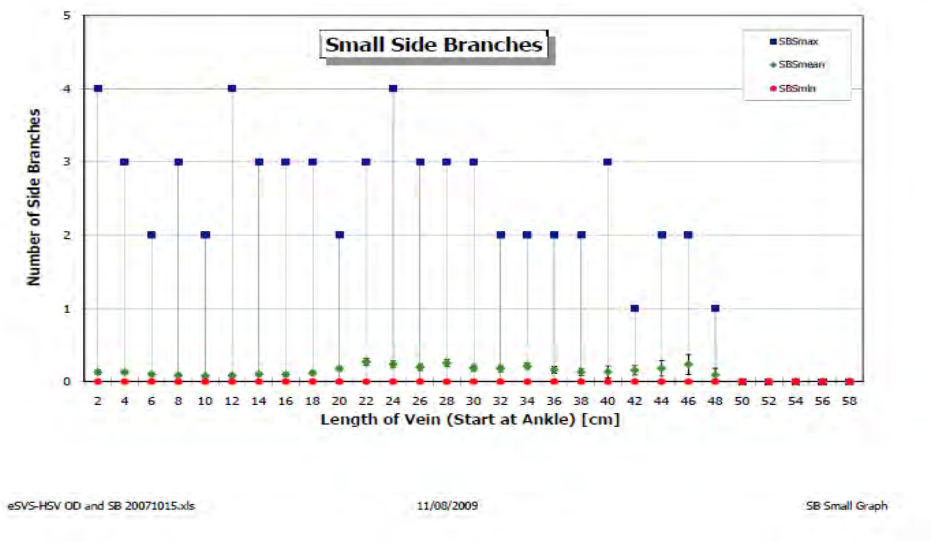

Figure 2.9: Graph illustrating the number of small side branches along the vein length (Human et al., 2009)

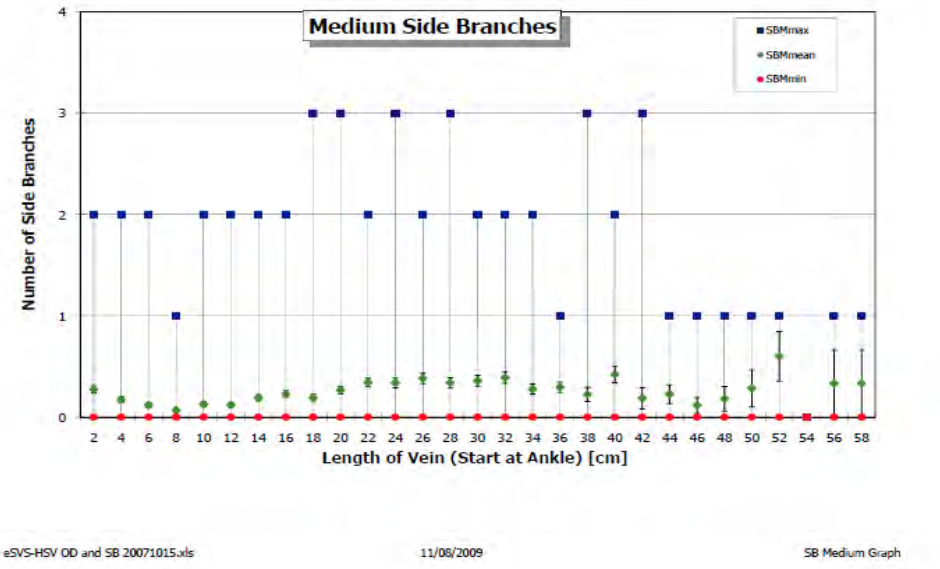

Figure 2.10: Graph illustrating the number of medium side branches along the vein length (Human et al., 2009)

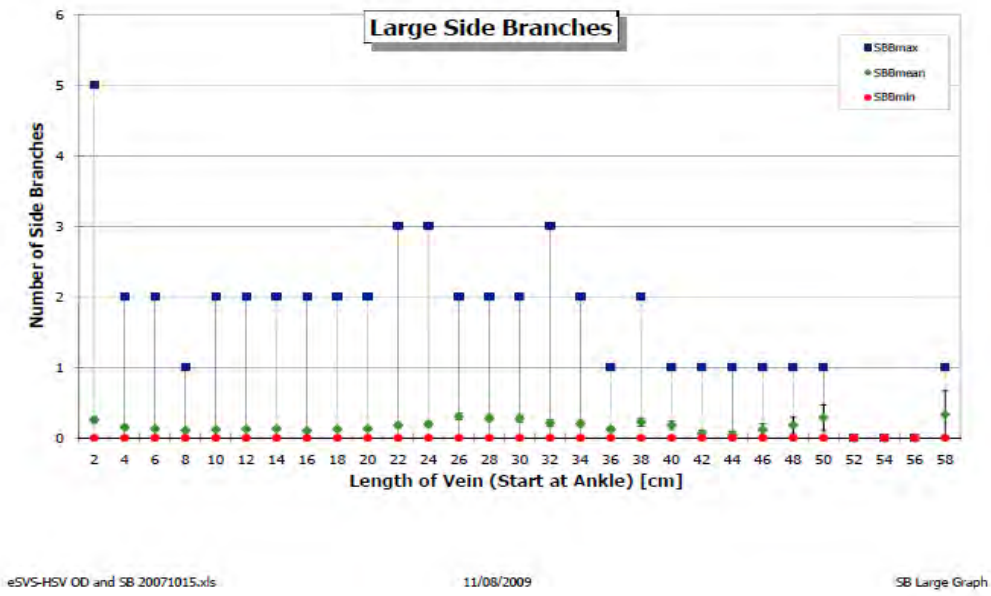

Figure 2.11: Graph illustrating the number of large side branches along the vein length (Human et al., 2009)

2.5 Blood and its properties

2.5.1 Blood composition

Blood is the main fluid which flows through the circulatory system. It is composed such that cellular elements are suspended in a complex fluid named plasma. The circulation of blood around the body ensures that essential nutrients and oxygen are delivered to cells, carbon dioxide is removed from cells and that the pH in the body is kept constant (Sherwood, 2004).

Ninety percent of plasma is water while the remainder consists mainly of proteins and organic and inorganic substances. The main types of cellular elements in blood are erythrocytes (red blood cells), leukocytes (white blood cells) and platelets. Erythrocytes

account for about fifty percent of blood volume and are disk shaped with a diameter of 7.6µm and thickness of 2.8µm. There is a rather varied range of leukocytes but most of them are rounder then erythrocytes. Platelets have a diameter of about 2.5µm and much smaller than the other two cell types (Fung, 1993). The constant flow of blood through the blood vessels ensures that there is generally an even distribution of cellular elements in the plasma.

2.5.2 Blood density

Red blood cells have a density of 1100kg/m^3 while plasma has a specific gravity of 1030kg/m^3 (Fung, 1993). The density of whole blood, however, was found to be approximately 1050kg/m^3 (Bell & Rhoades, 2009).

2.5.3 Blood viscosity

A fluid is defined as Newtonian if the shear stress is linearly proportional to the velocity gradient as seen in Eq. 2.1.

$$\tau = \mu \frac{du}{dy} \tag{2.1}$$

The viscosity of a Newtonian fluid is therefore constant over a wide range of tube dimensions and flows if the temperature is kept constant. A non-Newtonian fluid is one for which the shear stress is not linearly proportional to the strain rate (Levy & Pappano, 2007).

When investigating blood vessels larger than arterioles where the flow regime is steady and laminar, the blood can be considered a Newtonian fluid (Levy & Pappano, 2007). In such cases, the diameter of the red blood vessels is much smaller than that of the vessel hence the blood is considered to be a homogeneous fluid. For vessels which have a diameter

equivalent in size to arterioles or less than that, blood is considered to be non-Newtonian. In such instances, blood is considered a non-homogeneous fluid as there exists at least two phases: blood cells and plasma (Fung, 1993).

When dealing with blood in its non-Newtonian form, it is useful to consider two concepts, namely, apparent viscosity and relative viscosity. The apparent viscosity of blood varies as a function of the hematocrit ratio. This is defined as the ratio of the volume of red blood cells to the volume of whole blood. For a given hematocrit ratio, the apparent viscosity is dependent on the diameter of the tube which was utilised for estimating the viscosity. It has also been observed that this apparent viscosity diminishes as the tube dimensions get smaller and the shear rate increases (Levy & Pappano, 2007). The relative viscosity is a ratio of the apparent viscosity to the viscosity of plasma. Apparent viscosity can be applied to any flow regime as long as it is computed from a formula that has been proven to work for homogeneous Newtonian fluids. The relative viscosity is applicable to any flow system, even if the structural geometry and elasticity properties are not known. Both properties are not intrinsic blood properties and are dependent on the blood and blood vessel interactions (Fung, 1993).

When tested alone in a viscometer, plasma was found to behave as a Newtonian viscous fluid with a coefficient of viscosity of 1.2cP (0.0012 kg/ms). When whole blood was tested, however, it was found to behave as a non-Newtonian fluid (Fung, 1993). The viscosity of whole blood at a hematocrit ratio of 45% (the average percentage under normal conditions) is about 0.0032kg/ms (Kundu & Cohen, 2008).

2.6 Blood flow

2.6.1 Flow rate and velocity of flow

The flow rate refers to the volume of flow moving through a segment of the system per unit time. The velocity of flow refers to the linear speed with which the blood flows through a given segment. The flow rate of blood remains constant throughout the circulatory system at around 5l/min because the circulatory system is a closed one. It does, however, change in individual blood vessels. The velocity of flow varies because it is inversely proportional to the total cross sectional area of the vessels at a given level as is seen in Fig. 2.12 (Sherwood, 2004). According to Golledge et. al. (1997), the flow rate used to model blood flow in veins is 40ml/min ($6.67\times10^{-07}m^3/s$) (Golledge et al., 1997).

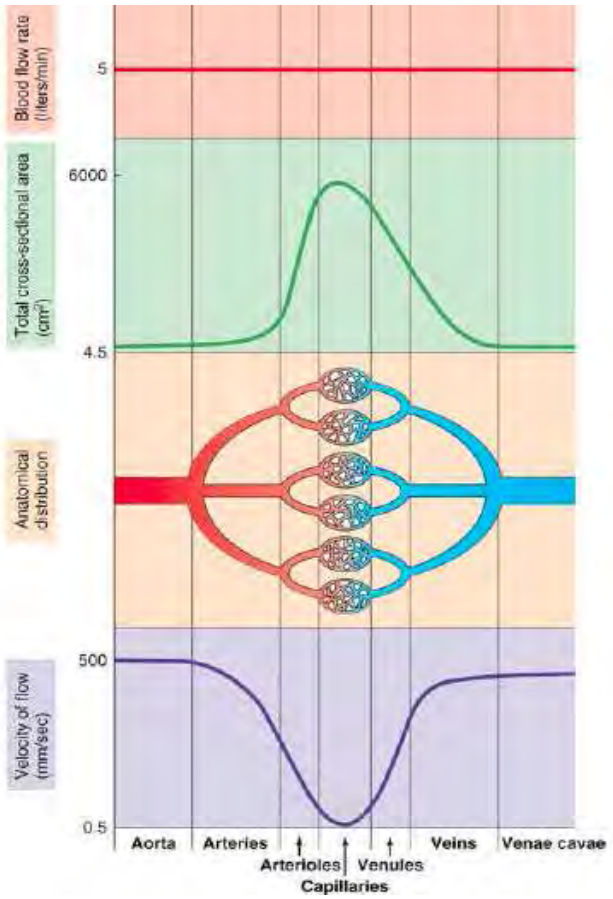

Figure 2.12: Flow rate and velocity of flow through the systemic circulatory circuit (Sherwood, 2004)

2.6.2 Factors that govern blood flow through vessels

Blood flow rate is directly proportional to the pressure gradient in the vessel and inversely proportional to the vascular resistance given by Eq. 2.2 below.

$$Q = \frac{\Delta P}{R} \tag{2.2}$$

Pressure gradient

Blood always flows from a region of higher pressure to that of lower pressure. It can therefore be said that the existence of a pressure gradient between two ends of a blood vessel is the reason for blood flow through the vessel. Pressure is imparted to the blood when the heart contracts. Owing to friction between the vessel walls and the blood, pressure losses occur along the blood flow path. The magnitude of the frictional loss is also related to the length of the blood vessel: the longer the blood vessel, the greater the frictional loss. This loss in pressure due to friction results in a pressure gradient between the beginning and end of the vessel which in turn results in blood flow through the vessel (Sherwood, 2004).

Resistance

According to Sherwood, resistance is “a measure of the hindrance or opposition to blood flow through a vessel caused by friction between the moving fluid and the stationary vascular walls” (Sherwood, 2004). This factor affects blood flow rate as an increase in resistance makes it more difficult for blood to pass through a vessel thus slowing down the flow of blood. In order to maintain a constant flow rate while the resistance increases, the pressure gradient would also have to increase. The resistance is determined by the blood viscosity, blood vessel length and blood vessel radius.

2.6.3 Pressure in blood vessels

As is seen in Fig. 2.13, pressure fluctuations exist in the circulatory system. The greatest fluctuations in blood pressure occur in the heart where pressure starts of at 0 mm Hg during diastole and peaks at 120 mm Hg during systole. This difference drops as one moves to the arteries where the fluctuation ranges between 80 mm Hg during diastole to 120 mm Hg during systole. When the blood moves to the arterioles, there is a large drop in the blood pressure and in the systole-diastole swing, also referred to as pulse pressure, due to the high resistance in the arterioles. By the time the blood reaches the veins, a relatively low, nonpulsatile pressure is observed (Sherwood, 2004). According to Golledge et. al (1997), the pressure used to model venous conditions is 20mmHg (Golledge et al., 1997).

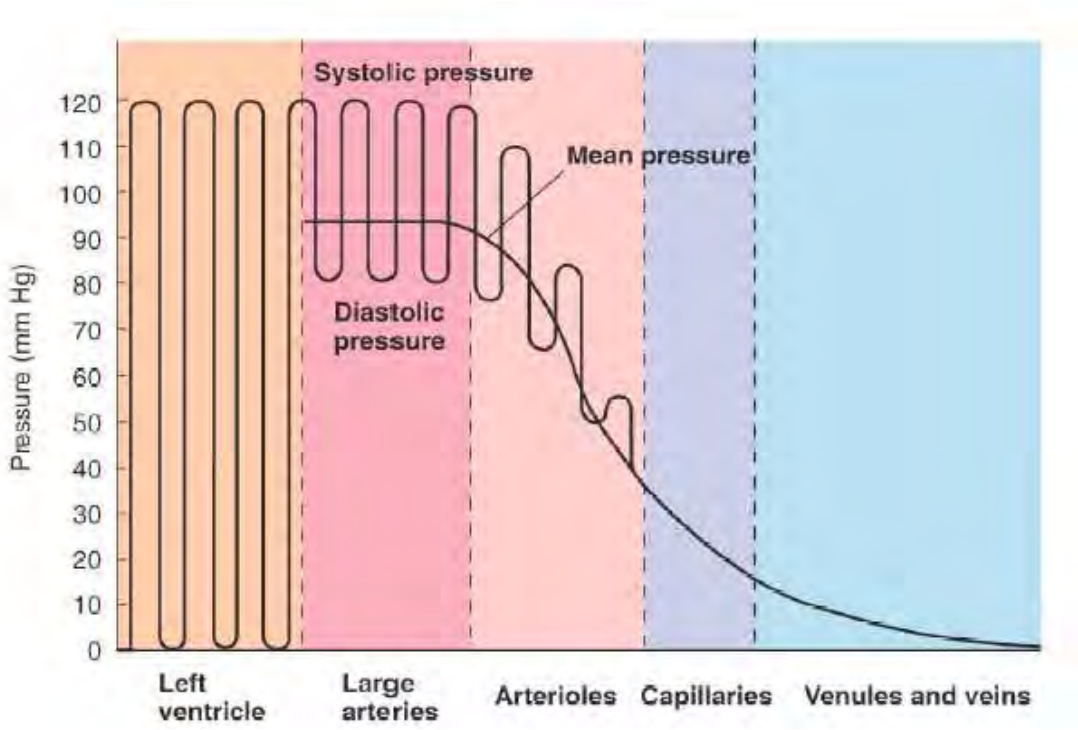

Figure 2.13: Pressure fluctuations through the systemic circulation (Sherwood, 2004)

2.6.4 Dimensionless numbers for steady and pulsatile flow

The Reynolds number is used when describing the steady nature of blood flow. This is the ratio of the inertial forces to viscous forces and is given by Eq. 2.3. In the circulatory system, it is applied to the veins where the blood flow is steady (Fung, 1997).

$$Re = \frac{Inertial\ force}{Viscous\ force} = \frac{\rho \dot{x} d}{\mu} \tag{2.3}$$

The Womersley number is used when describing pulsatile blood flow. This is a ratio of the unsteady inertial forces to viscous forces and is a composite parameter of the Strouhal number and the Reynolds number. In the circulatory system, it is applied to the arteries, where flow is pulsatile. The number is given by Eq. 2.4 (Kundu & Cohen, 2008).

$$\alpha = a\sqrt{\frac{\omega}{\nu}} \tag{2.4}$$

2.6.5 Laminar versus turbulent flow

In a tube, flow is considered laminar when all the fluid elements move in streamlines parallel to the tube axis. The fluid that moves along the axis moves at the fastest velocity while that in contact with the wall exhibits zero velocity relative to the wall, i.e. does not move. Flow in which random movements and irregular motions of the fluid elements are observed is known as turbulent flow and can be seen in.

The governing law for laminar, steady fluid flow through a tube is the Hagen-Poiseulle law which states that the volume flow rate is proportional to the pressure drop in the tube as seen in Eq. 2.5.

$$Q = \frac{\pi d^4}{128}\frac{\Delta p}{\mu L} \quad (2.5)$$

If the flow deviates from a laminar state and becomes turbulent, the Poiseulle law no longer holds and the Reynolds number becomes the governing factor. A Reynolds number of around 2300 is critical as it is at this point that the flow characteristics change from laminar to turbulent (Fung, 1997).

In general, a laminar flow regime is observed for blood flowing through blood vessels. The flow does tend to become turbulent when the flow velocity is high, fluid viscosity is low, when the tube diameter is large or the vessel wall is irregular. Turbulent flow is, however, confined to the specific cases mentioned and is not the characteristic flow regime of blood(Levy & Pappano, 2007).

2.6.6 Boundary layers and flow models

When relative motion occurs between a fluid and a surface, a condition known as 'no-slip' is applied at the interface. This condition states that the fluid and surface velocities are equal at this interface. As one moves further and further away from the surface, the velocity of the fluid increases. The transition zone in which the velocity change occurs is known as the boundary layer (Douglas et al., 2005).

The flow profile in a pipe is dependent on the boundary layer development at the entry of the pipe. The boundary layer development will determine whether the flow is laminar or turbulent, depending on the ratio of viscous to inertial forces in the fluid. The flow is said to be 'fully-developed' once the boundary layer is fully developed. From this point onwards, it can be assumed that the velocity profile will remain constant (Douglas et al., 2005).

For Newtonian blood flow, the Hagen-Poiseulle model for flow in pipes can be used. For this type of model, the velocity profile is parabolic once the stage of fully developed flow has been reached. This model is discussed in greater depth in section 4.3. For non-Newtonian blood flow, the Casson model is found to predict results which are in good agreement with experimental values over a wide range of shear rates. As a result, the model is often used for blood flow in smaller vessels. (Kundu & Cohen, 2008). In this thesis, the blood vessels modelled are large enough for the flow to be modelled as Newtonian.

2.7 Intimal thickening in human blood vessels

2.7.1 Overview of intimal hyperplasia

According to Subbotin (2007), intimal hyperplasia occurs when cells form a "multiple-layer compartment internally to the elastic membrane of the [blood vessel] wall" (Subbotin, 2007). This results in the reduction of lumen diameter. A picture of intimal cushions on a saphenous vein wall can be seen in Fig. 2.14 below. Human et. al. (2009) suggest that intimal cushions are an anatomical rather than pathological feature (Human et al., 2009).

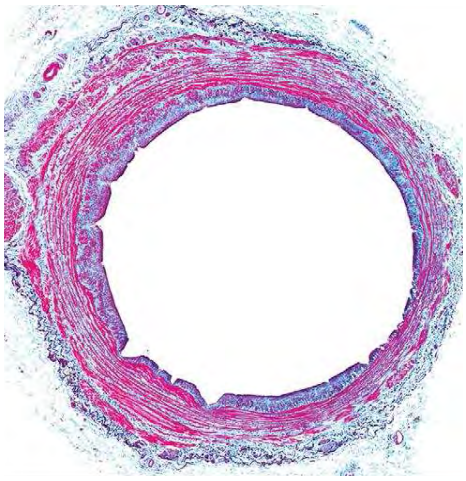

Figure 2.14: An image of intimal cushions on a human saphenous vein wall (Human et al., 2009)

In part of his hypothesis, Subbotin puts forward the notion that there are two types of intimal hyperplasia. He describes the first as a benign type of intimal hyperplasia which is part of the body's response to changes in blood pressure. He believes that this is a necessary process which ensures that the structural integrity of the vessels is maintained and that local physiological demands are met. This type of intimal hyperplasia is preceded by changes in hemodynamics and shear stress. He then suggests that disease-related intimal hyperplasia is a result of interactions between the blood-tissue interface. Even though the exact properties of blood flow which result in the thickening are not identified, he asserts that the moving fluid is able to result in changes in the structure of the vessel wall (Subbotin, 2007).

2.7.2 The relationship between fluid dynamics and intimal hyperplasia

Dobrin et. al. (1989) discuss the mechanical factors which predispose autogenous vein grafts to intimal hyperplasia. They observe that intimal hyperplasia was is greater in low flow velocity regions than in high flow velocity regions. They also state that intimal hyperplasia is not dependent on static deformation or stress (Dobrin, 1989).

A paper by Human et al. (2009) relates intimal hyperplasia to low shear forces and high circumferential stress. The stress conditions are a result of the mismatch between the diameters of the vein graft lumen and host artery lumen. The mismatch results in eddy blood flow typical of low shear regions and in turn results in intimal hyperplasia. It was found that if the vein graft diameter was constricted, the flow velocity in the region increased, resulting in increased shear forces. This, in turn, reduced intimal thickening (Human et al., 2009).

2.7.3 Shear stress and intimal thickening

A study carried out by Bonert et al. (2003) investigated the relationship between wall shear stresses and intimal thickening of the human abdominal aorta. In-vitro measurements of

wall shear stresses were taken from a healthy, thirty-five year old volunteer using a CT scan. The intimal thickening was then examined in autopsy cases using light microscopy. Important geometric factors taken into account were the cross-sectional area of the vessel and the vessel curvature. It was found that in regions where the vessel cross-sectional area increased, the wall shear stresses decreased. The converse was also found to be true. The vessel curvature in the abdominal aortic bifurcation region had an impact on the areas of high and low shear stress distribution. Several conclusions were drawn from this study. The first is that intimal thickening increases with age due to changes related to geometry. In addition to this, the data showed that "there is a statistically significant inverse correlation between wall shear stress and intimal thickening" (Bonert et al., 2003).

A study undertaken by Zilla et. al. (2009) in non-human primates found that a threshold value of 0.5 Pa suppressed the development of intimal hyperplasia. This was found to be true for femoral veins of Senescent Chacma baboons which had been subjected to femoral arterial conditions (Zilla, et al., 2009).

Porter et. al. (1996) developed an in vitro flow model of human saphenous vein graft intimal hyperplasia where harvested saphenous veins were exposed to arterial and venous flows in a closed circulatory system model. From this study, it was observed that for arterial conditions (shear stress of approximately 0.9 Pa), intimal thickening was prevented. For venous conditions, however, where the shear stress is approximately 0.1 Pa, the intimal thickening was only partially suppressed. These values were found to be in agreement with those of studies conducted previously. (Porter et al., 1996)

CHAPTER 3: COMPUTATIONAL FLUID DYNAMICS

3.1 Overview of Computational Fluid Dynamics

Computational fluid dynamics (CFD) is a technique which is used to simulate problems related to fluid flow, heat flow and other related fields, such as multiphase mixing by making use of computers. The technique makes use of numerical methods to solve for complex problems. Several iterations are carried out until the solution converges within a specified tolerance range (Versteeg & Malalasekera, 2007).

The method is sometimes a good alternative to traditional experiment-based approaches for several reasons. CFD results in huge time and cost savings and once the software packages and necessary hardware have been purchased, they can be used for a wide variety of experiments. The cost of setting up CFD calculations and obtaining results is far less than that of setting up a technologically advanced laboratory and the software can be used to model situations which would be dangerous in real life. Finally, experiments which would be difficult to set up in a laboratory can be set up with less difficulty using CFD software and one can examine them to as much detail as is desired (within the limits of the operating system) (Versteeg & Malalasekera, 2007).

3.2 The functioning of a CFD code

CFD packages make use of numerical algorithms to solve or analyse the problems. They are made up of a pre-processor, a solver and a post-processor. Each section is explained in a paragraph below (Versteeg & Malalasekera, 2007).

3.2.1 Pre-processor

The pre-processor allows the user to define the flow problem. The first step is the definition of the computational domain which will be used. From there, a grid is generated. This is achieved by dividing the domain into smaller units known as control volumes. One then defines the phenomena that need to be studied in that particular case and assigns fluid properties. Lastly, the boundary conditions are specified (Versteeg & Malalasekera, 2007). GAMBIT was used as the pre-processor for this study.

3.2.2 Solver

The solver makes use of numerical algorithms to solve the governing equations for that specific problem. Different algorithms can be used including the finite element method, the finite volume method and spectral methods. Most commercial CFD codes make use of the finite volume method which is a specialised form of the finite difference method (Versteeg & Malalasekera, 2007).

The numerical algorithm selected for solving CFD problems generally follows three steps. Firstly, the governing equations for the specific problem are integrated over all the control volumes. The integral equations are then converted into a system of equations into a process known as discretisation. Finally, an iterative method is used to solve the system of equations (Versteeg & Malalasekera, 2007).

3.2.3 Post-processor

The post-processor allows for the visualisation of data obtained from the solver. The data can be visualised in various forms including contours, vectors and plots (Versteeg & Malalasekera, 2007). FLUENT was used as the solver and post-processor for this study.

3.3 The finite volume method

The finite volume method is the most widely used numerical algorithm in CFD packages. It is used to solve partial differential equations. The method "calculates the values of the conserved variables averaged across the volume" (Weisstein, 2009). The method involves the subdivision of the domain into smaller finite volumes to which the governing equations are applied.

The characteristic transport equation which is applied to the finite volume method is expressed below in words and is given by equation 3.1. This equation can be applied to fluid flow problems (Versteeg & Malalasekera, 2007).

$$\begin{pmatrix} Rate\ of \\ increase \\ of\ \phi\ of\ fluid \\ element \end{pmatrix} + \begin{pmatrix} Net\ rate\ of \\ flow\ of\ \phi\ out \\ of\ fluid\ element \end{pmatrix} = \begin{pmatrix} Rate\ of \\ increase \\ of\ \phi\ due\ to \\ diffusion \end{pmatrix} + \begin{pmatrix} Rate\ of \\ increase\ of \\ \phi\ due\ to \\ sources \end{pmatrix}$$

$$\frac{\partial(\rho\phi)}{\partial t} + div(\rho\phi\boldsymbol{u}) = div(\Gamma grad\phi) + S_\phi \qquad (3.1)$$

3.4 Pressure-velocity coupling

The momentum equations for three-dimensional laminar steady flow are given below. Equation 3.2 is the x-momentum equation, Eq. 3.3 is the y-momentum equation and Eq. 3.4 is the z-momentum equation. Eq. 3.5 is the continuity equation.

$$\frac{\partial}{\partial x}(\rho uu) + \frac{\partial}{\partial y}(\rho vu) + \frac{\partial}{\partial z}(\rho wu) = \frac{\partial}{\partial x}\left(\mu\frac{\partial u}{\partial x}\right) + \frac{\partial}{\partial y}\left(\mu\frac{\partial u}{\partial y}\right) + \frac{\partial}{\partial z}\left(\mu\frac{\partial u}{\partial z}\right) - \frac{\partial p}{\partial x} + S_u \qquad (3.2)$$

$$\frac{\partial}{\partial x}(\rho uv) + \frac{\partial}{\partial y}(\rho vv) + \frac{\partial}{\partial z}(\rho wv) = \frac{\partial}{\partial x}\left(\mu\frac{\partial v}{\partial x}\right) + \frac{\partial}{\partial y}\left(\mu\frac{\partial v}{\partial y}\right) + \frac{\partial}{\partial z}\left(\mu\frac{\partial v}{\partial z}\right) - \frac{\partial p}{\partial y} + S_v \quad (3.3)$$

$$\frac{\partial}{\partial x}(\rho uw) + \frac{\partial}{\partial y}(\rho vw) + \frac{\partial}{\partial z}(\rho ww) = \frac{\partial}{\partial x}\left(\mu\frac{\partial w}{\partial x}\right) + \frac{\partial}{\partial y}\left(\mu\frac{\partial w}{\partial y}\right) + \frac{\partial}{\partial z}\left(\mu\frac{\partial w}{\partial z}\right) - \frac{\partial p}{\partial z} + S_w \quad (3.4)$$

$$\frac{\partial}{\partial x}(\rho u) + \frac{\partial}{\partial y}(\rho v) + \frac{\partial}{\partial z}(\rho w) = 0 \quad (3.5)$$

When looking at the first three equations, one will notice that the convective terms contain non-linear terms. For example, in Eq. 3.2, the first term contains ρu^2. It is also clear that all the equations are coupled as each equation contains u-,v- and w-velocity terms. Finally, each of the momentum equations contains a pressure term. There is, however, no additional transport equation for the pressure. This coupling of velocity and pressure is no as pressure-velocity coupling. Special iterative algorithms are required to solve such problems and are discussed in the subsequent paragraphs. The basic solving procedure is that a guessed pressure field is used in order to solve the momentum equations. From there, a pressure correction equation is deduced from the continuity equation and used to find the pressure correction field. This is then used for the next iteration and the process is repeated until convergence is reached (Versteeg & Malalasekera, 2007).

3.4.1 SIMPLE Algorithm

The Semi-Implicit Method for Pressure Linked Equations (SIMPLE) algorithm is an iterative method which solves for pressure and velocity fields. The basic steps followed in the algorithm can be seen in Fig. 3.1. This is a fairly simple yet effective method. The disadvantage of the method is that even though the pressure correction fairs well when dealing with the velocity field, it is not very accurate when correcting the pressure field (Versteeg & Malalasekera, 2007).

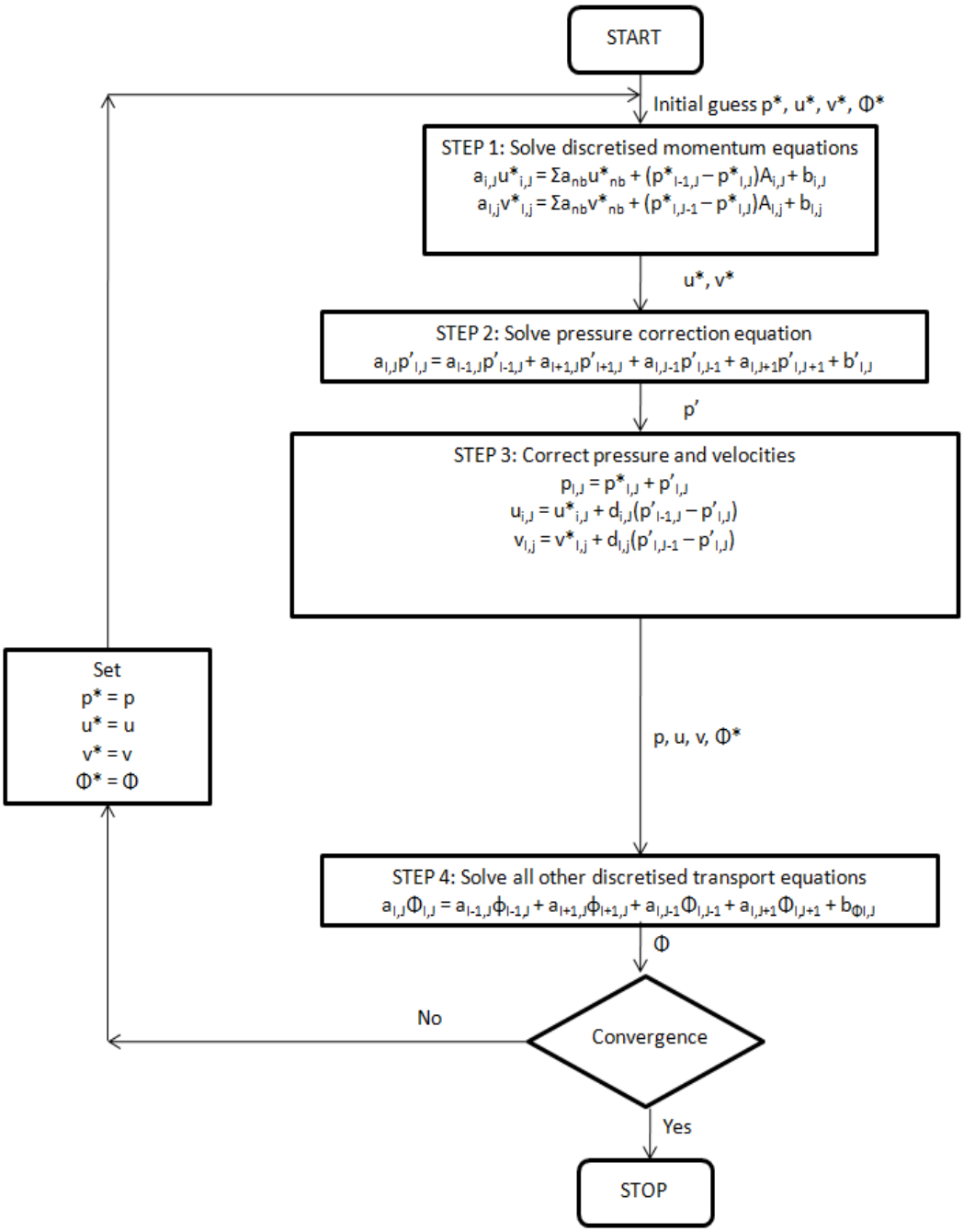

Figure 3.1: The SIMPLE algorithm (Versteeg & Malalasekera, 2007)

3.4.2 SIMPLER Algorithm

The SIMPLE Revised (SIMPLER) algorithm is based on the SIMPLE algorithm. Rather than making use of a pressure correction equation a discretised pressure equation is derived from a discretised continuity equation. This makes the procedure for correcting the pressure field more accurate than in the SIMPLE method. This algorithm is more efficient than

SIMPLE with regards computational effort. The procedure followed can be seen in Fig. 3.2 (Versteeg & Malalasekera, 2007).

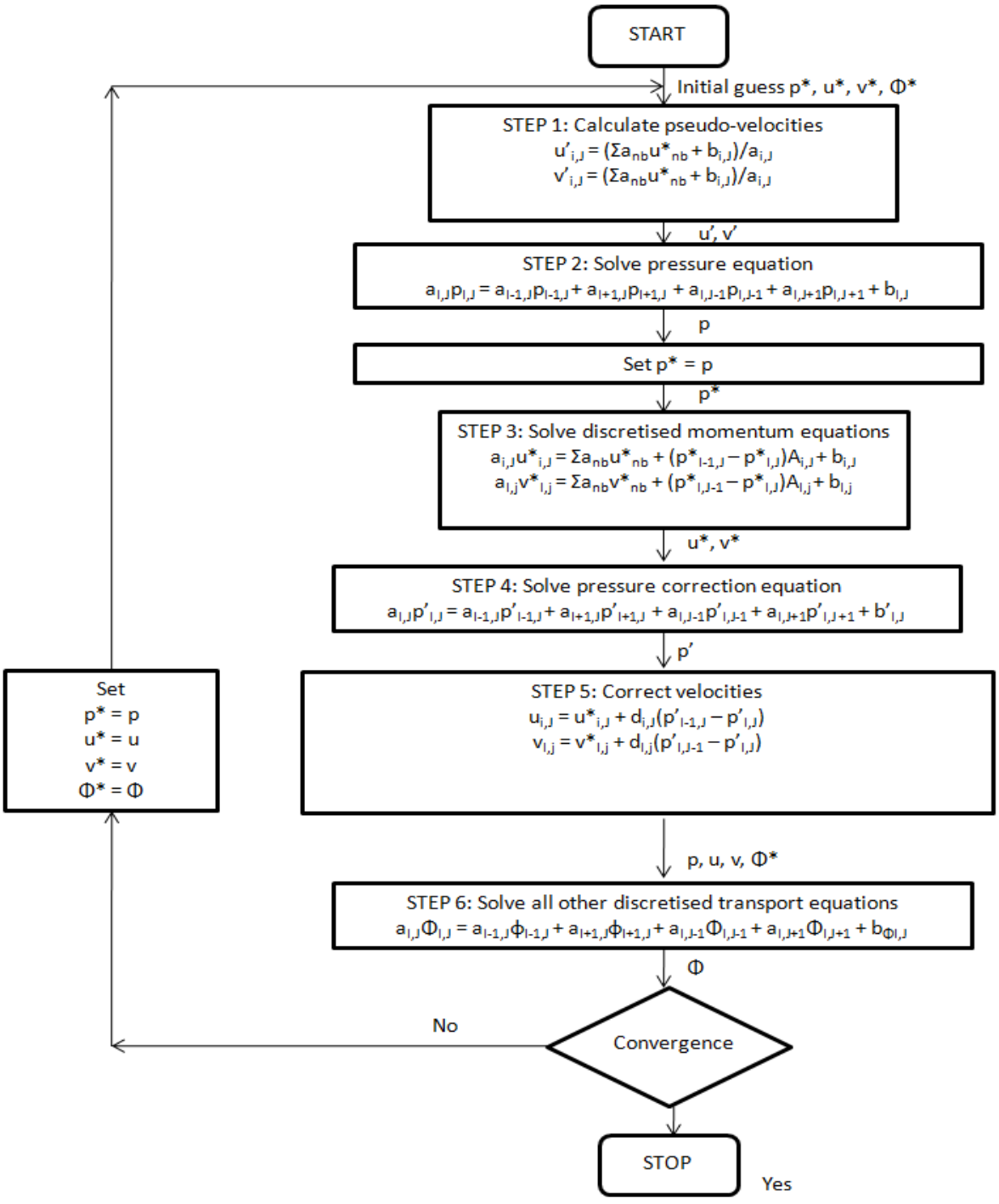

Figure 3.2: The SIMPLER algorithm (Versteeg & Malalasekera, 2007)

3.4.3 SIMPLEC Algorithm

The SIMPLE Consistent (SIMPLEC) algorithm is also based in the SIMPLE algorithm. In this case, however, velocity correction equation terms that are less important are omitted. This is achieved through the manipulation of the momentum equations. The steps followed in this algorithm are identical to those followed in the SIMPLE algorithm and can be seen in Fig. 3.3. This method has proved to be similar to the SIMPLER method in that it is just as efficient (Versteeg & Malalasekera, 2007).

3.4.4 PISO Algorithm

The Pressure Implicit with Splitting of Operators (PISO) algorithm was originally developed for non-iterative unsteady compressible flow problems but has been adapted to suit iterative steady flow computations. The method is similar to the SIMPLE formulation in that it is made of predictor and corrector steps. Unlike SIMPLE, however, it consists of two corrector steps which can be seen in Fig. 3.4. In comparison to the SIMPLER method, it is just as efficient and has the added advantage of being more efficient in terms of computational effort. It also exhibited better convergence characteristics (Versteeg & Malalasekera, 2007).

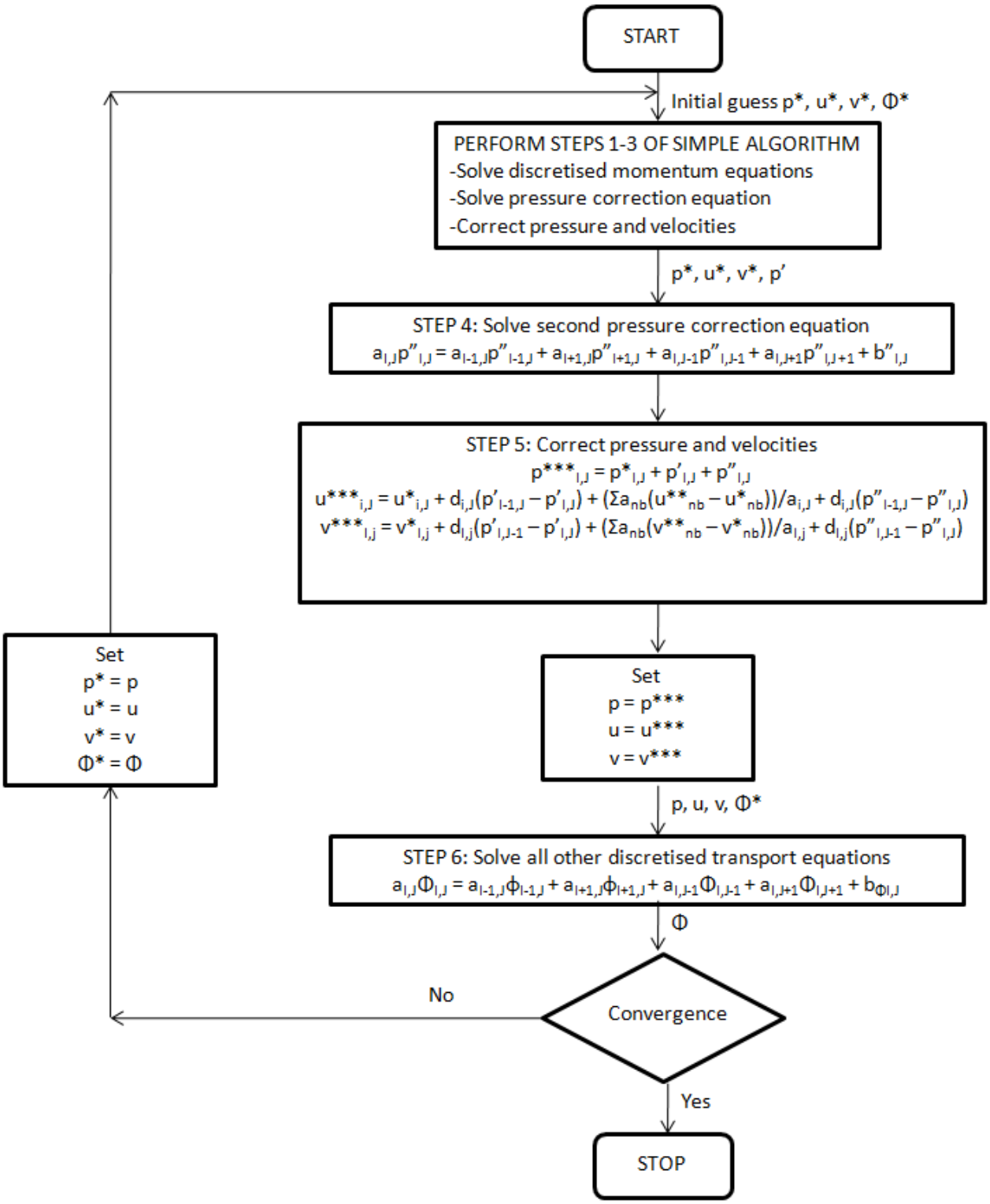

Figure 3.3: The PISO algorithm (Versteeg & Malalasekera, 2007)

CHAPTER 4: GOVERNING EQUATIONS

4.1 Conservation laws

In order to effectively represent fluid flow models, three conservation laws of physics need to be taken into account. The first, mass conservation, stipulates that the mass of the fluid needs to be conserved and can be seen in Eq. 4.1.

$$\frac{\partial \rho}{\partial t} + \frac{\partial (\rho u)}{\partial x} + \frac{\partial (\rho v)}{\partial y} + \frac{\partial (\rho w)}{\partial z} = 0 \tag{4.1}$$

The second, Newton's second law, states that the rate of change of momentum is equal to the forces that act on the fluid and can be seen in Eqs. 4.2 to 4.4. Equation 4.2 is the x-component of the momentum equation, Eq. 4.3 is the y-component of the momentum equation and Eq. 4.4 the z-component.

$$\rho \frac{Du}{Dt} = \frac{\partial (-p + \tau_{xx})}{\partial x} + \frac{\partial \tau_{yx}}{\partial y} + \frac{\partial \tau_{zx}}{\partial z} + S_{Mx} \tag{4.2}$$

$$\rho \frac{Dv}{Dt} = \frac{\partial \tau_{xy}}{\partial x} + \frac{\partial (-p + \tau_{yy})}{\partial y} + \frac{\partial \tau_{zy}}{\partial z} + S_{My} \tag{4.3}$$

$$\rho \frac{Dw}{Dt} = \frac{\partial \tau_{xz}}{\partial x} + \frac{\partial \tau_{yz}}{\partial y} + \frac{\partial (-p + \tau_{zz})}{\partial z} + S_{Mz} \tag{4.4}$$

The third, the first law of thermodynamics, states that the rate of change of energy is equal to the heat added to and work done on a fluid particle and can be seen in Eq. 4.5.

$$\rho \frac{DE}{Dt} = -div(p\boldsymbol{u}) + \left[\frac{\partial(u\tau_{xx})}{\partial x} + \frac{\partial(u\tau_{yx})}{\partial y} + \frac{\partial(u\tau_{zx})}{\partial z} + \frac{\partial(v\tau_{xy})}{\partial x} + \frac{\partial(v\tau_{yy})}{\partial y} + \frac{\partial(v\tau_{zy})}{\partial z} + \frac{\partial(w\tau_{xz})}{\partial x} + \frac{\partial(w\tau_{yz})}{\partial y} + \frac{\partial(w\tau_{zz})}{\partial z}\right] + div(kgradT) + S_E \quad (4.5)$$

4.2 Navier-Stokes equations for a Newtonian fluid

The Navier-Stokes equations are derived for fluid substances. They are derived from Newton's second law. Assumptions made when deriving the equations is that fluid stress is the sum of a diffusing viscous term and a pressure term. Solutions for the Navier-Stokes equations are velocity fields which can then be used to derive other variables, such as forces. The equations are given by Eqs. 4.6 to 4.8 below (Versteeg & Malalasekera, 2007).

$$\rho \frac{Du}{Dt} = -\frac{\partial p}{\partial x} + \frac{\partial}{\partial x}\left[2\mu \frac{\partial u}{\partial x} + \lambda div\boldsymbol{u}\right] + \frac{\partial}{\partial y}\left[\mu\left(\frac{\partial u}{\partial y} + \frac{\partial v}{\partial x}\right)\right] + \frac{\partial}{\partial z}\left[\mu\left(\frac{\partial u}{\partial z} + \frac{\partial w}{\partial x}\right)\right] + S_{Mx} \quad (4.6)$$

$$\rho \frac{Dv}{Dt} = -\frac{\partial p}{\partial y} + \frac{\partial}{\partial x}\left[\mu\left(\frac{\partial u}{\partial y} + \frac{\partial v}{\partial x}\right)\right] + \frac{\partial}{\partial y}\left[2\mu \frac{\partial v}{\partial y} + \lambda div\boldsymbol{u}\right] + \frac{\partial}{\partial z}\left[\mu\left(\frac{\partial v}{\partial z} + \frac{\partial w}{\partial y}\right)\right] + S_{My} \quad (4.7)$$

$$\rho \frac{Dw}{Dt} = -\frac{\partial p}{\partial z} + \frac{\partial}{\partial x}\left[\mu\left(\frac{\partial u}{\partial z} + \frac{\partial w}{\partial x}\right)\right] + \frac{\partial}{\partial y}\left[\mu\left(\frac{\partial v}{\partial z} + \frac{\partial w}{\partial y}\right)\right] + \frac{\partial}{\partial z}\left[2\mu \frac{\partial w}{\partial z} + \lambda div\boldsymbol{u}\right] + S_{Mz} \quad (4.8)$$

4.3 Hagen-Poiseulle flow

Hagen-Poiseulle flow is the fully developed flow of a Newtonian fluid through a circular tube with a constant radius. The tube is straight, rigid walled and cylindrical. The flow is laminar and steady. This model is not entirely accurate for blood flow through vessels as this kind of flow tends to be pulsatile and unsteady. Blood flow through the veins, however, is non-pulsatile and largely steady, hence this model can be applied to flow through the veins (Kundu & Cohen, 2008).

The axial velocity for Hagen-Poiseulle flow is given by Eq. 4.9 and is defined in terms of the pipe radius. The maximum velocity occurs at the centre of the tube (where the radius is zero) and is given by Eq. 4.10. The volume flow rate is given by Eq. 4.11 and is called the Poiseulle formula. The volume flow rate is expressed in terms of the maximum velocity in Eq. 4.12. The average velocity over the cross section is given by Eq. 4.13 while the shear stress is given by Eq. 4.14.

$$\dot{x} = \frac{a^2 - r^2}{4\mu}\left(\frac{dp}{dx}\right) \tag{4.9}$$

$$\dot{x}_{max} = \frac{a^2}{4\mu}\left(\frac{dp}{dx}\right) \tag{4.10}$$

$$Q = \frac{\pi a^4}{8\mu}\left(\frac{dp}{dx}\right) \tag{4.11}$$

$$Q = \frac{\dot{x}_{max}}{2}\pi a^2 \tag{4.12}$$

$$\dot{x}_{avg} = \frac{\dot{x}_{max}}{2} \tag{4.13}$$

$$\tau = \frac{4\mu\dot{Q}}{\pi r^3} \tag{4.14}$$

Blood vessels can be modelled as cylindrical tubes with laminar flow moving through them. The assumption holds so long as the tube is long and the flow remains steady. Flow is considered to be steady if the flow pattern does not change with time or distance. It is assumed that the flow obeys the Navier-Stokes equations of motion for incompressible fluids and that there is a no-slip condition at the vessel wall. The other boundary condition is that the flow is axisymmetric because the tube is axisymmetric, hence axial velocity is the only velocity which needs to be taken into account. This velocity is a function of the radius distance and not of the axial length because the flow is steady (does not change with axial distance) (Fung, 1993).

The parabolic velocity profile for blood flow described by Hagen-Poiseulle flow is circled in Fig. 4.1.

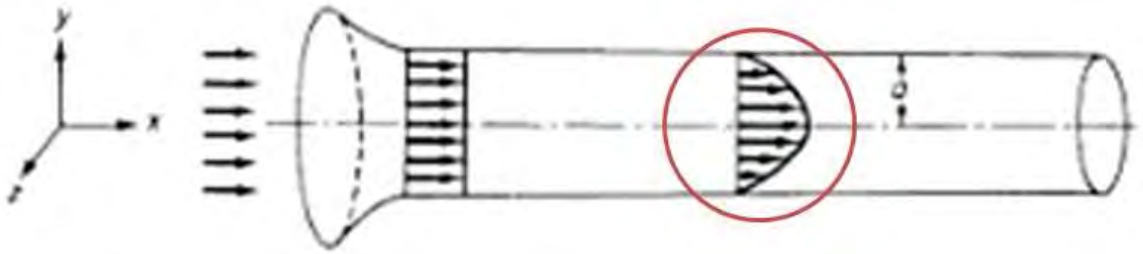

Figure 4.1: Parabolic velocity profile for Newtonian blood flow. (Fung, 1993)

CHAPTER 5: DESIGN OF EXPERIMENT

Owing to the complexity of the human body, there are many variables which could be considered when trying to evaluate the factors which contribute to intimal thickening in veins. It is therefore extremely important to outline the most important factors which need to be considered and then to define how these factors will be examined.

5.1 Overview of the factors to be considered

The three main factors which are thought to have a major influence on flow patterns and shear stresses in the vein are the number of side branches per portion of main vein, the ratio of the side branch diameter to the main vein diameter and the geometric configuration of the veins (the way in which the side branches attach to the main branch). Intimal hyperplasia is often associated with low shear stresses and low flow velocities. By examining the effect of the above-mentioned factors on shear stress and flow patterns, the link between these factors and intimal hyperplasia can be made.

The data from Human et al. (2009), gives the number of side branches for two centimetre portions of the saphenous vein. As a result, the investigation carried out will be for two centimetre portions of the main vein.

5.2 Number of side branches

According to the data collected by Human et al. (2009), the number of side branches per two centimetre portion of saphenous vein varies between zero and five (see Fig. 2.8). These

two figures are at the extreme ends of the spectrum. The most common maximum number of side branches for the harvested veins is three. This number can therefore be considered the general maximum. Models with one, two and three side branches were developed. The model with a single side branch was developed to obtain an idea as to the effect of a side branch on flow patterns, shear stress and pressure gradients. The triple side branch model was developed because this is the most commonly occurring maximum number of side branches. Finally, the double side branch model was developed to give an intermediate solution between the single and triple side branch models.

5.3 Ratio of the side branch diameter to the main vein diameter

The side branch diameter to main vein diameter ratio in the data collected by Human et al. (2009) varies between 0.189 and 0.500. Models were developed for a range of ratios (0.200, 0.300, 0.400 and 0.500) for single, double and triple side branch models. This was done as it was thought that this ratio would play a rather significant role in the development of intimal cushions. For the double and triple side branch models, all the side branches have the same ratio to the main vein.

5.4 Geometry

As was stated in chapter 2, there is great variability in the anatomy of the superficial veins of the leg. The task of varying the geometry of the veins, therefore, is rather cumbersome as there exists a large number of geometric configurations for these veins. In order to simplify the task of modelling the vein geometry, several assumptions were made. It was assumed that in most cases, the side branches attach to the main vein at a 45^{o} angle rather than 90^{o}. It was also assumed that the side branches which were attached at 45^{o} point in the direction of flow of blood through the main vein. Figure 5.1 gives a diagrammatic illustration of what is meant by the side branches pointing in the direction of flow. Despite this assumption,

both a 45^{o} and a 90^{o} model were investigated so as to determine the effect of geometry on fluid dynamics in the region of side branches. The final assumption made with respect to the geometry was that the main vein and the side branches all lie in the same plane.

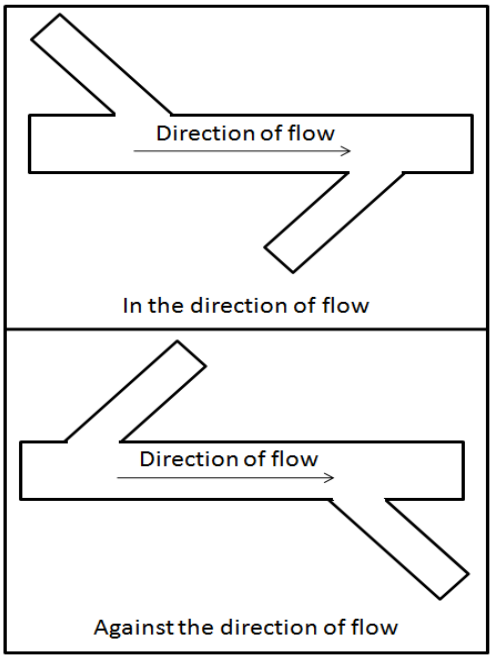

Figure 5.1: Diagram illustrating what is meant by 'in the direction of flow'.

5.5 Summary of simulations carried out

All the simulations which were run in order to determine the effects of the various factors on flow dynamics in the veins are listed in Table 5.1.

Table 5.1: Table illustrating the simulations carried out for the investigation

Geometry	*45°*			*90°*		
Side branches	1	2	3	1	2	3
Ratio	0.2	0.2	0.2	0.2	0.2	0.2
	0.3	0.3	0.3	0.3	0.3	0.3
	0.4	0.4	0.4	0.4	0.4	0.4
	0.5	0.5	0.5	0.5	0.5	0.5

5.6 Control configuration

A control simulation was run in order to establish benchmark figures. The model which was developed for this simulation is a main vein which has the same dimensions as the main veins used for all the other models. The difference with this model is that there are no side branches attached to it. This model therefore simulates the conditions to be expected in a normal vein without the side branches affecting the fluid dynamics in the vein. This control simulation, in conjunction with data found in literature, was used to evaluate the results obtained from the other simulations. By comparing the results obtained from the control simulation with the other simulations, judgements were made regarding the effect of side branches on fluid dynamics in veins.

CHAPTER 6: MODEL DEVELOPMENT

This section outlines the development of the model used for the blood flow through the veins. It details the method used for the simulations and the reasoning behind the method. The assumptions made when developing the model are detailed in the first section. From there, the geometry, mesh and FLUENT settings are outlined. The user-defined functions used are given in Appendix A while the inputs used for all the models can be found in Appendix B.

6.1 Assumptions made when developing the model

Assumptions pertaining to the physical model of the vein

1. The dimensions and cross-section of the veins remain constant along the entire length of the vein.
2. The veins have a circular cross-section.
3. The veins do not contain any valves.
4. For models where there is more than one side branch attaching to the main vein, all the side branches have the same dimensions.
5. For the 45^{o} model, the side branches point in the direction of flow of blood in the main vein.
6. The side branches lie in the same plane as the main vein.

Assumption pertaining to blood and blood flow

1. Blood is a homogeneous fluid with constant density and viscosity.
2. Blood flows through the venous system in a steady, non-pulsatile manner.
3. Blood in the main vein and side branches behaves in a Newtonian manner. This assumption can be made because all these veins have a sufficiently large diameter.

4. The flow can be adequately described using the Hagen-Poiseulle model.
5. The velocity of flow of the blood remains constant through the venous system. The velocity at the inflows will therefore be constant for all the inflows for a given model.
6. The flow rate at the outflow of all the models is constant and its value is 40ml/min ($6.67\times10\text{-}07m^3/s$).
7. The flow rate is proportional to the square of the diameter. The flow rates for the individual inflows for any given model are calculated accordingly. They do, however, satisfy the continuity equation and the sum of the inlet flow rates equals the outflow flow rate.
8. For any given model, the side branch flow rates are equal.

6.2 Geometry used for the models

The diagrams below show the geometry used for the different models and the elements used in different regions within these models. Figure 6.1 shows the geometry for the control model. Figure 6.2 shows the geometry for the 45^o, single side branch model, Fig. 6.3 for the 45^o, double side branch model and Fig. 6.4 for the 45^o, triple side branch model. Figure 6.5 shows the geometry for the 90^o, single side branch model, Fig. 6.6 for the 90^o, double side branch model at 90^o and Fig. 6.7 for the 90^o, triple side branch model. (Note: For all the diagrams shown below, the shaded regions represent hexahedral elements while the white regions represent tetrahedral elements.

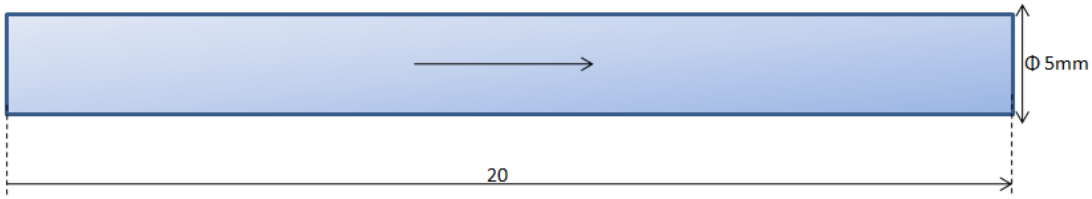

Figure 6.1: Geometric model for the control simulation

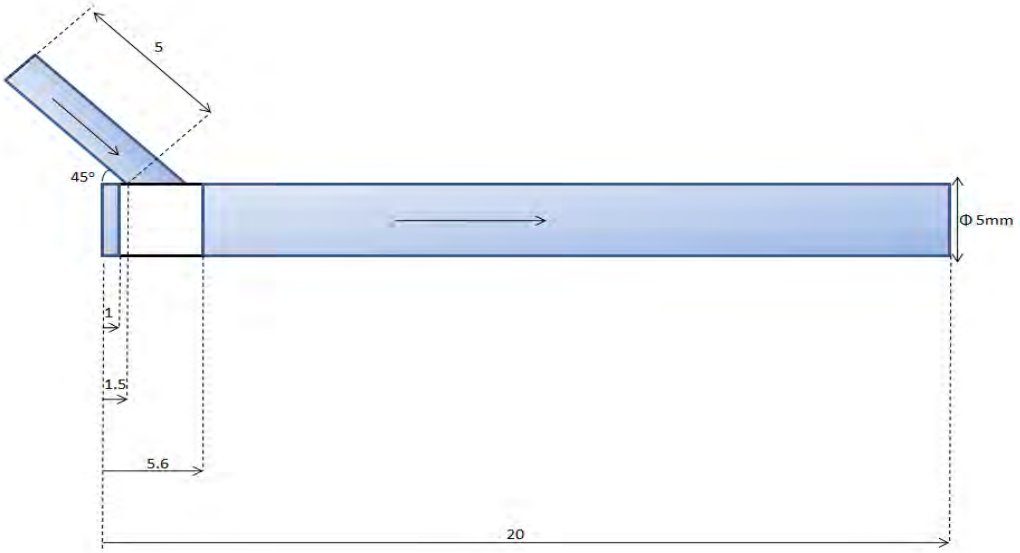

Figure 6.2: Geometric model for the single side branch 45^{o} model

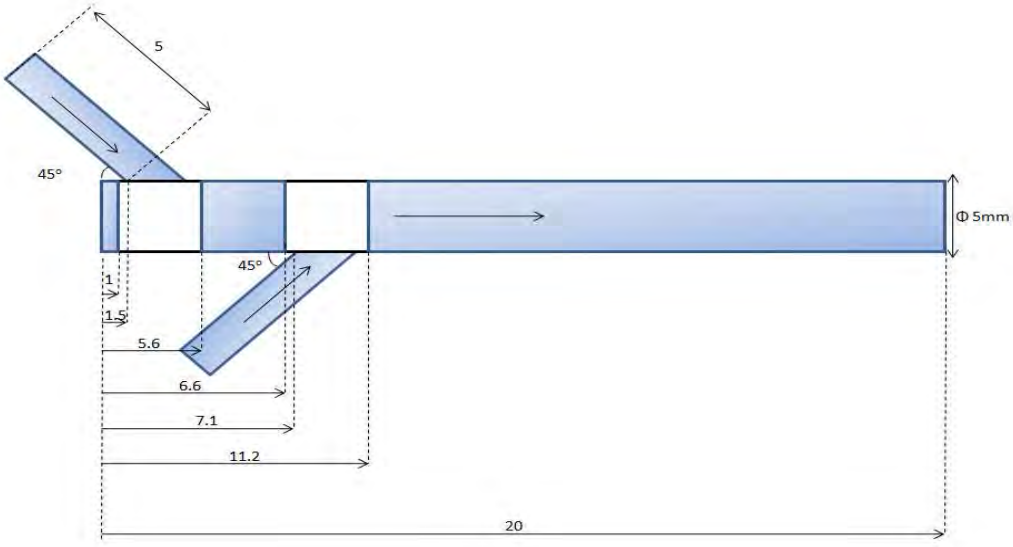

Figure 6.3: Geometric model for the double side branches 45^{o} model

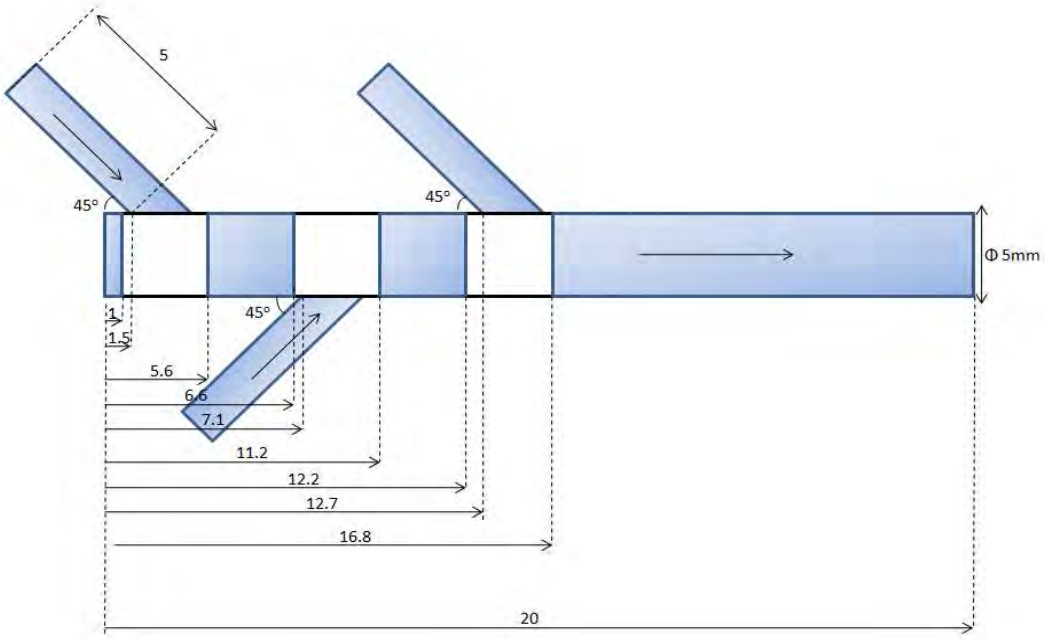

Figure 6.4: Geometric model for the triple side branches 45^o model

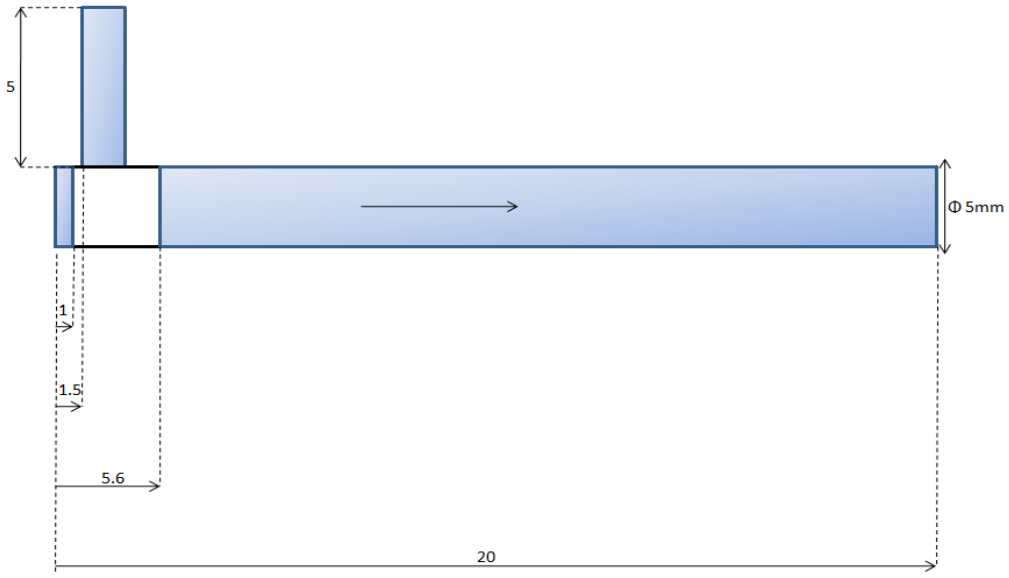

Figure 6.5: Geometric model for the single side branch 90^o model

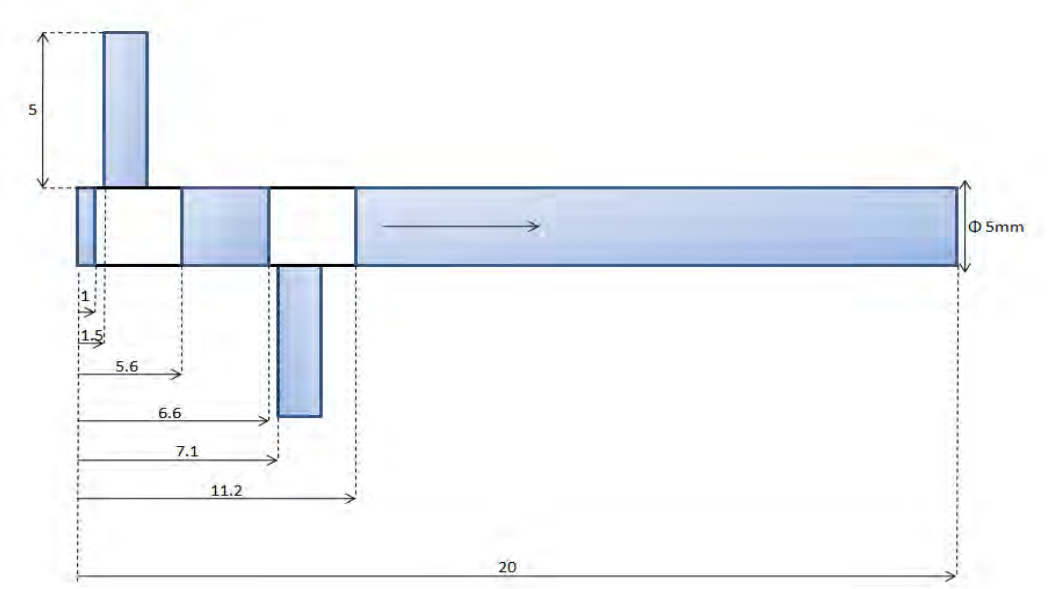

Figure 6.6: Geometric model for the double side branch 90^o model

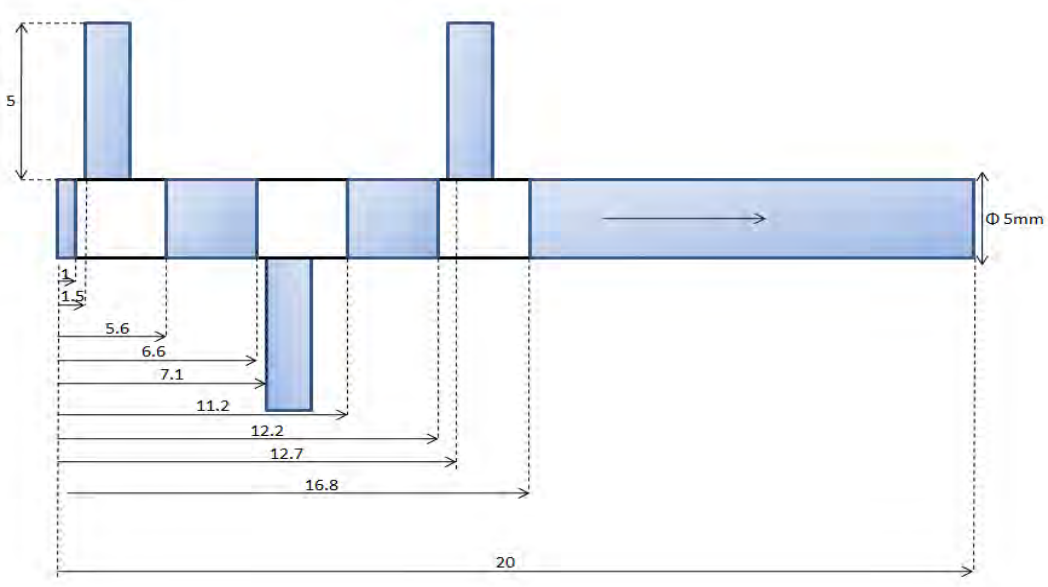

Figure 6.7: Geometric model for the triple side branches 90^o model

6.3 Mesh

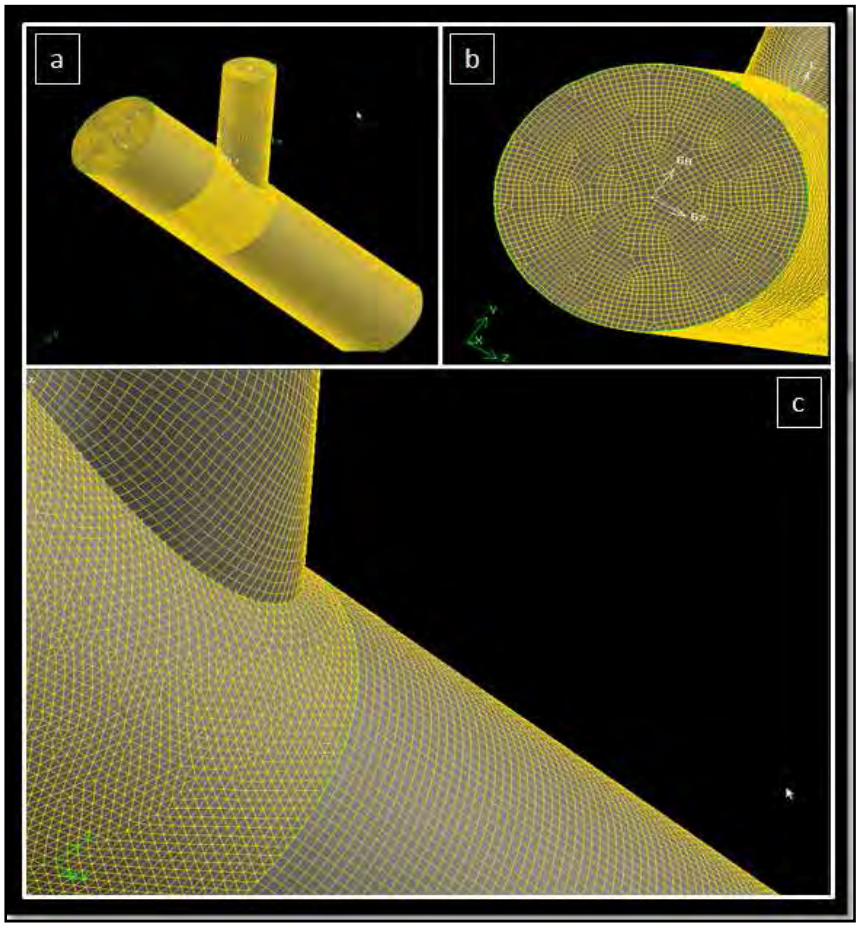

Figure 6.8: Diagram illustrating the mesh used for the first stage of simulations

All the meshes were developed using GAMBIT. The mesh utilised for the single branch model can be seen in Fig. 6.8(a). Most of the mesh is made up of hexahedral elements while the portion where the side branch attaches to the main vein is made up of tetrahedral elements as is seen in Fig. 6.8(b). This is different from the rest of the geometry because it is rather cumbersome to mesh a portion with a hole using hexahedral elements. The end face is paved in an unstructured quadrilateral mesh as is seen in Fig. 6.8(c). This is acceptable because parabolic inlet velocity profiles are used hence the gradient is relatively constant for the most part and it is not necessary to make some cells more refined than others as is seen in Fig. 6.9. The same approach is followed for both the double and triple branch models.

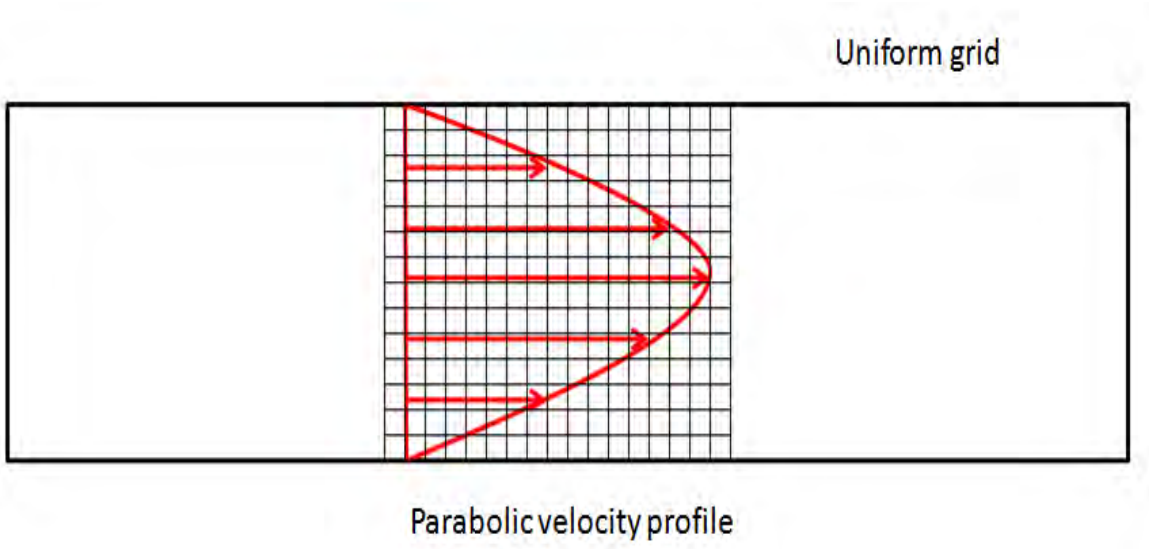

Figure 6.9: Diagram illustrating the gradual change in slope of a parabolic velocity profile thus justifying the use of a uniform grid.

6.4 Model symmetry

Even though the models are symmetric along the vein length, symmetry was not used when building the model. The symmetric nature of the model can be seen in Fig. 6.8(a). The main reason for this was that for some of the preliminary shear stress results, the shear stress contour patterns were not always symmetric. As a result, symmetry was not exploited.

6.5 Model regions and naming convention

Figure 6.10 illustrates the different model regions. This information was included because it becomes useful when reading through the results section where the descriptions sometimes refer to the different regions.

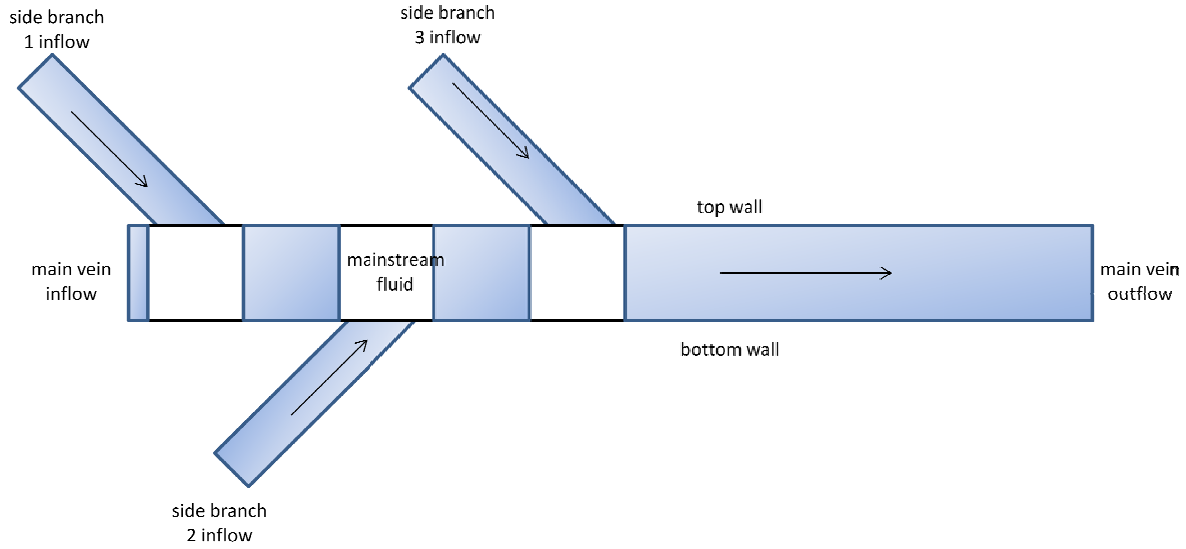

Figure 6.10: Diagram illustrating the different zones on the model

The models were named using the convention *"number of side branches_angle at which side branch is attached_ratio of side branch diameter to main vein diameter"*. For example, model 1_45_0.2 refers to a model with a single side branch attached at a 45^{o} angle. The ratio of the side branch diameter to main vein diameter is 0.2.

6.6 FLUENT Inputs

Table 6.1 details the general FLUENT settings. The specific settings for each model can be found in appendix B. All the models are developed in such a manner that the main vein diameter is kept constant at 5mm. This is done because the main intimal thickening observations were made on the main vein hence it was best to keep this diameter constant for comparison purposes.

The flow rate at the output of each model was kept constant at 40ml/min. The flow rate for each individual inflow was calculated in such a manner that the average velocity for all the

inflows for a given model were equal. The flow rates for all the side branches were also equal. This data can also be seen in appendix B.

Table 6.1: Table illustrating the general inputs for the FLUENT simulations

Variable	**Value/Input**
Material properties	
Blood density	1050kg/m^3
Blood dynamic viscosity	0.0032kg/ms
Solver type and solution methods	
Solver type	Pressure-based
Time	Steady
Pressure-velocity coupling scheme	SIMPLEC
Pressure setting	Standard
Momentum setting	Second order upwind

CHAPTER 7: RESULTS

This chapter presents the results for a selection of the most representative models developed in the study. The models are chosen in a manner such that the full spectrum of results is represented. Included in the section are the results from the control configuration. The full range of results can be found in appendix C. The chapter begins with a description of the criteria used to assess the results. This is followed by the flow pattern and velocity results, shear stress results and the pressure results. The final section is one which details the results from all the models including those presented in the former part of this chapter.

7.1 Criteria used when assessing the results

7.1.1 Flow pattern and velocity magnitude results

As discussed in section 2.6, intimal hyperplasia has been observed in lower flow velocity regions rather than higher flow velocity regions. The flow velocity in regions opposite the side branches was therefore examined relative to the flow velocity in the rest of the vein portion. Focus was placed on the highest and lowest flow velocity regions as well as the points at which they occurred. The high and low flow velocity regions were compared to each other and the individual models were compared to each other and to the control experiment.

7.1.2 Shear stress results

As discussed in section 2.6, the development of intimal hyperplasia is associated with regions of low shear stress. Zilla et. al (2009) found that the threshold value below which intimal hyperplasia was no longer suppressed was 0.5Pa while Porter et al. (1996) found that below a boundary shear stress value of 0.1Pa, intimal thickening was only partially suppressed in the native saphenous veins, i.e. in venous circulation. In the analysis the

major points focused on were those in the region of side branches and low shear stress points. The shear stress values in each model were examined and compared against the 0.5Pa and 0.1Pa threshold values. Finally, the individual models were compared with each other and with the control configuration.

7.1.3 Pressure results

Even though Dobrin et al. (1989) state that the formation of intimal hyperplasia is not related to static stress, the pressure in the regions of side branches was examined. The pressure results for individual models were compared to each other and to the control experiment.

7.2 Flow pattern and velocity magnitude results

The velocity magnitude graph plots the velocity data from the contour plot given in part A of each figure. The x-axis represents the distance along the length of the vein, i.e. from 0 to 0.02m. The y-axis represents the velocity magnitude values at the different points along the vein length. The models are all three-dimensional hence there will be multiple velocity values at any point along the x-axis, i.e. along the vein length. The y values closer to the origin represent the values closer to the wall of the vein. The maximum y values (the maximum y value for every x value) on the graph represent values closer to the centre of the flow (where the velocities are the highest).

Figure 7.1 shows the flow pattern and velocity magnitude results for the control configuration. As can be seen in Fig. 7.1(A), the model is a main vein without any side branches attached to it. The lowest velocity occurs at the walls of the vein and the maximum velocity occurs at the centre of the flow as is expected. The maximum velocity value is 0.0678m/s and can be seen in Fig. 7.1(B). All the velocity contours are straight and

parallel to each other with the thickest contour at the centre of the flow as seen in Fig. 7.1(A). Towards the vein wall, the velocity contours become narrower.

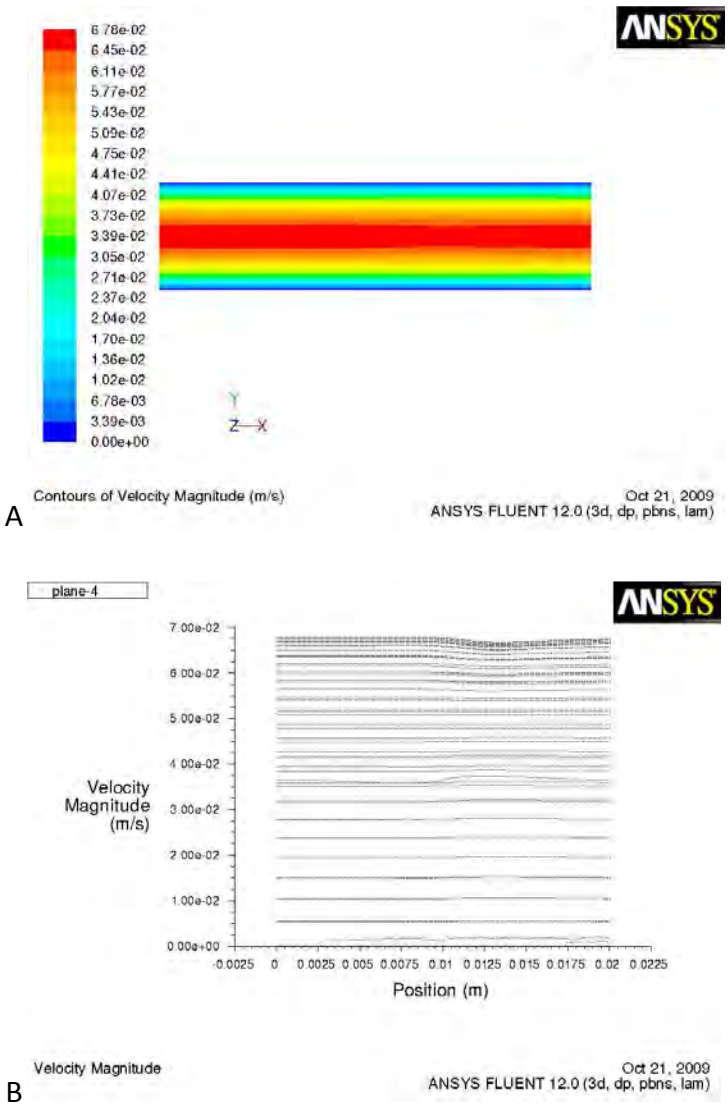

Figure 7.1: Velocity contour plot (A) and velocity magnitude graph (B) for the control configuration

Figure 7.2 shows the results for model 1_45_0.2. The velocity contours are somewhat similar to those of the control configuration. Most of the contours are parallel to each other with the exception of the higher flow velocity contours. In the vicinity of the side branch,

these are separated into two regions and have a parabolic shape as seen in Fig. 7.2(A). Fig. 7.2(B) shows that the maximum velocity occurs at the outflow of the model and has a value of 0.067m/s. The minimum velocity occurs in the region of the side branch and has a value of 0.061m/s.

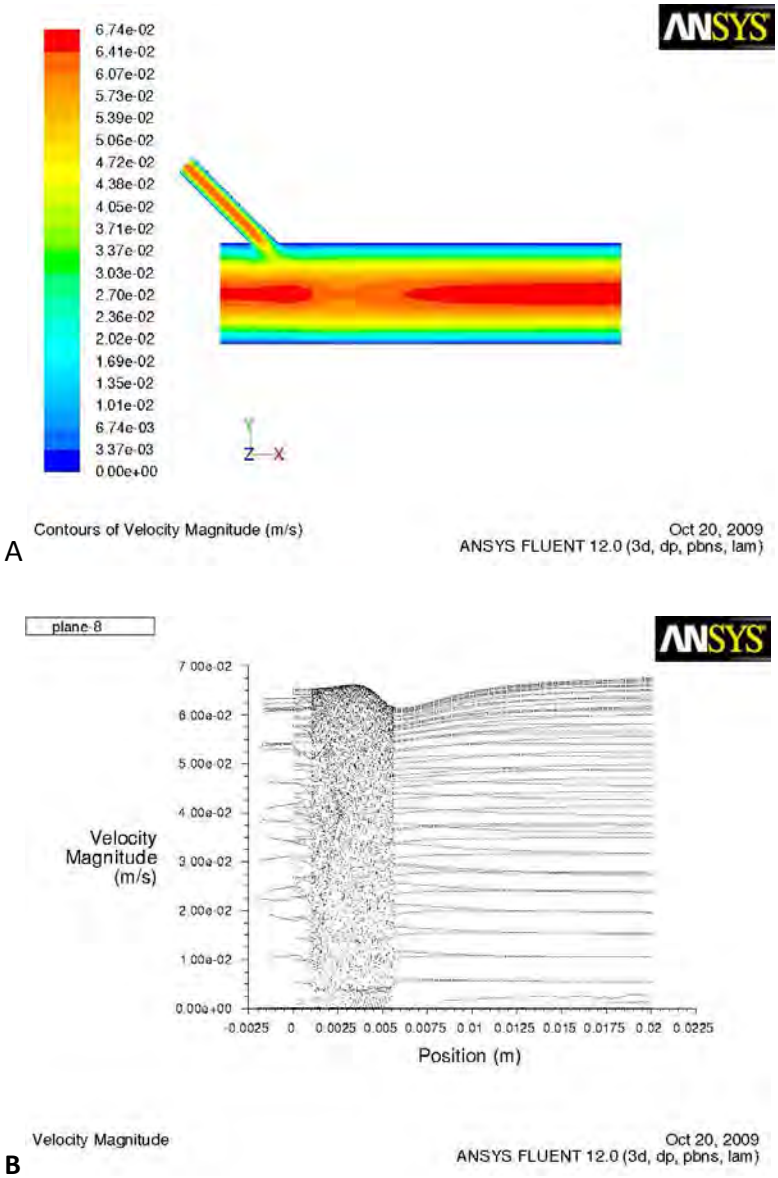

Figure 7.2: Velocity contour plot (A) and velocity magnitude graph (B) for 1_45_0.2

Figure 7.3 shows the results for model 1_45_0.5. The difference between this model and the one discussed in the previous paragraph is that the ratio between the side branch diameter and the main branch diameter is larger. In this model, the contours closest to the wall are parallel but towards the centre of the flow, the contours are somewhat distorted. The

contours closest to the centre of the flow are parabolic. Further out from the centre, the lower flow velocity contours extend into regions which would have been higher flow velocity regions had the model been the control configuration. This can be seen quite clearly in Fig. 7.3(A). Both the values of the maximum and minimum velocity can be extracted from Fig 7.3(B). The maximum velocity occurs at the centre of the outflow and has a value of 0.065m/s while the minimum velocity is 0.043m/s. This minimum occurs in the vicinity of the side branch.

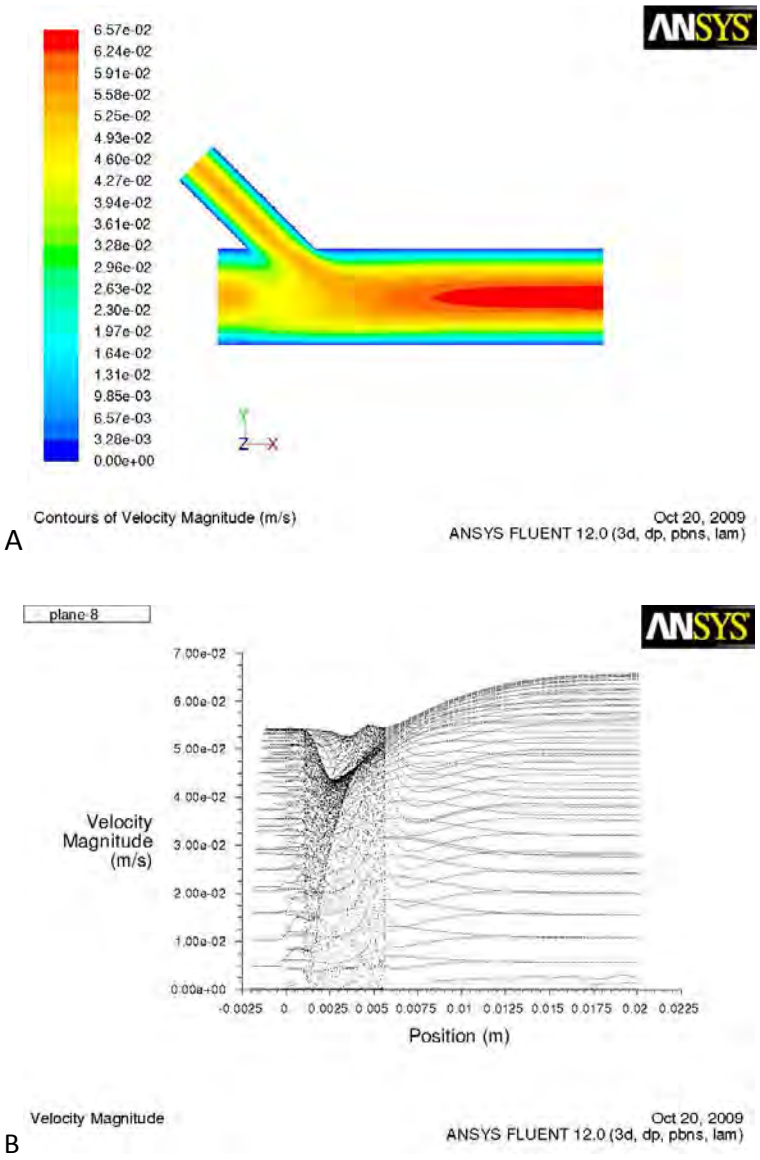

Figure 7.3: Velocity contour plot (A) and velocity magnitude graph (B) for 1_45_0.5

Figure 7.4 shows the results for model 1_90_0.2. The results are somewhat similar to those of model 1_45_0.2. The contour plot shows that the contours are parallel. As seen Fig. 7.4(A), those closest to the centre form a parabolic pattern which is divided into two regions in the vicinity of the side branch. From Fig 7.4(B), the maximum velocity is 0.0675m/s and occurs at the centre of the outflow. The minimum velocity is 0.0625m/s and occurs in the region of the side branch.

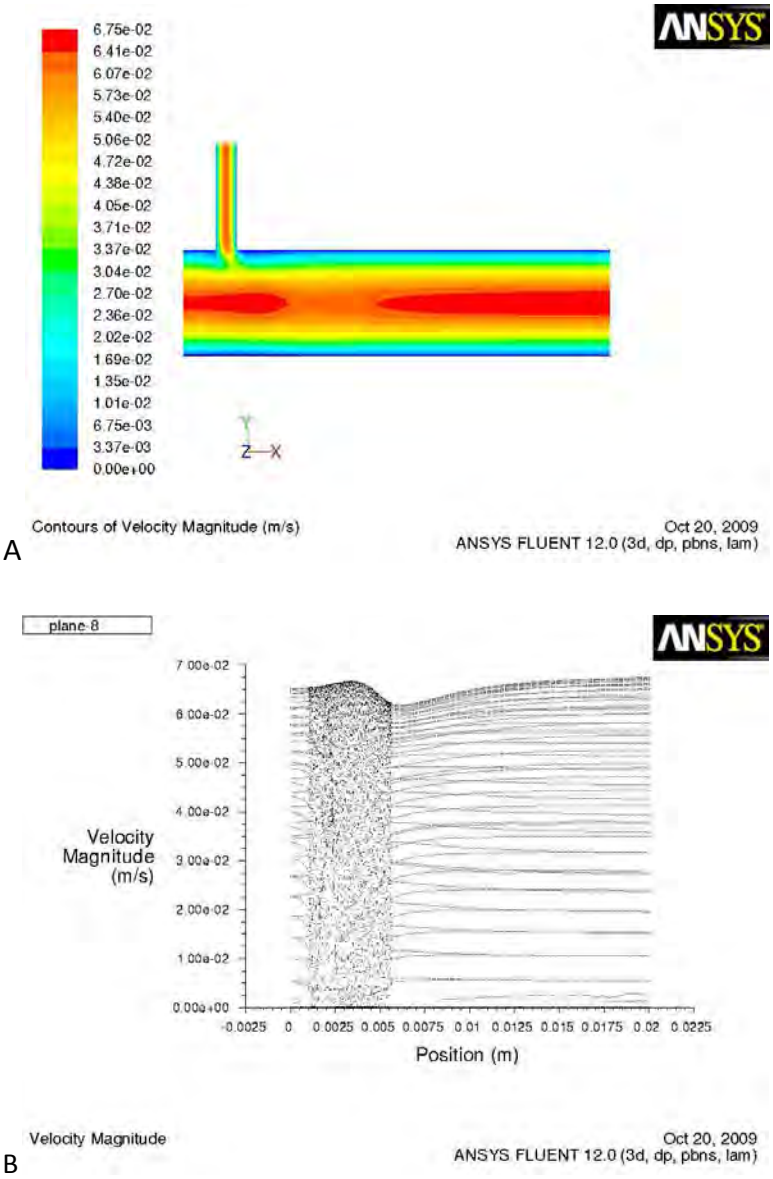

Figure 7.4: Velocity contour plot (A) and velocity magnitude graph (B) for 1_90_0.2

Figure 7.5 shows the results for model 2_45_0.5. The interaction of the flow from the two branches and the main vein flow results in a rather complex flow pattern as seen in Fig 7.5(A). The contours very close to the wall are parallel to the wall. The maximum velocity occurs very close to the outlet and its contour is parabolic in shape. The value of this contour is 0.063m/s. The flow close to the side branch is made up of relatively low flow velocity contours. These contours extend into regions which would have been higher flow velocity regions had the model been the control configuration. It is also interesting to note that even though the velocity in the region of side branches is lower than the surrounding vicinity, the side branch closer to the outflow has a higher flow velocity than the one closer to the main vein inflow. This can be seen in Fig 7.5(B). The minimum velocity, which occurs in the region of the side branch closest to the inflow, is 0.035m/s while the minimum velocity for the second side branch vicinity is 0.045m/s.

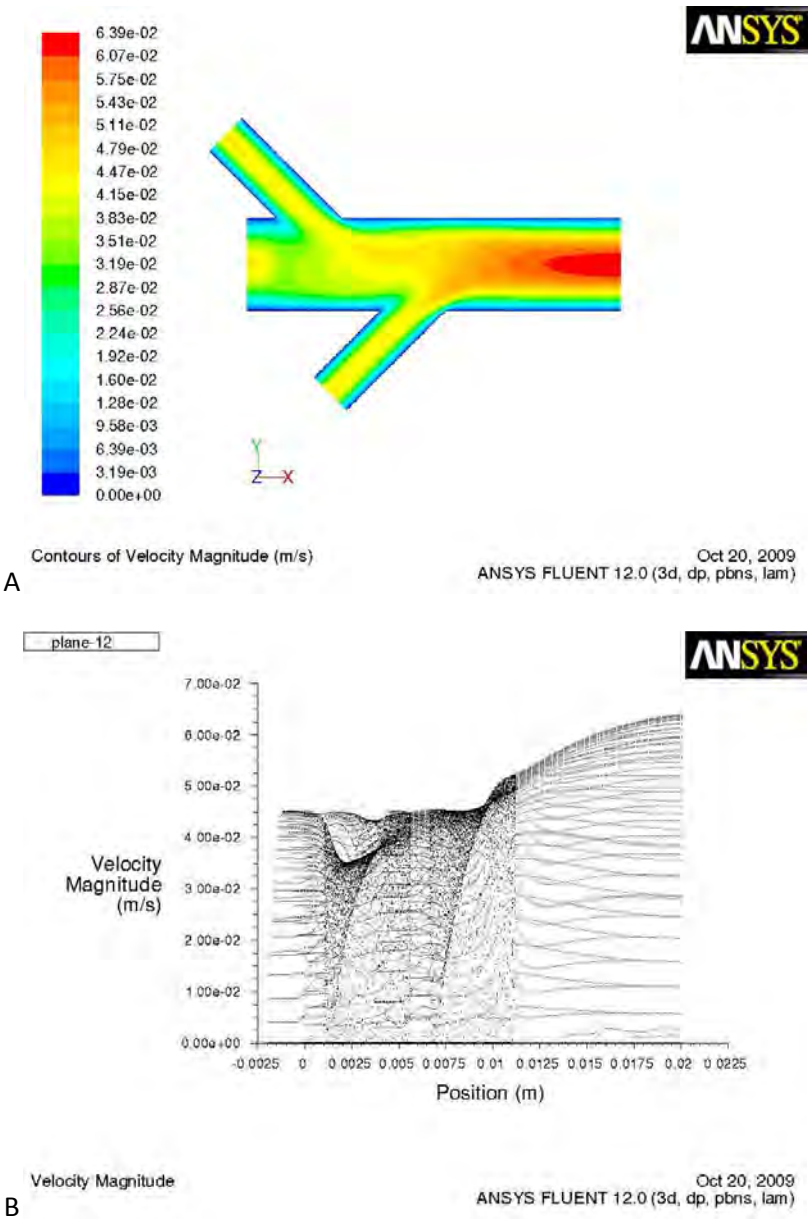

Figure 7.5: Velocity contour plot (A) and velocity magnitude graph (B) for 2_45_0.5

Figure 7.6 shows the results for model 3_45_0.5. The interaction of the flow between three side branches and the main vein flow results in the maximum flow velocity contour covering a rather small area relative to the models previously discussed. The value for this maximum velocity is 0.056m/s while the minimum velocity value is 0.03m/s as can be seen in Fig 7.6(B). This minimum velocity value occurs in the region of the side branch closest to the main vein inflow. The minimum velocity in the region of the second side branch is 0.0375m/s while that of the third side branch is 0.0468m/s. The contour shapes are rather

tricky to describe and can be seen in Fig 7.6(A). What is clear, however, is that the pattern of straight, parallel contours is broken and the lower flow velocity contours extend into what would be the higher flow velocity region for the control configuration.

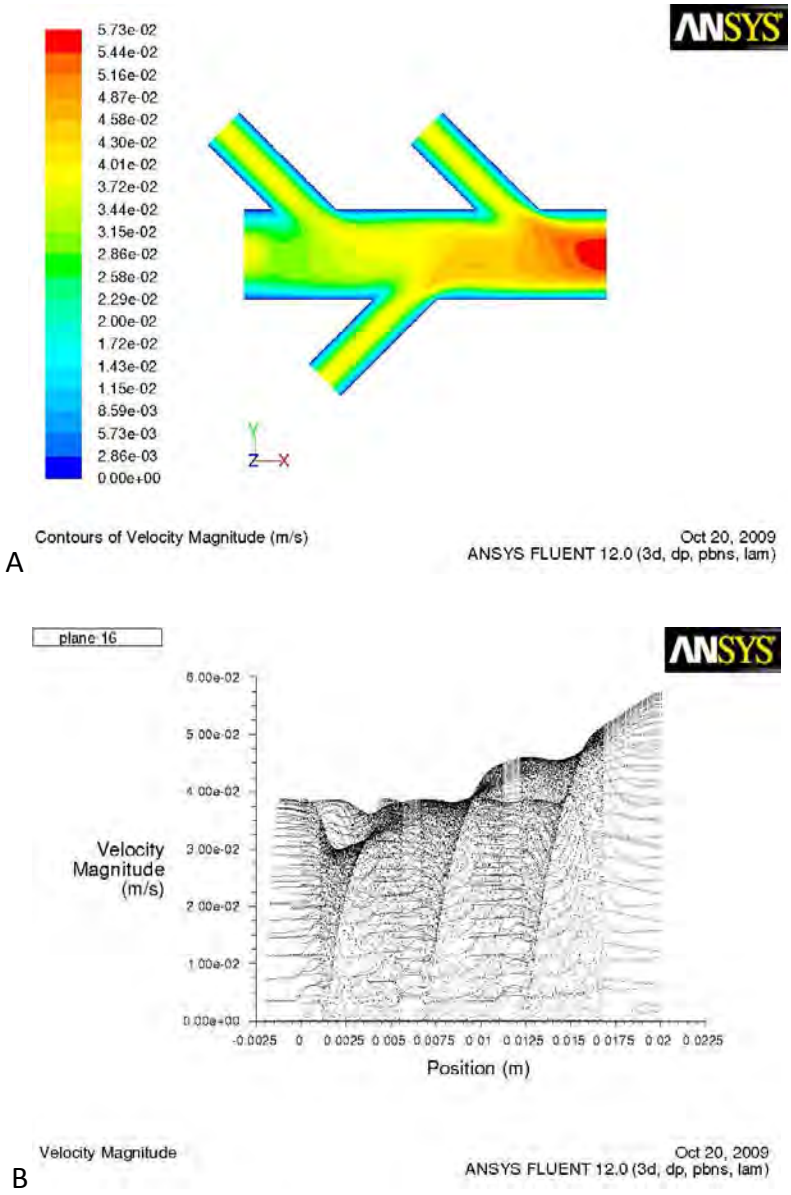

Figure 7.6: Velocity contour plot (A) and velocity magnitude graph (B) for 3_45_0.5

Figure 7.7 shows the results for model 3_90_0.5. The results are very similar to those of model 3_45_0.5. The flow pattern as seen on A is very similar to that of Fig. 7.6(A). From Fig. 7.7(B), the maximum velocity is found to be 0.057m/s while the minimum velocity is

0.031m/s. The maximum velocity occurs at the centre of the flow, very close to the outflow. The minimum velocity occurs close to the side branch closest to the main vein inflow.

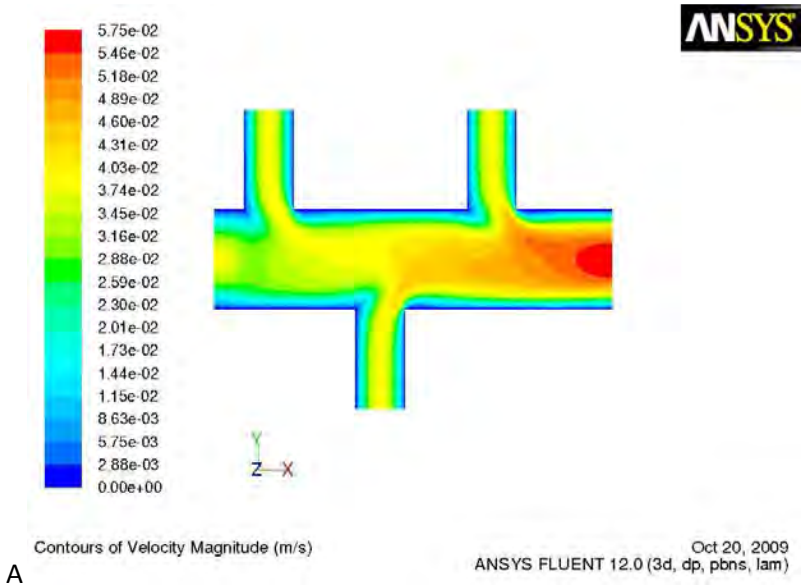

A

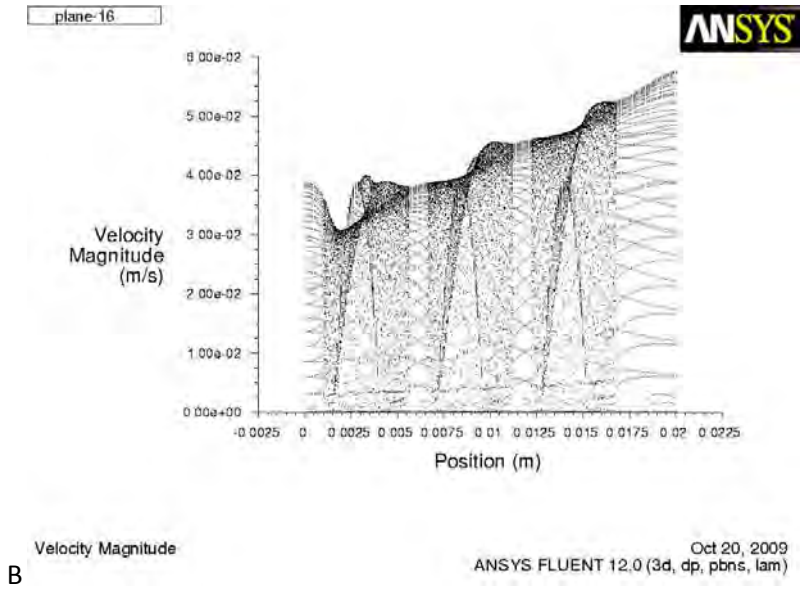

B

Figure 7.7: Velocity contour plot (A) and velocity magnitude graph (B) for 3_90_0.5

7.3 Shear stress results

Figure 7.8 shows the shear stress results for the control configuration. As can be seen from A, there is a constant shear stress over the entire wall surface and it has a value of 0.177Pa. Although B seems to disagree with this statement, it can be seen that the fluctuations shown on the graph happen over a very small range.

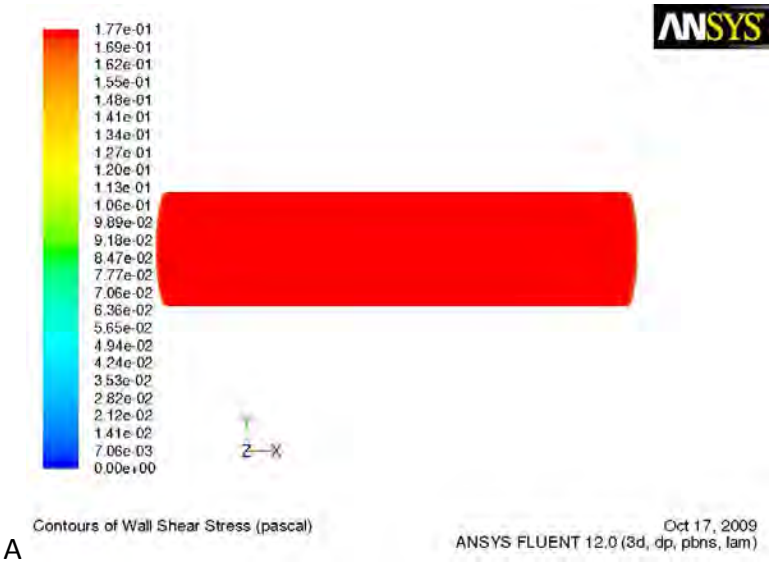

A

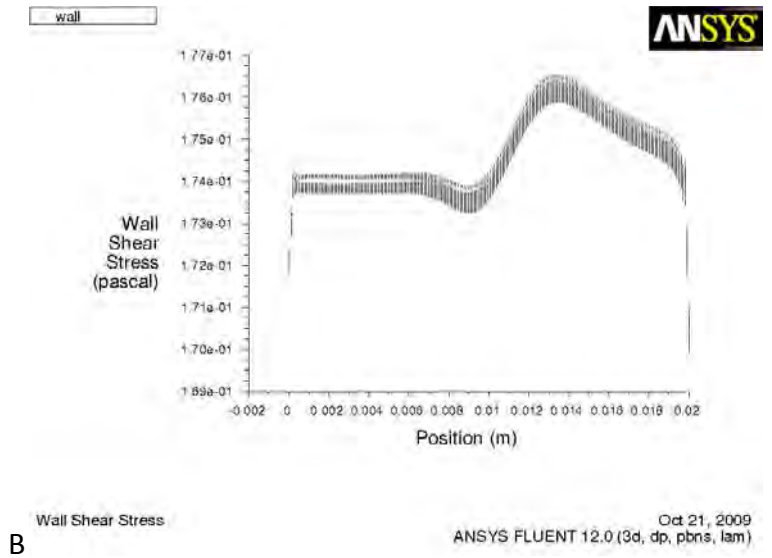

B

Figure 7.8: Shear stress contour plot (A) and wall shear stress graph (B) for the control configuration

Figure 7.9 shows the results for model 1_45_0.2. The shear stress on the wall shown in the diagram is fairly constant. There is, however, a slight increase in the shear stress on the central portion of the wall. This is the region opposite which the side branch joins onto the main vein. The shear stress for most of the vein is 0.168Pa while the stress in the central portion of the vein is 0.208Pa as can be seen in Fig. 7.9(A). From Fig. 7.9(B), it can be seen that the shear stress pattern for the entire wall is rather complex. The maximum shear stress (0.840Pa) occurs where the side branch attaches to the main vein while the lowest shear stress region occurs on either side of this region. The low shear stress region closer to the main vein inflow experiences a shear stress of 0.150Pa while that closer to the outflow experiences a minimum shear stress of 0.138Pa.

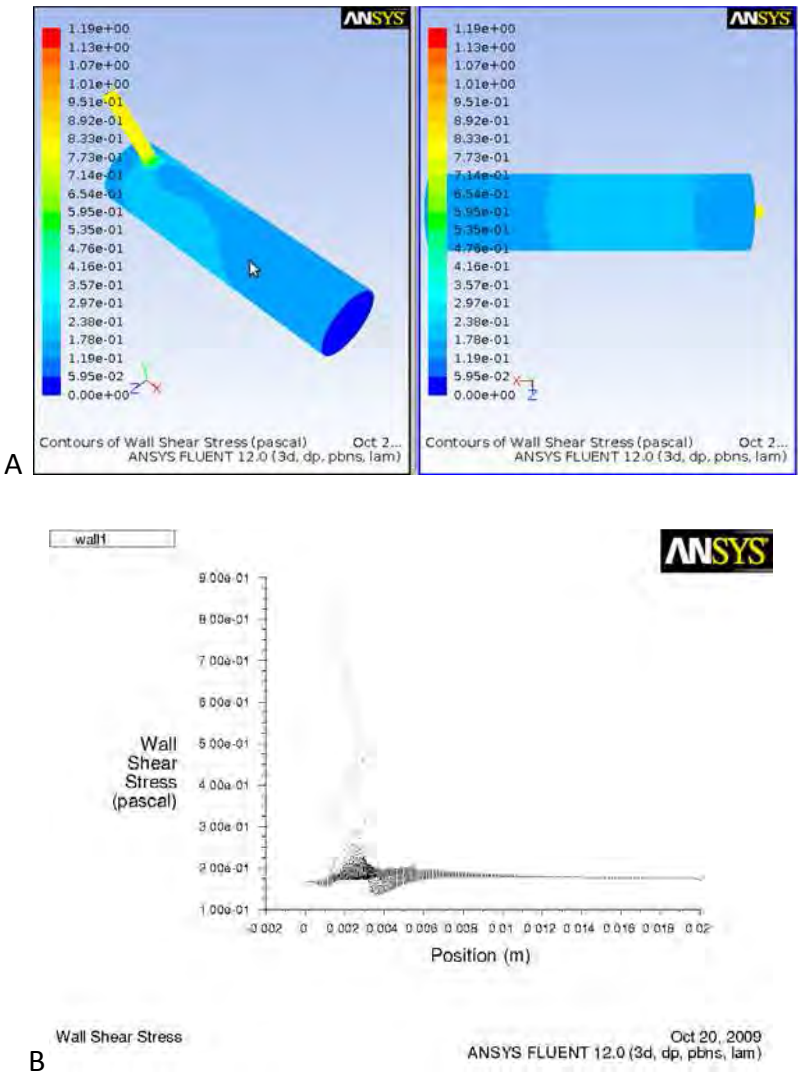

Figure 7.9: Shear stress contour plot (A) and wall shear stress graph (B) for model 1_45_0.2

Figure 7.10 shows the results for model 1_45_0.5. Bands of shear stress contours can be seen in Fig. 7.10(A) of the diagram with the lowest shear stress contour occurring close to the inflow of the main vein. This contour has a value of 0.138Pa while the rest of the vein, with the exception of the region opposite the side branch has a shear stress value of 0.175Pa. The region opposite the side branch has the highest shear stress of all the contours visible on the bottom wall as seen in Fig 7.10(A) and its value is 0.265Pa. Figure 7.10(B) shows the shear stress values over the entire main vein wall. From this, it can be seen that the vein experiences a maximum shear stress of 0.630Pa where the side branch attaches to the main vein. The regions of very low shear stress can be found adjacent to the region where the side branch attaches to the main vein. The region closer to the main vein inflow experiences a minimum shear stress of 0.120Pa while that closer to the outflow experiences a shear stress of 0.130Pa.

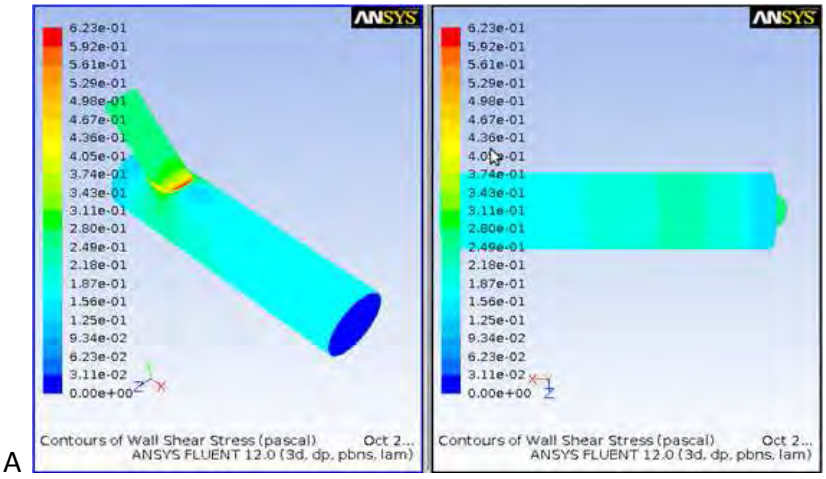

A

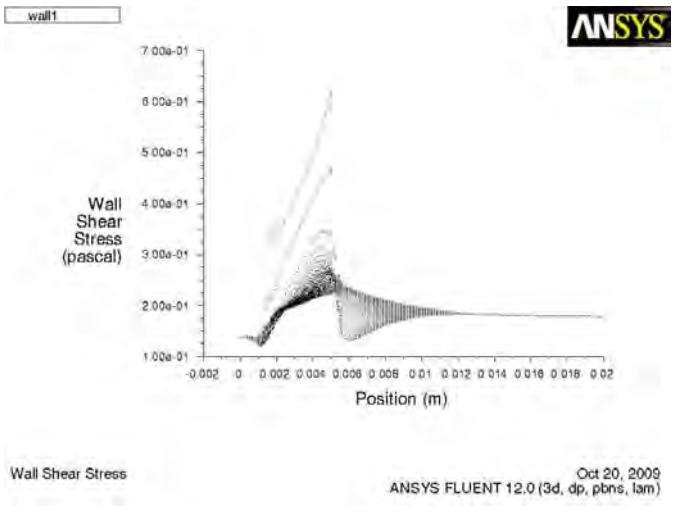

B

Figure 7.10: Shear stress contour plot (A) and wall shear stress graph (B) for model 1_45_0.5

Figure 7.11 shows the results for model 1_90_0.2. The shear stress as seen in Fig. 7.11(A) is constant and has a value of about 0.170Pa. From Fig. 7.11(B), it can be seen that the maximum shear stress occurs where the side branch attaches to the main vein and has a value of 0.850Pa. The minimum shear stress occurs in the regions adjacent to where the side branch joins the main vein. The region closer to the main vein inflow experiences a shear stress of 0.125Pa while that closer to the outflow experiences a shear stress of 0.025Pa.

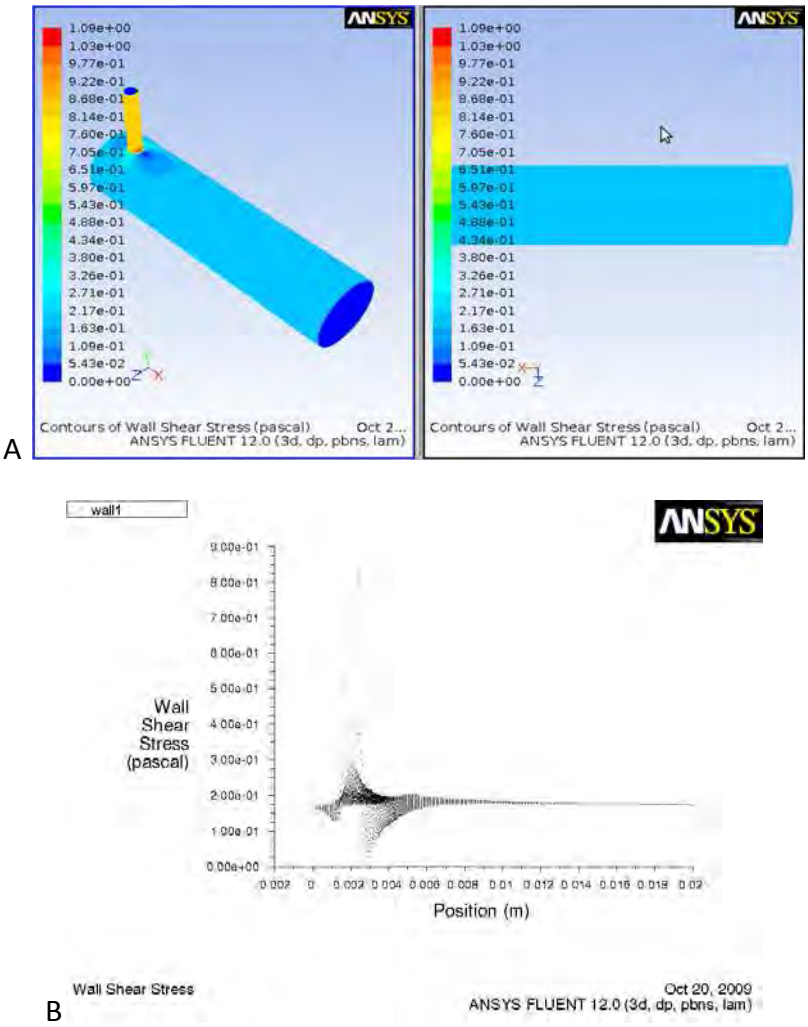

Figure 7.11: Shear stress contour plot (A) and wall shear stress graph (B) for model 1_90_0.2

Figure 7.12 shows the results for model 2_45_0.5. Rather interesting shear stress patterns can be seen in Fig 7.12(A). There are parallel contours close to the main vein inflow. The one closest to the inflow has a value of around 0.125Pa. The majority of the vein has a shear

stress of roughly 0.175Pa. Interesting patterns form around the point at which the second side branch attaches to the main vein. The shear stress in this region increases to about 0.280Pa. From Fig 7.12(B), it can be seen that for the entire main vein wall, the highest shear stress is experienced close to the points where the side branches join the main veins. This value reaches a maximum of 0.625Pa for the second side branch and has a value of 0.520Pa close to the second side branch. The low shear stress regions occur close to the side branches. The region closest to the main vein inflow has a minimum value of 0.110Pa, the region between the two side branches has a value 0.120Pa and the region closest to main vein outflow has a value of 0.160Pa.

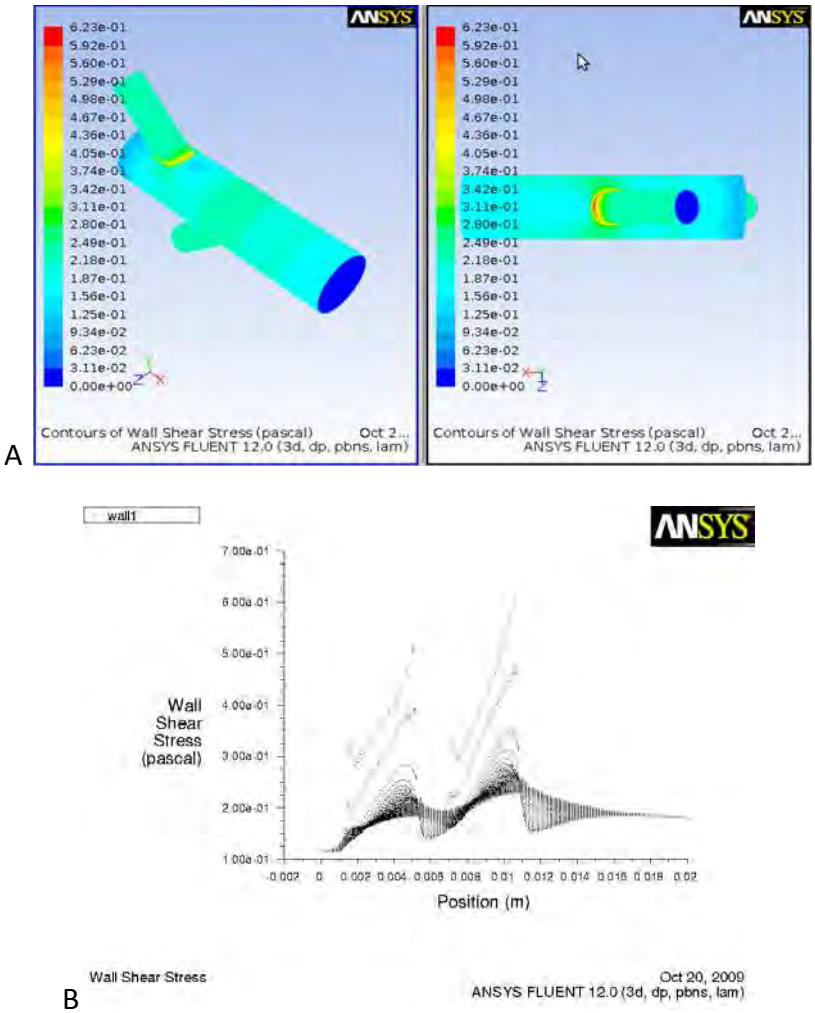

Figure 7.12: Shear stress contour plot (A) and wall shear stress graph (B) for model 2_45_0.5

Figure 7.13 shows the results for model 3_45_0.5. The contours form a rather complex pattern as seen in Fig 7.13(A). The lower shear stress regions on the contour plot occur in two main regions. The first occurs close to the second side branch in the region opposite the

first side branch and has a value of around 0.140Pa. The second occurs close to the main vein inflow and has a value of 0.110Pa. The higher shear stress regions on the plot occur in the region where the side branch attaches to the main vein and opposite the third side branch. Both have a value of around 0.250Pa. Fig 7.13(B) shows the absolute maximum and minimum for the vein wall. The highest shear stress values occur where the side branches attach to the main vein. The value is 0.430Pa for the first side branch region, 0.530Pa for the second and a maximum of 0.625Pa is reached for the third side branch region. The lowest shear stress regions occur adjacent to the side branch regions. The region closest to the main vein inflow experiences a shear stress of 0.100Pa; the region between the first and second side branches experiences a shear stress of 0.138Pa; the region between the second and third side branches experiences a shear stress of 0.160Pa and finally, the region closest to the main vein outflow has a shear stress value of 0.170Pa.

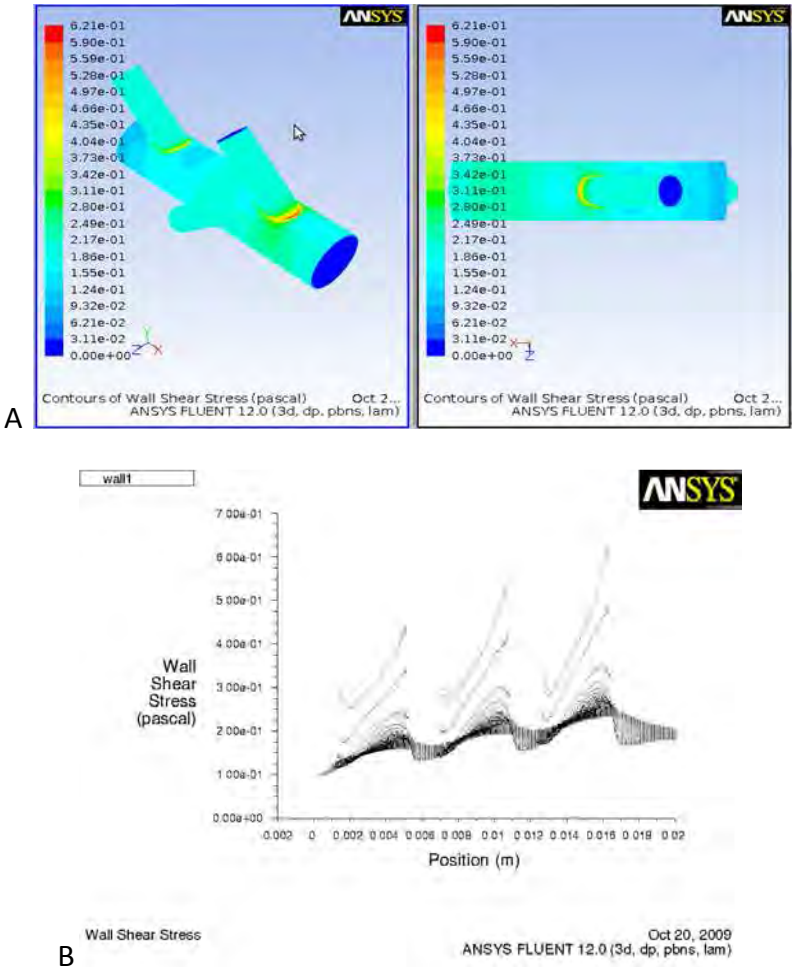

Figure 7.13: Shear stress contour plot (A) and wall shear stress graph (B) for model 3_45_0.5

Figure 7.14 shows the results for model 3_90_0.5. According to Fig 7.14(A), the lowest shear stress occurs close to the second side branch and has a value of 0.060Pa. The higher shear stress regions are seen opposite the side branches. The regions opposite the first and third side branches have a value of 0.279Pa. Fig 7.14(B) shows the maximum and minimum shear stresses over the entire main vein wall. The higher shear stress regions occur where the side branches attach to the main vein. The value for the first side branch is 0.600Pa; the value for the second is 0.710Pa while the third side branch has a value of 0.790Pa. The lower shear stresses occur in the regions adjacent to the side branches. The region closest to the main vein inflow has a value of 0.100Pa while that between the first and second side branches has a value of 0.030Pa. The region between the second and third side branches has a value of 0.060Pa and finally, the region closest to the main vein outflow has a value of 0.075Pa.

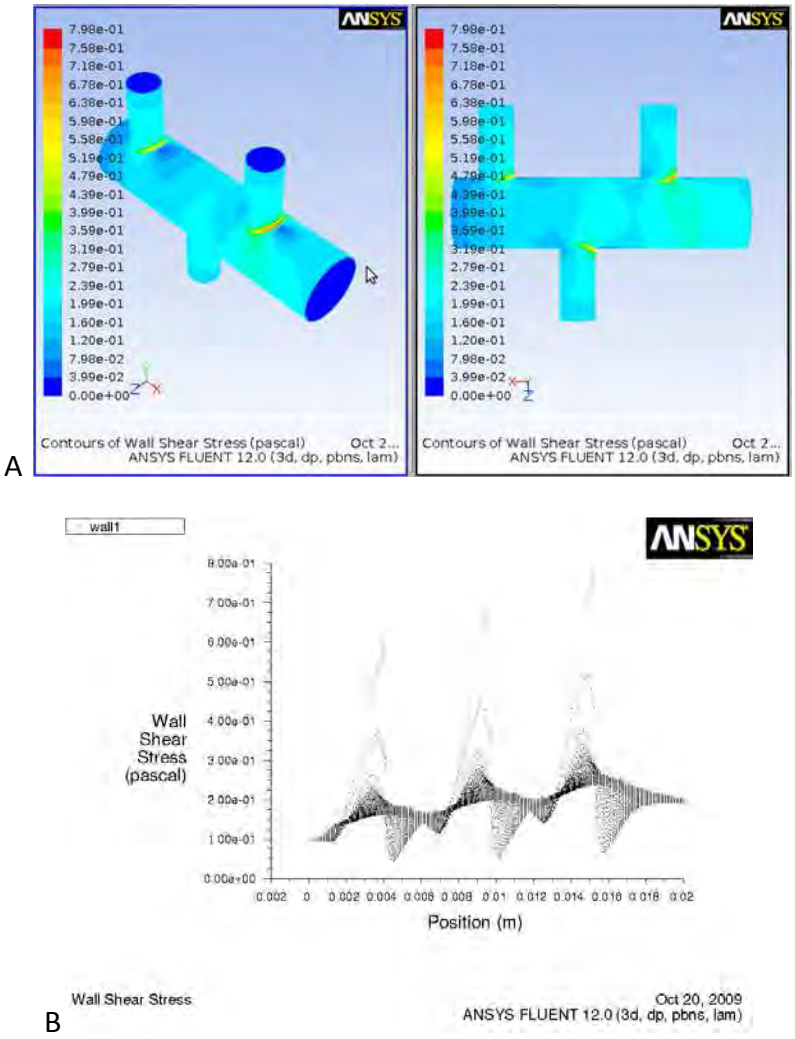

Figure 7.14: Shear stress contour plot (A) and wall shear stress graph (B) for model 3_90_0.5

7.4 Pressure results

As can be seen in Fig. 7.15, the pressure for the control configuration decreases linearly from 0.00158Pa at the inflow to -2.79Pa at the outflow.

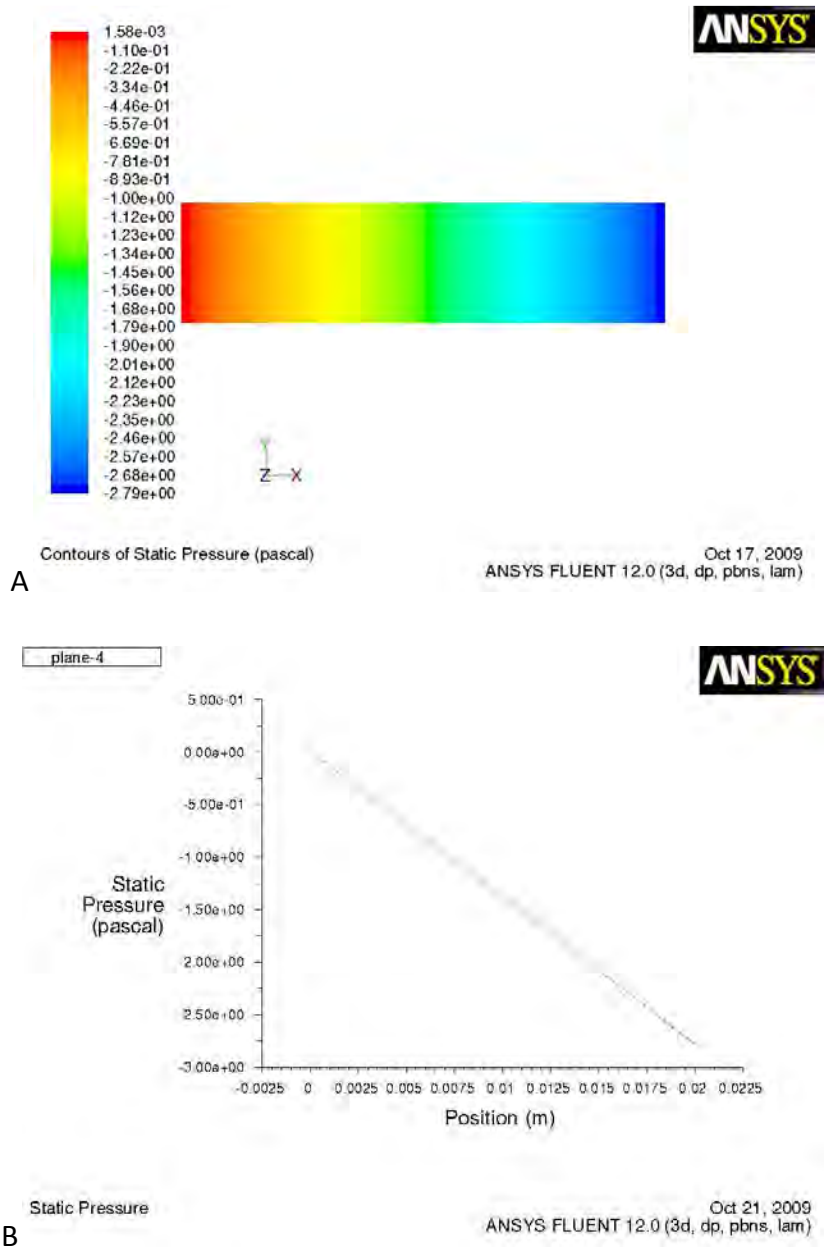

Figure 7.15: Pressure contour plot (A) and pressure graph (B) for the control configuration

Figure 7.16 shows the results for model 1_45_0.2. As can be seen from both Figs. 7.16(A) and 7.16(B), the pressure is at its maximum at the inflow of the side branch and has a value of 17.70Pa. The minimum value is -2.96Pa and occurs at the main vein outflow. The pressure decreases linearly in the side branch and in the main vein (from inflow to outflow). As can be seen on B, the pressure undergoes a slight increase and then decrease in the main vein where the side branch is attached. The pressure increases from 0Pa to 0.50Pa and then decreases to -0.25Pa.

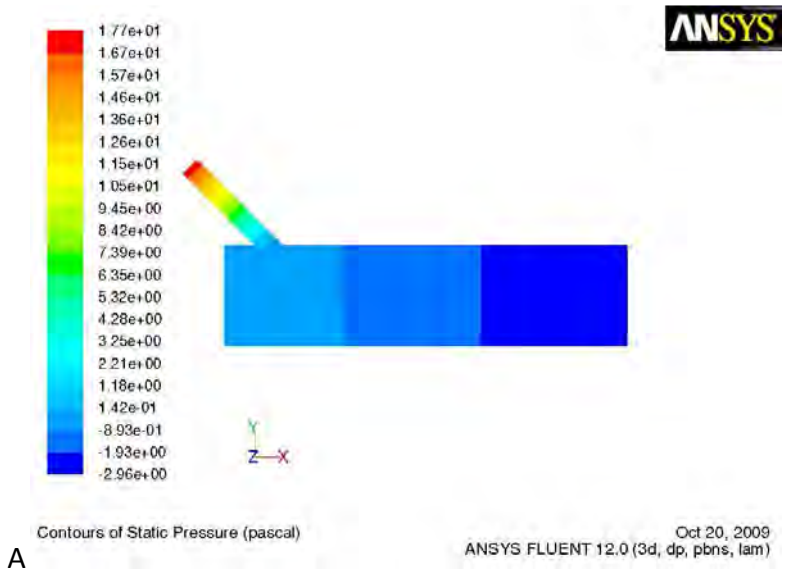

A

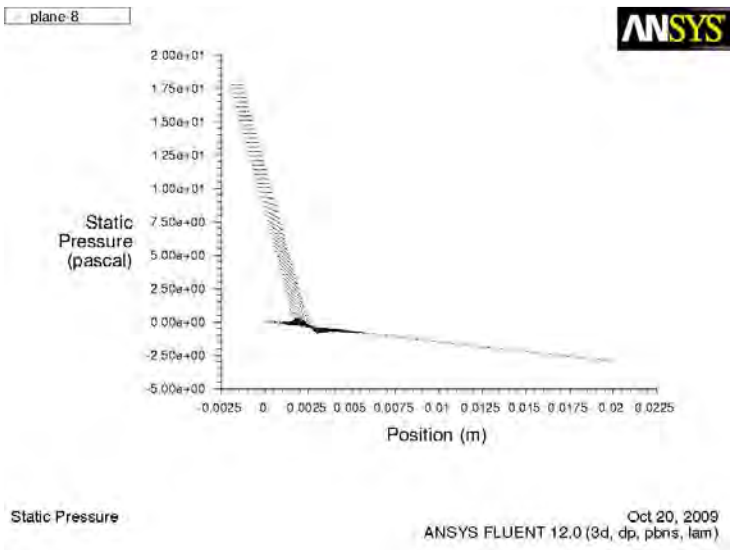

B

Figure 7.16: Pressure contour plot (A) and pressure graph (B) for model 1_45_0.2

Figure 7.17 shows the results for model 1_45_0.5. The maximum pressure occurs at the inflow of the side branch and has a value of 2.45Pa while the minimum pressure occurs at the main vein outflow and has a value of -3.37Pa as can be seen in Figs. 7.17(A) and 7.17(B). The pressure decreases linearly from the inflow in the side branch. In the main vein, the pressure contours are slightly distorted in the side branch reason unlike for the control experiment. They do, however, decrease linearly from inflow to outflow. As can be seen on B, the pressure undergoes a slight increase and then decrease in the region where the side branch joins onto the main vein. The pressure increases from 0Pa to 0.20Pa and then decreases to -1.75Pa.

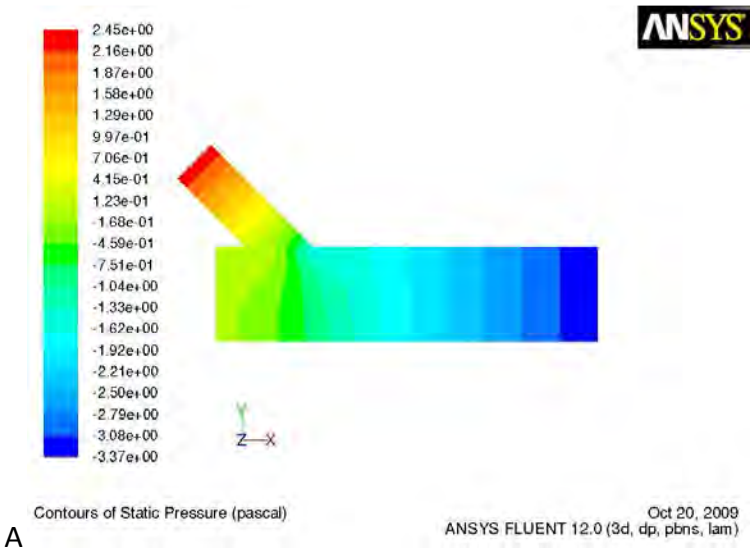

A

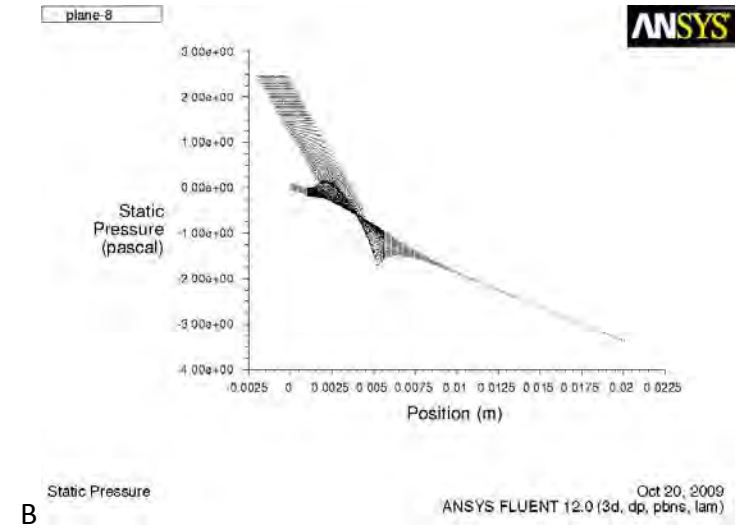

B

Figure 7.17: Pressure contour plot (A) and pressure graph (B) for model 1_45_0.5

Figure 7.18 shows the results for model 1_90_0.2. The maximum pressure occurs at the side branch inflow and has a value of 16.70Pa. The minimum pressure occurs at the main vein outflow and has a value of -2.98Pa. This is visible in Figs. 7.18(A) and 7.18(B). The pressure decreases linearly from the inflow in the side branch and the main vein. There is a slight distortion of the contours in the main vein in the region where the flow from the side branch enters the main vein stream. There As can be seen on B, the pressure undergoes a slight increase and then decrease in the side branch joins onto the main vein. The pressure increases from 0Pa to 0.50Pa and then decreases to -1.50Pa.

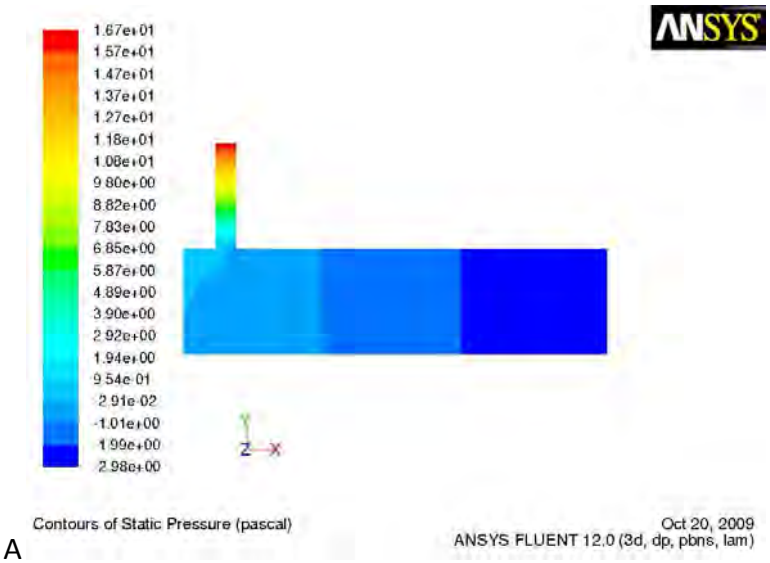

A

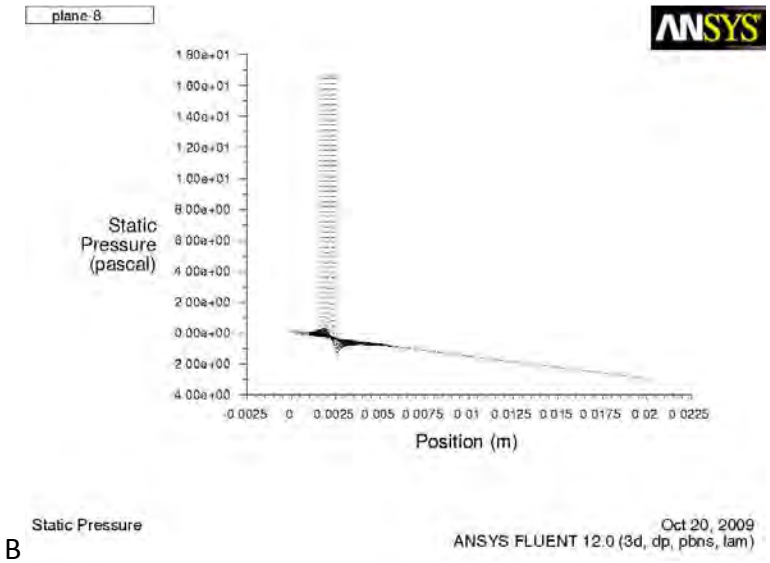

B

Figure 7.18: Pressure contour plot (A) and pressure graph (B) for model 1_90_0.2

Figure 7.19 shows the results for model 2_45_0.5. The maximum pressure occurs at the first side branch inflow and has a value of 1.99Pa. The second side branch inflow experiences a pressure of 1.00Pa. The minimum pressure occurs at the main vein outflow and has a value of -3.64Pa. The pressure decreases linearly from the inflow in both side branches. From Fig. 7.19(A), it can be seen that the main vein contours distort in the region of the side branches, even though they continue to decrease linearly from inflow to outflow. The pressure in the main vein experiences a slight increase and then a decrease at sites where a side branch joins on. Where the first side branch attaches, the pressure increases from 0Pa to 0.15Pa and then decreases to -1.40Pa. At the site where the second side branch attaches, the pressure increases from -1.00Pa to -0.80Pa and then decreases to -2.60Pa.

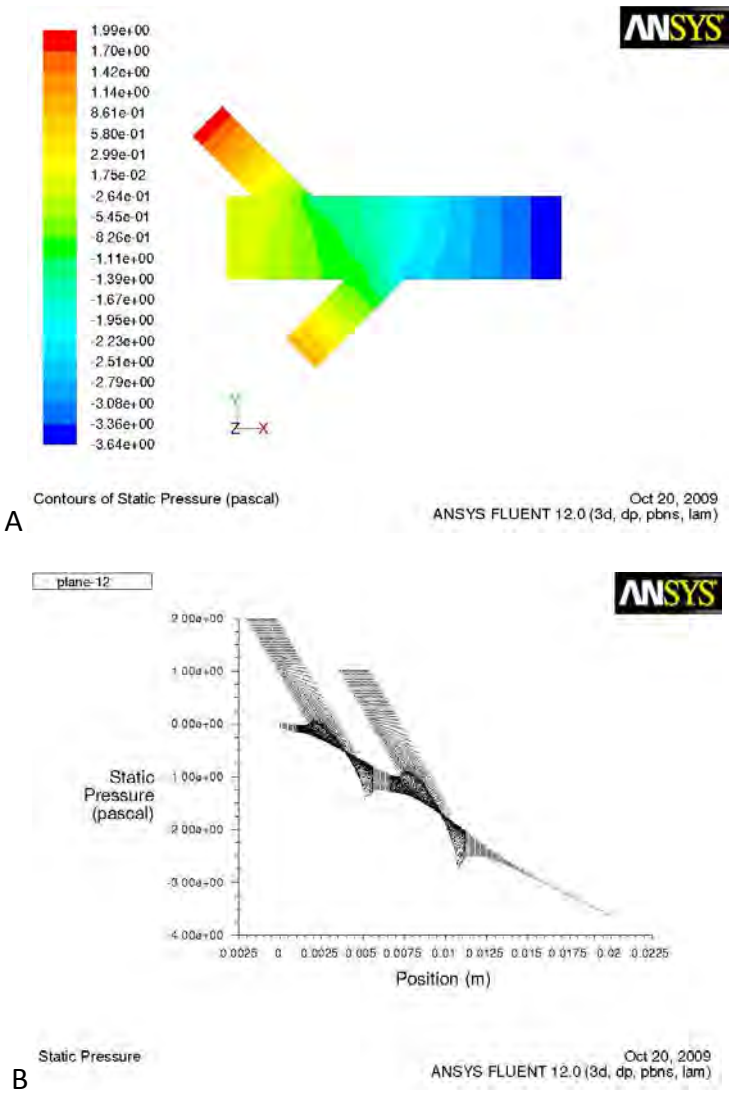

Figure 7.19: Pressure contour plot (A) and pressure graph (B) for model 2_45_0.5

Figure 7.20 shows the results for model 3_45_0.5. The maximum pressure occurs at the first side branch inflow and has a value of 1.67Pa. The second side branch inflow experiences a pressure of 0.80Pa and the third side branch inflow has a pressure of -0.20Pa. The minimum pressure occurs at the main vein outflow and has a value of -3.66Pa. The main vein and the side branches experience a linear decrease in pressure from inflow to outflow. The contours in the main vein are, however, somewhat distorted. It can be seen from Fig 7.20(B) that the main vein experiences an increase and then an immediate decrease in pressure at the sites where the side branches join on. For the first side branch, the pressure increases from 0Pa to 0.10Pa and then decreases to -1.20Pa. For the second side branch, the pressure increases from -0.90Pa to -0.75Pa and then decreases to -2.25Pa. For the third side branch, the pressure increases from -1.90Pa to -1.75Pa and then decreases to -3.50Pa.

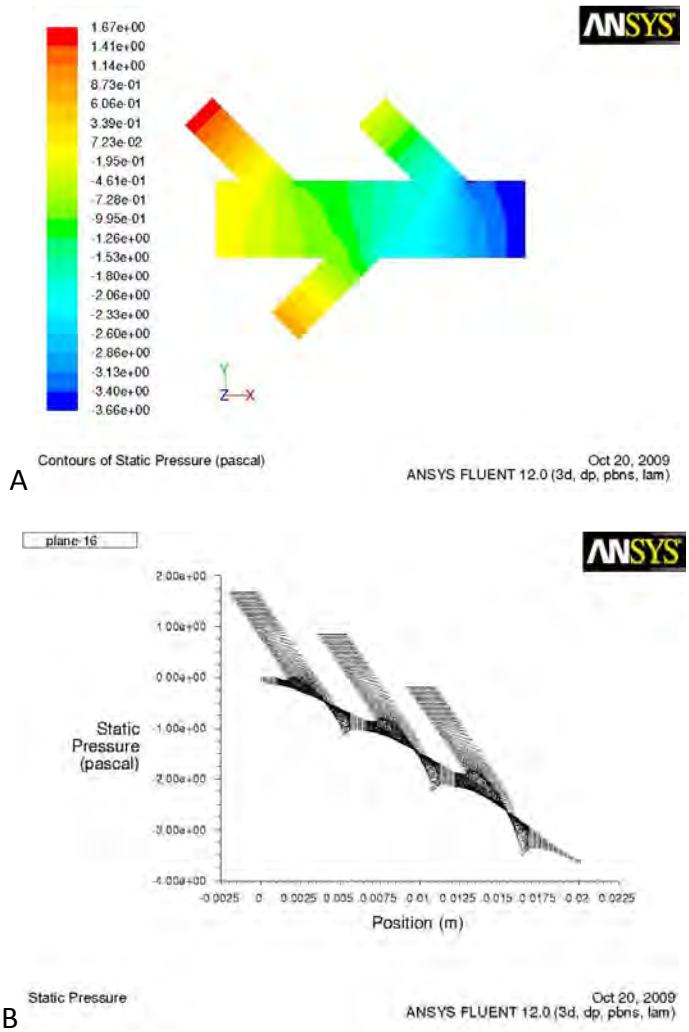

Figure 7.20: Pressure contour plot (A) and pressure graph (B) for model 3_45_0.5

Finally, figure 7.21 shows the results for model 3_90_0.5. The minimum pressure occurs at the main vein outflow and has a value of -4.26Pa. The maximum pressure occurs at the inflow of the first side branch and has a value 1.37Pa. The second side branch experiences a pressure of 0.50Pa at its inflow while third side branch has a pressure of -0.50Pa at its inflow. The pressure decreases linearly from inflow to outflow for the main vein and the side branches. As can be seen in Fig 7.21(B), the main vein pressure fluctuates slightly at the site where the side branch joins onto the main vein. For the first side branch, the pressure increases from 0Pa to 0.125Pa and then decreases to -1.75Pa. For the second side branch, the pressure increases from -0.80Pa to -0.75Pa and then decreases to -2.75Pa. For the third side branch, the pressure increases from -1.75Pa to -1.60Pa and then decreases to -4.25Pa.

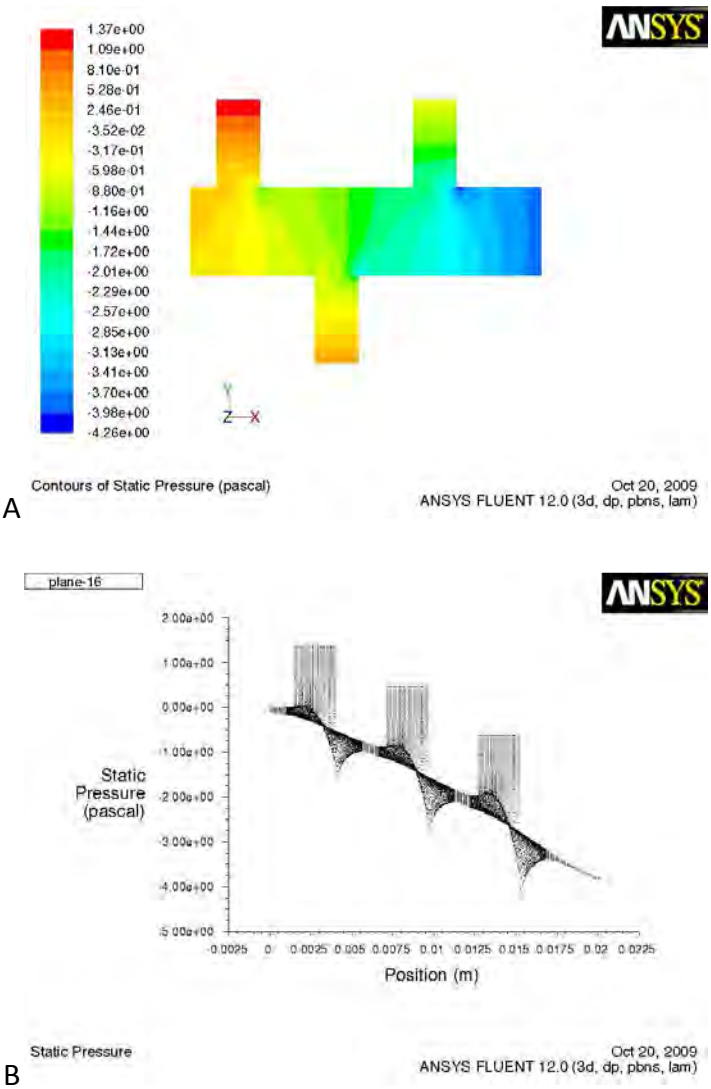

Figure 7.21: Pressure contour plot (A) and pressure graph (B) for model 3_90_0.5

7.5 Results from all the models

Table 7.1 shows the results from all the models developed for this study. The leftmost column of the table shows the models and the columns which follow on show the results of groups of models. For example, if groups with the same number of side branches and side branch attachment angle are compared, it can be noted that all the variables tend to decrease as the side branch diameter to main vein diameter ratio is increased. Other comparisons can be made across groups with the same side branch diameter to main vein diameter ratio and side branch angle. The pattern for this group is not as easy to recognize as the group where the ratios differ. The table was used to plot graphs for minimum shear stress, minimum velocity and maximum pressure in the region of the side branch against side branch diameter to main branch diameter ratio and number of side branches. The relationships are more clearly seen in these graphs. The comparison for the 45^{o} and 90^{o} models was made using graphs plotted for other variables.

Table 7.1: Table illustrating the results from all the models (Models whose results have been shown in the chapter are marked with an asterisk(*))

Model	Shear stress (Pa)		Velocity ($\times 10^{-2}$) (m/s)		Overall model pressure (Pa)		Side branch region pressure (Pa)	
	Min	*Max*	*Min*	*Max*	*Min*	*Max*	*Min*	*Max*
Control	0.173	0.176	6.78	6.78	-2.79	0.0016	-	-
1_45_0.2*	0.138	0.840	6.10	6.70	-2.96	17.7	-0.25	0.50
1_45_0.3	0.135	0.590	5.67	6.67	-3.10	7.66	-1.25	0.30
1_45_0.4	0.130	0.580	5.00	6.60	-3.24	4.12	-1.50	0.25
1_45_0.5*	0.120	0.630	4.30	6.50	-3.37	2.45	-1.75	0.20
1_90_0.2*	0.025	0.825	6.25	6.75	-2.98	16.7	-1.50	0.50
1_90_0.3	0.019	0.790	5.88	6.67	-3.13	6.87	-1.75	0.38
1_90_0.4	0.013	0.800	5.38	6.60	-3.30	3.50	-2.25	0.30
1_90_0.5	0.010	0.850	4.67	6.50	-3.46	1.99	-2.40	0.25
2_45_0.2	0.150	0.800	5.60	6.60	-3.11	17.1	-0.30	0.50
2_45_0.3	0.130	0.560	5.60	6.50	-3.35	7.14	-1.00	0.25
2_45_0.4	0.120	0.540	4.10	6.45	-3.55	3.60	-1.30	0.20
2_45_0.5*	0.110	0.625	3.50	6.30	-3.64	1.99	-1.40	0.15
2_90_0.2	0.025	0.800	5.60	6.60	-3.14	16.1	-1.20	0.40
2_90_0.3	0.020	0.750	4.80	6.50	-3.41	6.42	-1.50	0.30
2_90_0.4	0.015	0.740	4.15	6.50	-3.67	3.10	-1.75	0.25
2_90_0.5	0.010	0.825	3.60	6.25	-3.81	1.61	-2.00	0.20
3_45_0.2	0.140	0.750	5.00	6.25	-3.22	16.6	-0.75	0.50
3_45_0.3	0.125	0.540	4.15	5.80	-3.51	6.61	-1.00	0.30
3_45_0.4	0.118	0.575	3.50	5.75	-3.63	3.18	-1.15	0.20
3_45_0.5*	0.100	0.625	3.00	5.60	-3.66	1.67	-1.20	0.10
3_90_0.2	0.050	0.800	5.15	6.25	-3.29	15.6	-1.00	0.50
3_90_0.3	0.025	0.750	4.25	5.88	-3.75	5.97	-1.50	0.30
3_90_0.4	0.025	0.750	3.60	5.80	-4.10	2.73	-1.65	0.25
3_90_0.5*	0.030	0.790	3.10	5.70	-4.26	1.37	-1.75	0.13

Figures 7.22 to 7.27 illustrate several relationships which are discussed in the subsequent paragraphs. For each graph, the value given at zero is the value for the control experiment.

Figure 7.22 illustrates the relationship between the side branch diameter to main vein diameter ratio and the minimum shear stress along the main vein wall. The general trend which can be seen from this graph is that the minimum shear stress decreases as the ratio is increased. It is interesting to note that all the 45^{o} models have a minimum shear stress of greater than 0.1Pa while the 90^{o} models have a minimum shear stress of less than 0.1Pa. The values of all the models fall below the control experiment value of 0.173Pa

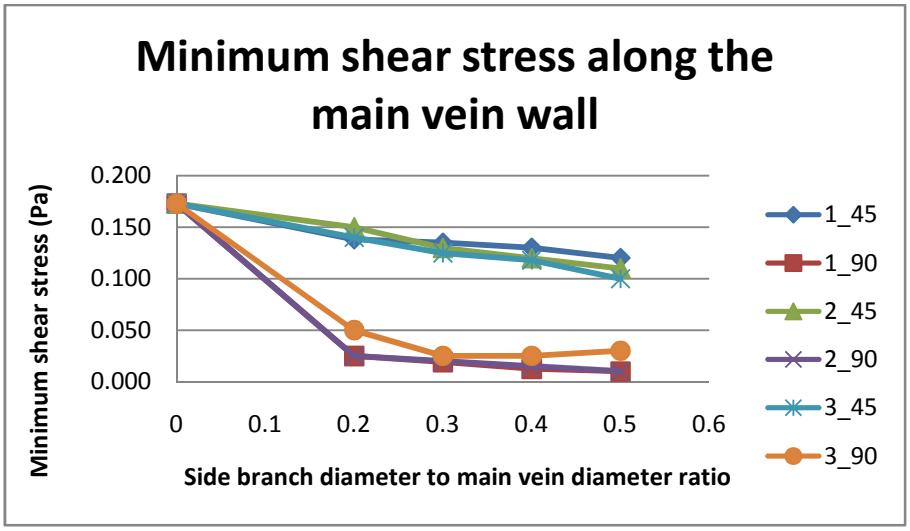

Figure 7.22: Graph illustrating the relationship between the side branch diameter to main branch diameter ratio and the minimum shear stress along the main vein wall.

Figure 7.23 illustrates the relationship between the side branch diameter to main branch diameter ratio and the minimum velocity experienced in the vein. Once again, the minimum flow velocities for the models fall below the control experiment value of 0.068m/s. The minimum flow velocity decreases as the ratio is increased. Generally, the 90^{o} models have higher minimum flow velocity values than their 45^{o} counterparts.

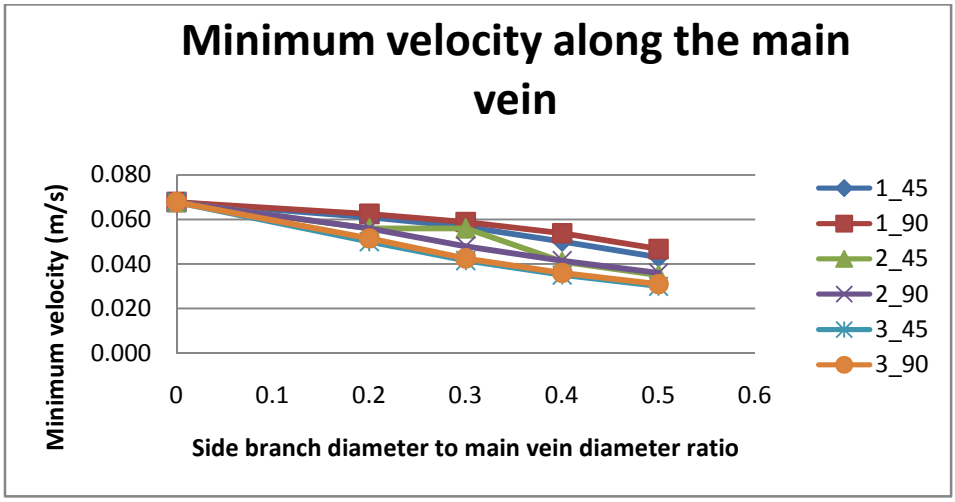

Figure 7.23: Graph illustrating the relationship between the side branch diameter to main branch diameter ratio and the minimum velocity along the main vein.

Figure 7.24 illustrates the relationship between the side branch diameter to main branch diameter ratio and the maximum pressure experienced where the side branch joins the main vein. The pressure decreases as the ratio is increased and the 90^{o} models generally experience greater pressure than their 45^{o} counterparts. The control experiment pressure is zero because it does not have any side branches attached to it.

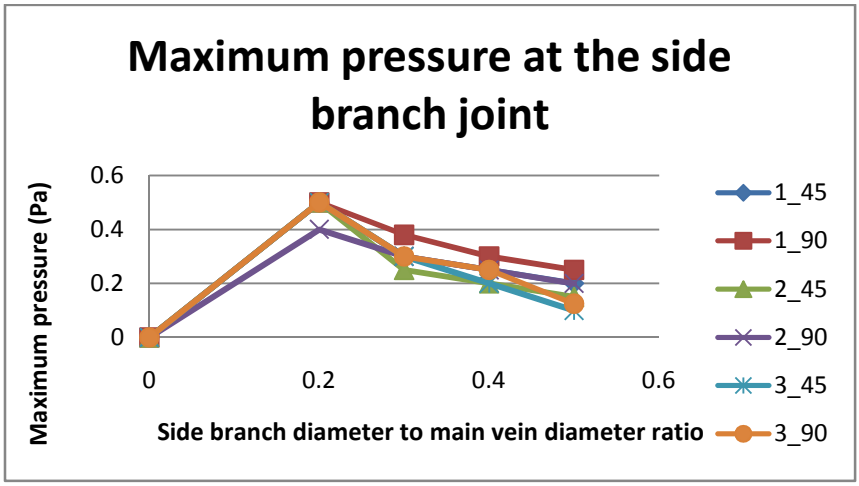

Figure 7.24: Graph illustrating the relationship between the side branch diameter to main branch diameter ratio and the maximum pressure at the side branch joint.

Figure 7.25 illustrates the relationship between the number of side branches and the minimum shear stress experienced along the main vein wall. From the graph, it can be seen that there is no clear pattern. The 45° models seem to experience a decrease in shear stress as the number of side branches is increased while the opposite seems to happen for the 90° models.

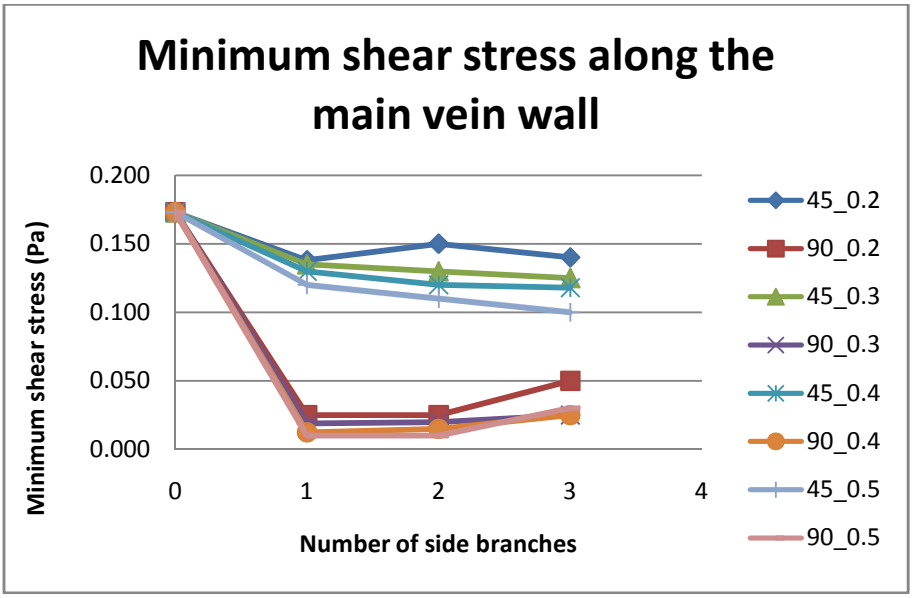

Figure 7.25: Graph illustrating the relationship between the number of side branches and the minimum shear stress along the main vein wall.

Figure 7.26 illustrates the relationship between the number of side branches and the minimum velocity in the main vein. The graph shows that the minimum velocity decreases as the number of side branches is increased and that in general, the 90° models experience higher minimum flow velocities than their 45° counterparts.

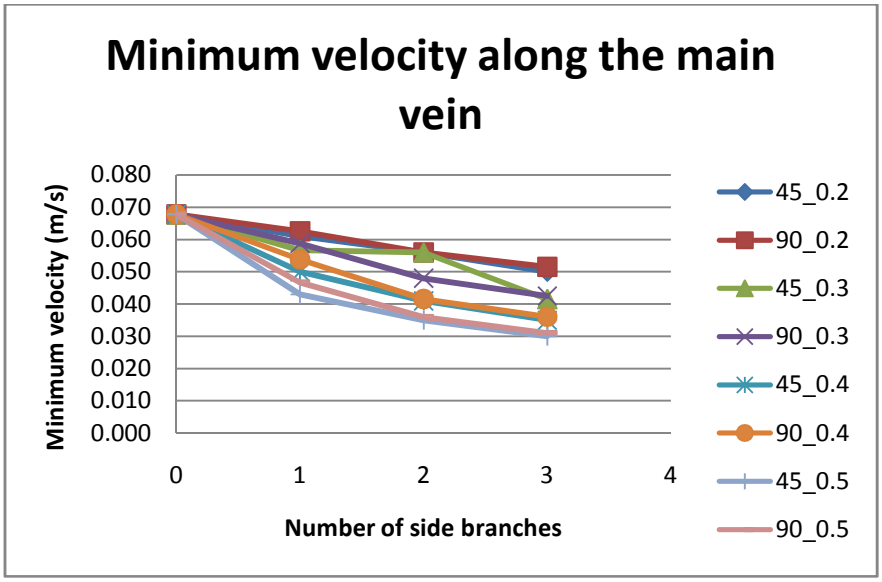

Figure 7.26: Graph illustrating the relationship between the number of side branches and the minimum velocity along the main vein.

Figure 7.27 illustrates the relationship between the number of side branches and the maximum pressure experienced at the junction between the side branch and the main vein. From the graph, there is not a clear trend which immediately stands out. The pressures are fairly constant and the 45^{o} and 90^{o} models have similar results.

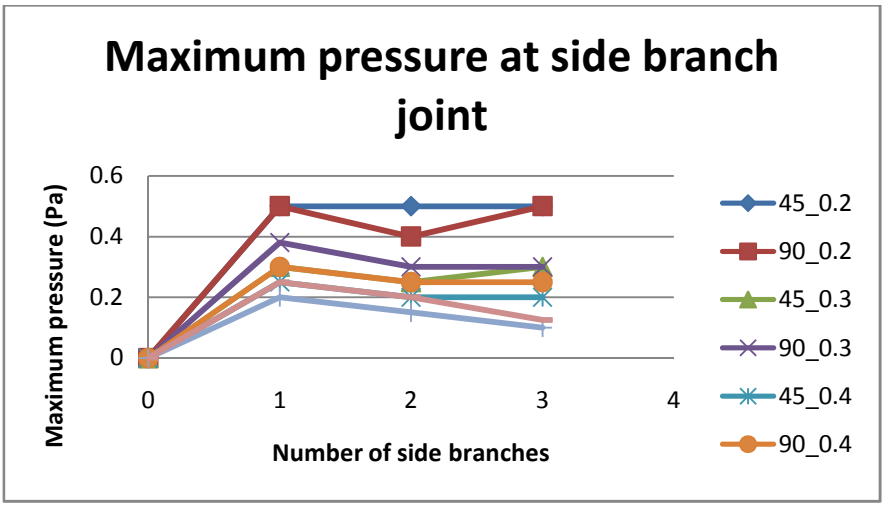

Figure 7.27: Graph illustrating the relationship between the number of side branches and the maximum pressure at the side branch joint.

CHAPTER 8: DISCUSSION OF RESULTS

This chapter aims to take an in depth look at the results obtained from the models. A link is then made between these results and the development of intimal hyperplasia in the human saphenous vein.

8.1 Effect of varying the side branch diameter to main vein diameter ratio

As the side branch diameter to main vein diameter ratio is varied, the volumetric flow rates through the side branches and the main vein vary. As the ratio is increased, the flow rate through the side branches increases while that through the main vein decreases. It is therefore expected that the flow from the side branches for higher ratios will have a more significant impact on the main vein flow than that from lower ratios.

Figure 7.1A shows a flow pattern plot of the control configuration. As is expected, the flow contours are straight and parallel to each other. The maximum flow velocity occurs at the centre of the flow and the minimum occurs at the vein wall. There is a difference between this flow pattern and flow patterns from higher ratio models. Even though the ratio 0.2 is considered small in comparison with other models, there is a marked difference between the flow patterns seen in Figs 7.1A, 7.2A and 7.4A. Figures 7.2A and 7.4A show the flow patterns for 0.2 ratio models. The maximum flow velocity contour is divided into two regions as a result of the flow from the side branch. A further increase of the ratio leads to an even more complex flow pattern as seen in Fig. 7.3A, the flow pattern contour plot for model 1_45_0.5. In this diagram, lower flow velocity contours extend into regions which are higher flow velocity regions in the control configuration. All these contour plots clearly show that the minimum flow velocity in the vein occurs in the region of the side branch.

An examination of the velocity magnitude graphs shown in Figs. 7.1B, 7.2B and 7.4B show that as the ratio is increased, the velocity magnitude in the side branch region decreases. If Figs. 7.2B and 7.3B are compared, the velocity in the side branch region is much lower in Fig.7.3 B than it is in Fig. 7.2B. The observation that an increase in the ratio results in a decrease in the side branch region flow velocity is further supported by the data in Table 7.1. Figure 7.23 is a graph which show that the minimum flow velocity in the vein decreases as the ratio is increased. This is true across all model groups. It is interesting to note that the exact point at which the minimum velocity occurs gets closer to the side branch as the ratio is increased. The minimum velocity on Fig. 7.2B occurs at 0.005m while that on Fig.7.3B occurs at 0.0035m. This is observed because as the ratio is increased, the volumetric flow rate of that particular side branch increases hence the flow coming through the side branch has a greater effect on its immediate surroundings than what a lower ratio side branch would have.

Figure 7.8 shows the shear stress results for the control configuration. As is expected, the shear stress is constant throughout the vein wall. As the ratio is increased, the shear stress pattern on the wall becomes more complex. Figures 7.9B and 7.11B illustrate the shear stress graph for the 0.2 ratio models. The shear stress experienced by these two models is lower than that experienced by the control configuration. Comparing Figs. 7.9B and 7.10B reveals that increasing the ratio leads to a further decrease in the shear stress. The contour diagram shown in Fig. 7.10A has a more complex shear stress pattern and a lower shear stress value opposite the side branch than the one shown in 7.9A. Table 7.1 shows that the minimum shear stress value decreases as the ratio is increased. The graph in Fig. 7.22 also supports this observation and is true across all the model groups.

It is important to identify the regions in which the minimum and maximum shear stresses occur. From the graphs shown in Figs. 7.9B and 7.11B, it is evident that maximum shear stress is experienced in the side branch region. The minimum shear stress is experienced in the regions adjacent to the side branch. Figure 7.9A also shows that the region opposite the side branch experiences a higher shear stress than the rest of the vein. Figure 8.1 reveals

that the regions which experience the minimum and maximum shear stresses. The maximum shear stress is experienced at the point where the side branch attaches to the main vein and the minimum shear stress is experienced adjacent to that region. Even though this is the case, it remains important to observe the region opposite the side branch relative to the rest of the vein.

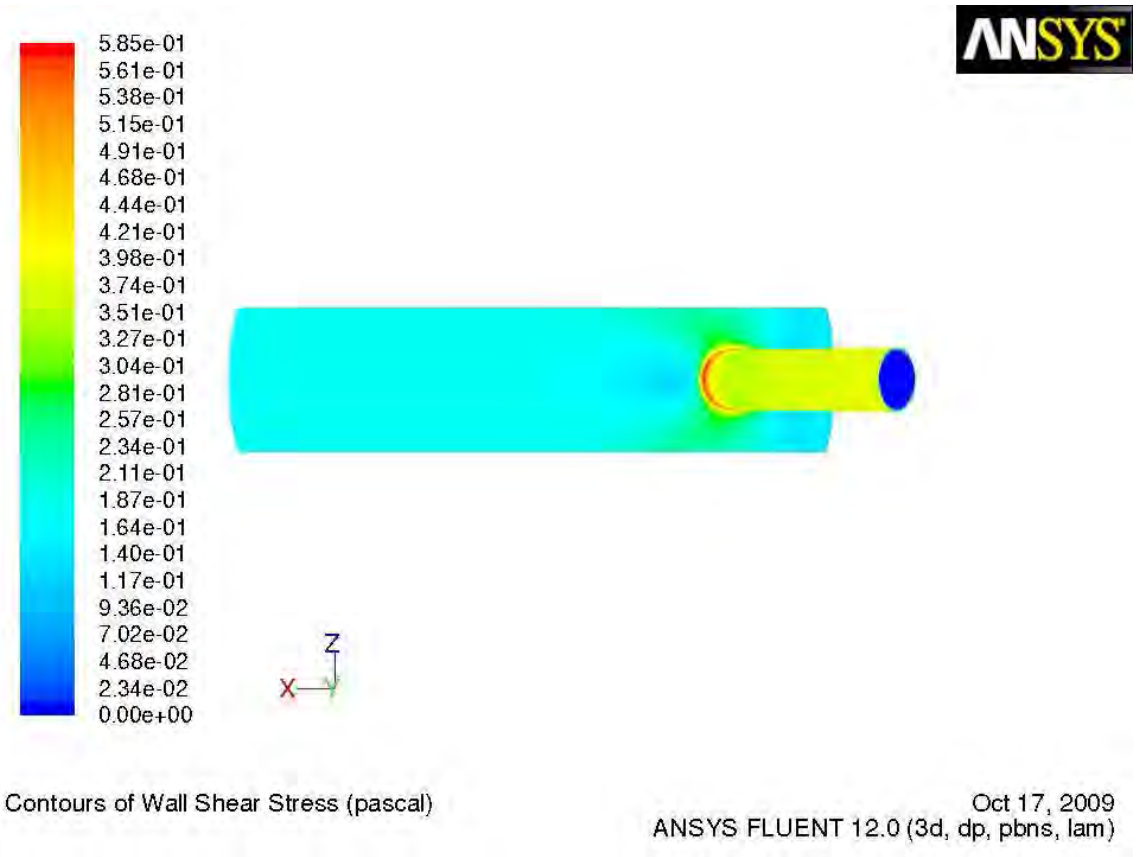

Figure 8.1: Diagram illustrating the minimum and maximum shear stress regions (Model 1_45_0.4)

Table 7.1 shows that the minimum shear stress values decrease as the ratio is increased. Those for the 45^{o} group models all fall below 0.5Pa and above 0.1Pa. Model 3_45_0.5 experiences a shear stress of 0.1Pa. It has been suggested that at this shear stress value, intimal hyperplasia is no longer fully suppressed. Even though their minimum shear stress

values decrease as the ratio is increased, all 90^{o} group models experience very low shear stresses below 0.1Pa.

Figure 7.15A shows the pressure plot for the control configuration. It is evident that the pressure decreases linearly from the inflow to the outflow of the main vein. This pattern is noticed for all the pressure plots. By comparing Figs. 7.15B, 7.16B, and 7.17B it is evident that in increase in the ratio results in a slight change in pressure condition. The graphs from Figs. 7.16 and 7.17 illustrate that there is an increase in the pressure at the junction between the side branch and the main vein. Both Table 7.1 and Fig. 7.24 show that this pressure decreases as the side branch is increased.

It is evident from the previous paragraphs that the side branch diameter to main vein diameter ratio has a rather significant impact on fluid flow dynamics in the region of the side branch. An increase in this ratio results in a decrease in the minimum flow velocity, minimum shear stress and maximum pressure in the region. This is to be expected as low flow velocity is often associated with low shear stress. In addition to this, the flow velocity of the flow from the side branch is decreased as the ratio is increased. Side branch flow with lower velocity would be expected to exert a smaller pressure on the main vein wall than higher velocity flow.

Intimal hyperplasia is often associated with low velocity flow and low shear stress regions. As the ratio is increased, the flow velocity decreases in the region opposite the side branch where intimal hyperplasia has been observed. All the shear stress values fall below the 0.5Pa threshold value. The shear stress values also decrease as the ratio increases, tending more towards the threshold value of 0.1Pa for the 45^{o} models. Even though their shear stress value decreases as the ratio is increased, the 90^{o} models all fall far below 0.1Pa. The maximum pressure is seen to decrease as the ratio is increased. If the shear stress and velocity results show increased chances of intimal hyperplasia development with a decreased ratio, one would expect an increase in pressure for increased ratios and would

make the statement in the previous sentence seem counterintuitive. There seems to be a correlation between an increase in the ratio and a decrease in the minimum shear stress, minimum velocity and maximum pressure values. Even though this is the case, it cannot be stated that a decrease in the ratio is linked to intimal hyperplasia development because the minimum shear stress values fall between or below the threshold values and the regions of minimum shear stress do not necessarily occur opposite the side branch. It can be seen though, that this ratio does have a significant effect on side region flow dynamics and it can therefore be suggested that it plays an important role in intimal hyperplasia development.

8.2 Effect of varying the number of side branches

As with the ratio discussed in the previous section, the number of side branches attached to the main vein has an influence on the flow rates through the side branch and the vein. As the number of side branches increases, the flow rates through these branches and the main vein decrease. Even though this is the case, an increase in the number of side branches would be expected to have a rather significant effect on the results.

Figures 7.3A, 7.5A and 7.6A illustrate the flow patterns for single, double and triple side branch models. These contour plots show that the complexity of the contours increases as more side branches are added on. A comparison between Fig. 7.1A and Fig. 7.6A shows that for models with a greater number of side branches, the lower velocity contours extend into regions which would normally be higher velocity regions for the control configuration.

Figures 7.3B, 7.5B and 7.6B show that as the number of side branches is increased, the minimum velocity magnitude decreases. It can also be seen from these graphs that the minimum velocity point moves closer to the side branch region as the number of side branches increases. From Fig. 7.6B, it can be seen that the minimum velocity occurs in the region of the first side branch. While the other side branches have lower flow velocities

relative to their surrounding regions, their velocities are higher than that of the first side branch. The second side branch's velocity is lower than that of the third. This pattern is seen for all the results. Table 7.1 and Fig. 7.26 also support the observation that an increase in the number of side branches results in a decreased minimum velocity value across all model groups.

Figures 7.10A, 7.12A and 7.13A show the increasing complexity of the shear stress contour plots as the number of side branches is increased. Figures 7.12A and 7.13A show that the lowest shear stress region is located close to the first side branch while the highest shear stress region occurs in the region of the second side branch for Fig. 7.12A and the third for Fig.7.13A. Figure 7.10A is mainly composed of thick contour lines while Fig. 7.13A shows that the interaction between the flows from the different side branches results in several low shear stress regions close to the visible side branch. The maximum shear stress for this diagram occurs at the point where the side branch joins onto the main vein.

Figures 7.10B, 7.12B and 7.14B all show that the maximum shear stress occurs in the region of the side branch. The lower shear stress regions are located adjacent to the high shear stress regions. The relationship between the minimum shear stress and the number of side branches is not a simple one. From Fig. 7.25, it can be seen that generally, the minimum shear stress decreases as the number of side branches is increased. This is true for the 45^{o} models. For the 90^{o} models, however, the minimum shear stress increases as the side branches increase. Table 7.1 supports these observations.

Figures 7.17A, 7.19A and 7.20A show that an increase in the number of side branches results in a greater distortion of the pressure contours in the main vein. For all these models, the maximum pressure occurs at first side branch's inflow. From Figs. 7.19A and 7.20A, it can be seen that the other side branches' inflows experience a lesser pressure than the first inflow. From Table 7.1, it is evident that the pressure at the first side branch's inflow decreases as the number of side branches is increased.

Figures 7.19B and 7.20B show that the maximum pressure experienced by the main vein in the region of the side branch decreases for each additional side branch. This is to be expected as the inflow pressure for each additional side branch also decreases. From Table 7.1 and Fig. 7.27, it can be seen that there is no obvious relationship between the number of side branches and the maximum pressure experienced at the junction between the first side branch and the main vein. For some model groups, the value seems to remain constant while for others, there is a decrease in the pressure. The 90_0.2 and 45_0.3 model groups seem to have equal maximum pressures for the single and triple side branch models and a lower pressure for the double side branch model.

The previous paragraphs have highlighted the role that the number of side branches plays in the fluid flow dynamics of side branch regions. An increase in the number of side branches seems to result in lower flow velocity regions opposite the side branch. It also seems to result in an increased number of low shear stress regions close to the side branches. The minimum shear stress in the vein wall tends to decrease as the number of side branches increases for the 45^{o} models. This value increases for the 90^{o} models. The pressure seems to remain fairly constant (within 0.1Pa) for models within the same group. The correlation between low flow velocity and low shear stress regions makes good sense. As the flow velocity decreases, the shear stress is also expected to decrease. It seems that the pressure is more dependent on the side branch diameter to main vein diameter ratio than it is on the number of side branches. This would explain the fairly constant pressure across the model groups as the models are grouped based on this ratio.

The development of intimal hyperplasia is generally associated with low flow velocity and low shear stress regions. From the previous paragraphs, it is evident that the minimum flow velocity in the side branch region decreases as the number of side branches is increased. The relationship between the shear stress and the number of side branches is somewhat more complex. As was stated in the previous section, the shear stress values either fall

between the 0.1Pa and 0.5Pa threshold values as in the case of the 45^{o} models (where the values are closer to 0.1Pa) or they all fall below the 0.1Pa threshold value as in the case of the 90^{o} model. The pressure seems to remain fairly constant within the model groups. It is rather difficult to make a judgement about the development of intimal hyperplasia based on the shear stress and pressure results. Even though the velocity results show a clear relationship between the number of side branches and the minimum flow velocity, a judgement cannot be made based on this variable alone. It seems that the number of side branches has a somewhat significant role on the fluid dynamics in side branch regions. This change in the fluid dynamics from what is seen in the control experiment seems rather significant and this change is often seen to be instrumental in the development of intimal hyperplasia. It could be suggested that this variable has some effect on intimal hyperplasia development but the extent to which it plays a role is unknown.

8.3 Effect of varying the geometry

The third variable which was examined was the angle at which the side branch attached to the main vein. At 45^{o}, the flow from the side branch has a much gentler entry into the mainstream flow while at 90^{o}, the flow has a more abrupt entry. It was thought that this would have a significant effect on the mainstream flow results.

A comparison of Figs. 7.2A and 7.4A shows that there is very little difference between the flow patterns for the two models. Both these models are 0.2 ratio models; hence the side branch flow is not expected to have that great an impact on the mainstream flow pattern. Figures 7.6A and 7.7A are then also compared and their flow patterns are also very similar. From inspecting the flow pattern contours, it seems that there is not much difference between the 45^{o} and 90^{o} models. Figures 7.2B and 7.4B are also very similar and as are Figs. 7.6B and 7.7B. Their minimum velocity points occur in the same place and have the same values. Both Figs. 7.23 and 7.26 show that the 45^{o} and 90^{o} models have very similar minimum flow velocity results.

The change in the side branch angle does yield different results for the shear stresses. Figures 7.9A and 7.11A show the difference between a 45^o and 90^o model respectively. The 45^o model has a higher shear flow region in the centre of the wall whereas the 90^o model has constant shear stress. In addition to this, all the 45^o models have shear stress value above 0.1Pa while the 90^o models all have shear stress values far below 0.1Pa. This is evident in Figs. 7.13B, 7.14B, 7.22, 7.25 and Table 7.1. This may suggest that positioning the side branches at 90^o to the main vein causes the flow through them to have a much greater impact on the mainstream flow. This reasoning, however, does not seem to agree with the flow velocity results.

There are differences in the pressure results for the 45^o models and the 90^o models. Figures 7.16A and 7.18A show that the contour plots for the single branch, 0.2 models are quite similar. Figures 7.20A and 7.21A are quite different. There seems to be a more irregular pattern in the contours in Fig. 7.21A while the contours in Fig. 7.20A follow a more regular pattern, even though both are distorted. There is a greater difference in the maximum pressures reached in Figs 7.20B and 7.21B than in 7.16B and 7.18B. In the region of the side branches, the 90^o model pressures are generally slightly higher than the 45^o model pressures as seen in Fig. 7.24. Figure 7.27 shows that the pressure results for the two model groups are either very similar or only slightly different. In the cases where a difference exists, the 90^o results are slightly higher than the 45^o results.

The comparison between the 45^o and 90^o model groups yields somewhat unexpected results. The flow velocities of the two groups are very similar but the shear stresses are very different. The 45^o group has shear stresses greater than or equal to 0.1Pa while the 90^o group has very low shear stresses (all below 0.1Pa). The 90^o model group generally yields pressure results which are greater than or equal to the 45^o group.

From the discussion in this section, it is evident that it would be very difficult to comment on the effect of side branch geometry on the development of intimal hyperplasia. The

velocity results give the impression that the angle would not contribute its development while the shear stress results paint a completely different picture. More research would have to be conducted over a greater range of geometries before a link between the side branch angle and the development of intimal hyperplasia could be made.

CHAPTER 9: SCOPE FOR FURTHER INVESTIGATION

From the results and discussion chapters, it is evident that there are still a number of unanswered questions regarding the development of intimal hyperplasia in native veins. This chapter aims to highlight some of these questions and give some recommendations as to what further work can be done in order to better understand this complex subject. Preliminary investigations were carried out in order to establish whether or not the suggested future studies are worth exploring.

9.1 Model geometry

As was stated in chapters 2 and 5, the geometry of the saphenous veins varies greatly in different individuals. Much work can be done in order to cover the effect of geometry on the development of intimal hyperplasia more comprehensively and potentially patient-specifically. Two different ways of further altering the geometry of the models are discussed in this section.

9.1.1 Intermediate side branch angles

It was difficult to determine the effect of the side branch angle from developing only two models. A third model was developed in order to try and gain a deeper understanding of the effect of this variable on intimal hyperplasia development. This model has a side branch angle of 68^{o}, a single side branch and a ratio of 0.5 (1_68_0.5). The velocity pattern, shear stress and pressure results from this model follow on from this paragraph. These results are followed by a brief discussion.

Results

Figure 9.1 shows the flow pattern and velocity magnitude results for model 1_68_0.5. The flow pattern is similar to the patterns for 1_45_0.5 and 1_90_0.5 and can be seen in Fig. 9.1(A). Even though this is the case, there are slight differences. Model 1_45_0.5 has a maximum flow velocity of 0.0657m/s, 1_68_0.5 has one of 0.066m/s and 1_90_0.5 has a maximum flow velocity of 0.0665m/s. Its minimum flow velocity falls between the other two models' minimum flow velocity and has a value of 0.065m/s.

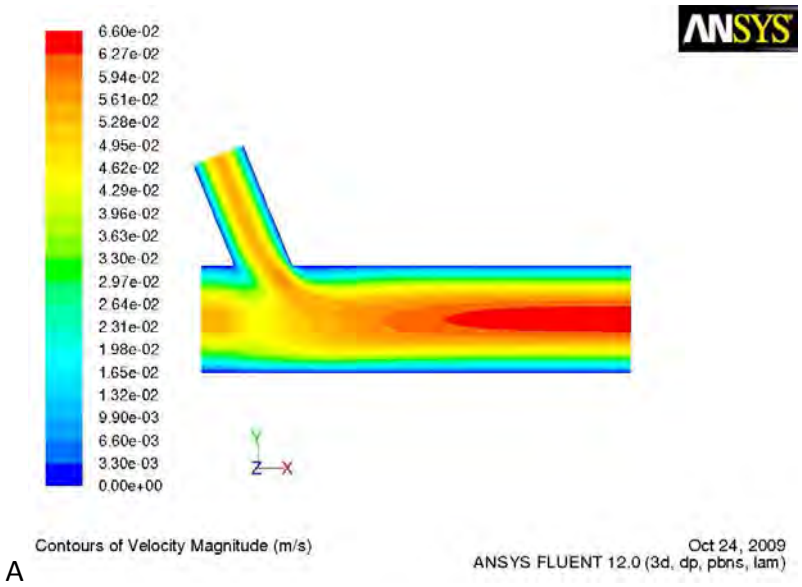

A

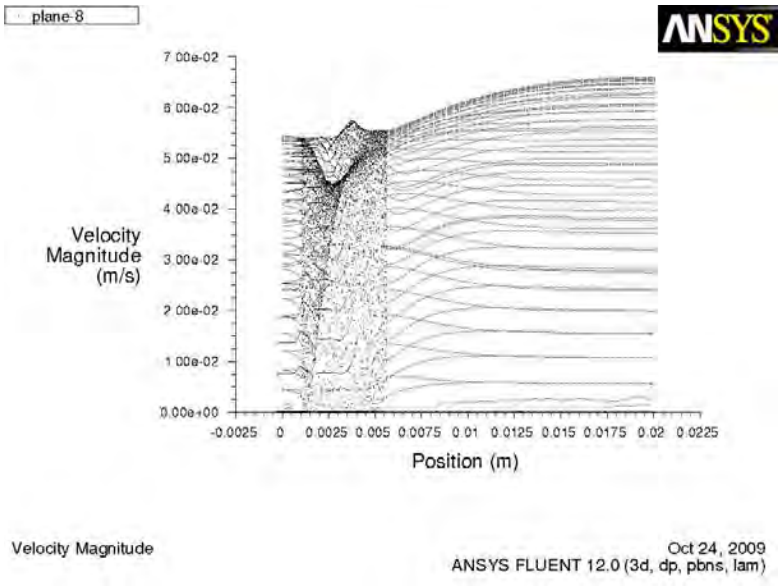

B

Figure 9.1: Velocity contour plot (A) and velocity magnitude graph (B) for model 1_68_0.5

Figure 9.2 shows the shear stress contour plot and graph for model 1_68_0.5. From the Fig 9.2(B), it can be seen that the graph has a minimum shear stress value of 0.068Pa. This value falls between the low shear stress value obtained for the 90^{o} model and the shear stress value for the 45^{o} model. The values for the other models can be seen in Table 7.1.

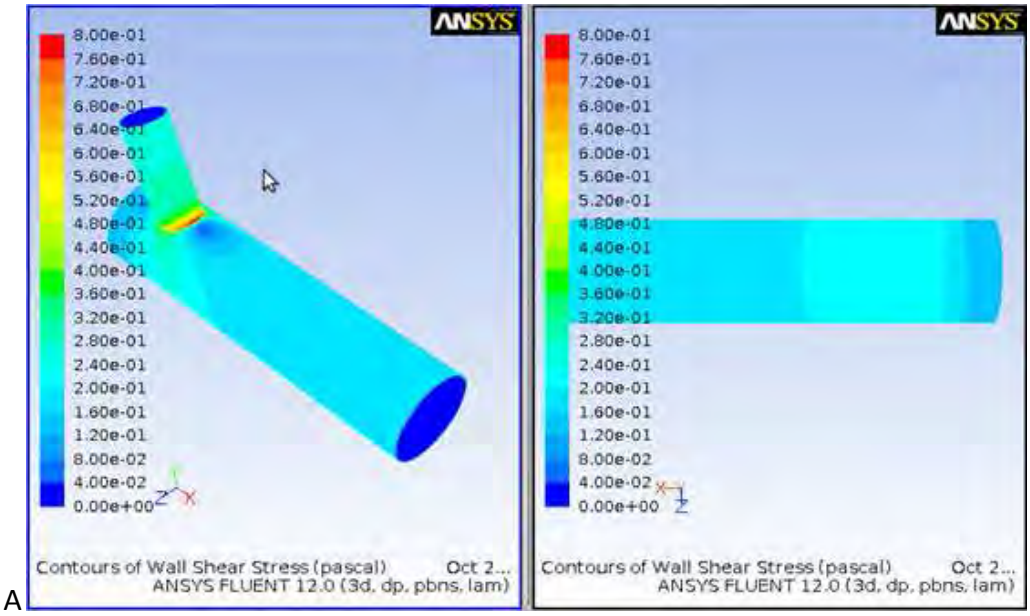

A

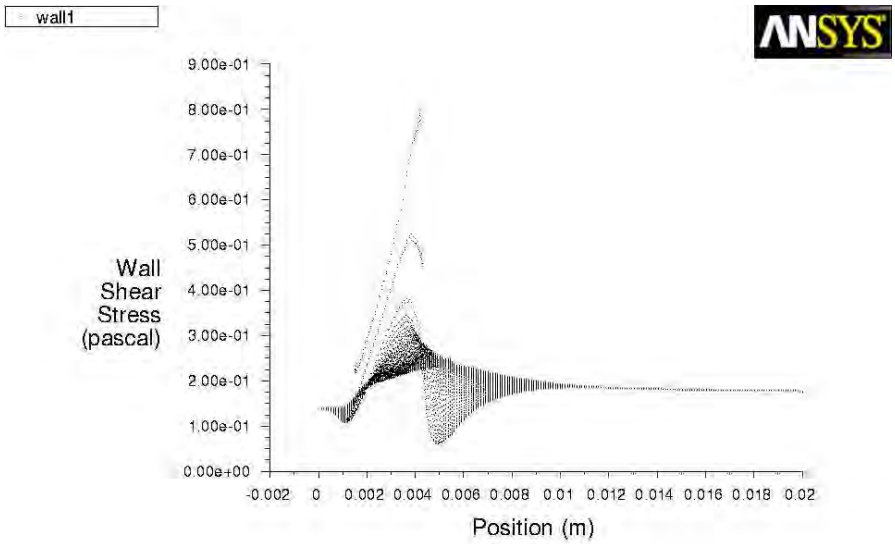

B

Figure 9.2: Shear stress contour plot (A) and wall shear stress graph (B) for model 1_68_0.5

Figure 9.3 shows the pressure plot for model 1_68_0.5. As with models 1_45_0.5 and 1_90_0.5, the maximum pressure occurs at the side branch inflow and the minimum pressure at the main vein outflow. The maximum pressure reached in the side branch region is 0.25Pa. This value falls in the same range as the other two models.

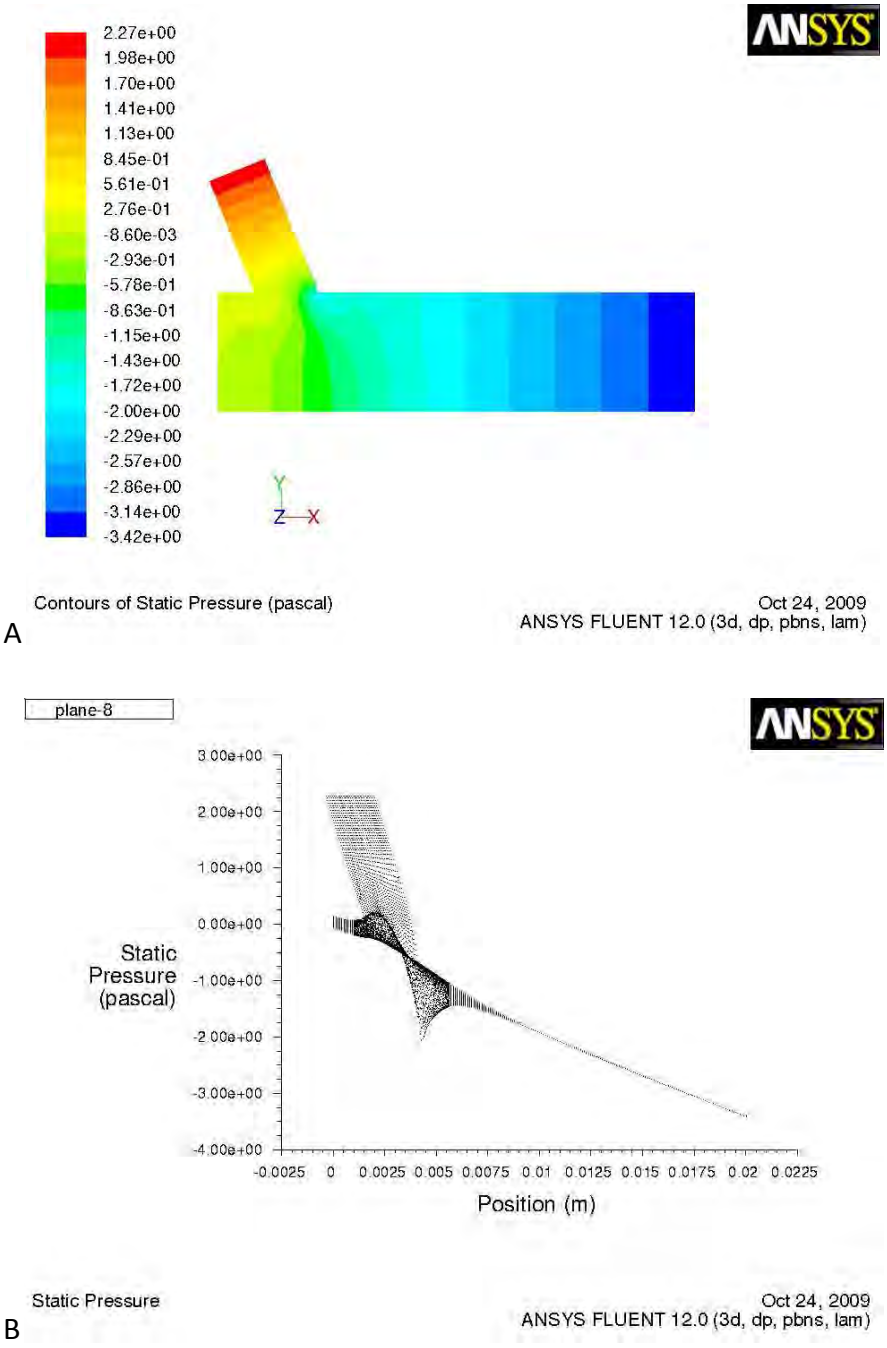

Figure 9.3: Pressure contour plot (A) and pressure graph (B) for model 1_68_0.5

The results from model 1_68_0.5 show that the side branch angle does seem to have an effect on the results. It may therefore be useful to further explore the effect of the side branch angle on flow patterns, shear stress and pressure as this may make a contribution to the understanding of intimal hyperplasia development. A study which examines side branch angles could also help pinpoint the angle at which shear stress drops below 0.1Pa, the value at which intimal hyperplasia is no longer fully suppressed.

9.1.2 General geometry of the model

Several assumptions were made regarding the geometry of the models. One of these was that all the side branches were in the same plane as the main vein. A triple side branch, 45^{o}, 0.5 ratio model was developed. In this model, the side branches were spaced out at 120^{o} to each other as seen in Fig. 9.4. The results for this model are presented below and are followed by a brief discussion.

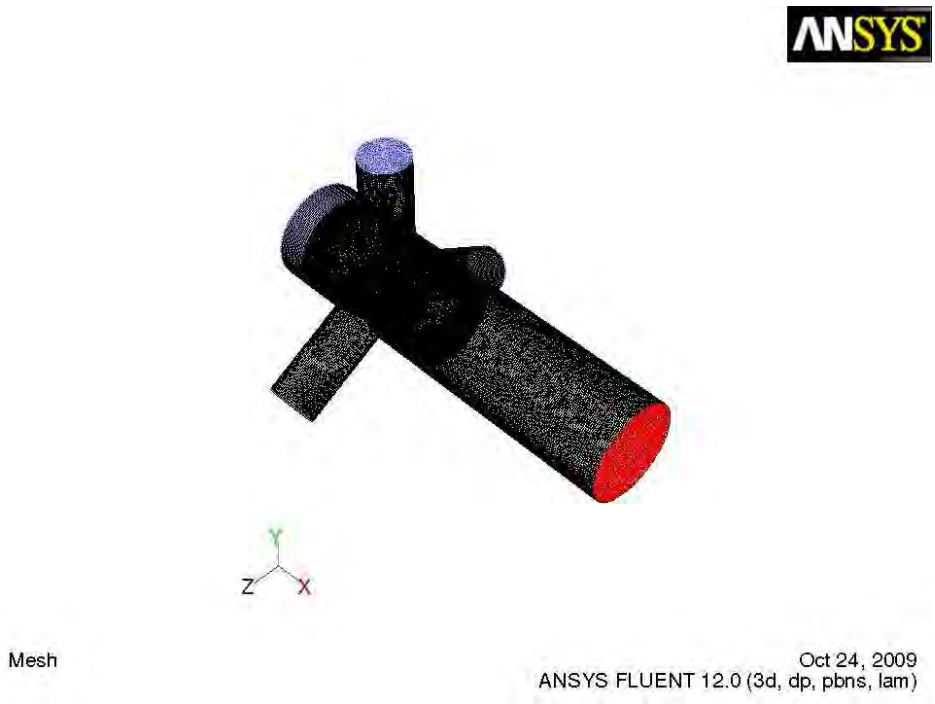

Figure 9.4: Mesh of the 120^{o} model: For this geometry the side branches are positioned at 120^{o} to each other

Results

Figure 9.5 shows the flow pattern and velocity magnitude plots for the 120^{o} model. Compared to the models where all the side branches lie in the plane of the main vein, the velocity magnitude in the region of the side branch is much lower as seen in both the Figs 9.5(A) and 9.5(B). The values for the other models can be found in Table 7.1.

A

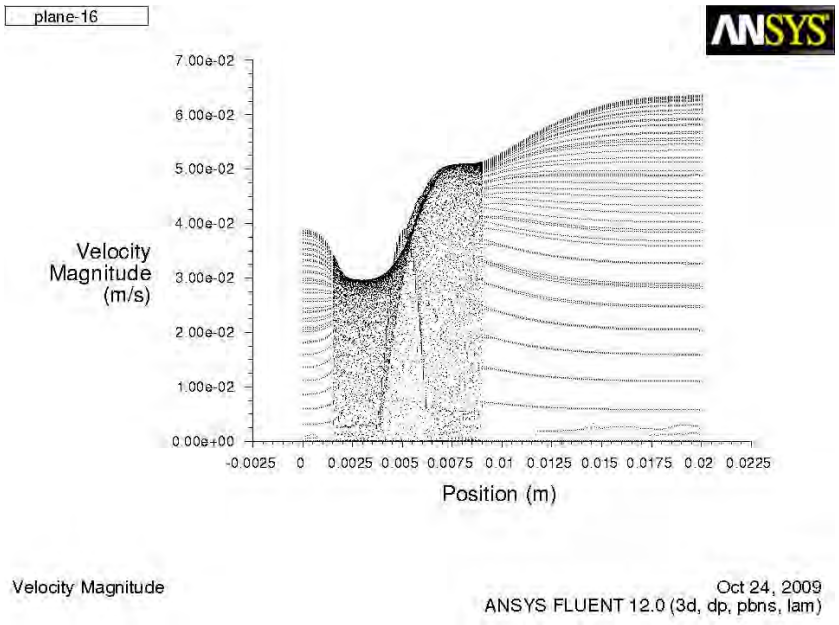

B

Figure 9.5: Velocity contour plot (A) and velocity magnitude graph (B) for the 120^{o} model

Figure 9.6 shows the shear stress pattern and plot for the 120^{o} model. There seems to be a number of low shear stress regions close to the side branches. As with the other models, the highest shear stress is reached in the side branch region. The minimum shear stress along the main vein wall is 0.1Pa.

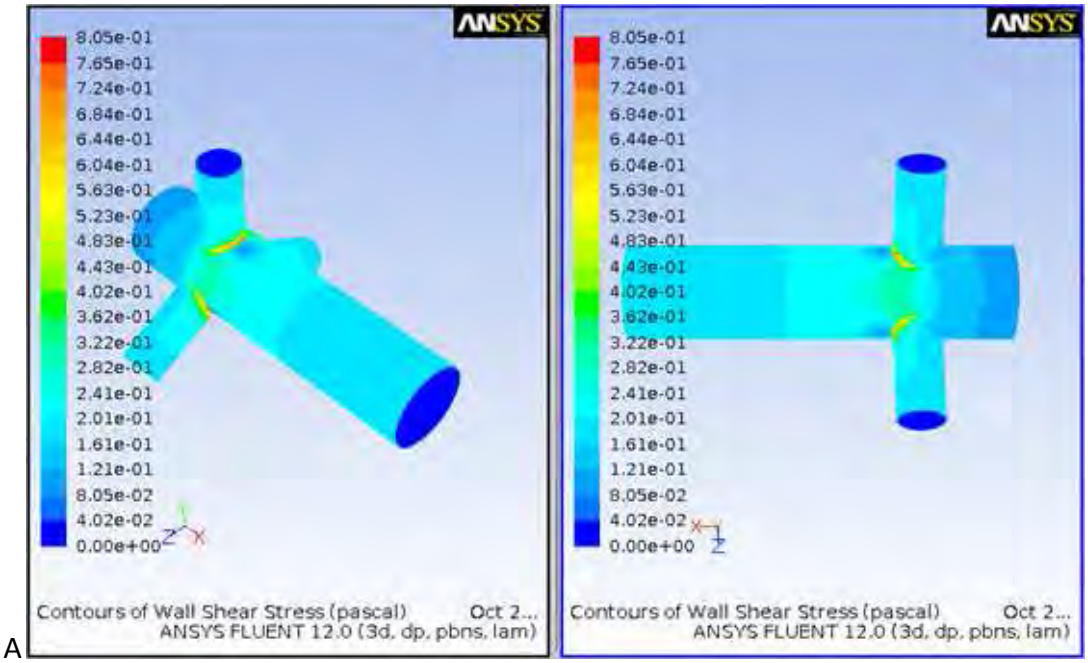

A

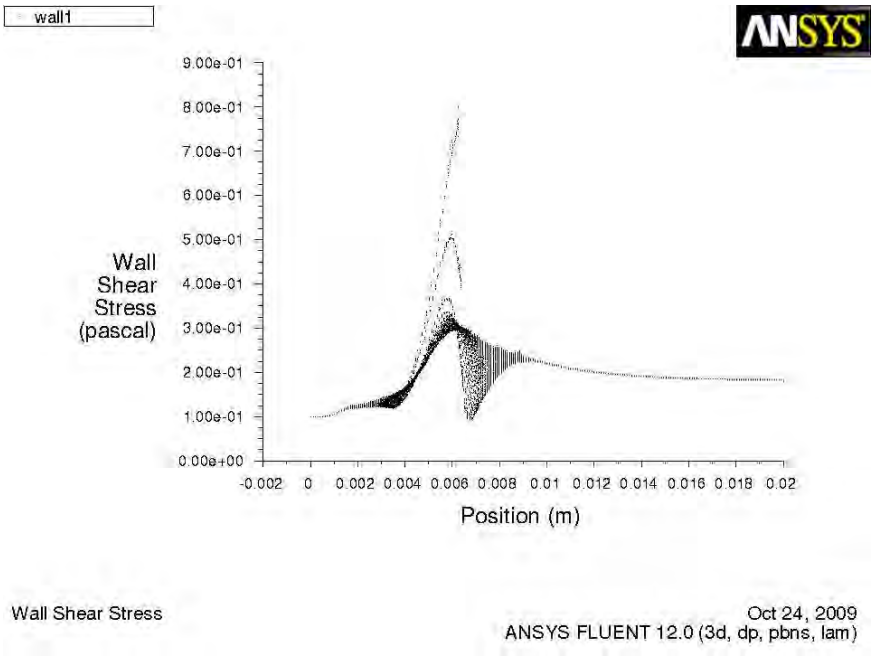

B

Figure 9.6: Shear stress contour plot (A) and wall shear stress graph (B) for the 120^{o} model

Figure 9.7 shows the pressure contour plot and graph for the 120^{o} model. The pressure values are comparable to all the other triple branch models developed. Figure 9.7(B) shows that like the other models, there is an increase in pressure at the intersection between the side branch and the main vein. This is followed by a pressure drop.

A

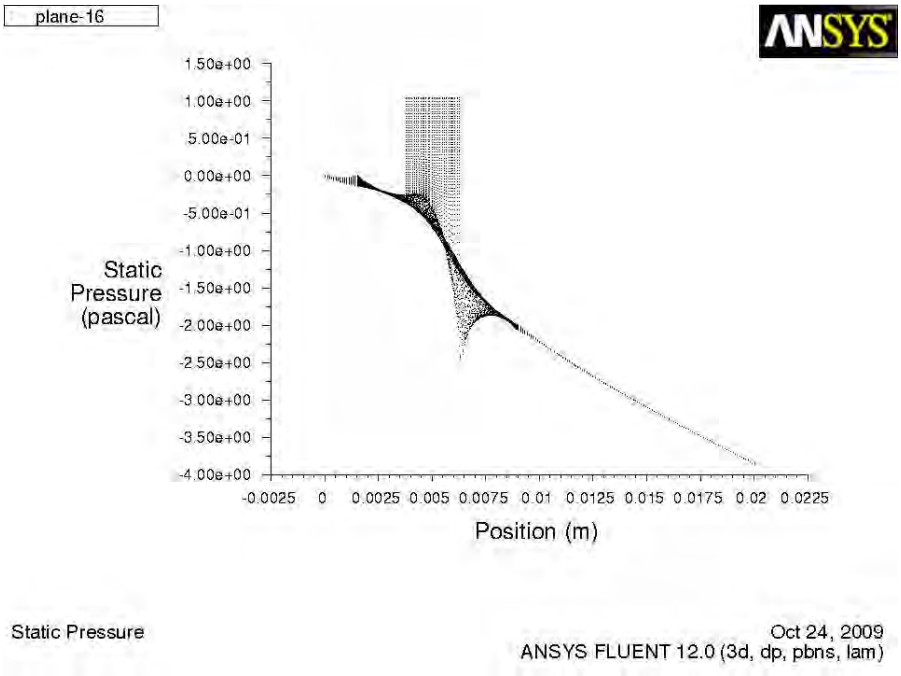

B

Figure 9.7: Pressure contour plot (A) and pressure graph (B) for the 120^{o} model

Although the pressure and shear stress magnitudes of the 120^{o} model are comparable to the other triple branch models developed, the velocity and shear stress contour results are rather different. From this, it can be seen that altering the geometric configuration of the side branches has an effect on the flow dynamics in the vein. For this reason, a study involving models with different geometric configurations could be useful for gaining more insight into the development of intimal hyperplasia.

9.2 Flow assumptions

One of the assumptions in chapter 6 states that the average velocity remains constant across all the inflows for a given model. An alternative assumption which could be made is that the flow rate is constant across all the inflows for a given model and that the average velocities are calculated accordingly.

A single side branch, 45^{o} angle and 0.5 ratio model was used. Rather than specifying a constant average velocity across the velocity inflows, a constant flow rate was specified. The results for this model are presented and are followed by a brief discussion.

Results

Figure 9.8 shows the flow pattern and velocity magnitude results. The constant flow rate assumption implies that the average velocities at the inlets will not have the same value. This can clearly be seen in Fig. 9.8(A). The main vein velocity is much slower than the side branch velocity and much velocity change occurs in the side branch region. Unlike the other models, the minimum flow velocity occurs at the main vein outflow, as seen in Fig 9.8(B).

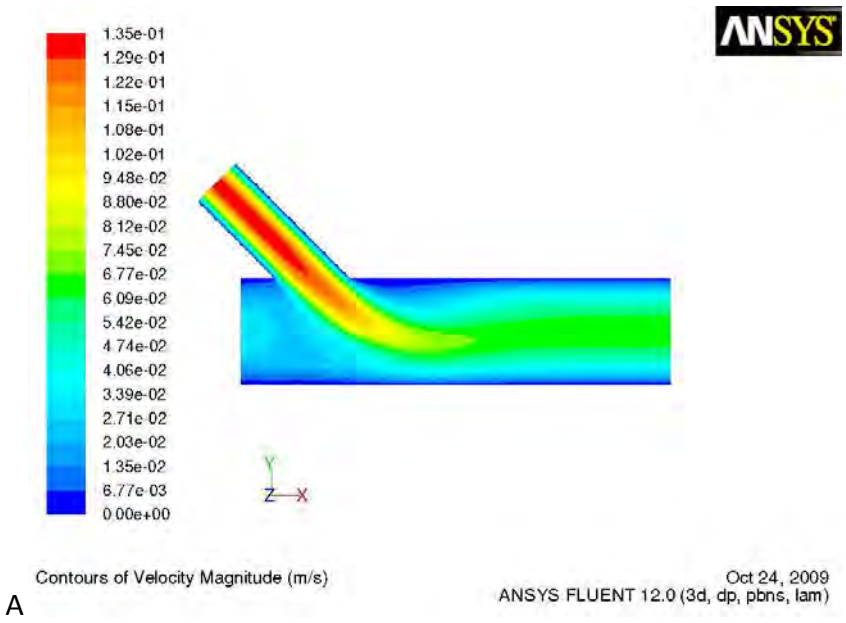

A

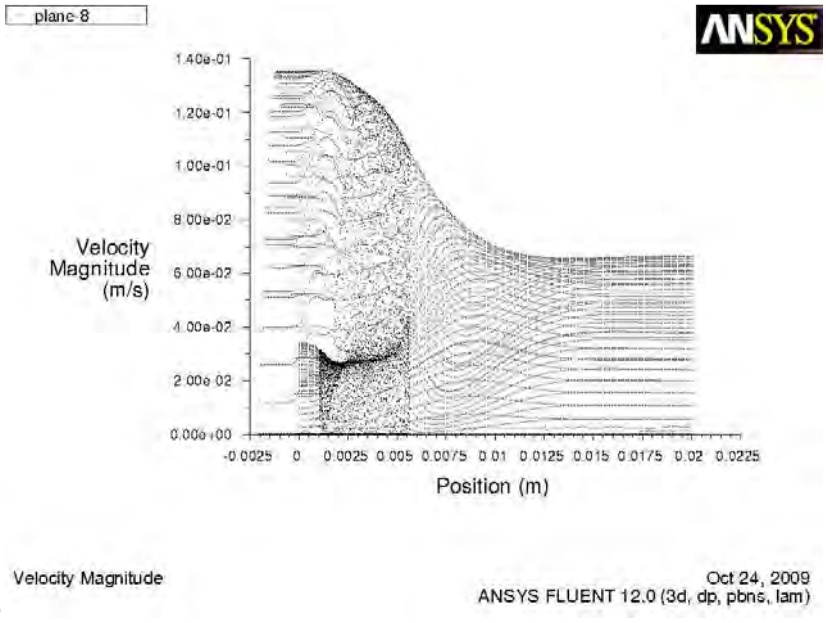

B

Figure 9.8: Velocity contour plot (A) and velocity magnitude graph (B) for the constant flow model

Figure 9.9 shows the shear stress contour and plot for the constant flow model. The minimum shear stress occurs close to the side branch region and has a value of less than 0.025Pa as seen in Figure 9.9(B). Figure 9.9(A) shows several low shear stress regions.

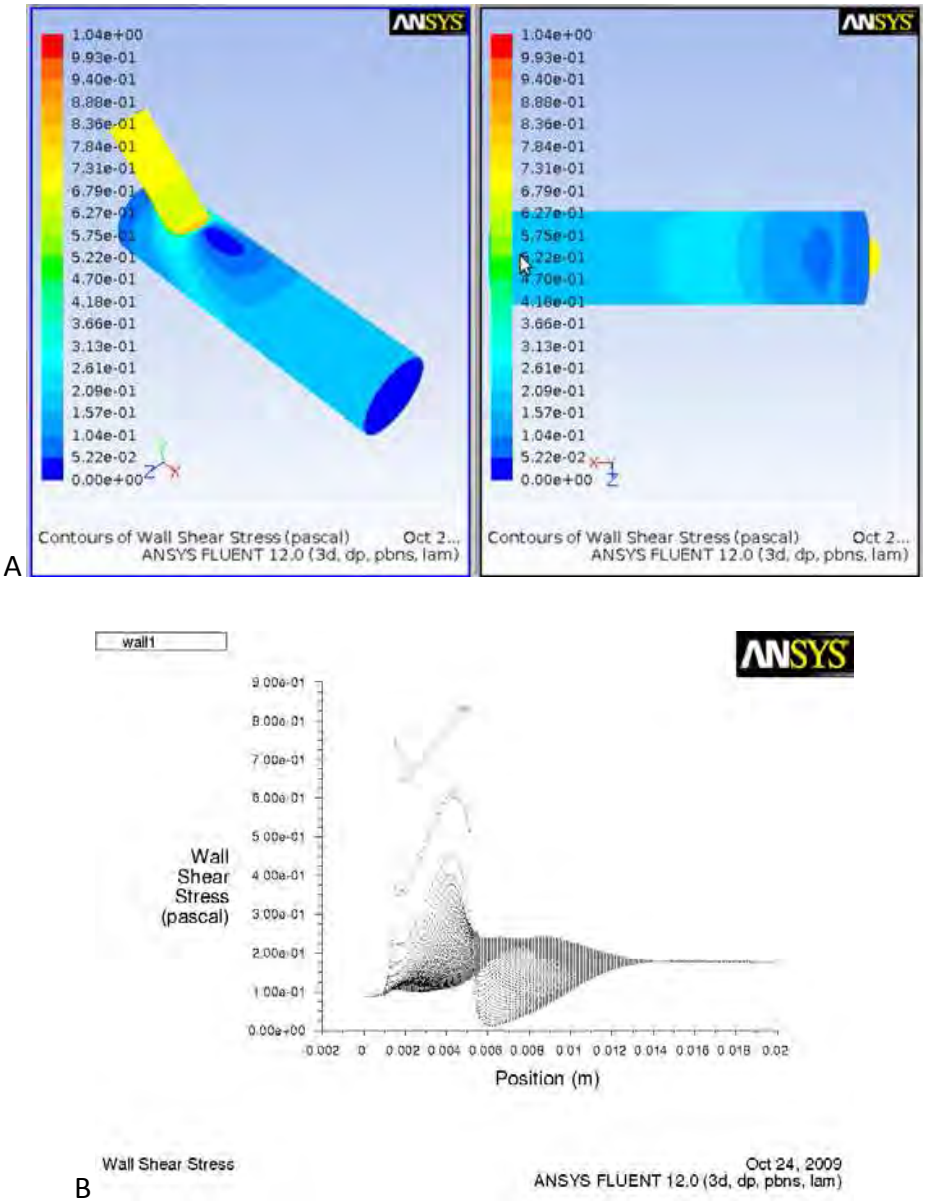

Figure 9.9: Shear stress contour plot (A) and wall shear stress graph (B) for the constant flow model

Figure 9.10 shows the pressure plot and graph for the constant flow model. As with the other models, the maximum pressure occurs at the side branch inflow and the minimum pressure occurs at the main vein outflow. Fig 9.10(A) does, however, show an interesting pressure pattern. Even though the pressure rise in the side branch region seen in Fig 9.10(B)

is common to all the models, the pressure drop following that is much greater for this model.

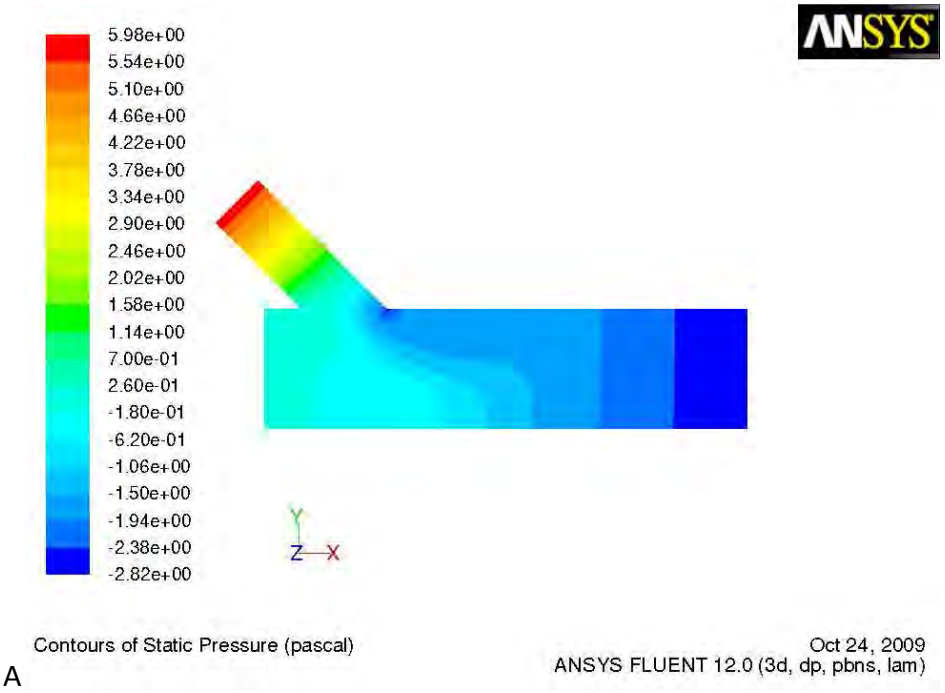

A

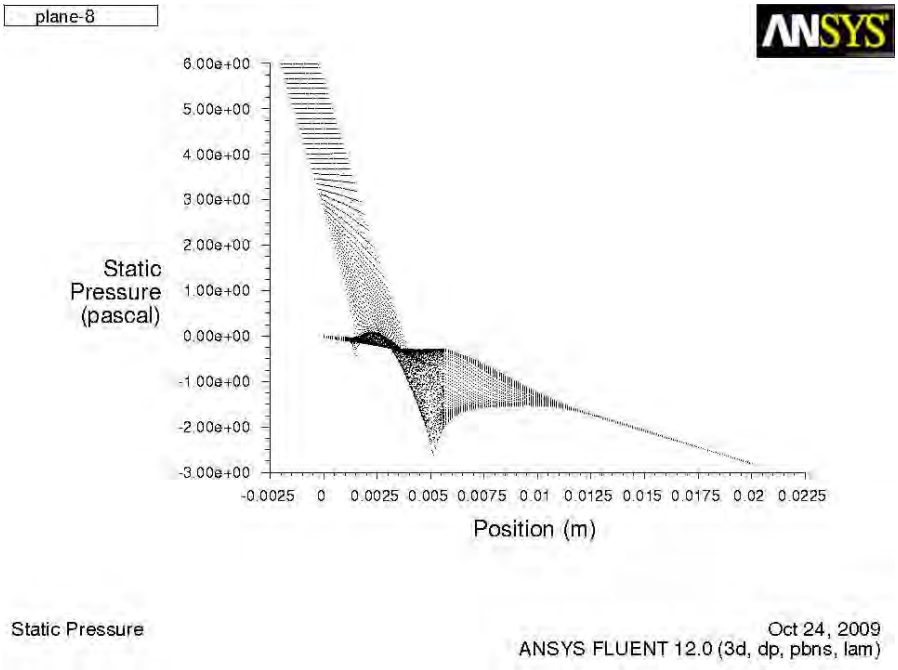

B

Figure 9.10: Pressure contour plot (A) and pressure graph (B) for the constant flow model

The results for the constant outflow model are different to the constant average velocity model results. For this reason, it may be interesting to conduct a comparative study of the two models in order to try and better understand the factors which affect the development of intimal hyperplasia.

9.3 Number of side branches

The discussion around the effect of the number of side branches in chapter 8 showed that it was difficult to determine the exact role that this variable played in the development of intimal hyperplasia. More side branches could be added in different configurations in order to better understand the effect of this variable. A four branch model was developed. The side branches are attached at 90^{o} and a ratio of 0.4 is used. The results and a brief discussion follow.

Results

Figure 9.11 shows the flow pattern and velocity results for the four branch model. The flow patterns are rather complex as seen in Fig. 9.11(A). From Fig. 9.11(B), it can be seen that the maximum velocity is 0.0534m/s. This is lower than the maximum velocity for the three branch model, which has a value of 0.0580m/s. The minimum velocity has a value of 0.0325m/s, while that of the three branch model is 0.0360m/s.

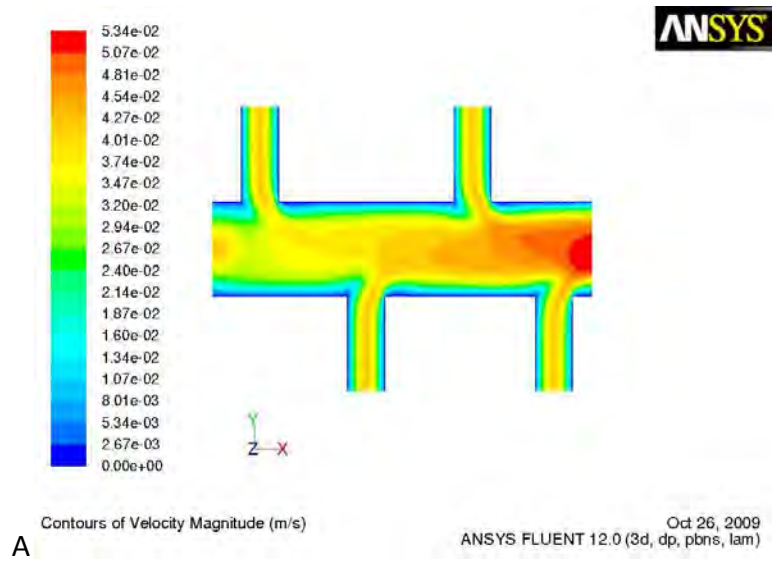

A

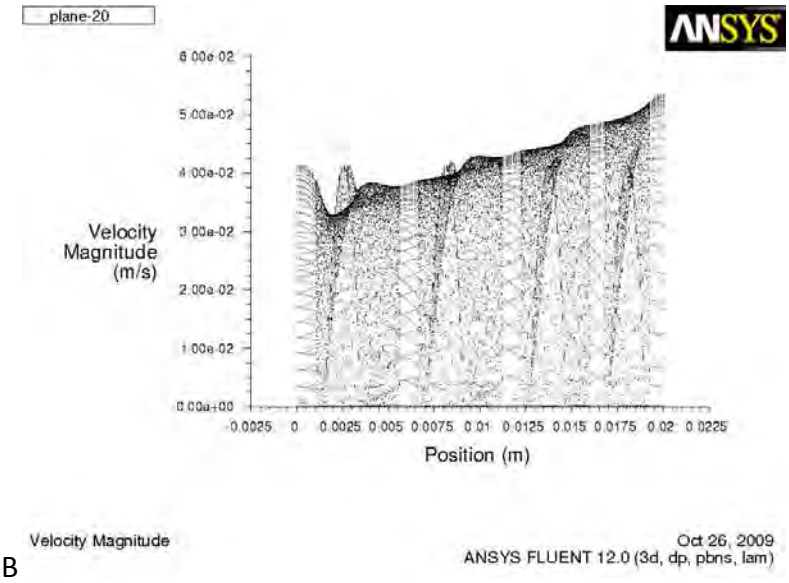

B

Figure 9.11: Velocity contour plot (A) and velocity magnitude graph (B) for the 4 branch model

Figure 9.12 shows the shear stress results for the four branch model. The shear stress values are comparable to the ones for the other models developed but there are more low shear stress regions as is expected. The shear stress values can be extracted from Fig. 9.12(B) while the low shear stress regions can be seen on Fig. 9.12(A).

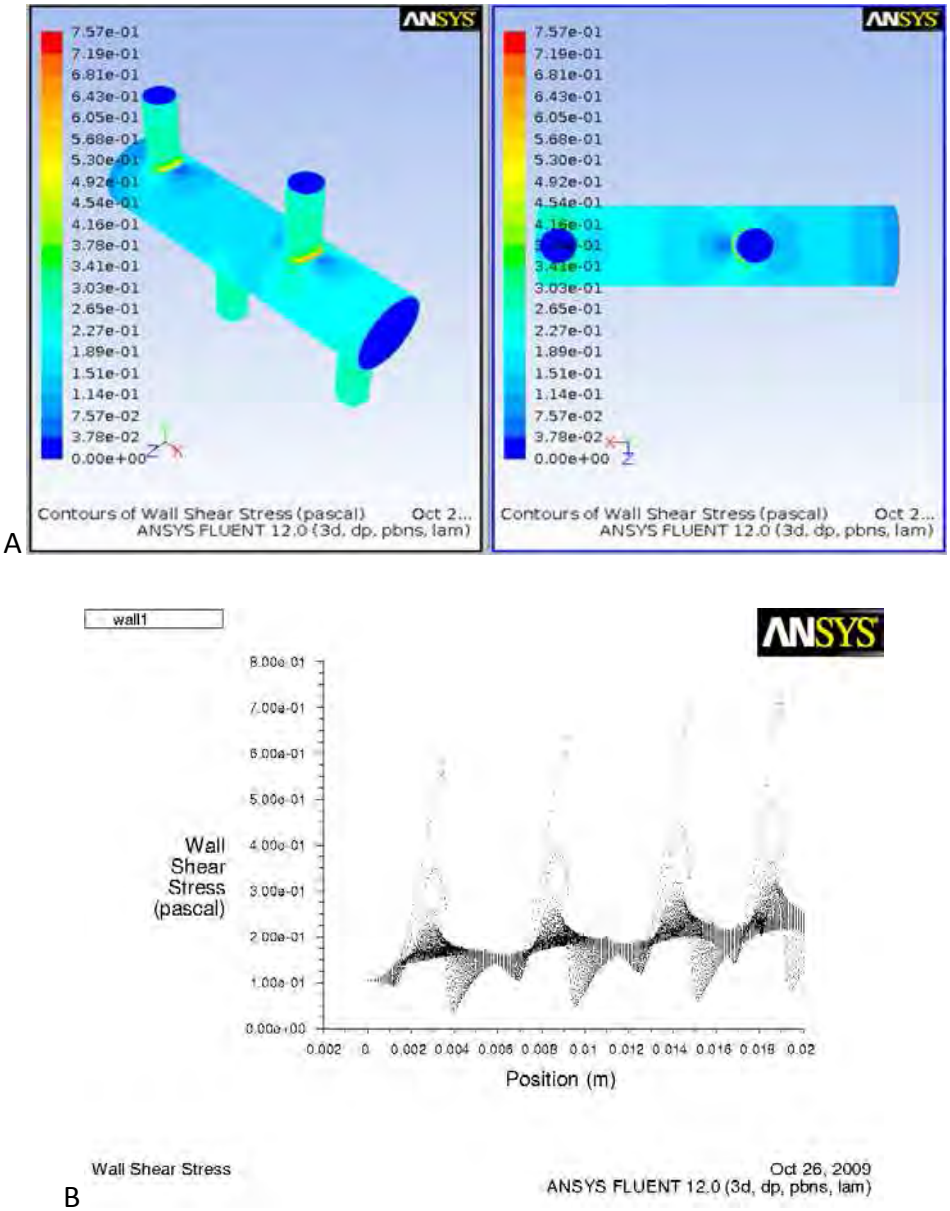

Figure 9.12: Shear stress contour plot (A) and wall shear stress graph (B) for the 4 branch model

Figure 9.13 shows the pressure results for the four branch model. Like the other models, the maximum pressure occurs at the first side branch inflow and the minimum occurs at the main vein outflow. The main vein pressure contours are distorted as seen in Fig. 9.13(A). There is an increase in pressure at the intersection of the main vein and the side branch as seen in Fig. 9.13(B).

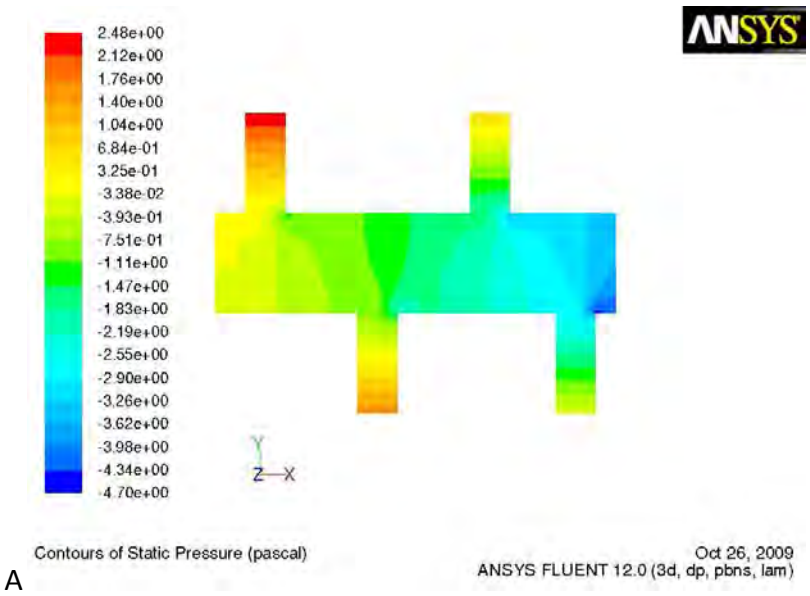

A

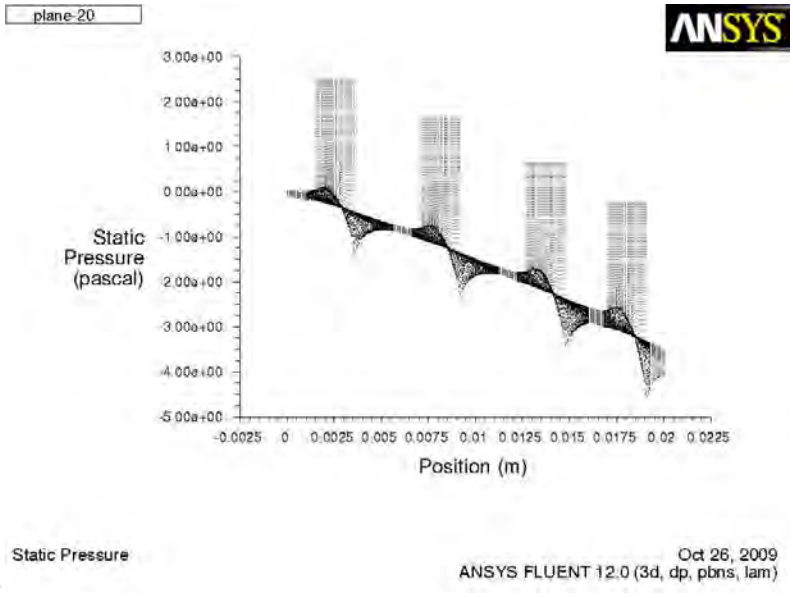

B

Figure 9.13: Pressure contour plot (A) and pressure graph (B) for the 4 branch model

There are notable differences between the 4 branch model and other similar models. The velocity values are lower and the shear stress patterns are different. A study exploring different numbers of side branches would therefore be worthwhile.

CHAPTER 10: CONCLUSIONS AND RECOMMENDATIONS

10.1 Introduction

The aim of this study was to determine the contribution of various factors to the development of intimal cushions in native veins in the region of side branches. The factors chosen were side branch to main vein diameter ratio, number of side branches and side branch angle. The effect of these factors was judged through the results obtained from different models. Flow pattern, shear stress and pressure results were examined. These results were compared against each other, a control model and information found in literature.

Twenty four different models were developed. The results from these models were studied and assessed. The judgement of the results was based on the control experiment and information found in literature. In addition, the models were grouped according to the factor being examined and models within the same group were judged against each other. The contribution that each factor made to the development of intimal cushions was then assessed based on these results.

10.2 Conclusions

Intimal hyperplasia is often associated with low flow velocities and low shear stress regions. For the models developed, the minimum flow velocity regions were generally in the side branch region. The minimum shear stress also coincided with the side branch region; however the minimum shear stress often occurred next to and not opposite the side branch. The pressure results all showed a pressure rise at the intersection of the main vein and the side branch.

The side branch diameter to main vein diameter ratio seemed to have the most significant impact on flow dynamics in the vein and in the side branch region. As the ratio was increased, the minimum shear stress and minimum velocity values decreased. It was therefore suggested that this ratio plays an important role in the development of intimal hyperplasia.

There was a direct correlation between the number of side branches and the minimum flow velocity. As the number of side branches increased, the minimum flow velocity decreased. The relationship between the number of side branches and the shear stress was a bit more difficult to determine. Based on that, it could be said that the number of side branches do play a role in the development of intimal hyperplasia but that the extent to which they have an influence is not known.

Determining the effect of the side branch angle proved somewhat difficult. All the values for the 45^{o} models fell below the 0.5Pa threshold value and above 0.1Pa. The results from the 90^{o} model all fell below 0.1Pa. In addition to this, the flow pattern and velocity magnitude results for the two model groups were similar. It was therefore difficult to find the link between the side branch angle and the development of intimal hyperplasia and further research would need to be conducted before any conclusions can be reached.

10.3 Limitations

As seen in chapter 6, many approximations were made regarding the physical nature of the veins, including the vein and side branch geometric configuration, vein cross-section and presence of valves. In addition to this, several assumptions were made regarding blood flow. As a result, the models deviated from real veins.

The meshes developed used a combination of tetrahedral and hexahedral elements as it proved rather difficult to use a single element type as there were side branches attached. Ideally, hexahedral elements would have been used throughout the mesh as the transition between the two element types may have had an influence on the results.

The exact shear stress, pressure and velocity data at which intimal hyperplasia develops was not known. This was largely due to the fact that such data would vary for different individuals. The analysis of the results was based on the approximate values which had been found in literature.

It proved rather difficult to plot graphs of the data found in chapter 7 as a three dimensional model was used. As a result, the plots used were the ones generated by FLUENT. Extracting information from these plots was sometimes difficult and being able to recognise which part of the vein the plots referred to was dependent on the ability to match up the contour plots with the information on the graphs.

10.4 Validity of results

The magnitude of the results was found to be in the same order of magnitude as data which had been found in literature. The inputs used for this study were also found in literature. These include the blood properties, vein dimensions and flow rates.

10.5 Recommendations

More research should be conducted in order to better understand the development of intimal hyperplasia in veins. Studies looking into the side branch angle, general geometric

configuration and number of side branches could be conducted. In addition, some of the assumptions could be changed in order to obtain a more accurate model of the human vein. Chapter 9 takes a more in-depth look at the scope for further development.

REFERENCES

1. American Venous Forum: Edited Gloviczki, P. and Yao, J. (2001). *Handbook of venous disorders. 2nd edition. Guidelines of the American Venous Forum.* New York: Arnold Publishers.

2. Athanasiou, K., & Natoli, R. (2008). *Introduction to continuum biomechanics.* New Jersey: Morgan and Claypool Publishers.

3. Bayer Schering Pharma AG. (2008). *Role of venous valves*. Retrieved September 1, 2009, from Thrombosis Adviser: http://www.thrombosisadviser.com/scripts/pages/en/image.php?image=venous-valves-blood-flow&category=haemostasis

4. Bell, D., & Rhoades, R. (2009). *Medical Physiology: Principles for Clinical Medicine. 3rd edition.* Baltimore: Lippincott Williams & Wilkins.

5. Bergel, D. (1972). Introduction. In D. Bergel, *Cardiovascular fluid dynamics: Volume I* (pp. 1-10). London: Academic Press.

6. Bonert, M., Leask, R., Butany, J., Ethier, C., Myers, J., Johnston, K., et al. (2003). The relationship between wall shear stress distributions and intimal thickening in the human abdominal aorta. *BioMedical Engineering OnLine* , 2:18-31.

7. Cleveland Clinic. (2009). *Circulation in the legs*. Retrieved September 1, 2009, from Cleveland Clinic: http://my.clevelandclinic.org/heart/disorders/vascular/circulationlegs.aspx

8. Dobrin, P., Littooy, F., & Endean, E. (1989). Mechanical factors predisposing to intimal hyperplasia and medial thickening in autogenous vein grafts. *Surgery* , 105:393-400.

9. Douglas, J., Gasiorek, J., Swaffield, J., & Jack, L. (2005). *Fluid Mechanics, 5th edition.* Essex: Pearson Education Limited.

10. Franz, T., Human, P., Moodley, L., Scherman, J., & Zilla, P. (2009). Dimensional analysis of human saphenous vein grafts: Implications for external mesh support. *Journal of Thoracic Cardiovascular Surgery* , 137:1101-1108.

11. Fung, Y. (1997). *Biomechanics: Circulation. 2nd edition.* New York: Springer-Verlag.

12. Fung, Y. (1993). *Biomechanics: Mechanical properties of living tissue. 2nd edition.* New York: Springer-Verlag.

13. Golledge, J., Turner, R., Harley, S., Springall, D., & Powell, J. (1997). Development of an in vitro model to study the response of saphenous vein endothelium to pulsatile arterial flow and circumferential deformation. *European Journal of Endovascular Surgery* , 13:605-612.

14. Gramoll, K., & Ngo, C. (n.d.). *Fluid mechanics - Theory*. Retrieved September 1, 2009, from ECourses: http://www.ecourses.ou.edu/cgi-bin/eBook.cgi?doc=&topic=fl&chap_sec=08.3&page=theory

15. Gray, H. (1858). *Gray's Anatomy.* Bath: Parragon.

16. Iaizzo, P. (2006). *Atlas of human cardiac anatomy*. Retrieved September 1, 2009, from University of Minnesota: Visible Hearts Laboratory: http://www.vhlab.umn.edu/atlas/phystutorial/phystutorial2.shtml

17. Kundu, P., & Cohen, I. (2008). *Fluid mechanics.* San Diego: Academic Press.

18. Levy, M., & Pappano, A. (2007). *Cardiovascular physiology. 9th edition.* Philadelphia: Mosby Elsevier.

19. Porter, K., Nydahl, S., Dunlop, P., Varty, K., Thrush, A., & London, N. (1996). The development of an in vitro flow model of human saphenous vein graft intimal hyperplasia. *Cardiovascular Research* , 31:607-614.

20. Sherwood, L. (2004). *Human physiology: From cells of systems. 5th edition.* Belmont: Brooks/Cole.

21. Subbotin, V. M. (2007). Analysis of arterial intimal hyperplasia: review and hypothesis. *Theoretical Biology and Medical Modelling* , 4:41-60.

22. Vascular-Web. (2003). *Vasc104: Basic venous anatomy*. Retrieved September 1, 2009, from Vascular-Web: http://www.vascular-web.com/asp/samples/sample104.asp

23. Versteeg, H., & Malalasekera, W. (2007). *An introduction to computational fluid dynamics: The finite volume method. 2nd edition.* Essex: Pearson Education Limited.

24. Weisstein, E. (2009, August 31). *Finite volume method*. Retrieved September 2, 2009, from Wolfram MathWorld: http://mathworld.wolfram.com/FiniteVolumeMethod.html

25. Zilla, P., Wolf, M., Rafiee, N., Moodley, L., Bezuidenhout, D., Black, M., et al. (2009). Utilization of shape memory in external vein-graft meshes allows extreme diameter constriction for suppressing intimal hyperplasia: A non-human primate study. *Journal of Vascular Surgery* , 49:1532-1542.

APPENDIX A: User-defined functions

User-Defined Functions (UDFs) are FLUENT functions which the user can specify in order to build on functions already available in FLUENT. For this study, UDFs were specified for the inlet velocity profiles.

1. **Velocity inlet profile for the main vein**

```
#include "udf.h"

static const float dpdx = 667.08;
static const float u = 0.0032;
static const float a = 0.0025;

DEFINE_PROFILE(inlet1_velocity,thread,i)


{
 real x[ND_ND];
 real y;
 real r;
 cell_t c;



 begin_c_loop(c,thread)
 {
        C_CENTROID (x,c,thread);
        y = x[2];
        r = sqrt((x[1]*x[1]) + (y*y));
        F_PROFILE(c,thread,i) = (dpdx/(4*u))*((a*a) - (r*r));
 }
 end_c_loop(c,thread)
}
```

2. Velocity inlet profile for a side branch

```
#include "udf.h"

static const float dpdx = 1334.16;
static const float u = 0.0032;
static const float a = 0.00125;
static const float offx = 0.002348349570;
static const float offy = 0.006919417382;


DEFINE_PROFILE(inlet2_velocity,thread,i)


{
 real x[ND_ND];
 real y;
 real z;
 real r;
 cell_t c;



 begin_c_loop(c,thread)
 {
        C_CENTROID (x,c,thread);
        y = x[1];
        z = x[2];
        r = sqrt(((x[0] - offx)*(x[0] - offx)) + ((y - offy)*(y - offy)) + (z*z));
        F_PROFILE(c,thread,i) = (dpdx/(4*u))*((a*a) - (r*r));
  }
 end_c_loop(c,thread)
}
```

Explanation of the code

The code loops through each cell on a given face (in this case, the inlet face). The C_CENTROID function returns the x-, y- and z-co-ordinates of each face. These are used to calculate the radius of that face from the centre. The radius is then used to calculate the value of the velocity for that face. Owing to their respective orientations, the main vein

model only makes use of the y- and z-co-ordinates to calculate the radius while the side branch model makes use of the x-, y- and z-co-ordinates. The offx and offy values for the side branch velocity profile account for the fact that the branch is not located at the origin.

APPENDIX B: UDF Velocity Profile Calculations

Table B1: Constants used when making calculations for the FLUENT inputs

Flow rate	40	*ml/min*
	6.66667E-07	*kg/ms*
Main vein radius	0.0025	*m*
Main vein area	1.9635E-05	m^2
Viscosity	0.0032	*kg/ms*

Formulae used for the calculations

$$Side\ branch\ area = \pi(side\ branch\ radius)^2 \quad \text{Eq. B1}$$

$$Total\ area = No. \times Side\ branch\ area + Main\ vein\ area \quad \text{Eq. B2}$$

$$v_{avg} = \frac{Flow\ rate}{Total\ area} \quad \text{Eq. B3}$$

$$v_{max} = 2 \times v_{avg} \quad \text{Eq. B4}$$

$$\frac{dp}{dx} = \frac{4 \times v_{avg} \times viscosity}{radius^2} \quad \text{Eq. B5}$$

Table B2: Area, velocity and pressure gradient calculations for the velocity profiles

Ratio	Side branch radius	No.	Side branch area	Total area	v_{avg}	v_{max}	dp/dx main	dp/dx side branch
	m		m^2	m^2	*m/s*	*m/s*	*Pa/m*	*Pa/m*
1 branch								
0.2	0.0005	1	7.85398E-07	2.042E-05	0.03265	0.06529	133.72	3343.07
0.3	0.00075	1	1.76715E-06	2.1402E-05	0.03115	0.06230	127.59	1417.65
0.4	0.001	1	3.14159E-06	2.2777E-05	0.02927	0.05854	119.89	749.31
0.5	0.00125	1	4.90874E-06	2.4544E-05	0.02716	0.05432	111.26	445.03
2 branch								
0.2	0.0005	2	7.85398E-07	2.1206E-05	0.03144	0.06288	128.77	3219.25
0.3	0.00075	2	1.76715E-06	2.3169E-05	0.02877	0.05755	117.86	1309.53
0.4	0.001	2	3.14159E-06	2.5918E-05	0.02572	0.05144	105.36	658.48
0.5	0.00125	2	4.90874E-06	2.9452E-05	0.02264	0.04527	92.71	370.86
3 branch								
0.2	0.0005	3	7.85398E-07	2.1991E-05	0.03032	0.06063	124.17	3104.28
0.3	0.00075	3	1.76715E-06	2.4936E-05	0.02673	0.05347	109.51	1216.73
0.4	0.001	3	3.14159E-06	2.906E-05	0.02294	0.04588	93.97	587.30
0.5	0.00125	3	4.90874E-06	3.4361E-05	0.01940	0.03880	79.47	317.88
Control								
0	0	3	0	1.9635E-05	0.03395	0.06791	139.07	

APPENDIX C: Complete set of results

Appendix C presents the total set of results. This includes the flow pattern and velocity, shear stress and pressure results for the models developed for this study. A brief explanation of how the contour plots and graphs were interpreted is given, followed by a table listing all the diagrams included in this appendix.

Interpretation of the velocity magnitude graphs

The velocity magnitude graph plots the velocity data from the contour plot given in part A of each figure. The x-axis represents the distance along the length of the vein, i.e. from 0 to 0.02m. The y-axis represents the velocity magnitude values at the different points along the vein length. The models are all three-dimensional hence there will be multiple velocity values at any point along the x-axis, i.e. along the vein length. The y values closer to the origin represent the values closer to the wall of the vein. The maximum y values (the maximum y value for every x value) on the graph represent values closer to the centre of the flow (where the velocities are the highest).

Contents of Appendix C

Figure C1: Flow plot and velocity magnitude for 1_45_0.2	C3	Figure C37: Shear plot and wall shear stress graph for 2_90_0.2	C21
Figure C2: Flow plot and velocity magnitude for 1_45_0.3	C3	Figure C38: Shear plot and wall shear stress graph for 2_90_0.3	C21
Figure C3: Flow plot and velocity magnitude for 1_45_0.4	C4	Figure C39: Shear plot and wall shear stress graph for 2_90_0.4	C22
Figure C4: Flow plot and velocity magnitude for 1_45_0.5	C4	Figure C40: Shear plot and wall shear stress graph for 2_90_0.5	C22
Figure C5: Flow plot and velocity magnitude for 1_90_0.2	C5	Figure C41: Shear plot and wall shear stress graph for 3_45_0.2	C23
Figure C6: Flow plot and velocity magnitude for 1_90_0.3	C5	Figure C42: Shear plot and wall shear stress graph for 3_45_0.3	C23
Figure C7: Flow plot and velocity magnitude for 1_90_0.4	C6	Figure C43: Shear plot and wall shear stress graph for 3_45_0.4	C24
Figure C8: Flow plot and velocity magnitude for 1_90_0.5	C6	Figure C44: Shear plot and wall shear stress graph for 3_45_0.5	C24
Figure C9: Flow plot and velocity magnitude for 2_45_0.2	C7	Figure C45: Shear plot and wall shear stress graph for 3_90_0.2	C25
Figure C10: Flow plot and velocity magnitude for 2_45_0.3	C7	Figure C46: Shear plot and wall shear stress graph for 3_90_0.3	C25
Figure C11: Flow plot and velocity magnitude for 2_45_0.4	C8	Figure C47: Shear plot and wall shear stress graph for 3_90_0.4	C26
Figure C12: Flow plot and velocity magnitude for 2_45_0.5	C8	Figure C48: Shear plot and wall shear stress graph for 3_90_0.5	C26
Figure C13: Flow plot and velocity magnitude for 2_90_0.2	C9	Figure C49: Pressure plot and graph for 1_45_0.2	C27
Figure C14: Flow plot and velocity magnitude for 2_90_0.3	C9	Figure C50: Pressure plot and graph for 1_45_0.3	C27
Figure C15: Flow plot and velocity magnitude for 2_90_0.4	C10	Figure C51: Pressure plot and graph for 1_45_0.4	C28
Figure C16: Flow plot and velocity magnitude for 2_90_0.5	C10	Figure C52: Pressure plot and graph for 1_45_0.5	C28
Figure C17: Flow plot and velocity magnitude for 3_45_0.2	C11	Figure C53: Pressure plot and graph for 1_90_0.2	C29
Figure C18: Flow plot and velocity magnitude for 3_45_0.3	C11	Figure C54: Pressure plot and graph for 1_90_0.3	C29
Figure C19: Flow plot and velocity magnitude for 3_45_0.4	C12	Figure C55: Pressure plot and graph for 1_90_0.4	C30
Figure C20: Flow plot and velocity magnitude for 3_45_0.5	C12	Figure C56: Pressure plot and graph for 1_90_0.5	C30
Figure C21: Flow plot and velocity magnitude for 3_90_0.2	C13	Figure C57: Pressure plot and graph for 2_45_0.2	C31
Figure C22: Flow plot and velocity magnitude for 3_90_0.3	C13	Figure C58: Pressure plot and graph for 2_45_0.3	C31
Figure C23: Flow plot and velocity magnitude for 3_90_0.4	C14	Figure C59: Pressure plot and graph for 2_45_0.4	C32
Figure C24: Flow plot and velocity magnitude for 3_90_0.5	C14	Figure C60: Pressure plot and graph for 2_45_0.5	C32
Figure C25: Shear plot and wall shear stress graph for 1_45_0.2	C15	Figure C61: Pressure plot and graph for 2_90_0.2	C33
Figure C26: Shear plot and wall shear stress graph for 1_45_0.3	C15	Figure C62: Pressure plot and graph for 2_90_0.3	C33
Figure C27: Shear plot and wall shear stress graph for 1_45_0.4	C16	Figure C63: Pressure plot and graph for 2_90_0.4	C34
Figure C28: Shear plot and wall shear stress graph for 1_45_0.5	C16	Figure C64: Pressure plot and graph for 2_90_0.5	C34
Figure C29: Shear plot and wall shear stress graph for 1_90_0.2	C17	Figure C65: Pressure plot and graph for 3_45_0.2	C35
Figure C30: Shear plot and wall shear stress graph for 1_90_0.3	C17	Figure C66: Pressure plot and graph for 3_45_0.3	C35
Figure C31: Shear plot and wall shear stress graph for 1_90_0.4	C18	Figure C67: Pressure plot and graph for 3_45_0.4	C36
Figure C32: Shear plot and wall shear stress graph for 1_90_0.5	C18	Figure C68: Pressure plot and graph for 3_45_0.5	C36
Figure C33: Shear plot and wall shear stress graph for 2_45_0.2	C19	Figure C69: Pressure plot and graph for 3_90_0.2	C37
Figure C34: Shear plot and wall shear stress graph for 2_45_0.3	C19	Figure C70: Pressure plot and graph for 3_90_0.3	C37
Figure C35: Shear plot and wall shear stress graph for 2_45_0.4	C20	Figure C71: Pressure plot and graph for 3_90_0.4	C38
Figure C36: Shear plot and wall shear stress graph for 2_45_0.5	C20	Figure C72: Pressure plot and graph for 3_90_0.5	C38

Velocity Results

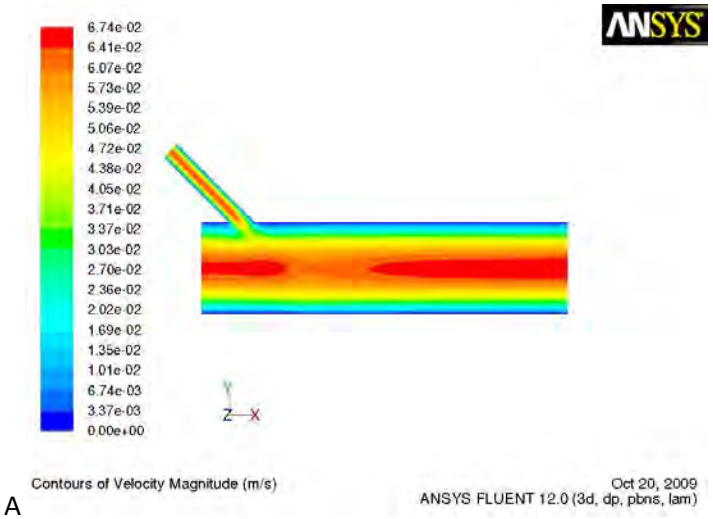

A

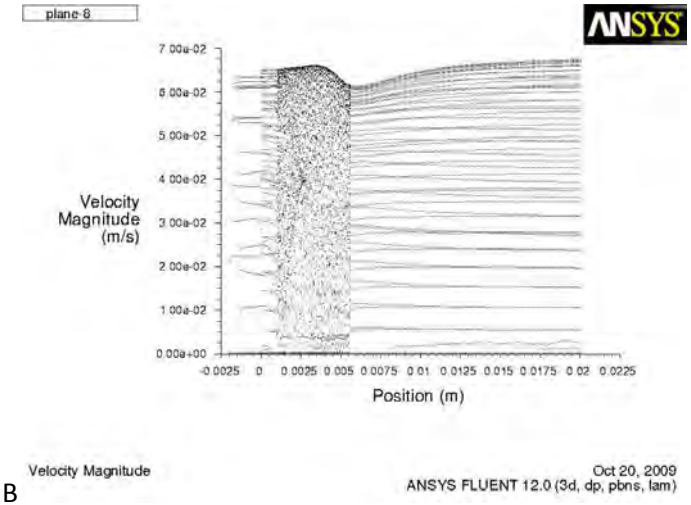

B

Figure C1: Flow plot (A) and velocity magnitude graph (B) for 1_45_0.2

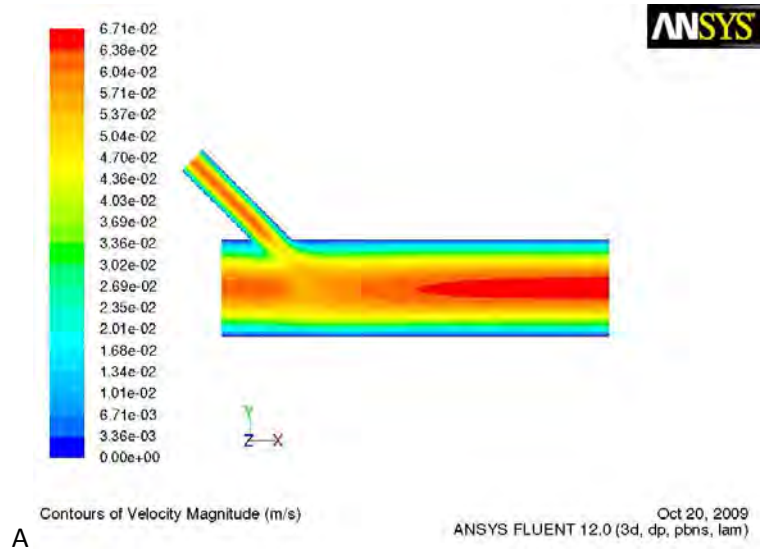

A

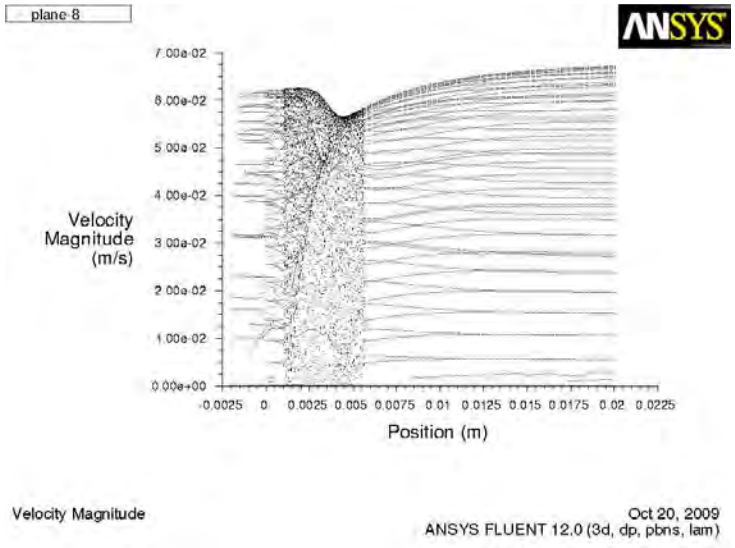

B

Figure C2: Flow plot (A) and velocity magnitude graph (B) for 1_45_0.3

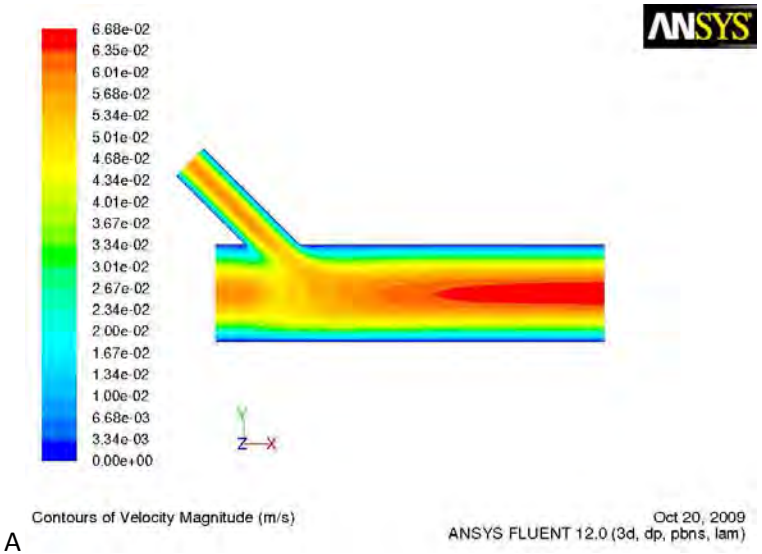

A

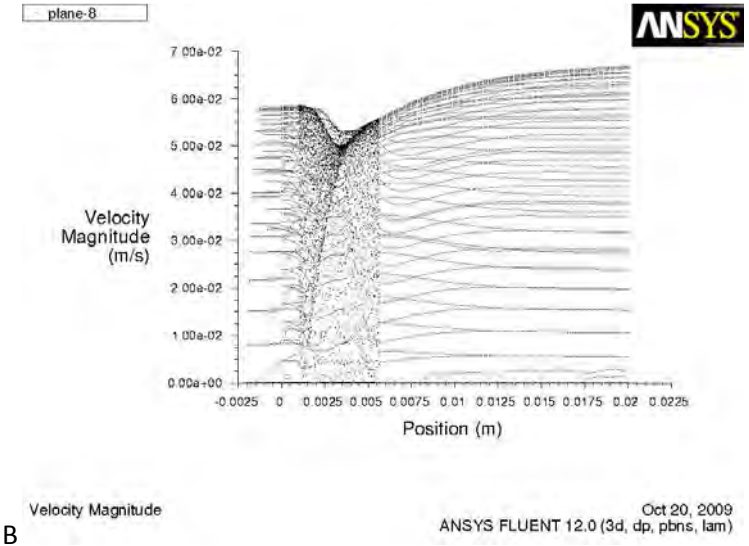

B

Figure C3: Flow plot (A) and velocity magnitude graph (B) for 1_45_0.4

A

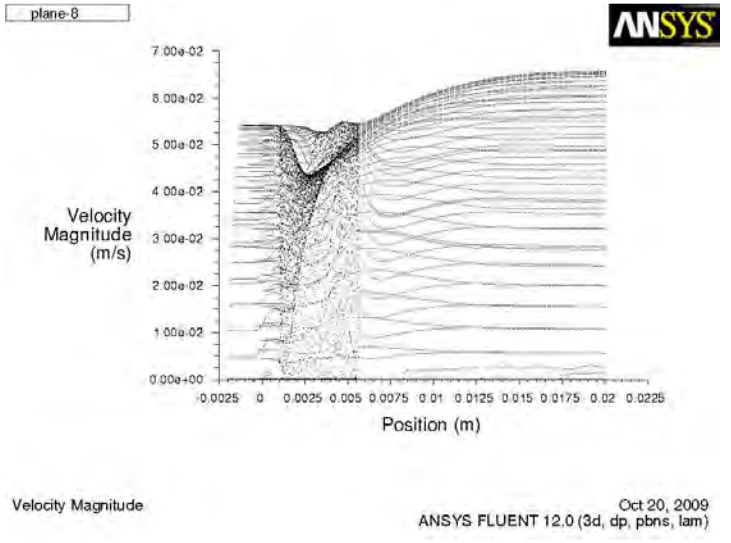

B

Figure C4: Flow plot (A) and velocity magnitude graph (B) for 1_45_0.5

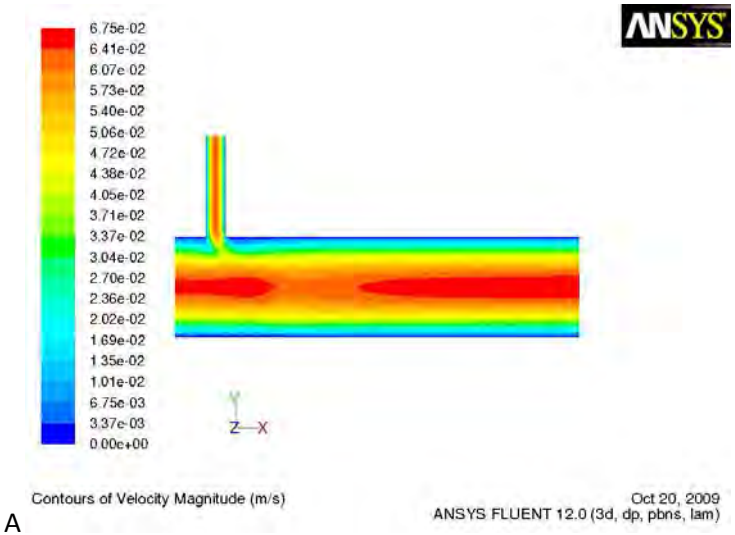

A

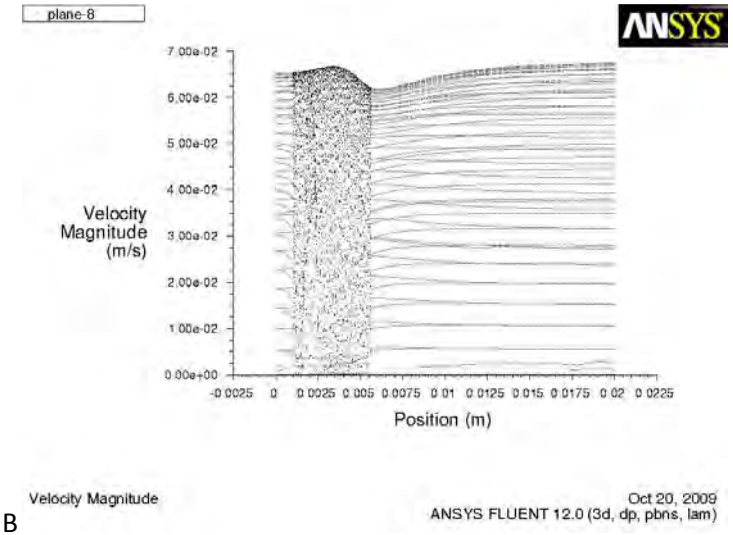

B

Figure C5: Flow plot (A) and velocity magnitude graph (B) for 1_90_0.2

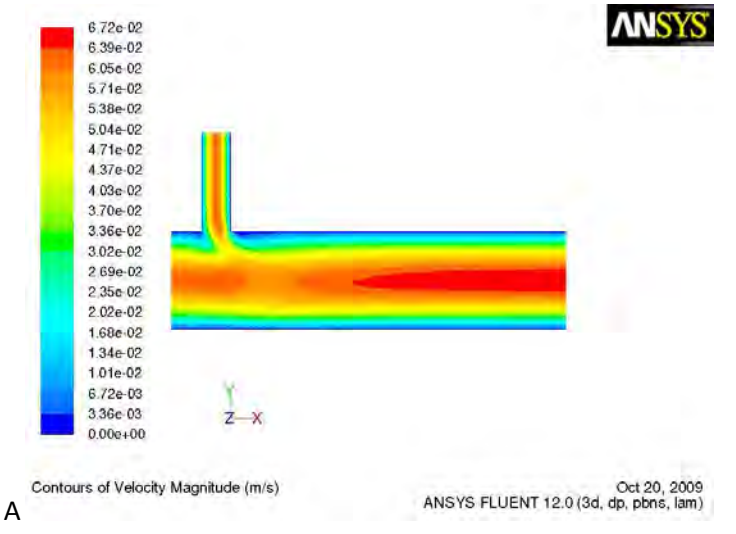

A

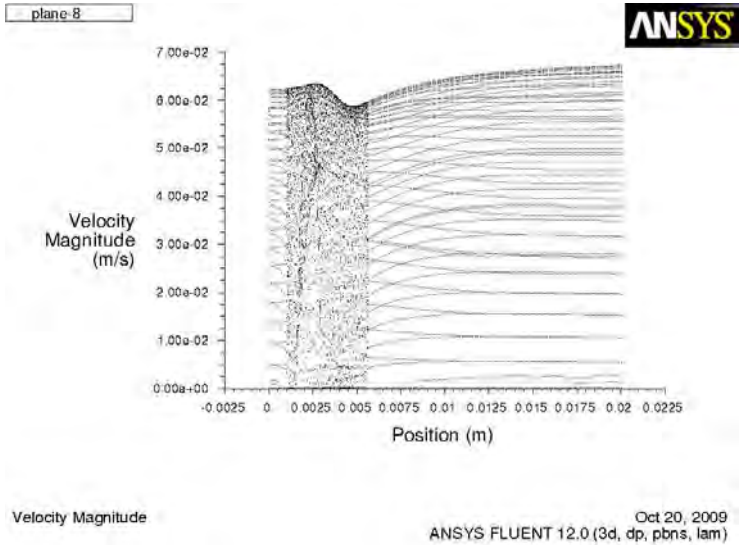

B

Figure C6: Flow plot (A) and velocity magnitude graph (B) for 1_90_0.3

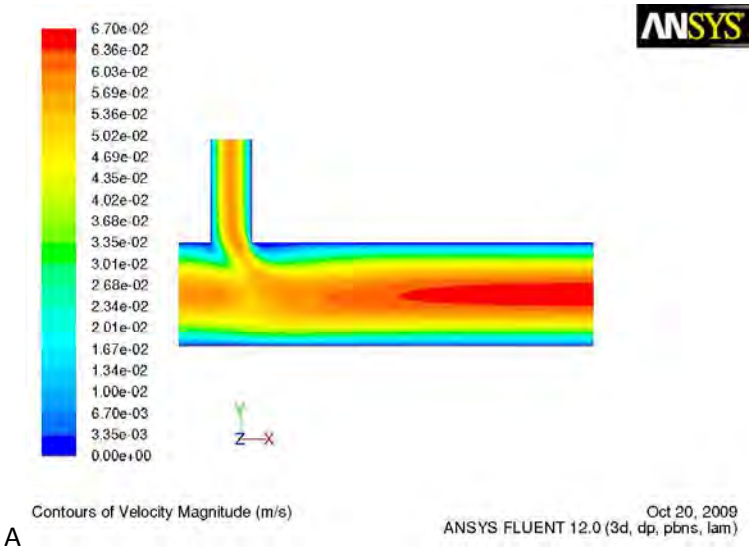

A

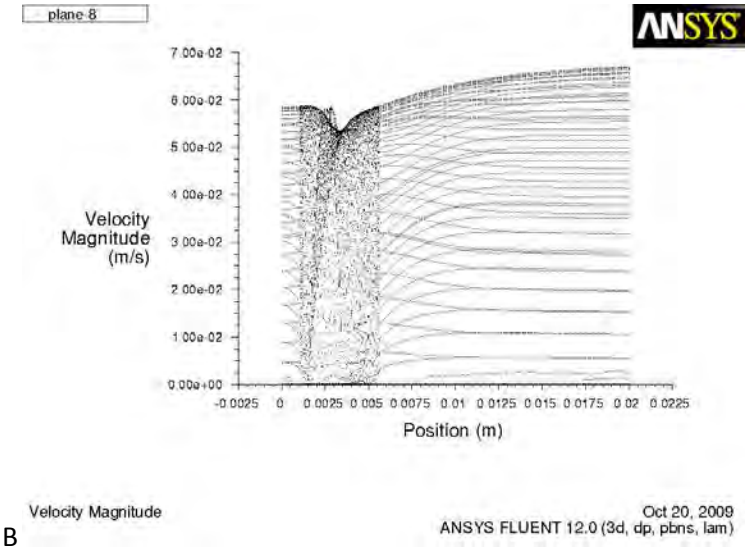

B

Figure C7: Flow plot (A) and velocity magnitude graph (B) for 1_90_0.4

A

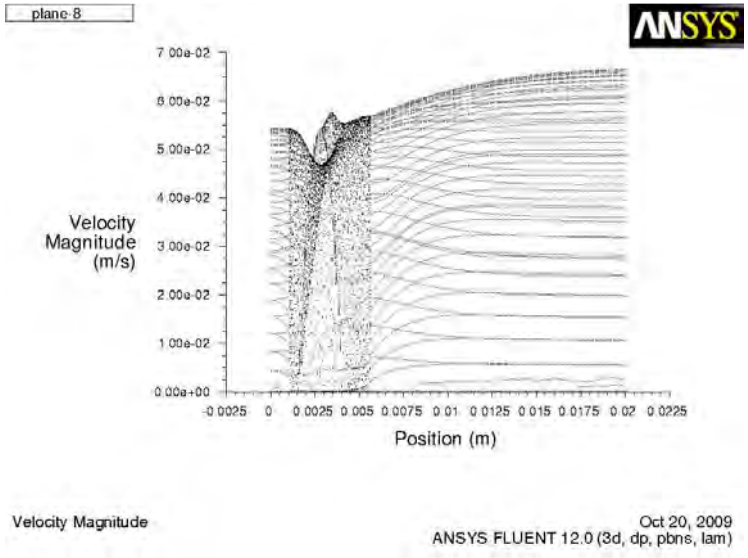

B

Figure C8: Flow plot (A) and velocity magnitude graph (B) for 1_90_0.5

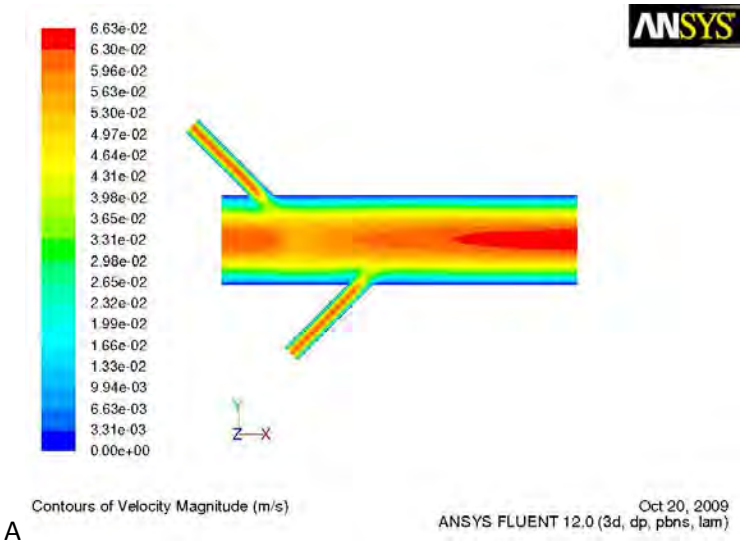

A

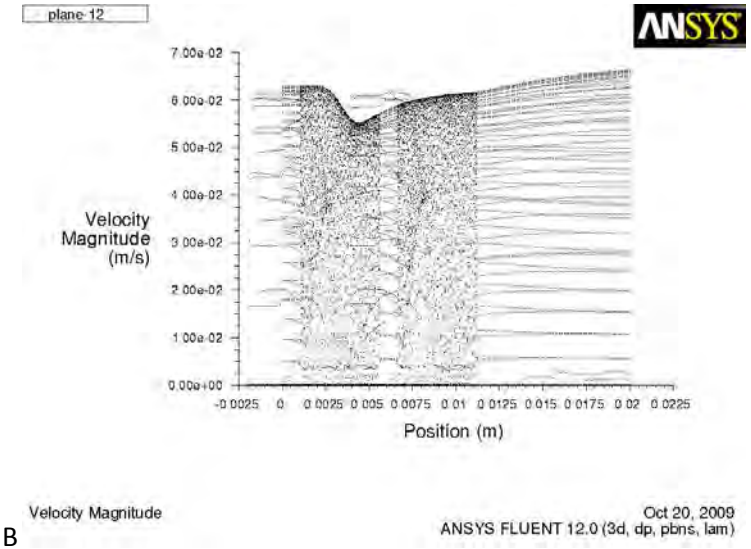

B

Figure C9: Flow plot (A) and velocity magnitude graph (B) for 2_45_0.2

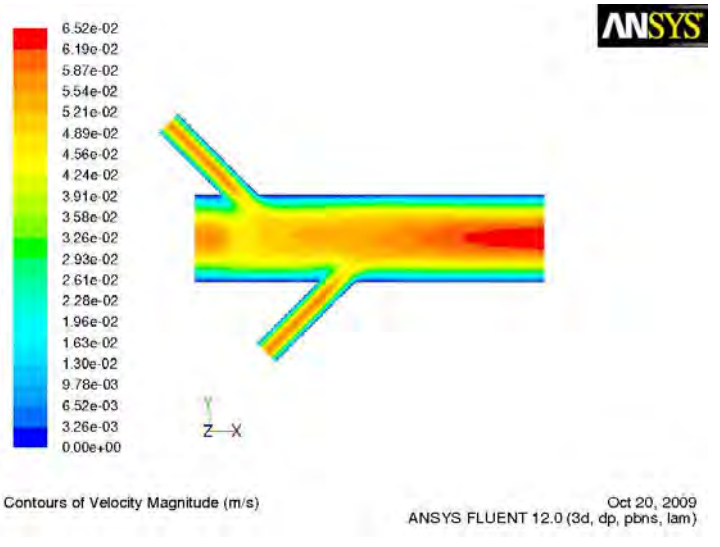

A

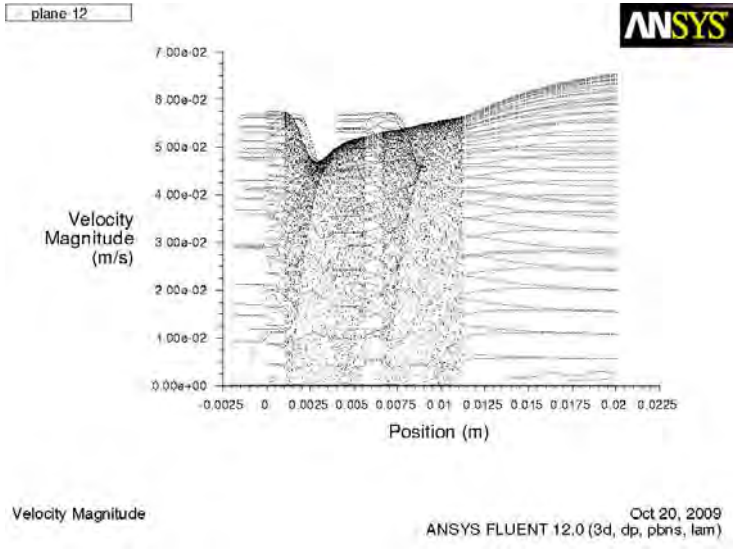

B

Figure C10: Flow plot (A) and velocity magnitude graph (B) for 2_45_0.3

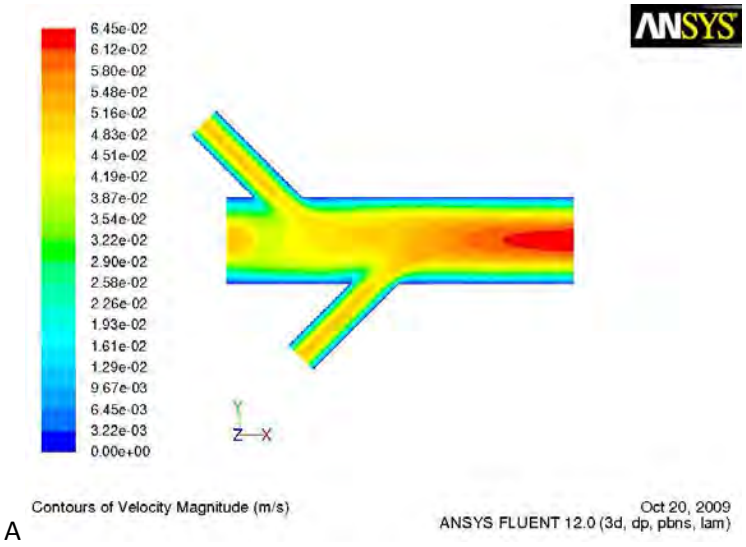

A

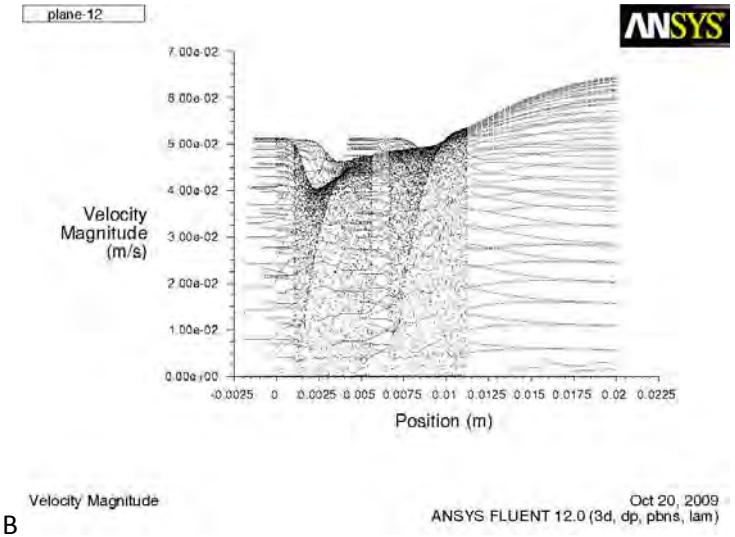

B

Figure C11: Flow plot (A) and velocity magnitude graph (B) for 2_45_0.4

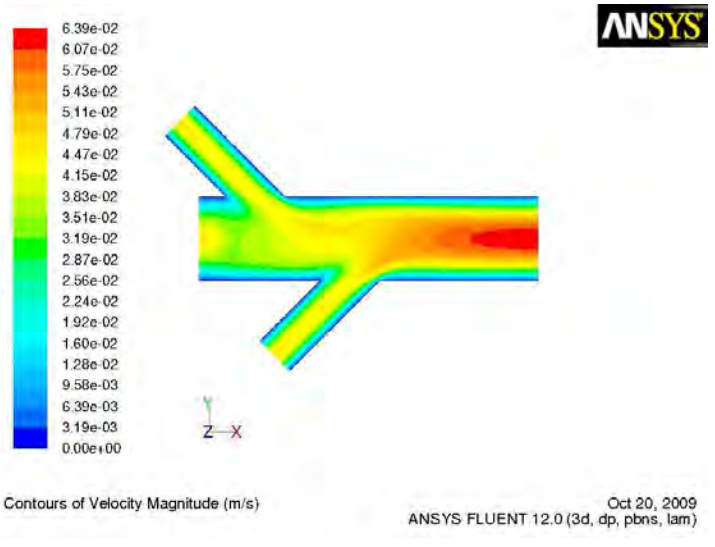

A

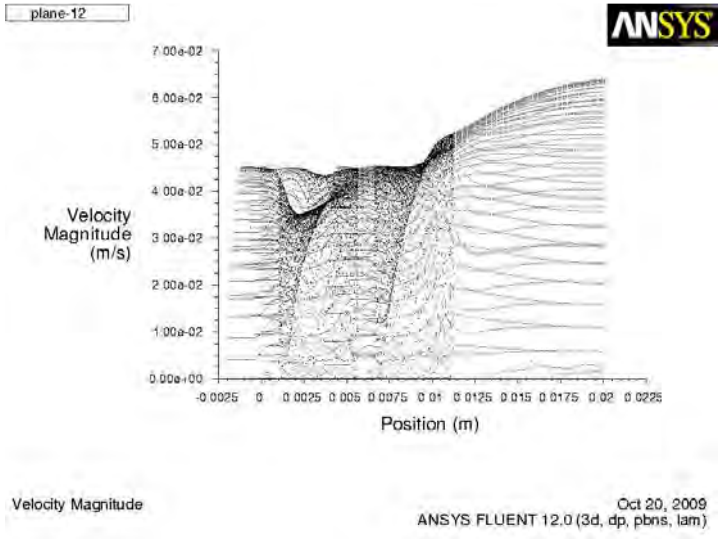

B

Figure C12: Flow plot (A) and velocity magnitude graph (B) for 2_45_0.5

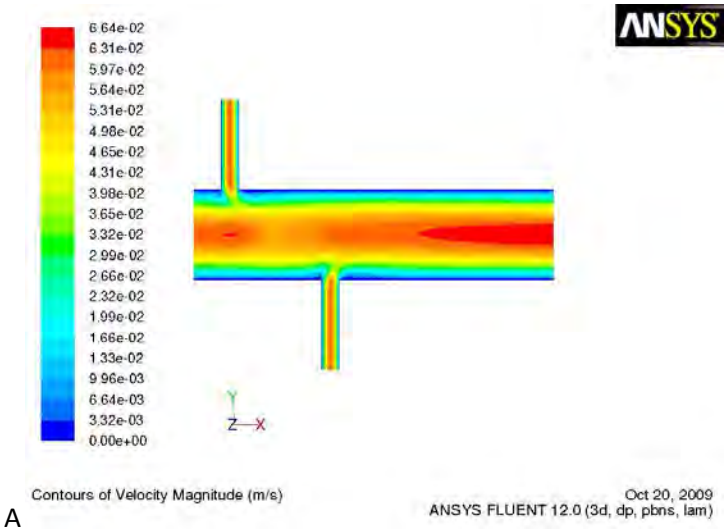

A

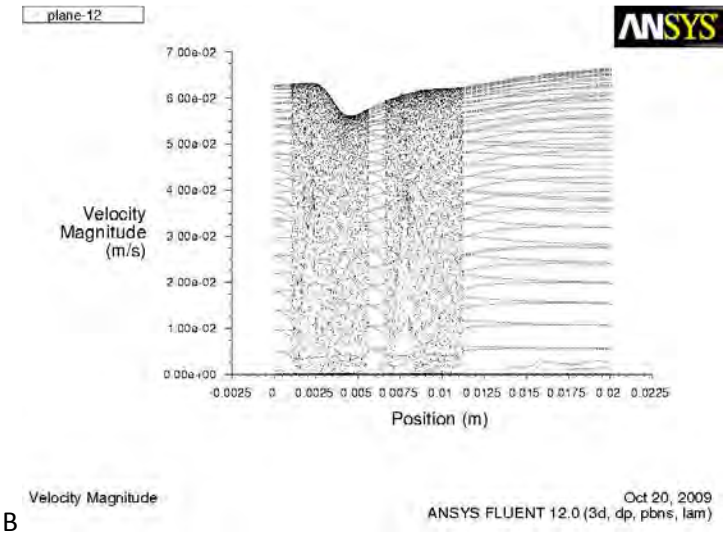

B

Figure C13: Flow plot (A) and velocity magnitude graph (B) for 2_90_0.2

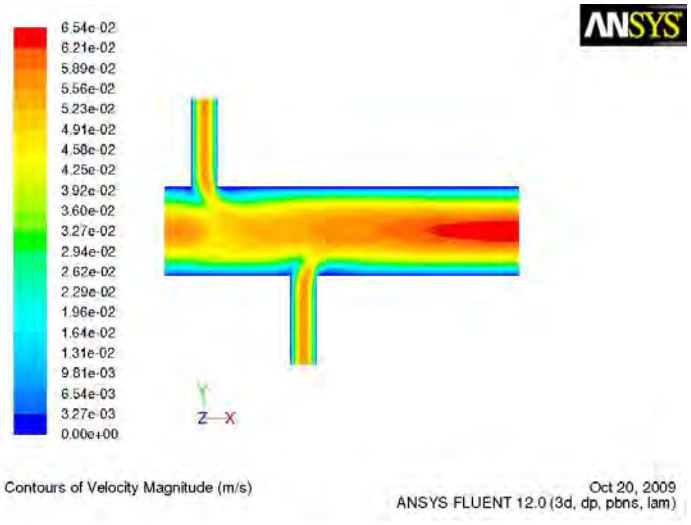

A

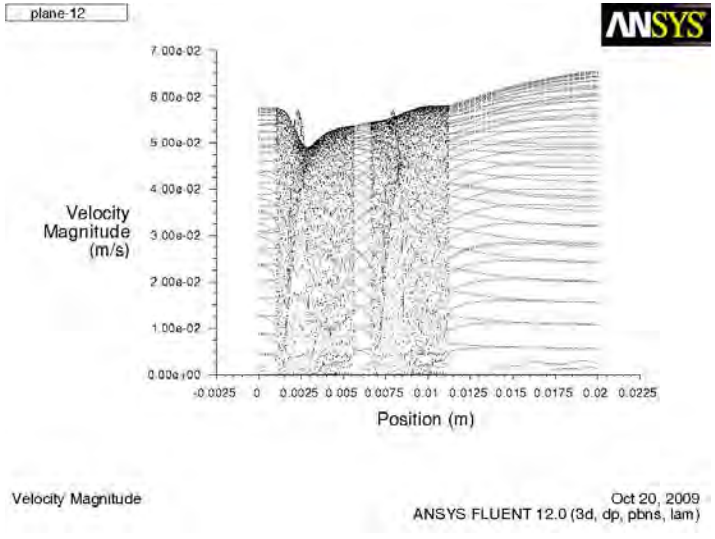

B

Figure C14: Flow plot (A) and velocity magnitude graph (B) for 2_90_0.3

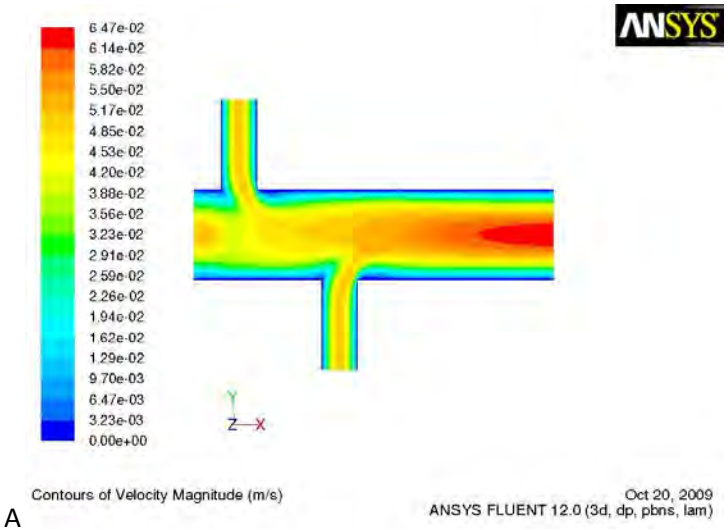

A

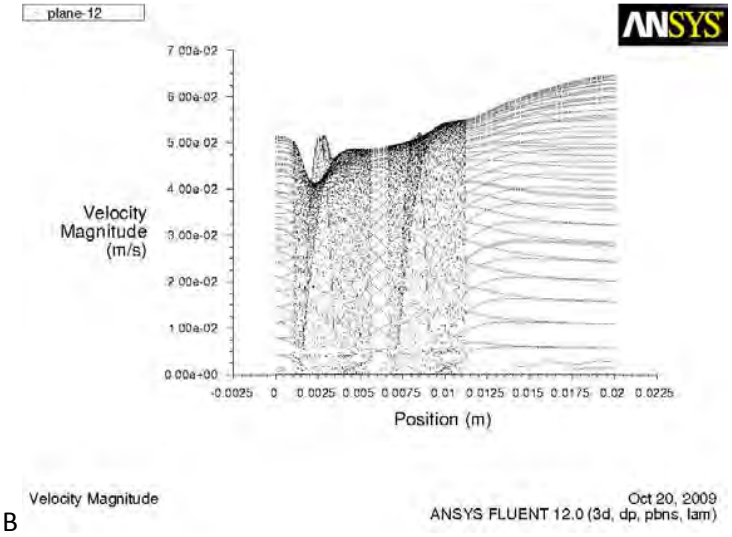

B

Figure C15: Flow plot (A) and velocity magnitude graph (B) for 2_90_0.4

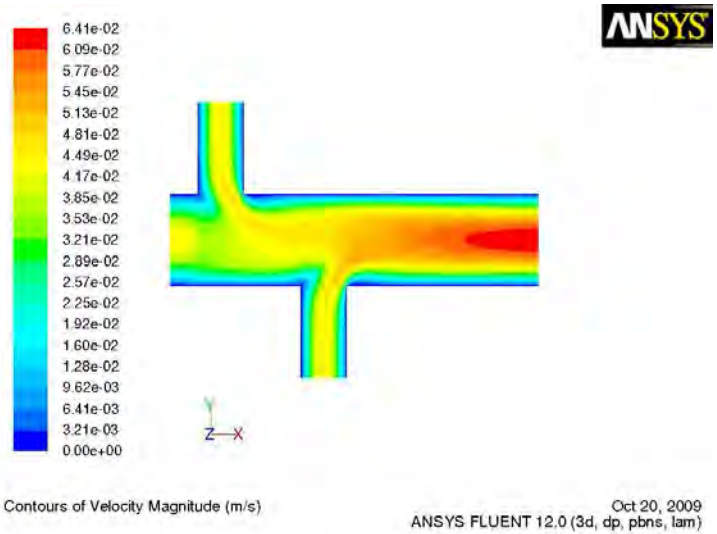

A

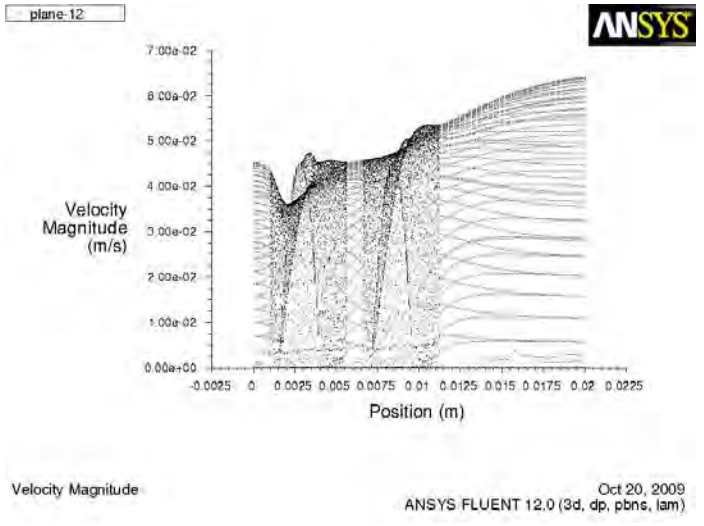

B

Figure C16: Flow plot (A) and velocity magnitude graph (B) for 2_90_0.5

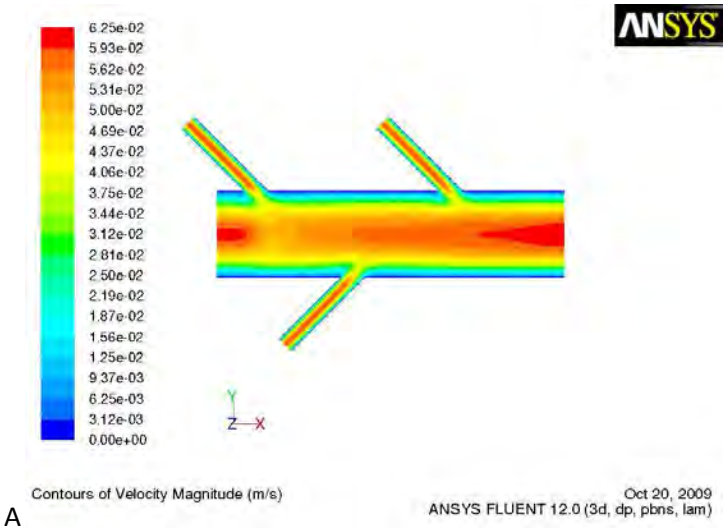

A

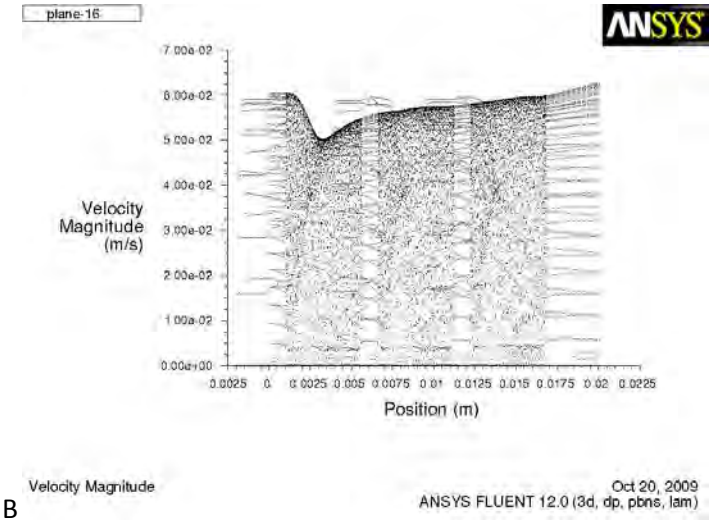

B

Figure C17: Flow plot (A) and velocity magnitude graph (B) for 3_45_0.2

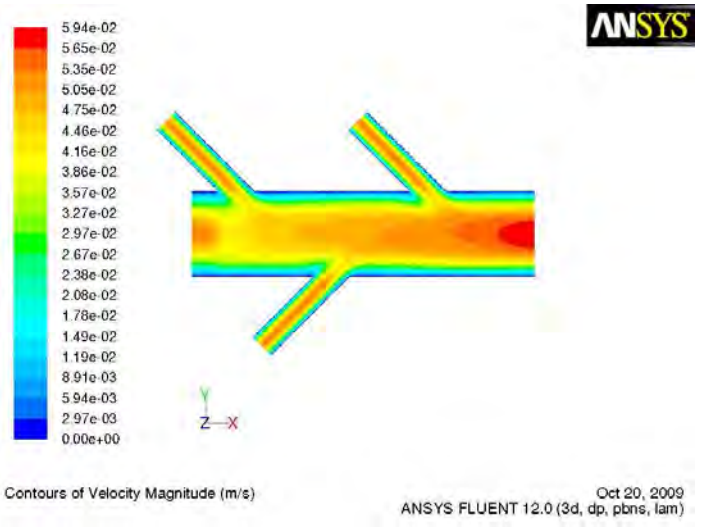

A

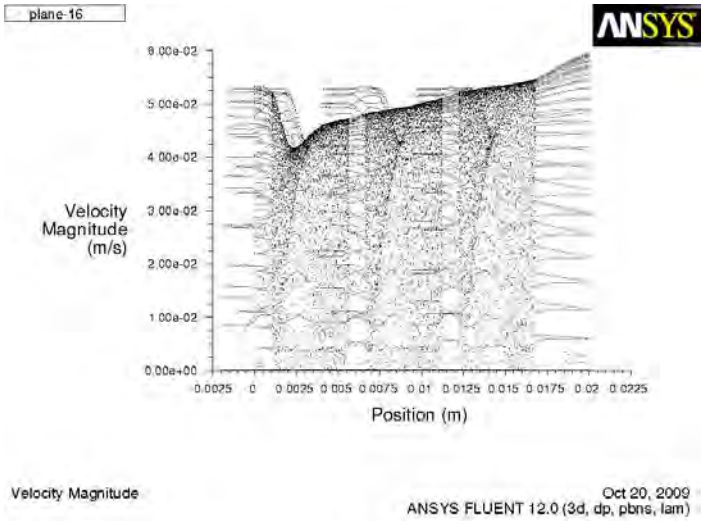

Figure C18: Flow plot (A) and velocity magnitude graph (B) for 3_45_0.3

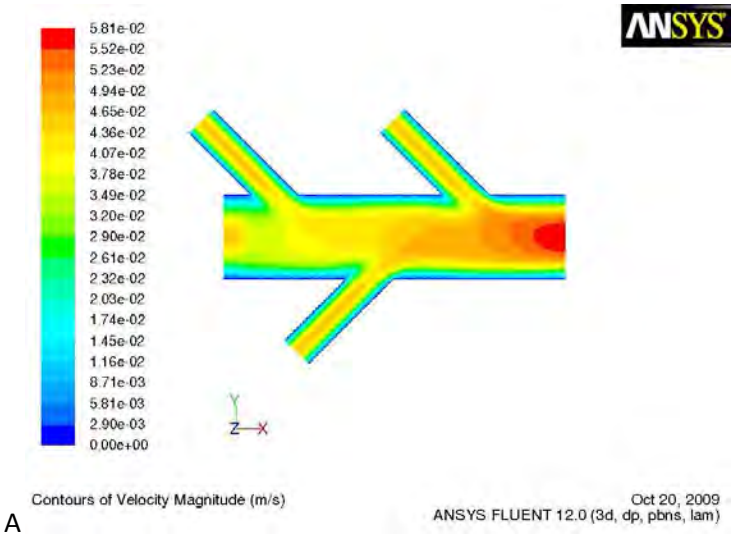

A

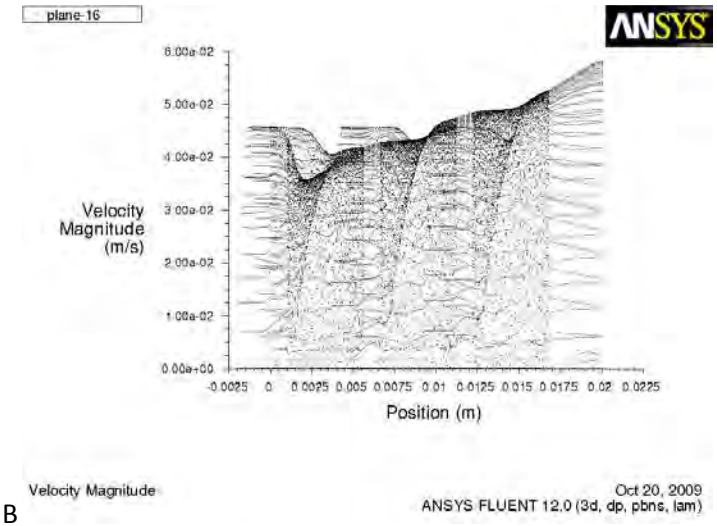

B

Figure C19: Flow plot (A) and velocity magnitude graph (B) for 3_45_0.4

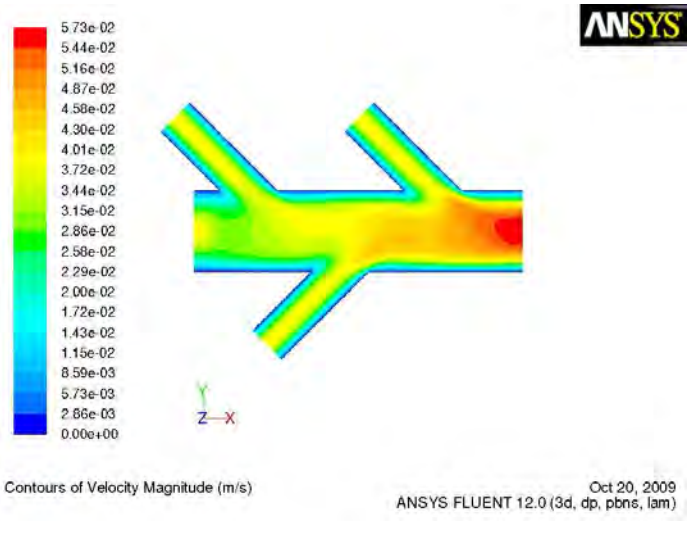

A

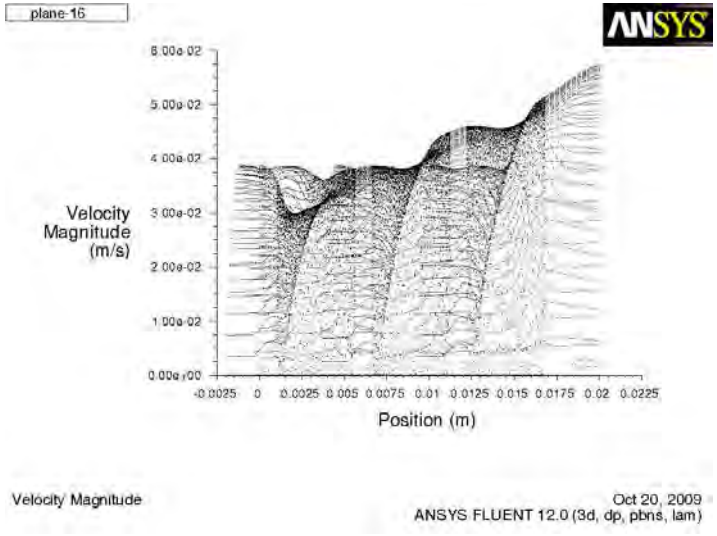

B

Figure C20: Flow plot (A) and velocity magnitude graph (B) for 3_45_0.5

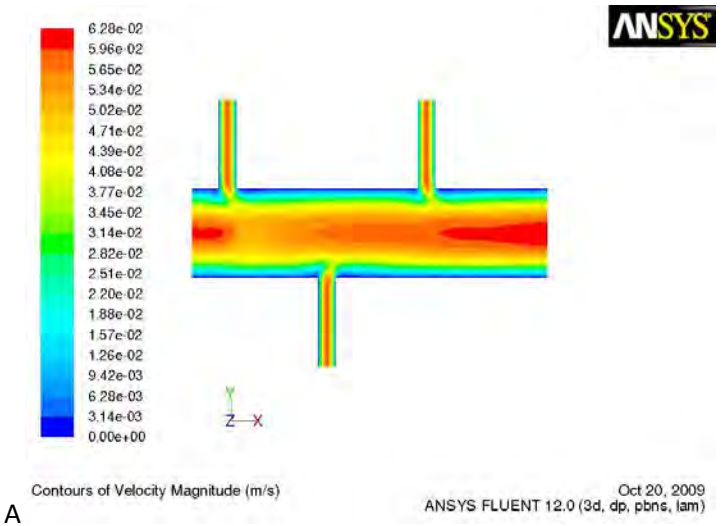

A

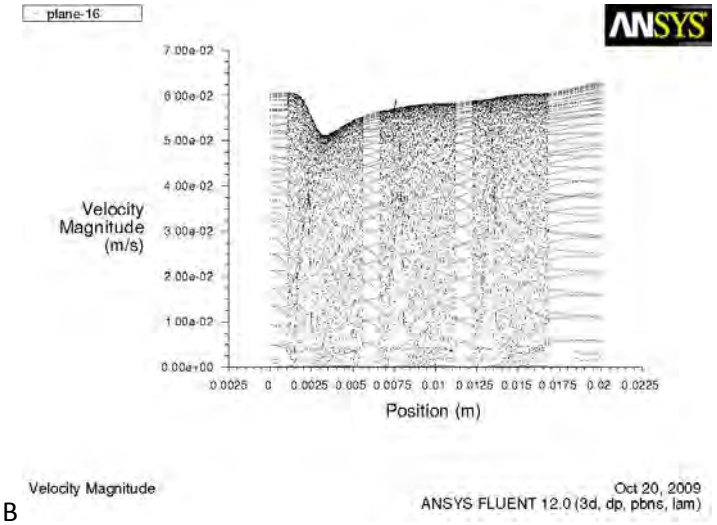

B

Figure C21: Flow plot (A) and velocity magnitude graph (B) for 3_90_0.2

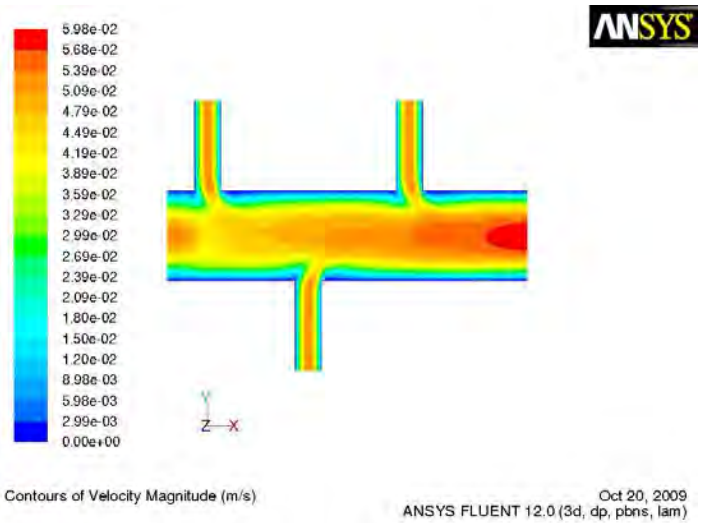

A

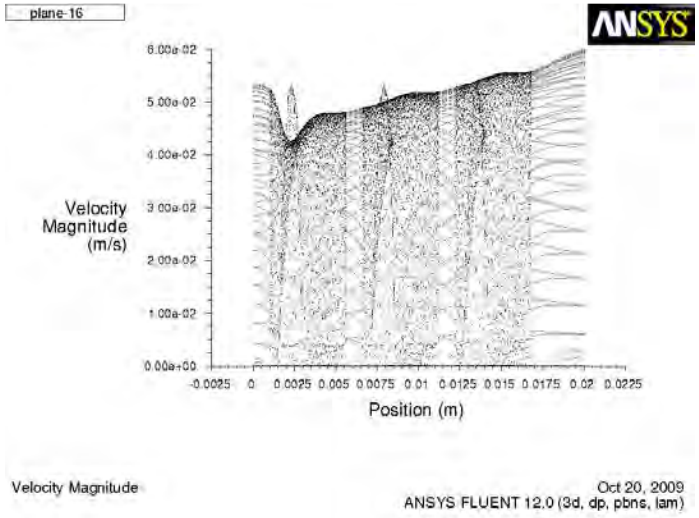

B

Figure C22: Flow plot (A) and velocity magnitude graph (B) for 3_90_0.3

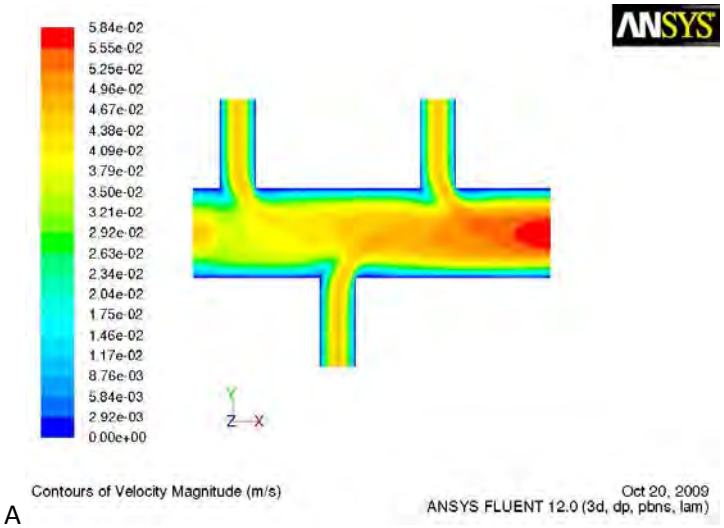

A

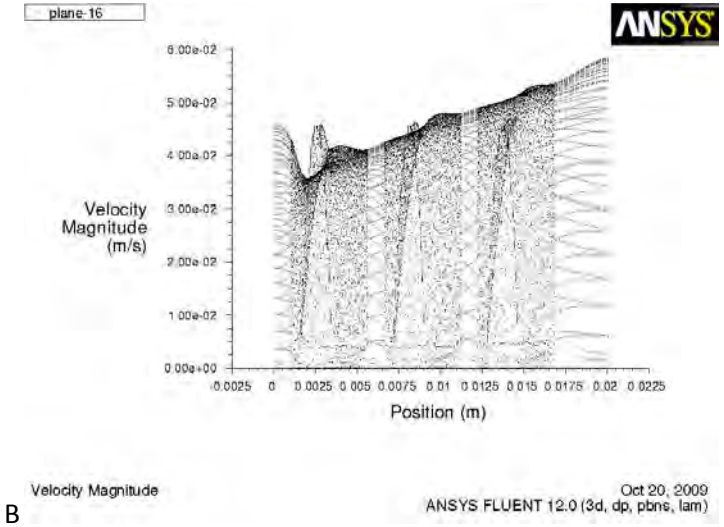

B

Figure C23: Flow plot (A) and velocity magnitude graph (B) for 3_90_0.4

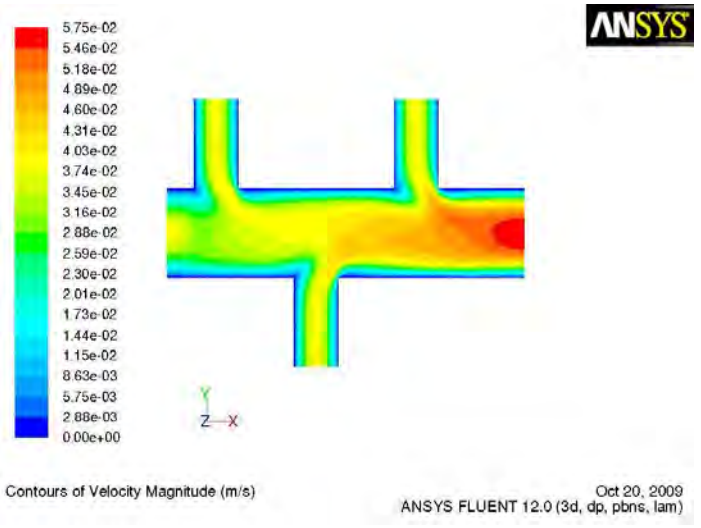

A

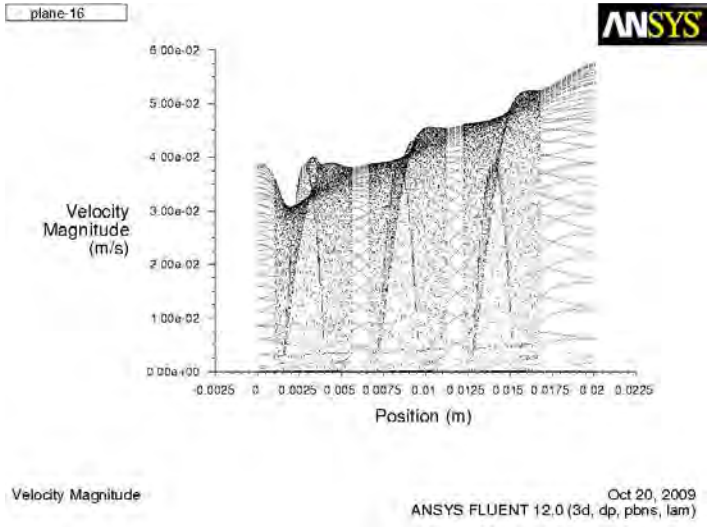

B

Figure C24: Flow plot (A) and velocity magnitude graph (B) for 3_90_0.5

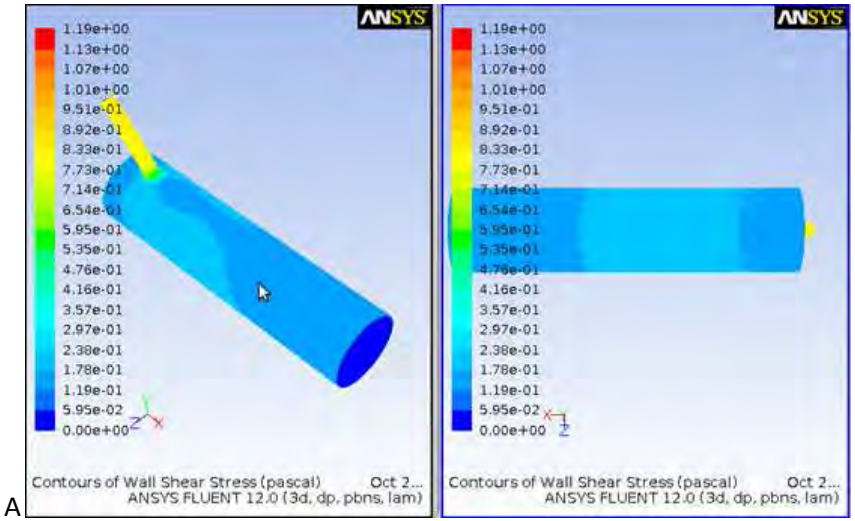

A

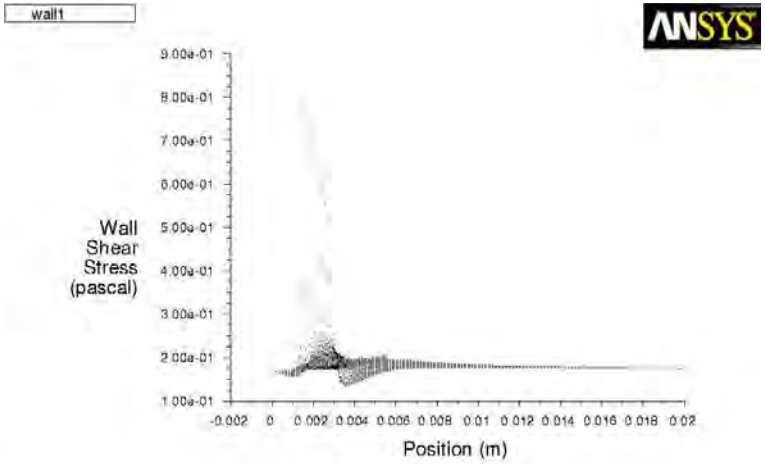

B

Figure C25: Shear plot (A) and wall shear stress graph (B) for 1_45_0.2

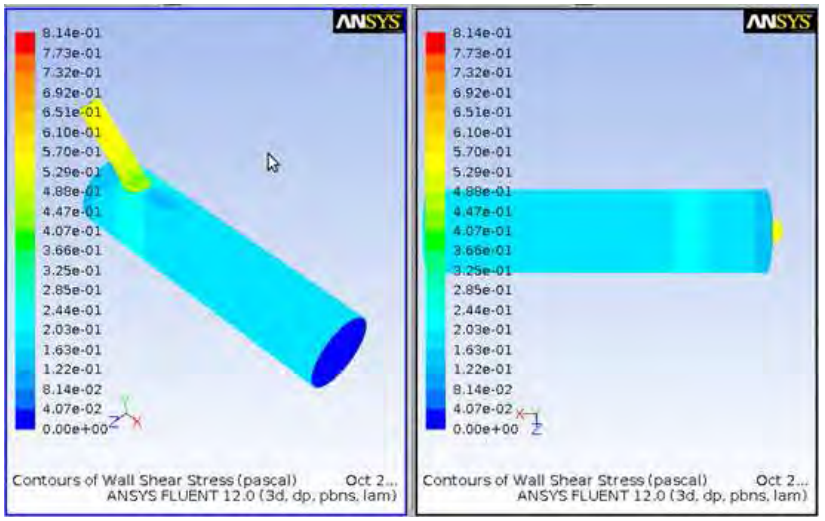

A

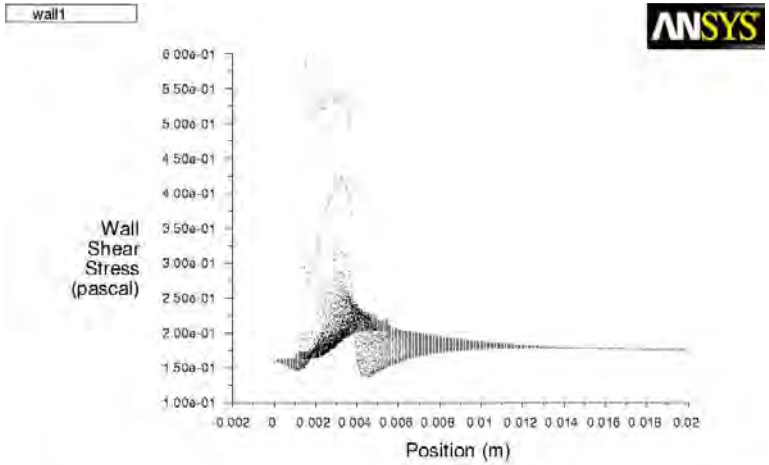

B

Figure C26: Shear plot (A) and wall shear stress graph (B) for 1_45_0.3

A

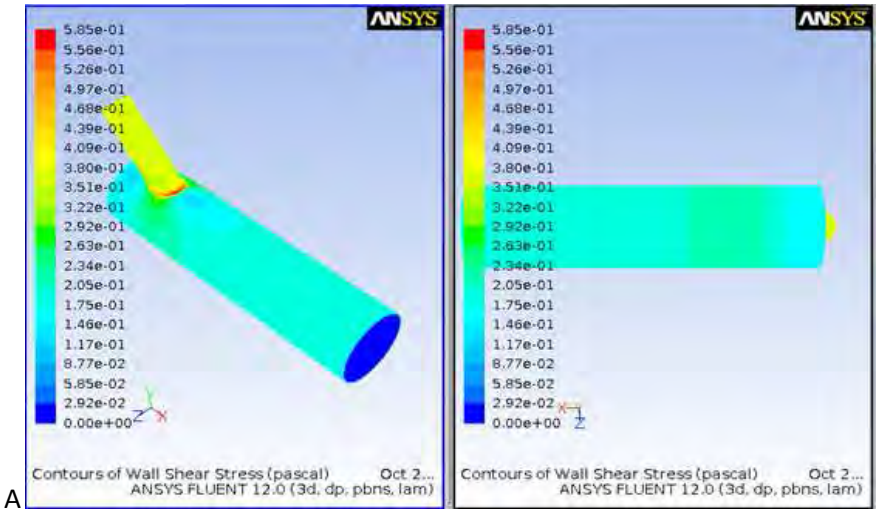

B

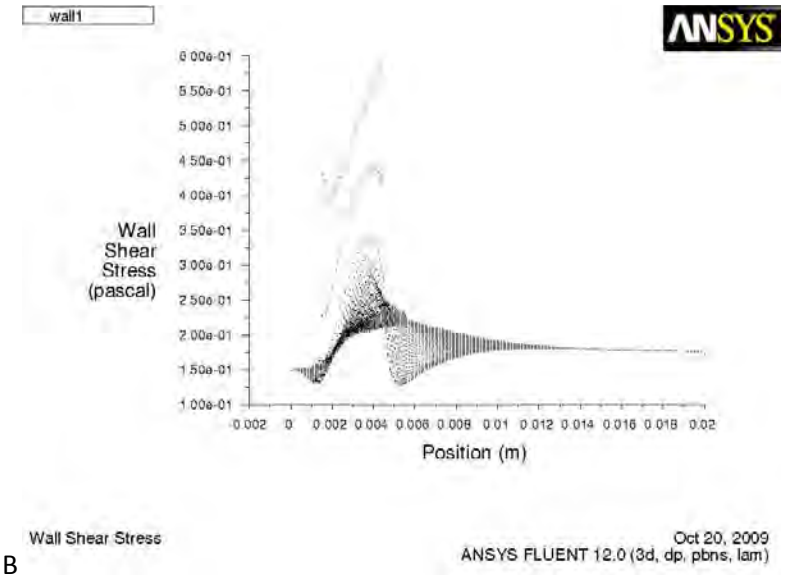

Figure C27: Shear plot (A) and wall shear stress graph (B) for 1_45_0.4

A

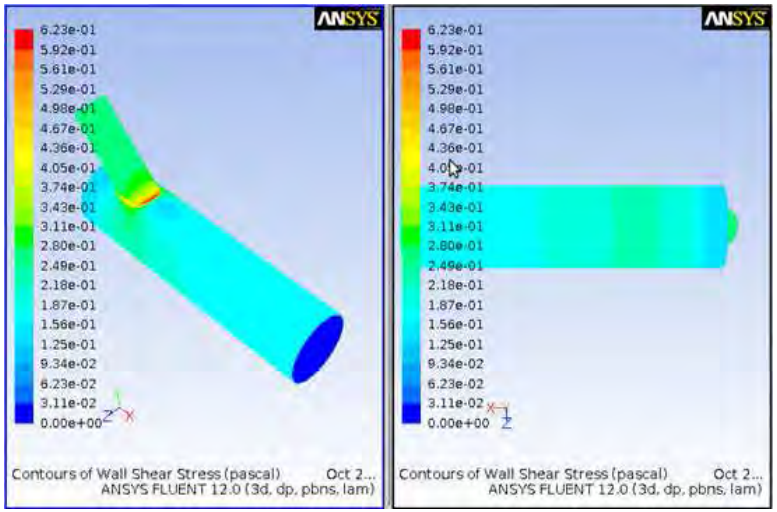

B

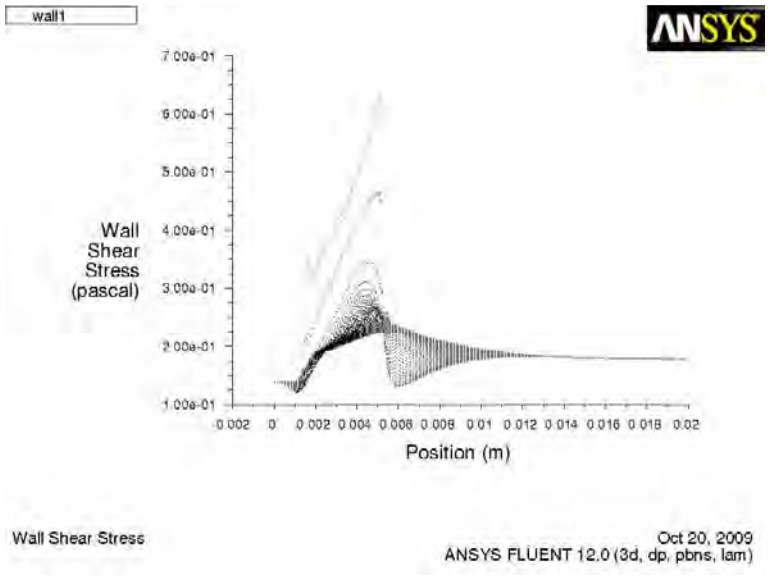

Figure C28: Shear plot (A) and wall shear stress graph (B) for 1_45_0.5

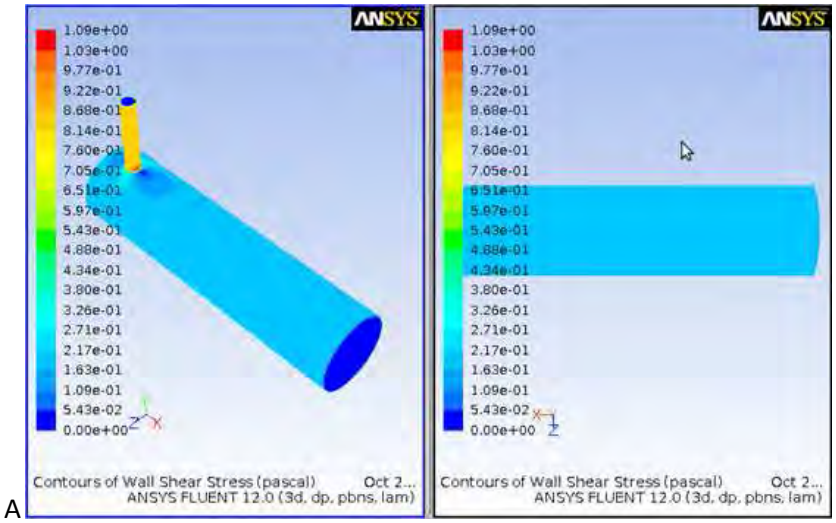

A

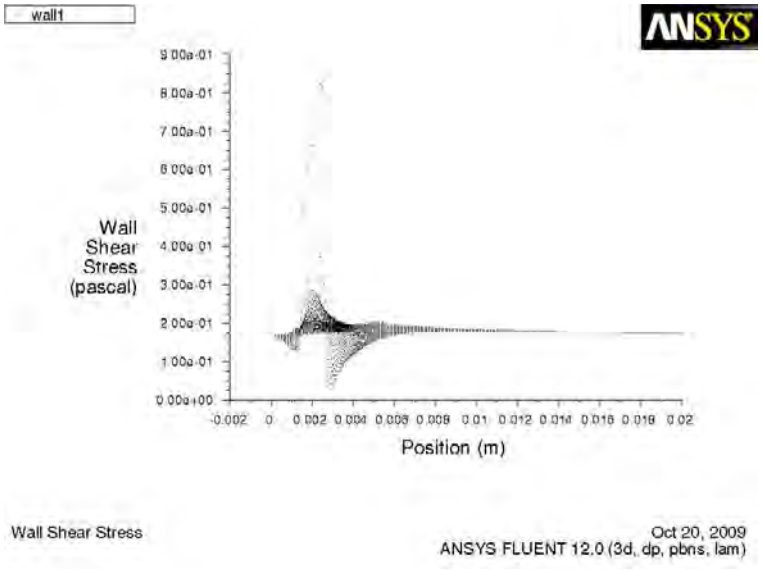

B

Figure C29: Shear plot (A) and wall shear stress graph (B) for 1_90_0.2

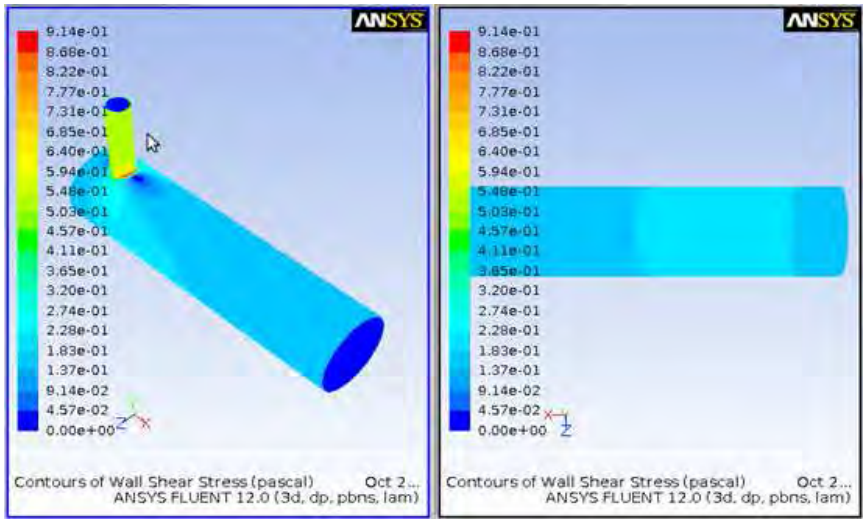

A

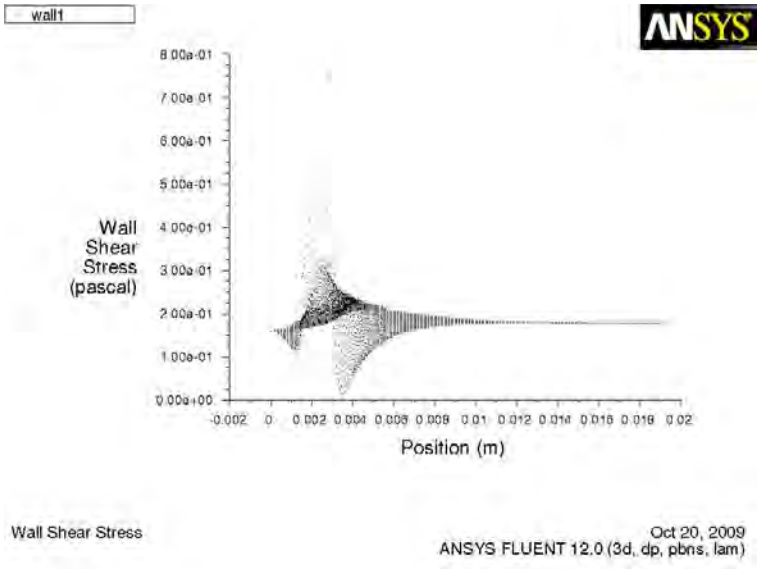

B

Figure C30: Shear plot (A) and wall shear stress graph (B) for 1_90_0.3

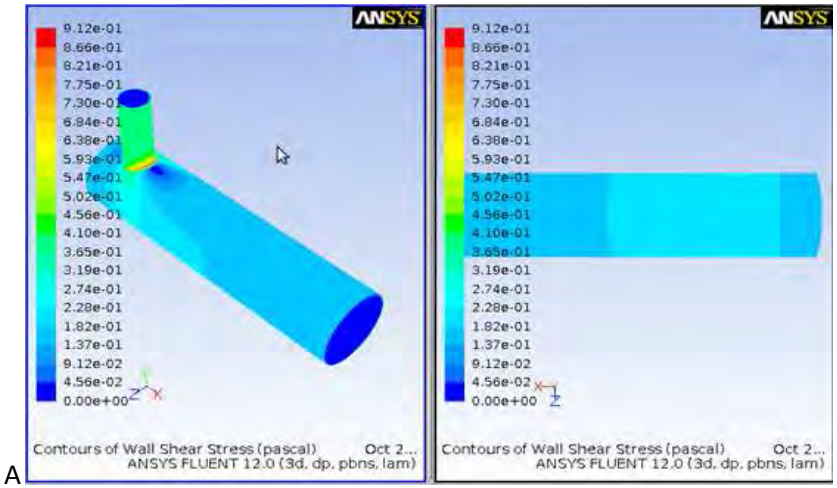

A

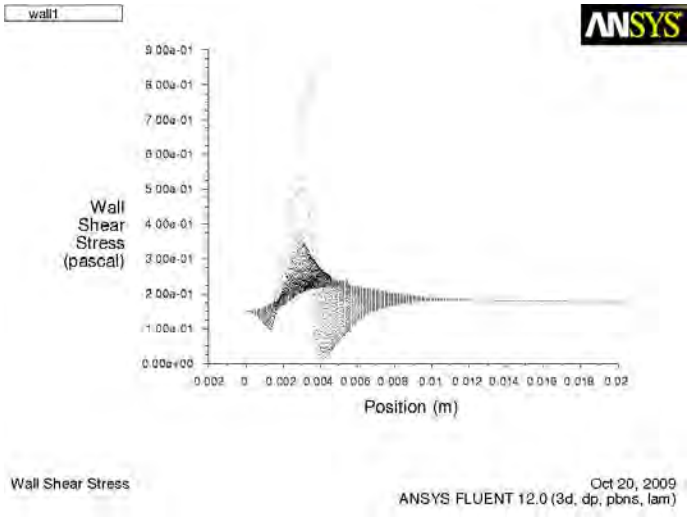

B

Figure C31: Shear plot (A) and wall shear stress graph (B) for 1_90_0.4

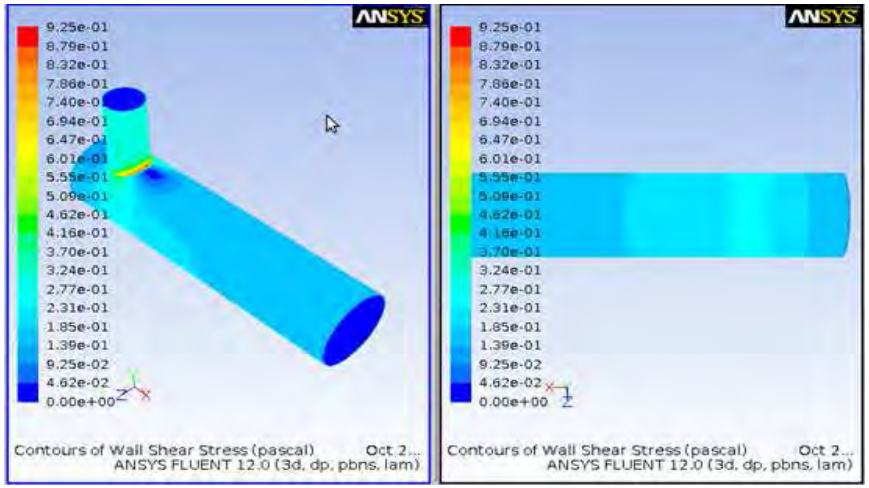

A

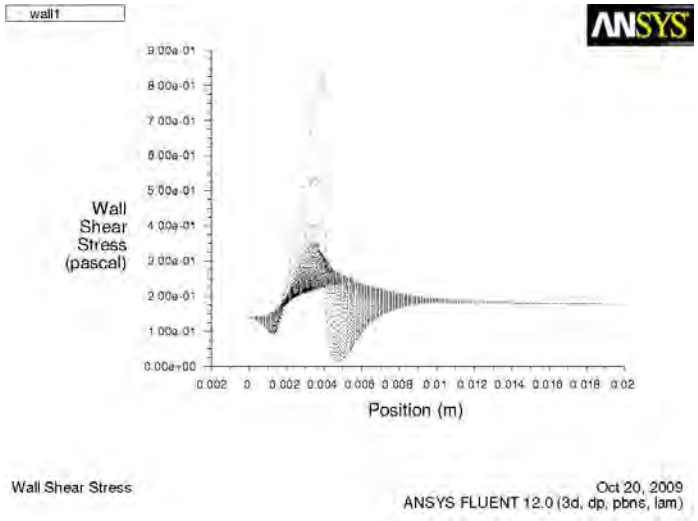

B

Figure C32: Shear plot (A) and wall shear stress graph (B) for 1_90_0.5

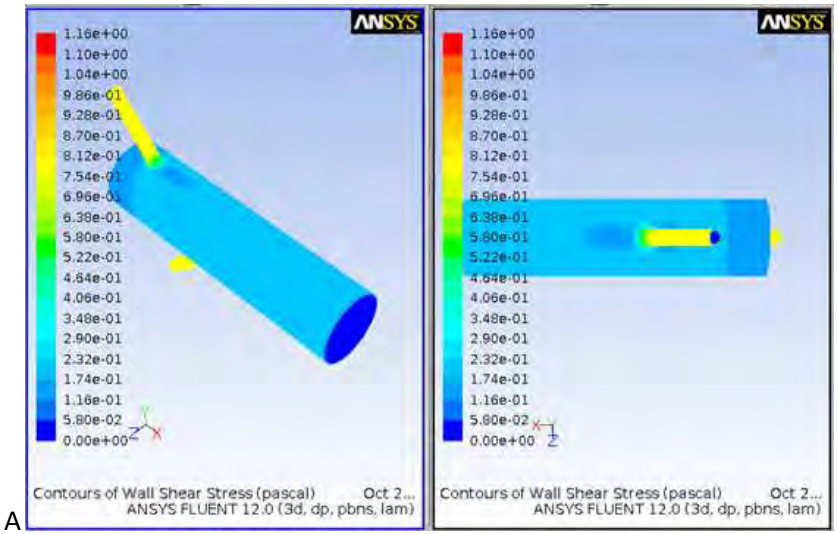

A

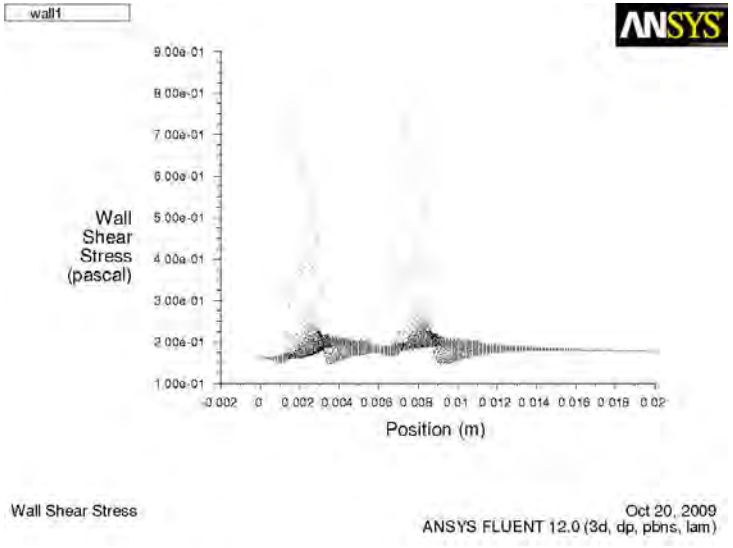

B

Figure C33: Shear plot (A) and wall shear stress graph (B) for 2_45_0.2

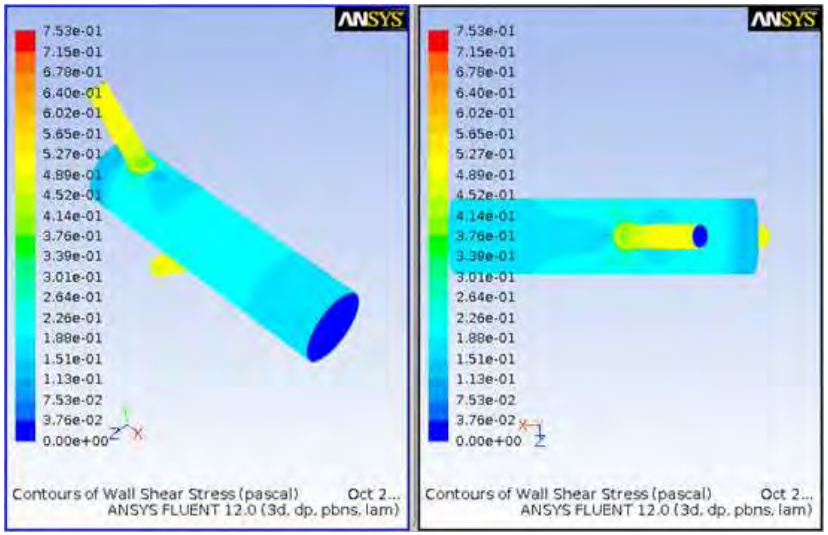

A

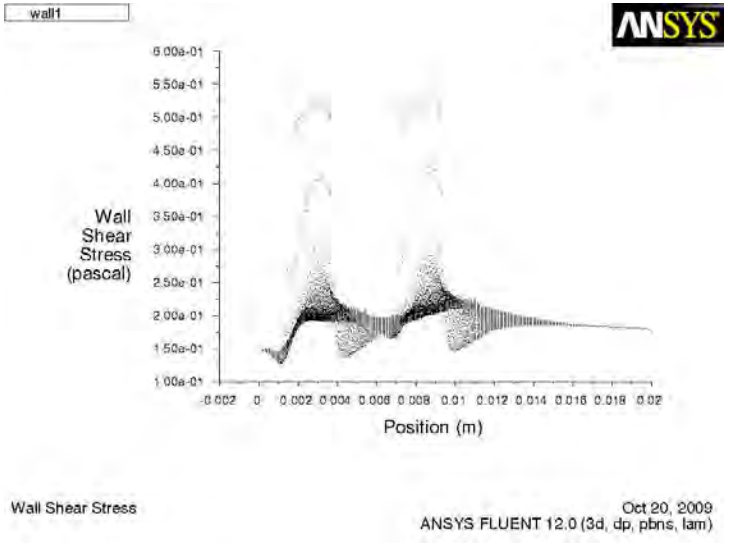

B

Figure C34: Shear plot (A) and wall shear stress graph (B) for 2_45_0.3

A

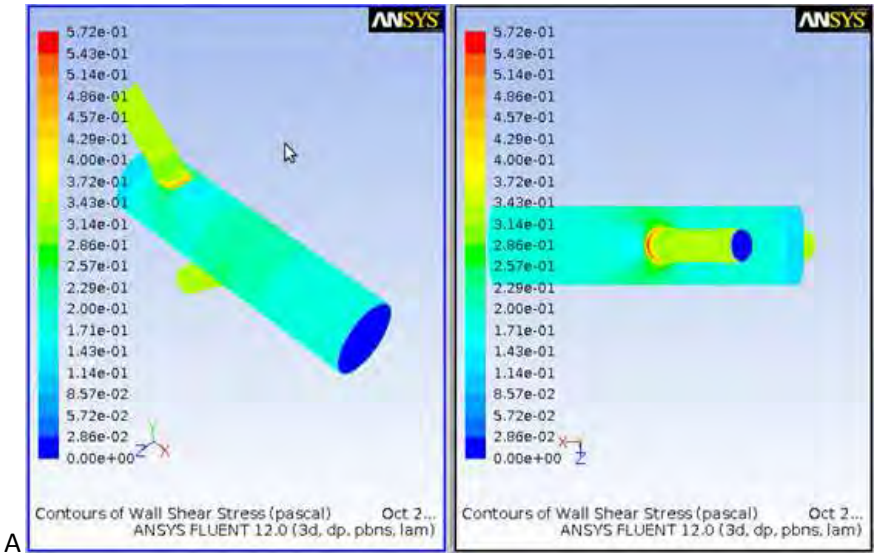

B

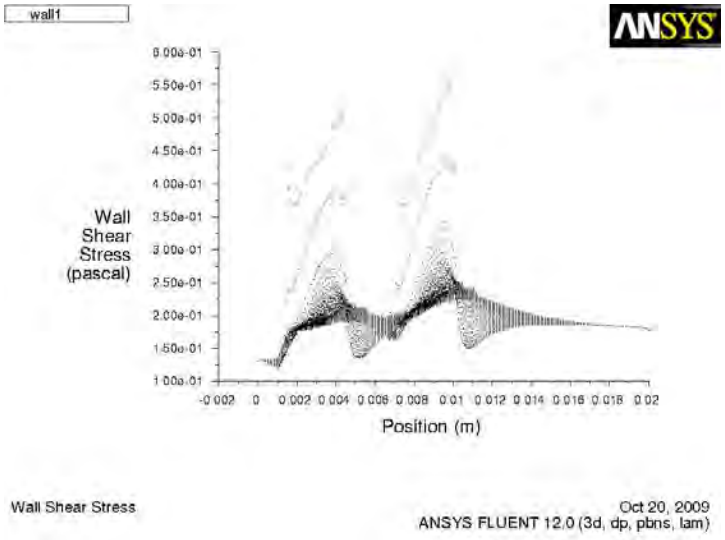

Figure C35: Shear plot (A) and wall shear stress graph (B) for 2_45_0.4

A

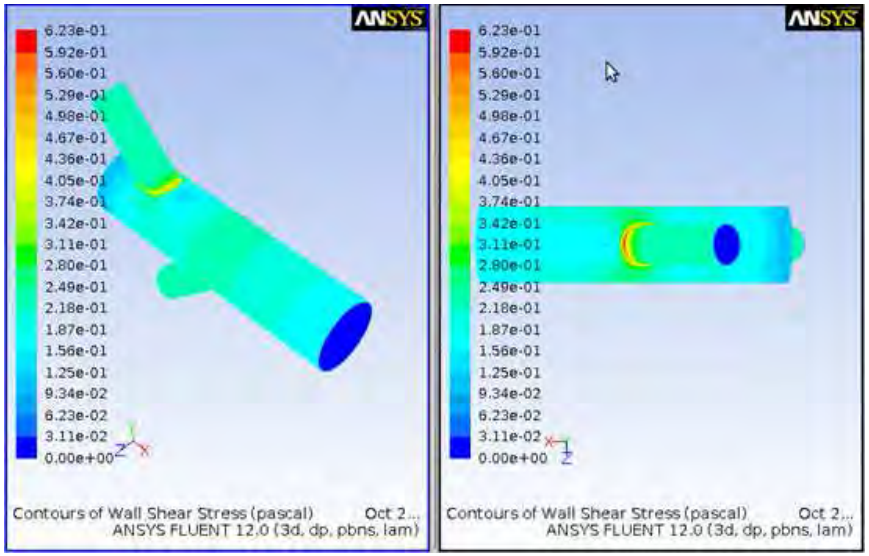

B

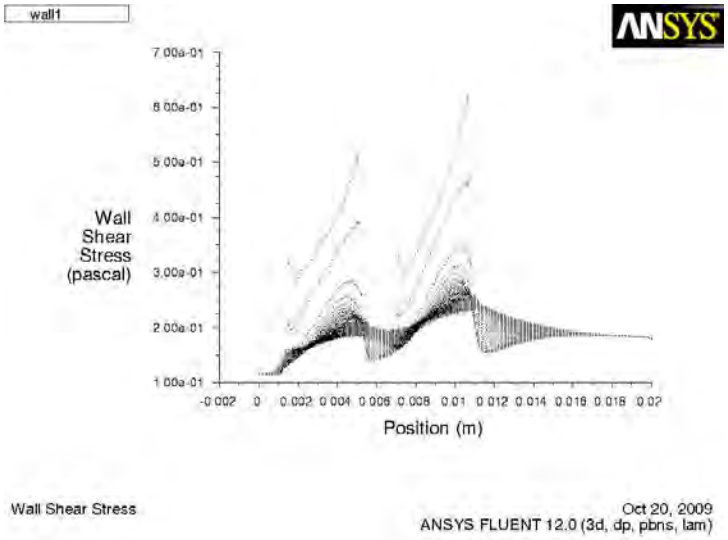

Figure C36: Shear plot (A) and wall shear stress graph (B) for 2_45_0.5

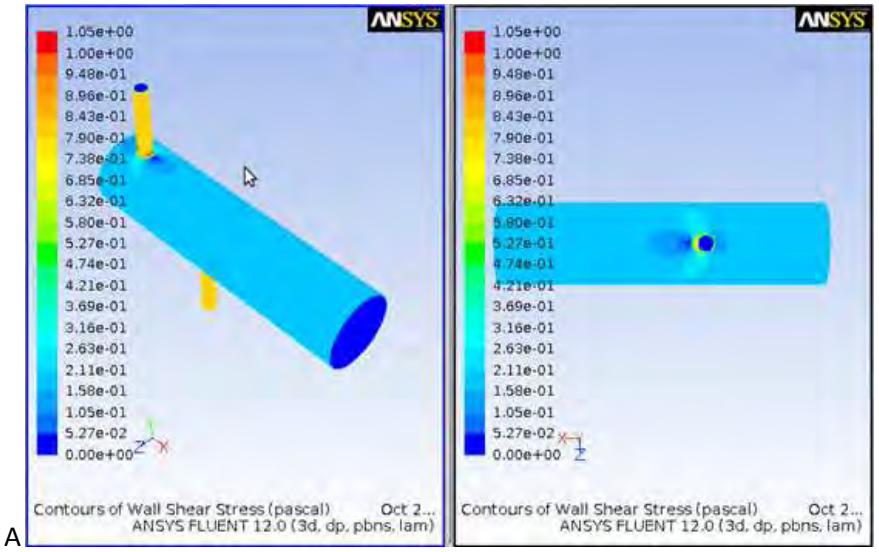

A

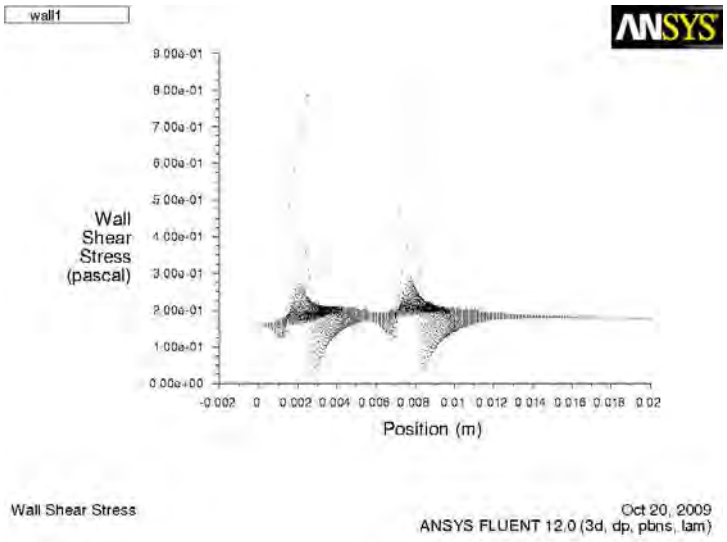

B

Figure C37: Shear plot (A) and wall shear stress graph (B) for 2_90_0.2

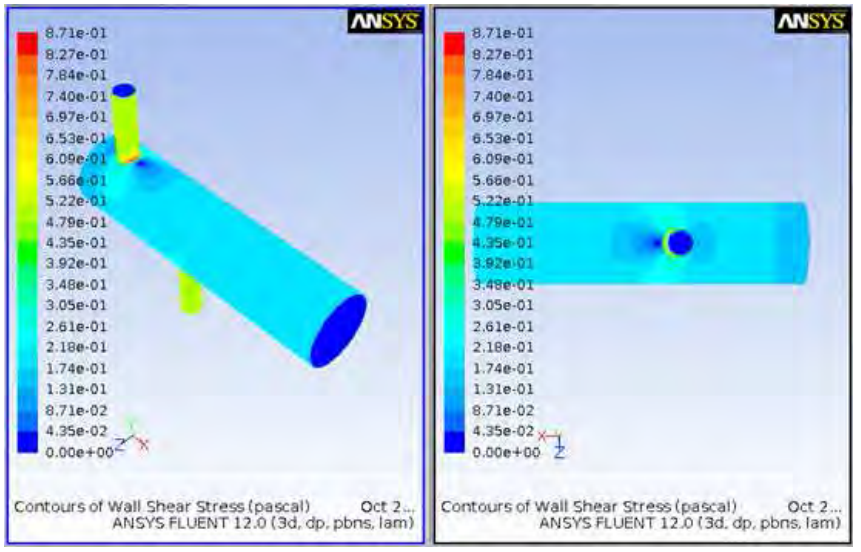

A

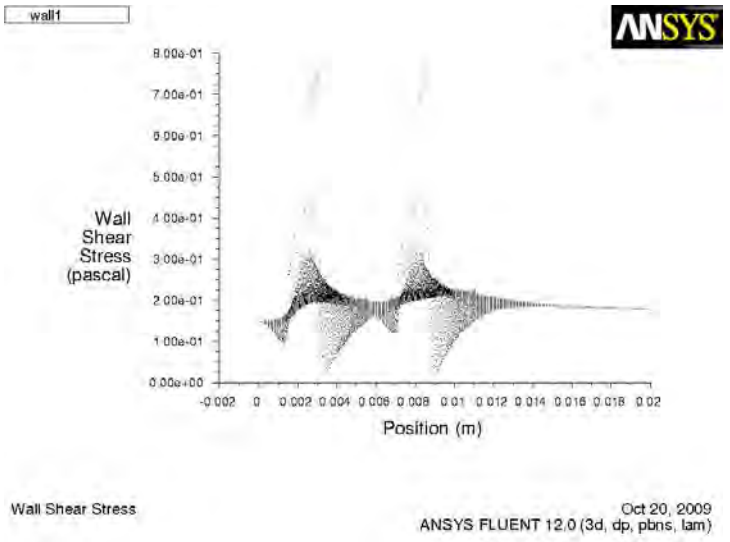

B

Figure C38: Shear plot (A) and wall shear stress graph (B) for 2_90_0.3

A

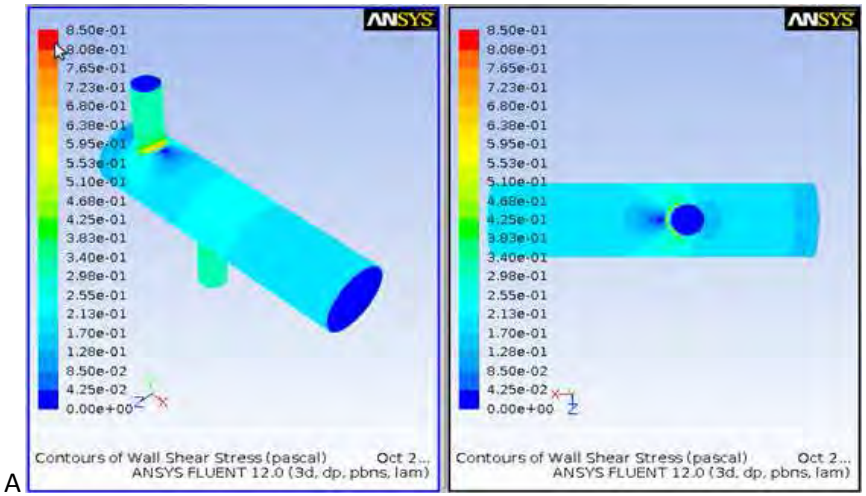

B

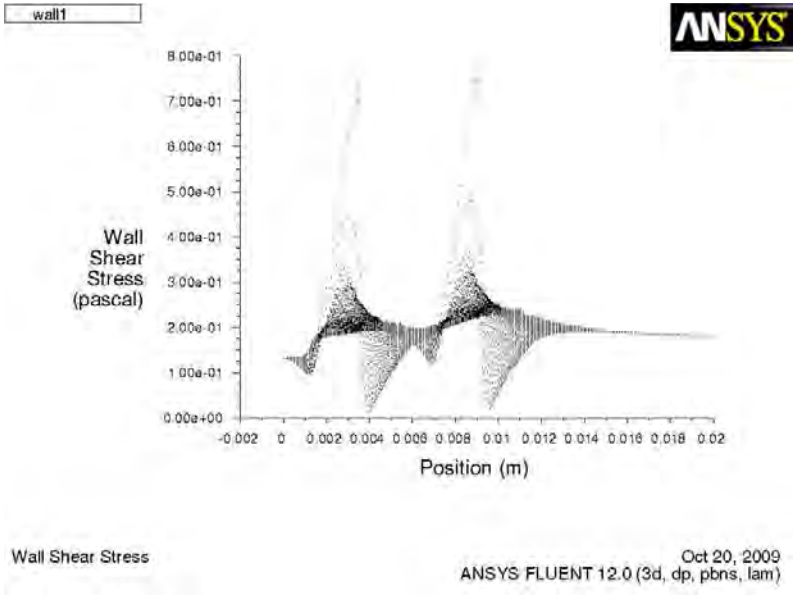

Figure C39: Shear plot (A) and wall shear stress graph (B) for 2_90_0.4

A

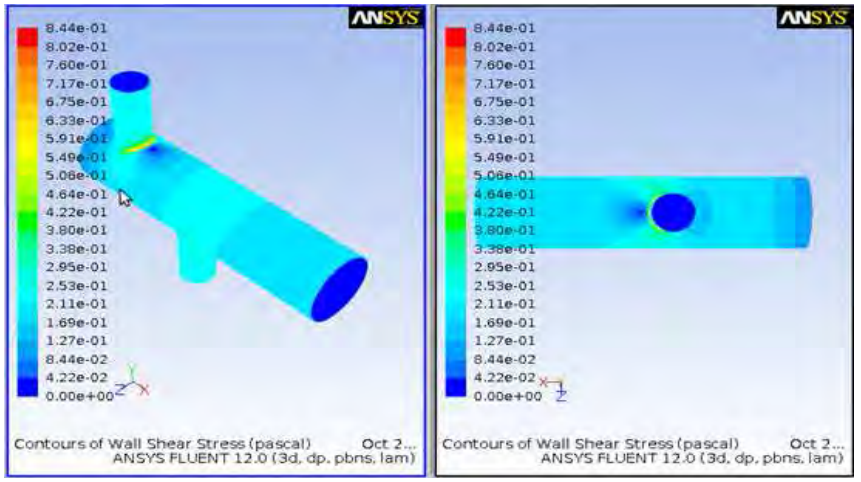

B

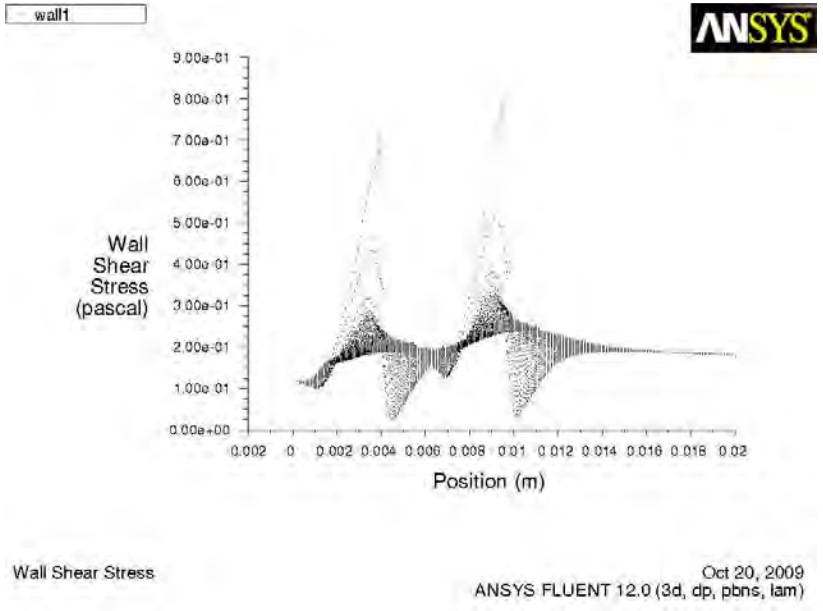

Figure C40: Shear plot (A) and wall shear stress graph (B) for 2_90_0.5

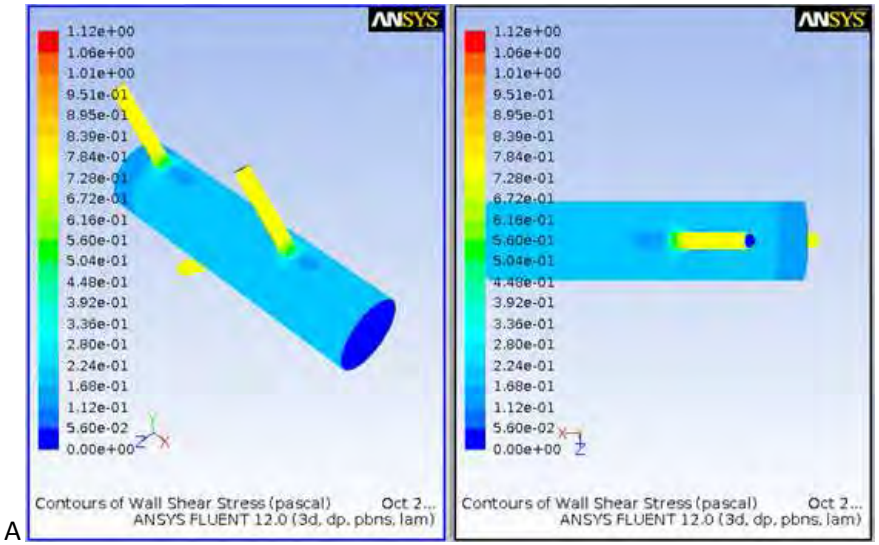

A

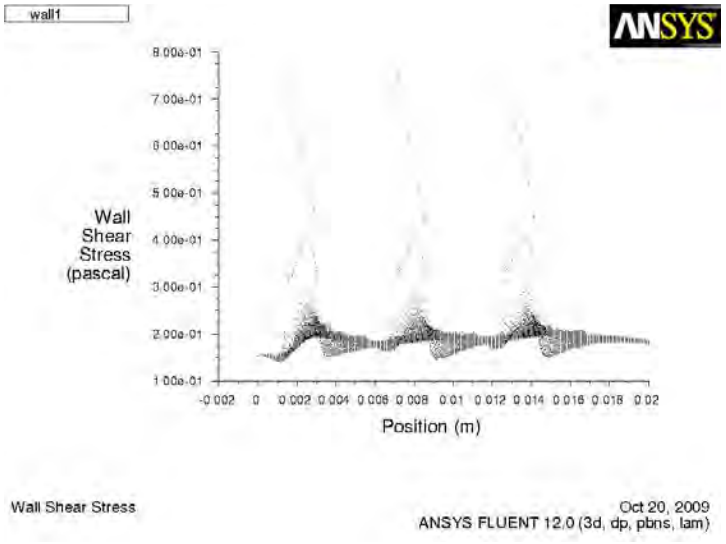

B

Figure C41: Shear plot (A) and wall shear stress graph (B) for 3_45_0.2

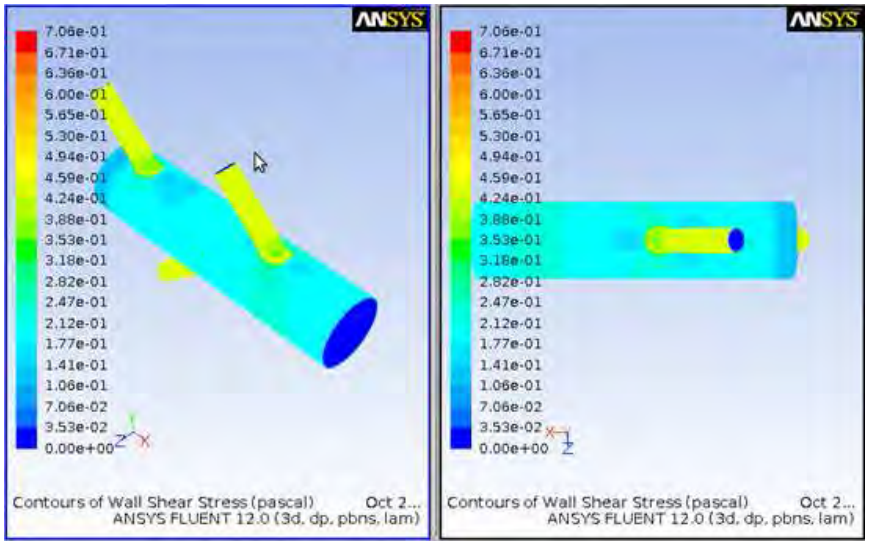

A

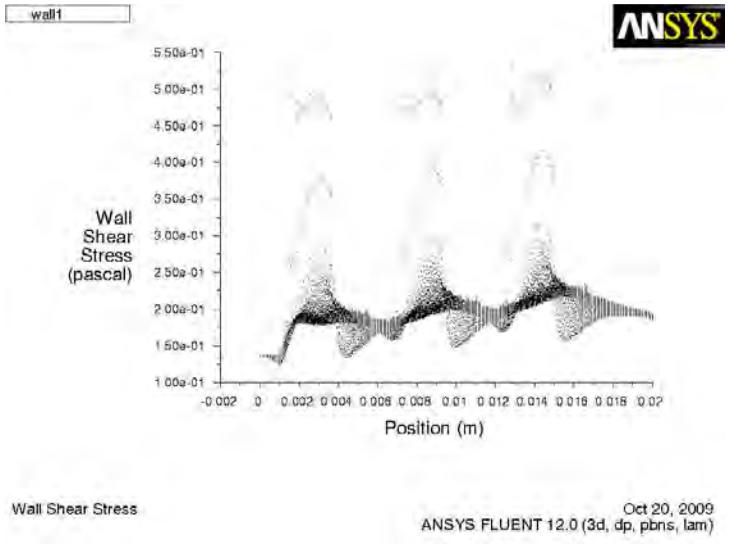

B

Figure C42: Shear plot (A) and wall shear stress graph (B) for 3_45_0.3

A

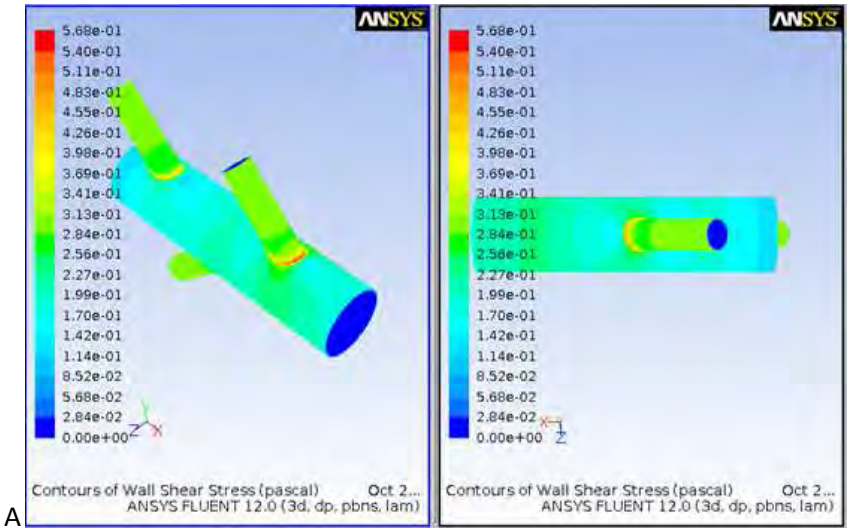

B

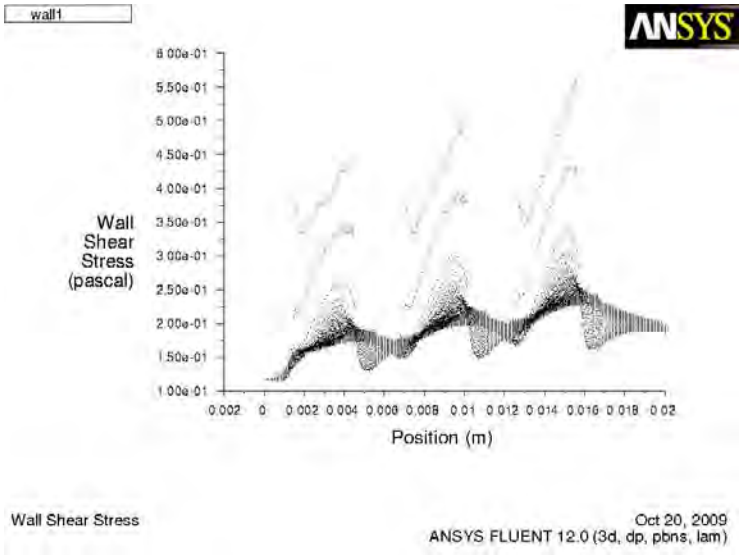

Figure C43: Shear plot (A) and wall shear stress graph (B) for 3_45_0.4

A

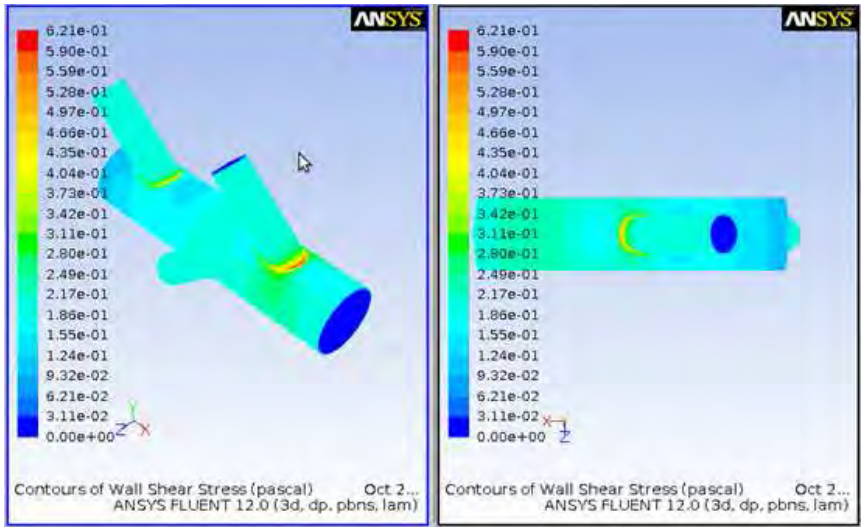

B

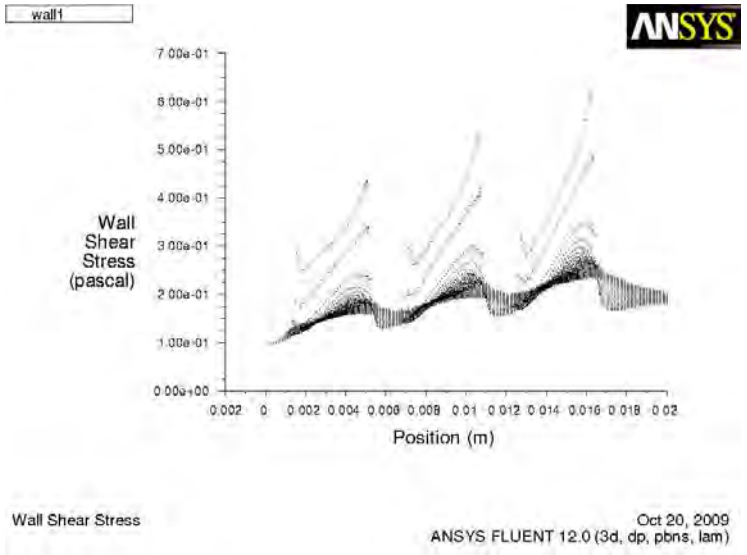

Figure C44: Shear plot (A) and wall shear stress graph (B) for 3_45_0.5

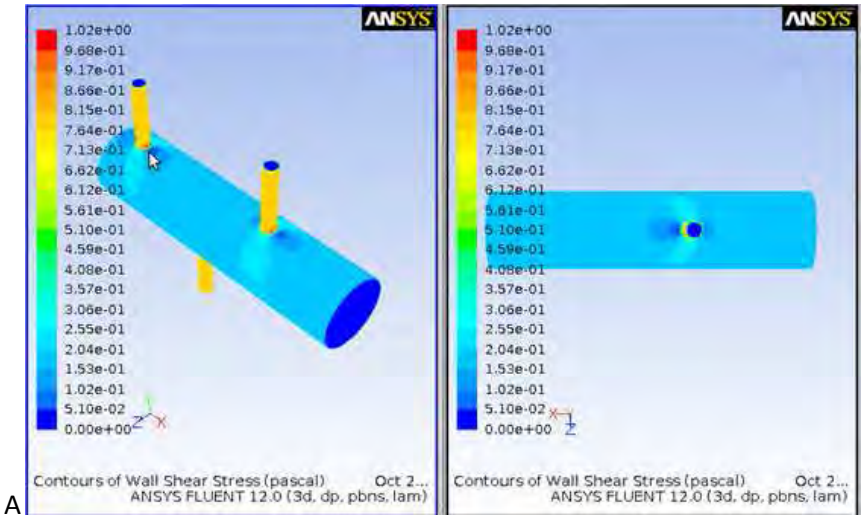

A

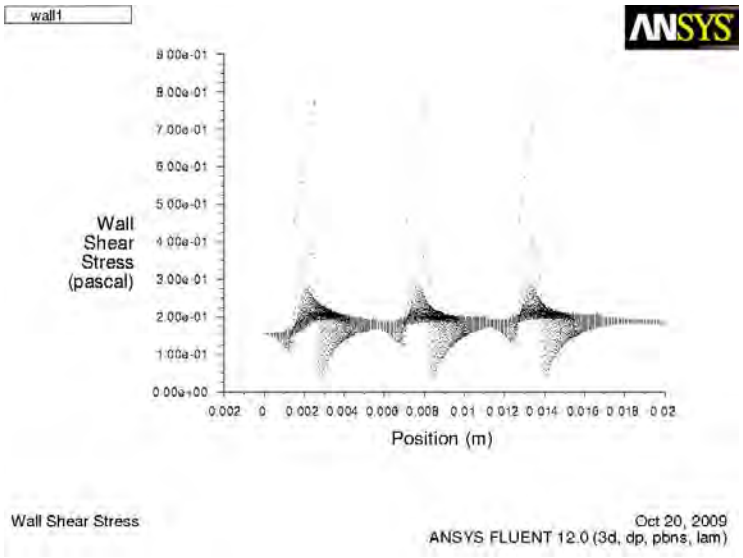

B

Figure C45: Shear plot (A) and wall shear stress graph (B) for 3_90_0.2

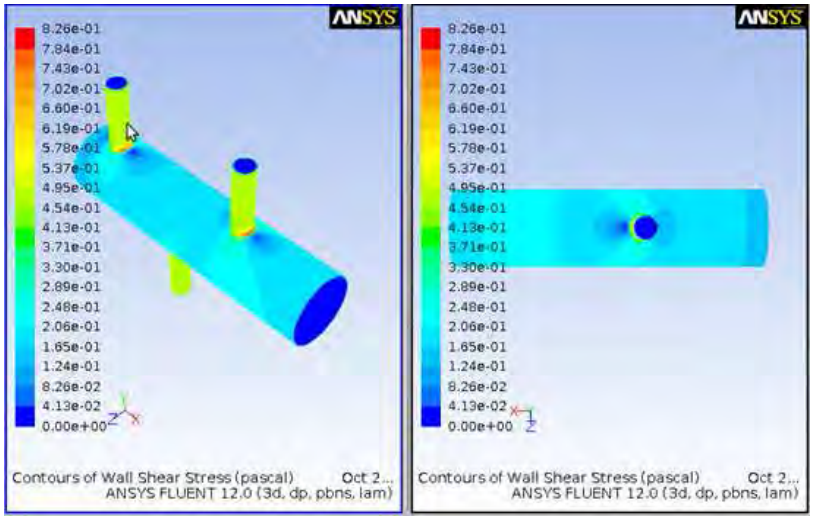

A

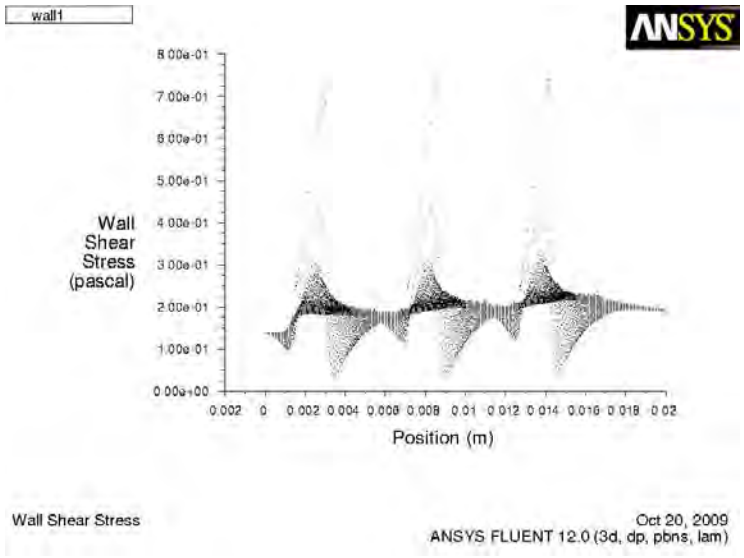

B

Figure C46: Shear plot (A) and wall shear stress graph (B) for 3_90_0.3

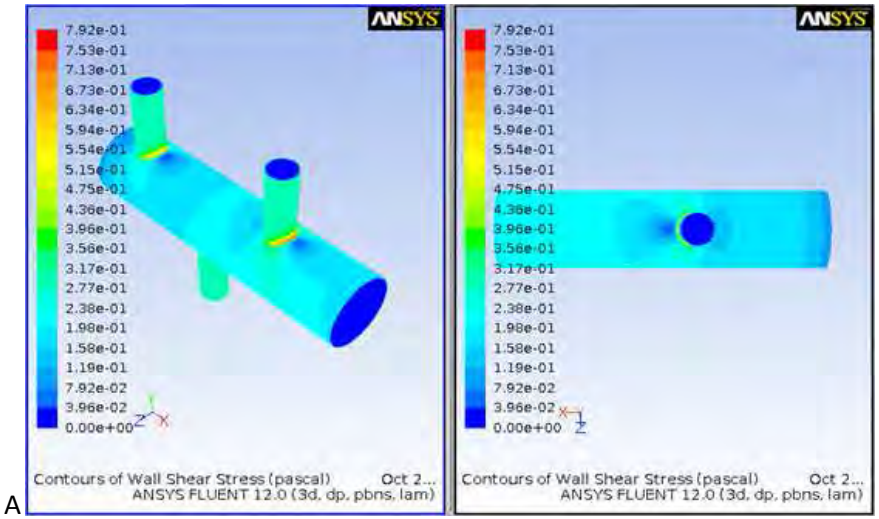

A

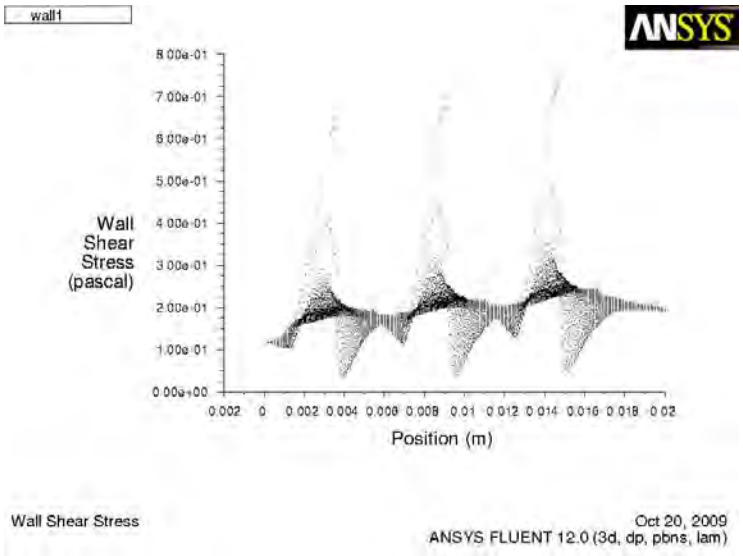

B

Figure C47: Shear plot (A) and wall shear stress graph (B) for 3_90_0.4

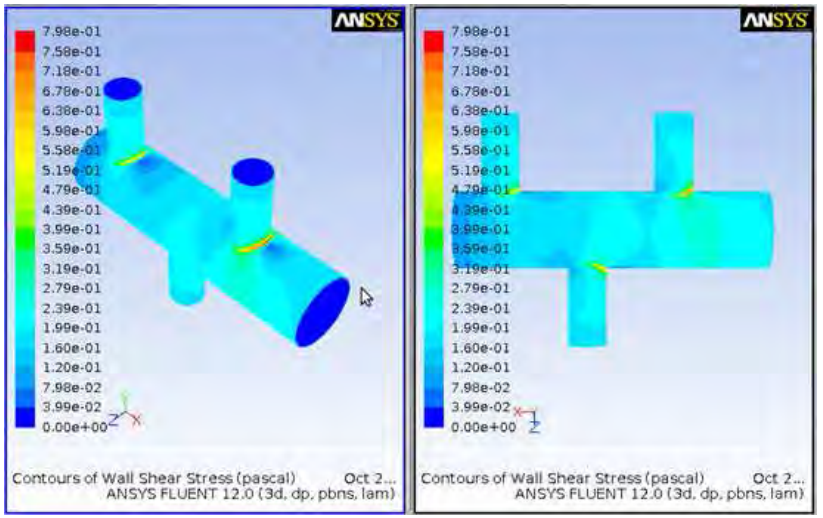

A

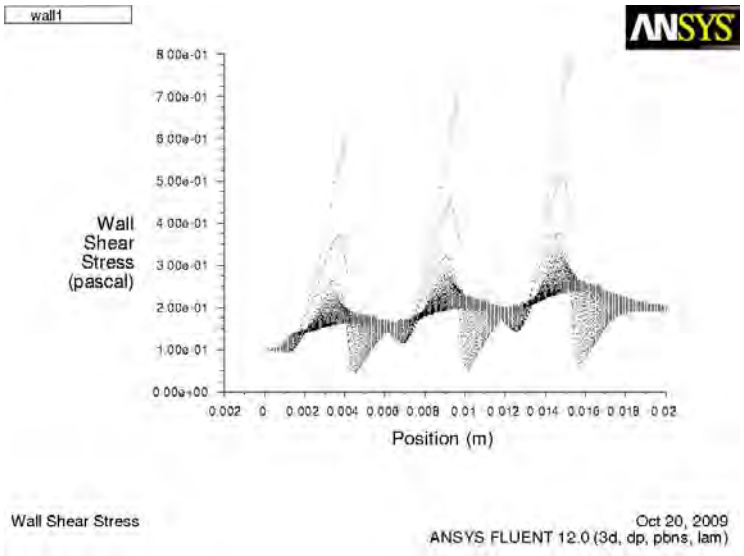

B

Figure C48: Shear plot (A) and wall shear stress graph (B) for 3_90_0.5

Pressure Results

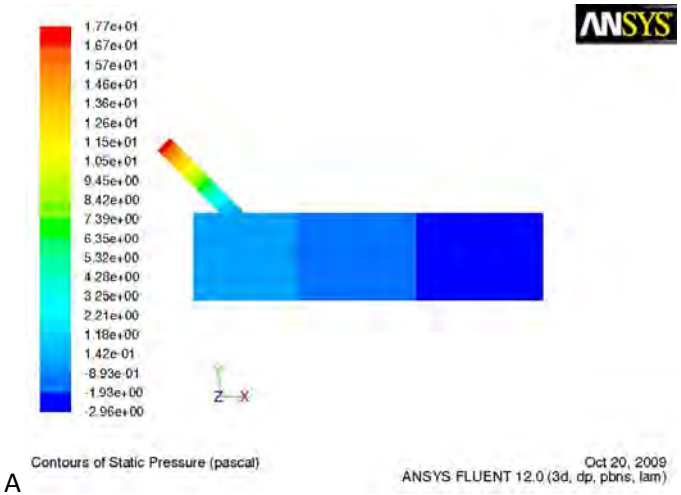

A

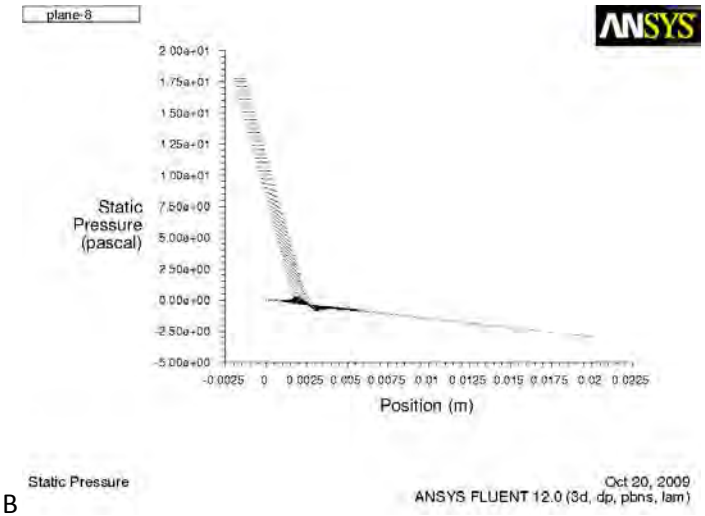

B

Figure C49: Pressure plot (A) and pressure graph (B) for 1_45_0.2

A

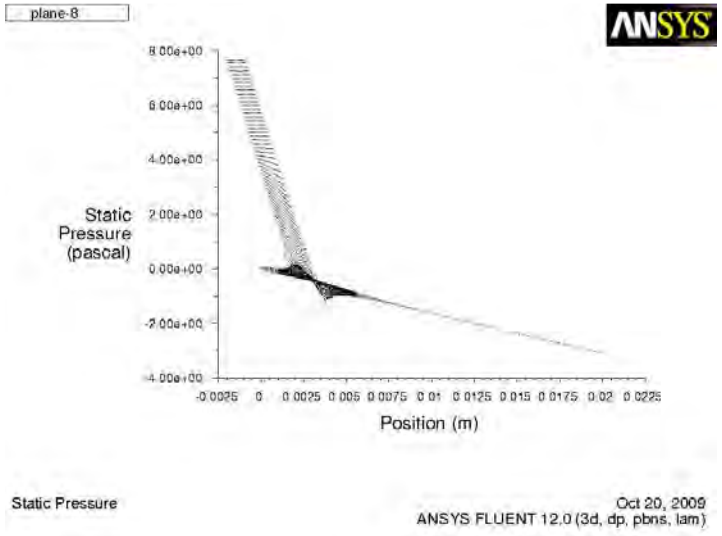

B

Figure C50: Pressure plot (A) and pressure graph (B) for 1_45_0.3

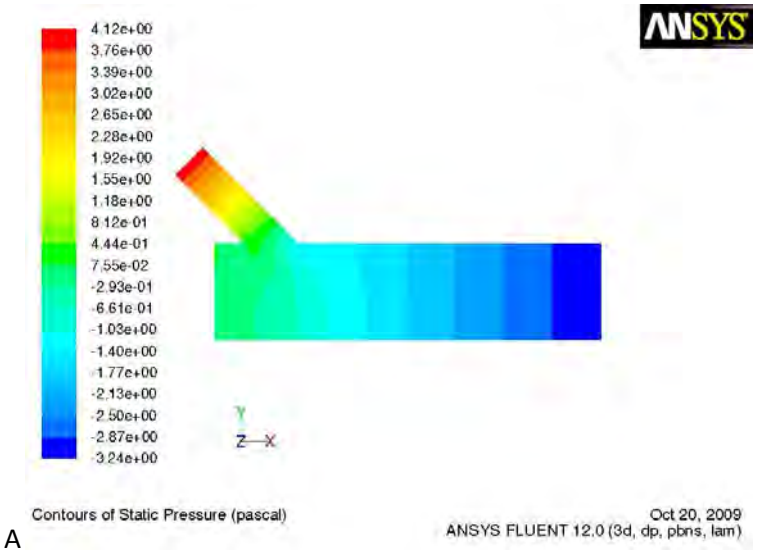

A

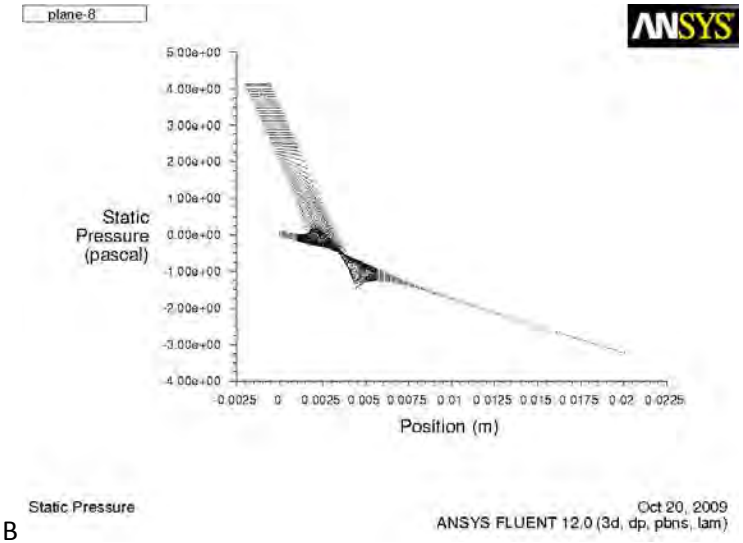

B

Figure C51: Pressure plot (A) and pressure graph (B) for 1_45_0.4

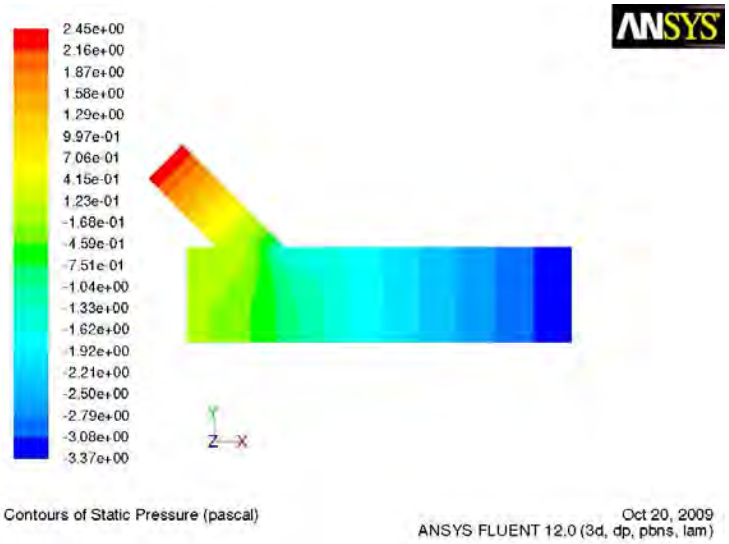

A

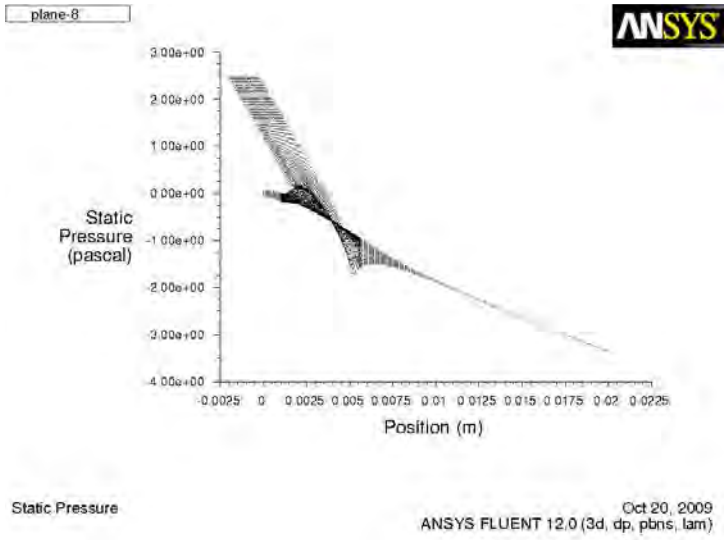

B

Figure C52: Pressure plot (A) and pressure graph (B) for 1_45_0.5

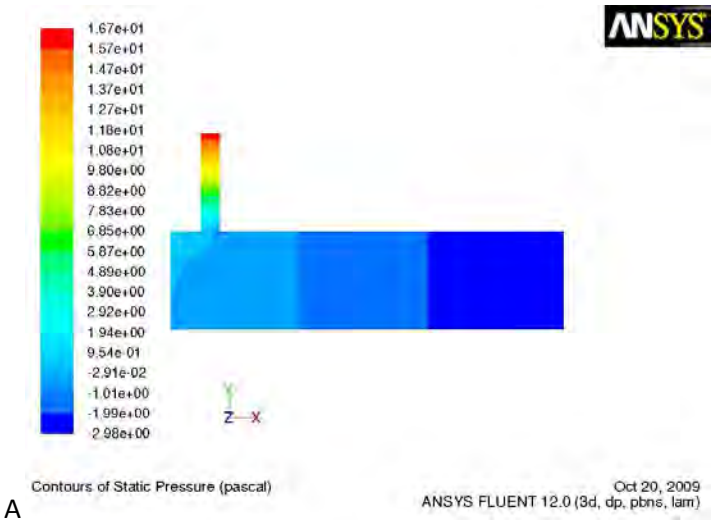

A

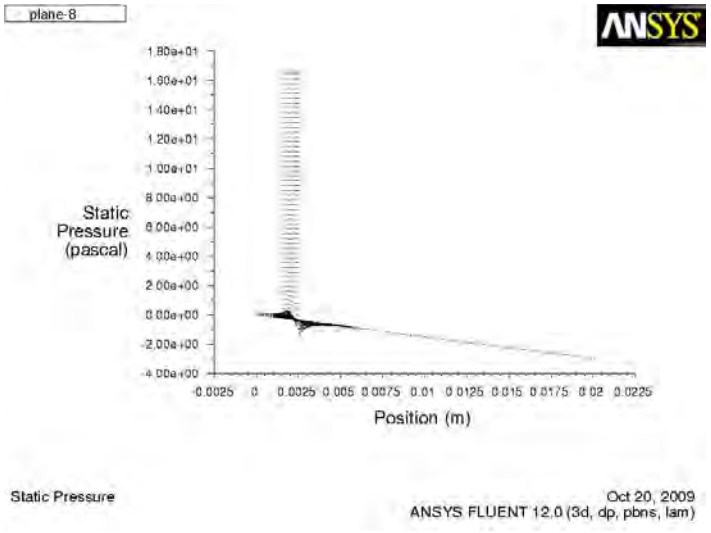

B

Figure C53: Pressure plot (A) and pressure graph (B) for 1_90_0.2

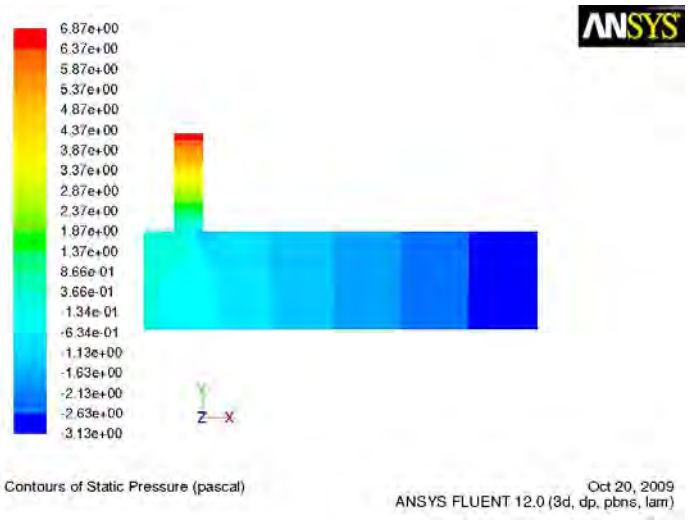

A

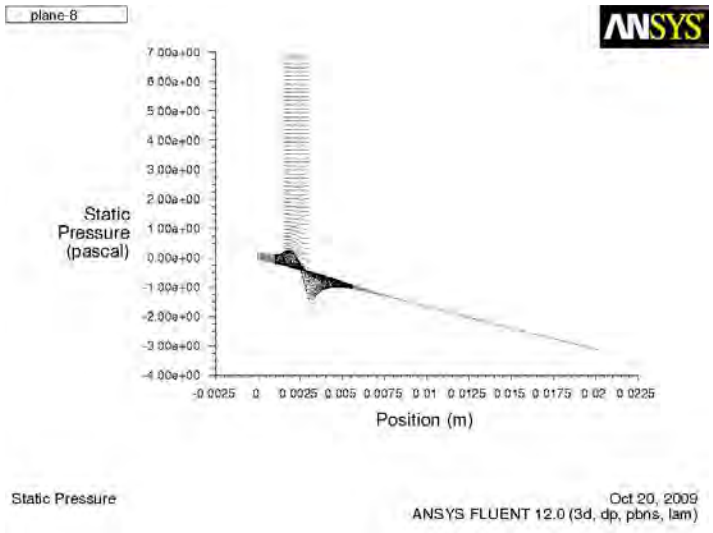

B

Figure C54: Pressure plot (A) and pressure graph (B) for 1_90_0.3

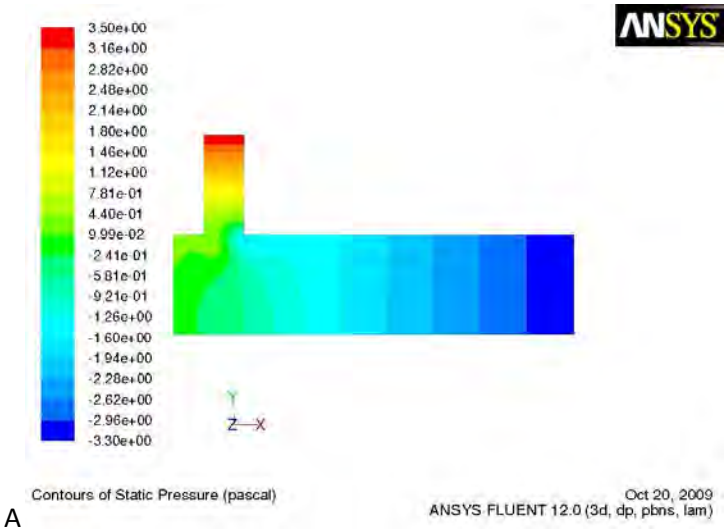

A

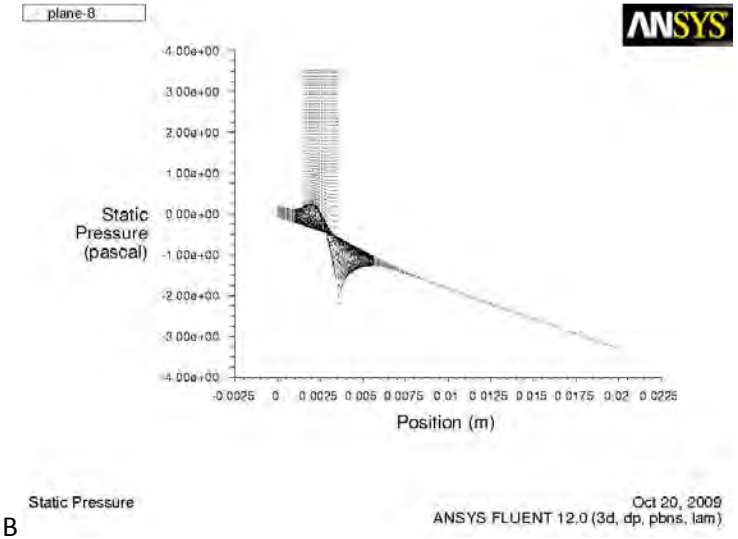

B

Figure C55: Pressure plot (A) and pressure graph (B) for 1_90_0.4

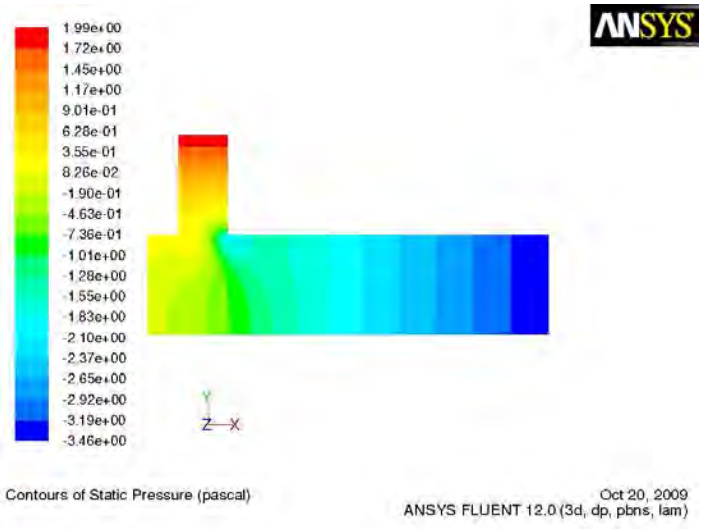

A

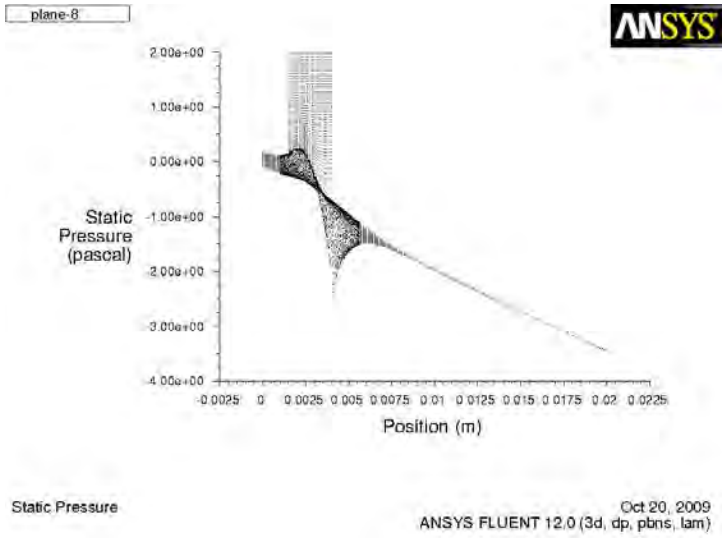

B

Figure C56: Pressure plot (A) and pressure graph (B) for 1_90_0.5

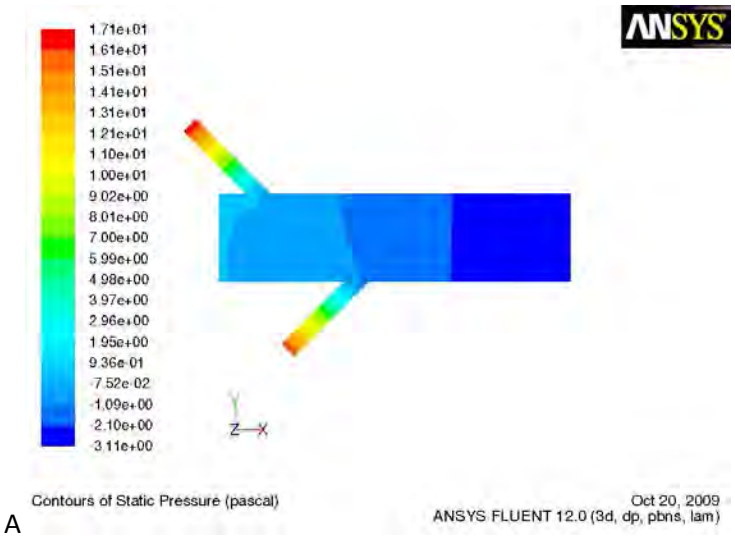

A

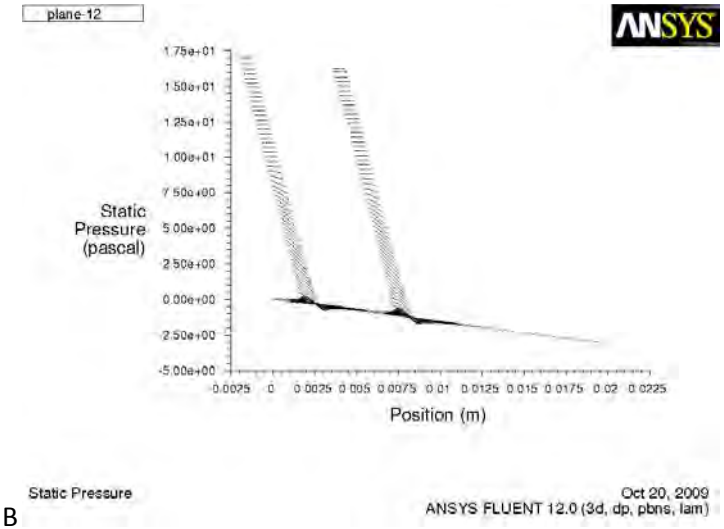

B

Figure C57: Pressure plot (A) and pressure graph (B) for 2_45_0.2

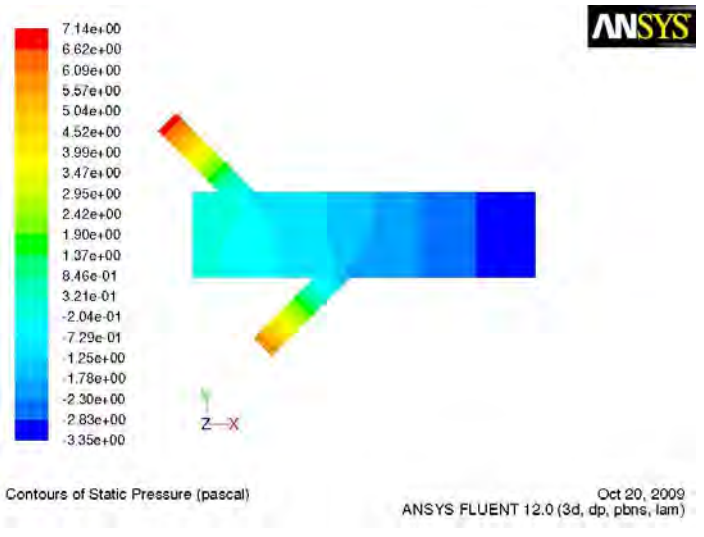

A

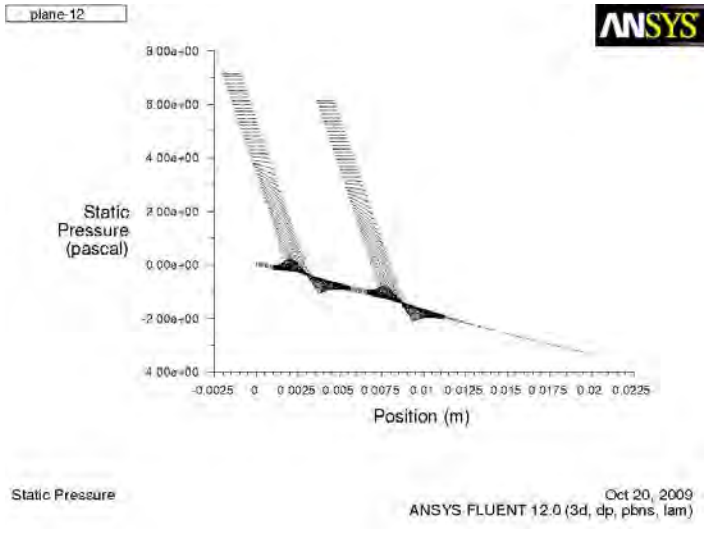

B

Figure C58: Pressure plot (A) and pressure graph (B) for 2_45_0.3

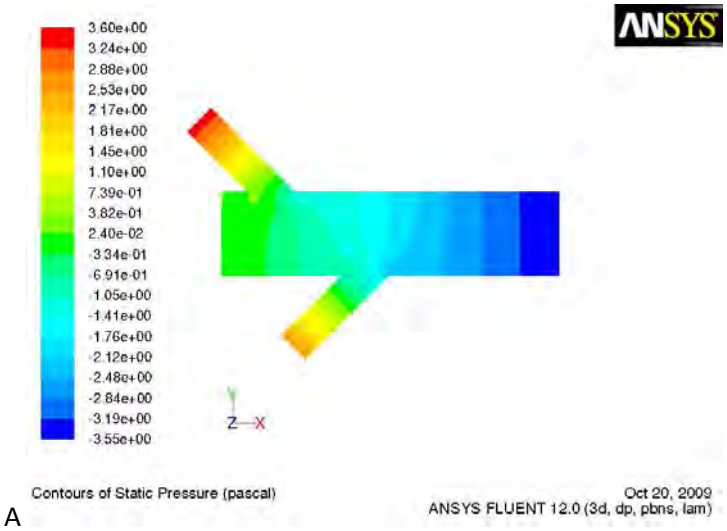

A

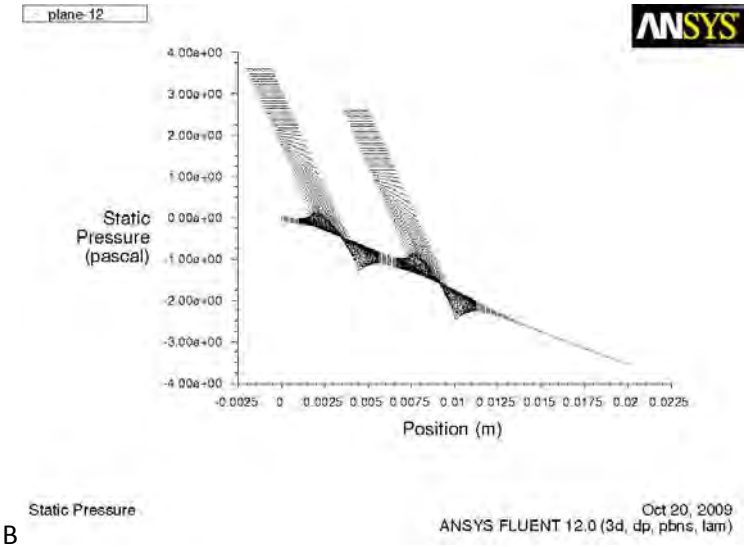

B

Figure C59: Pressure plot (A) and pressure graph (B) for 2_45_0.4

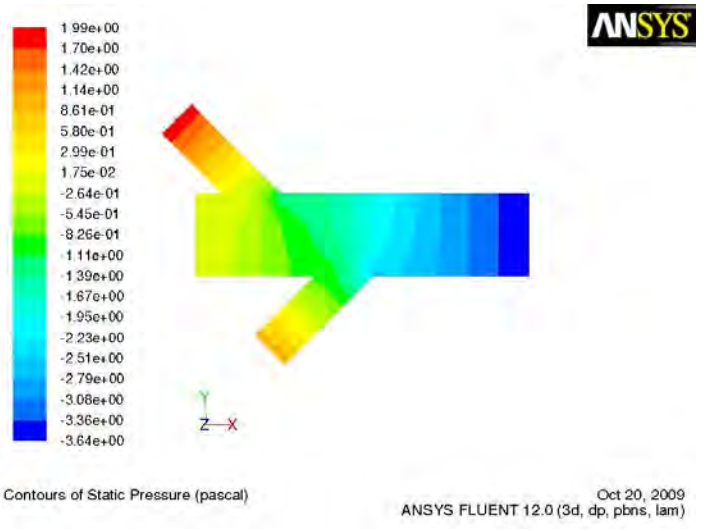

A

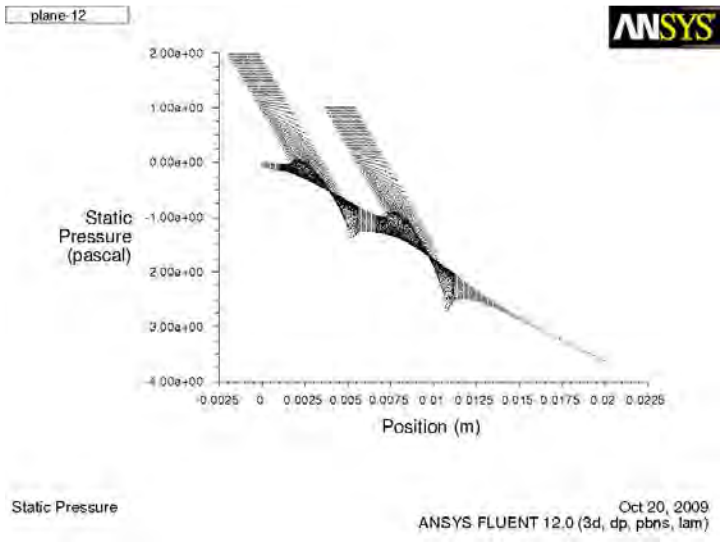

B

Figure C60: Pressure plot (A) and pressure graph (B) for 2_45_0.5

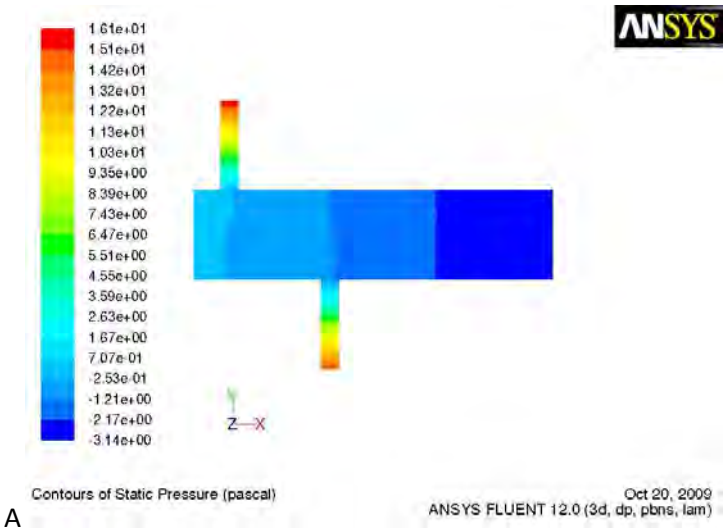

A

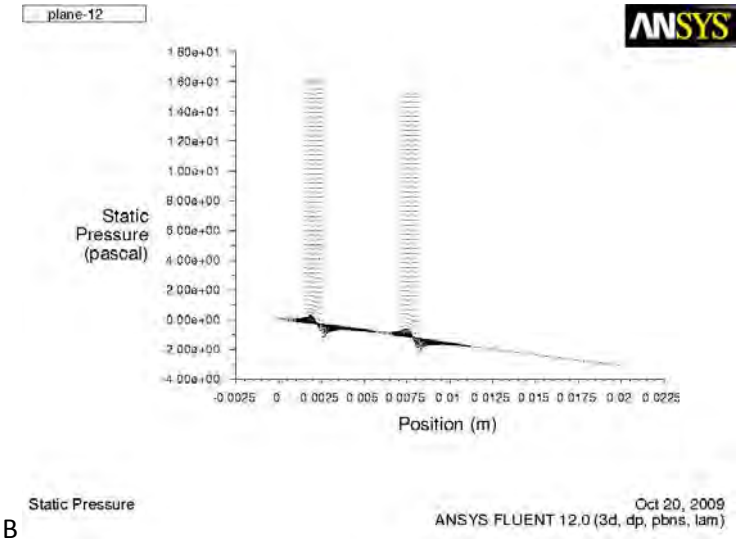

B

Figure C61: Pressure plot (A) and pressure graph (B) for 2_90_0.2

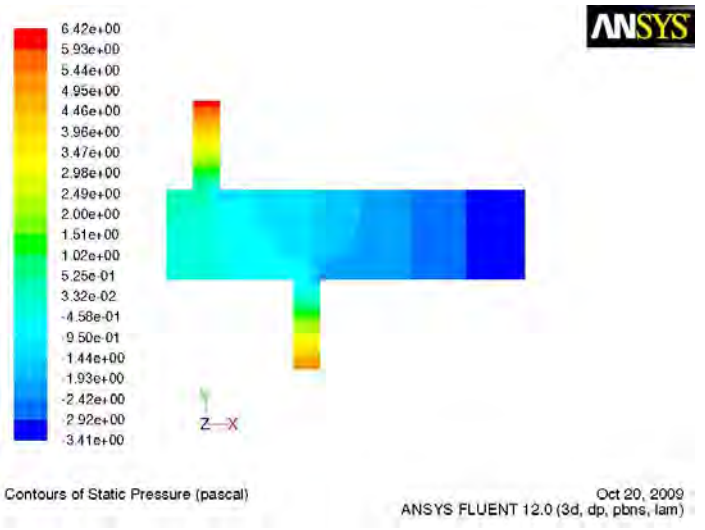

A

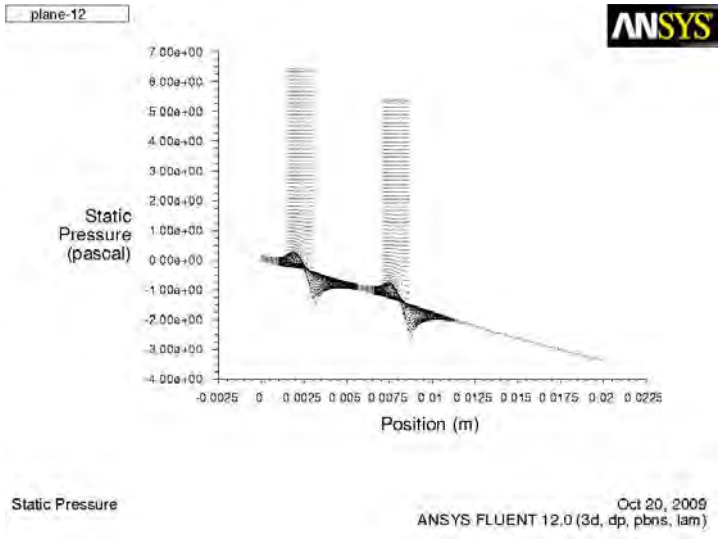

B

Figure C62: Pressure plot (A) and pressure graph (B) for 2_90_0.3

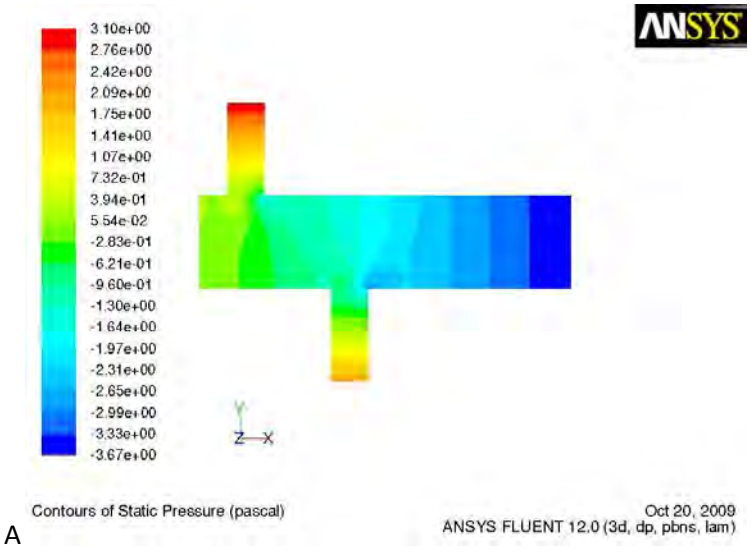

A

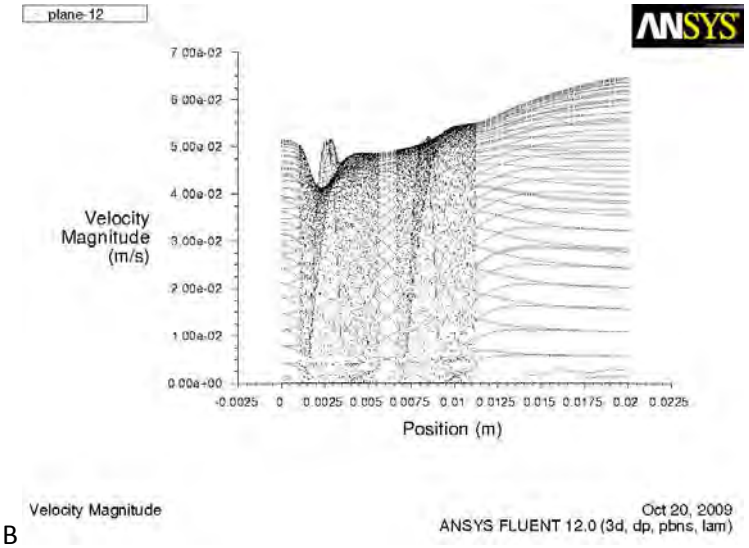

B

Figure C63: Pressure plot (A) and pressure graph (B) for 2_90_0.4

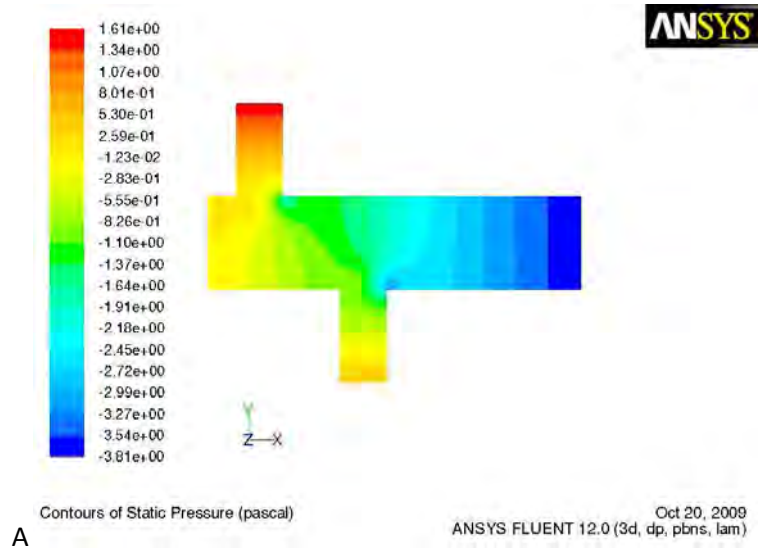

A

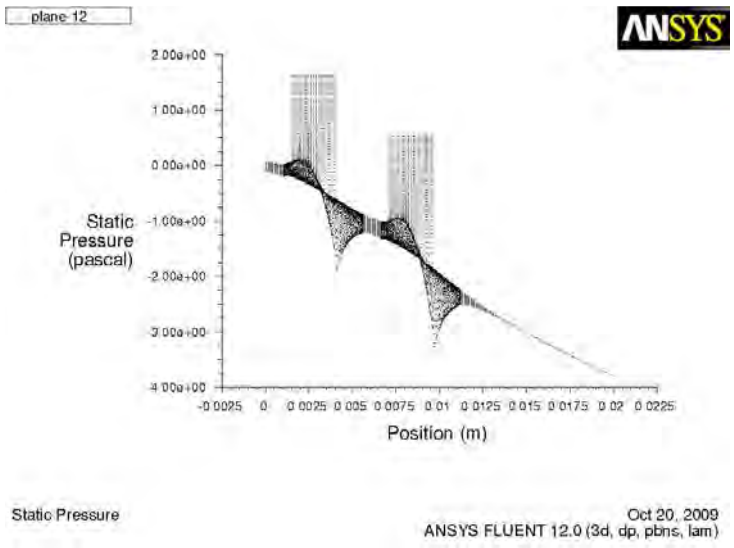

B

Figure C64: Pressure plot (A) and pressure graph(B) for 2_90_0.5

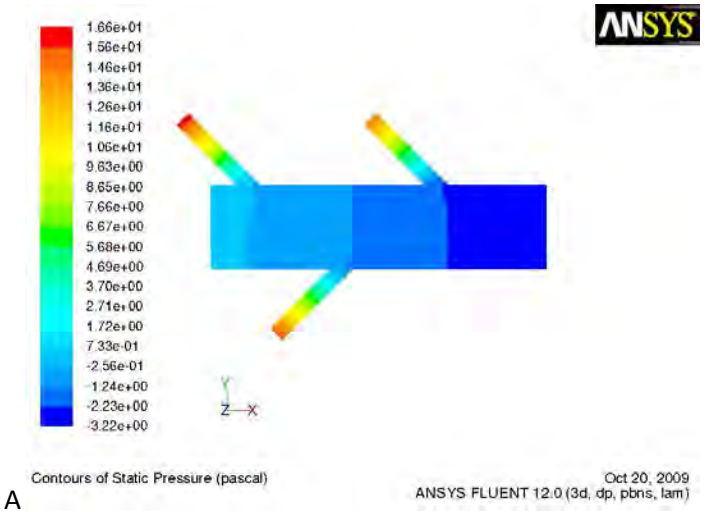

A

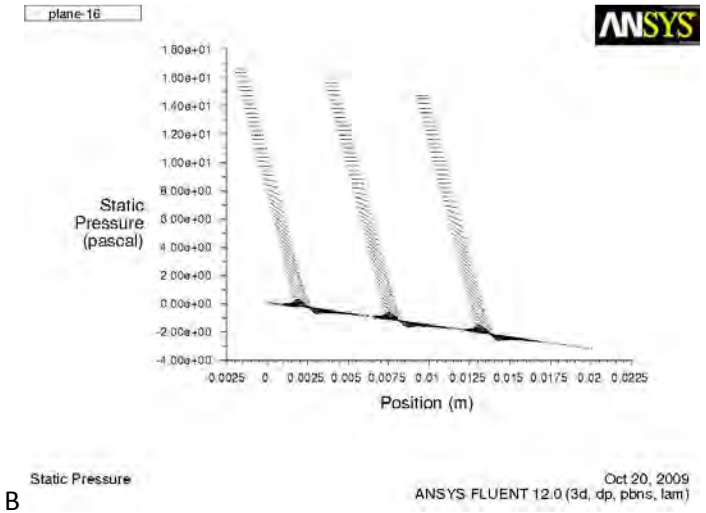

B

Figure C65: Pressure plot (A) and pressure graph (B) for 3_45_0.2

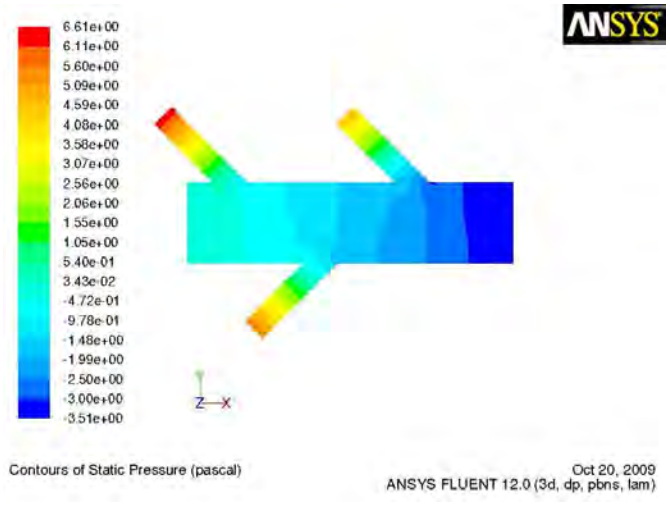

A

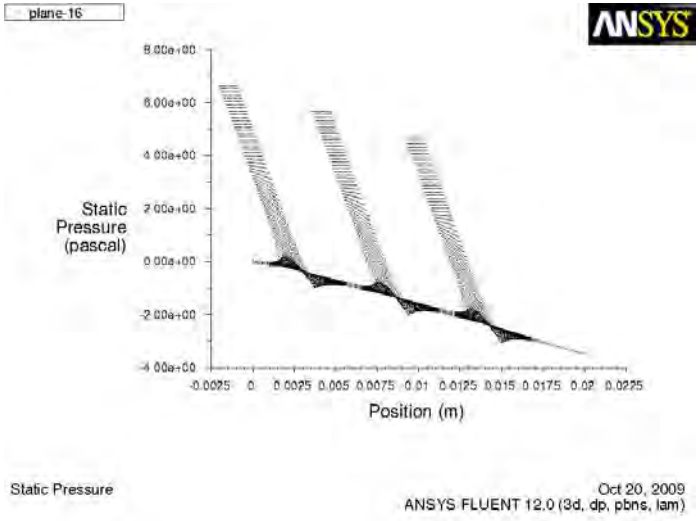

B

Figure C66: Pressure plot (A) and pressure graph (B) for 3_45_0.3

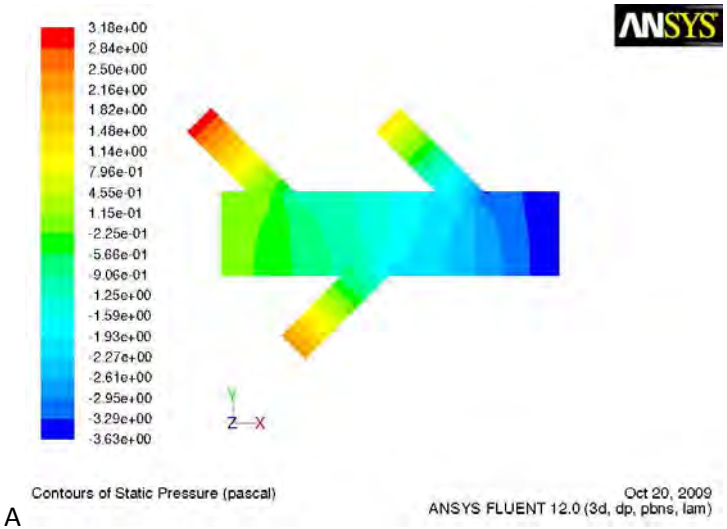

A

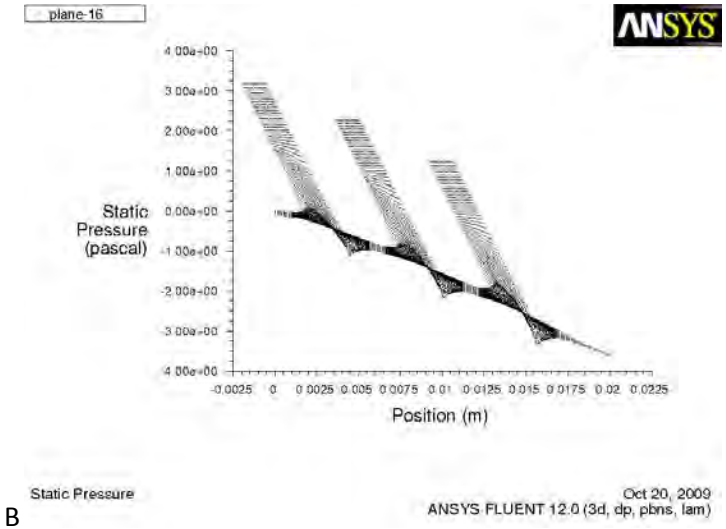

B

Figure C67: Pressure plot (A) and pressure graph (B) for 3_45_0.4

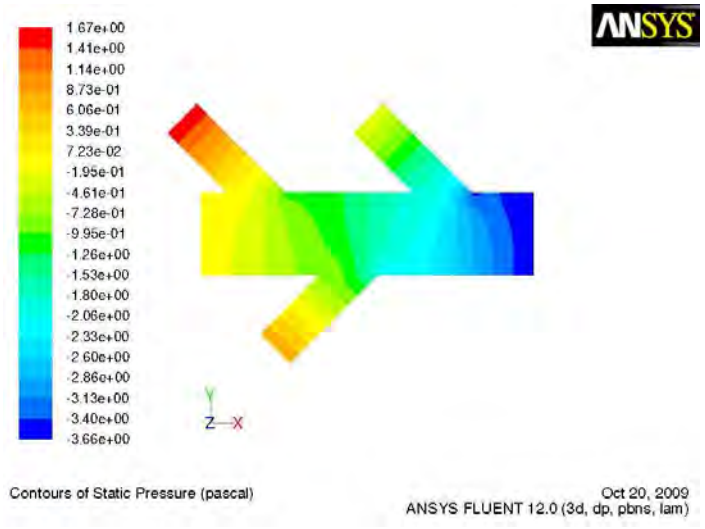

A

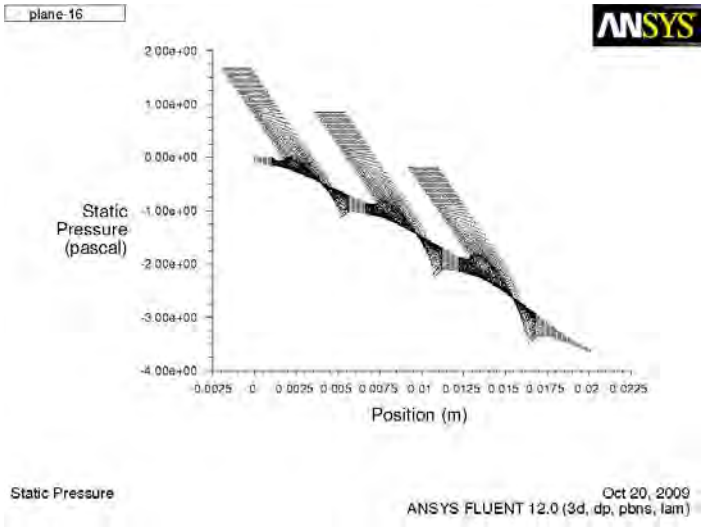

B

Figure C68: Pressure plot (A) and pressure graph (B) for 3_45_0.5

A

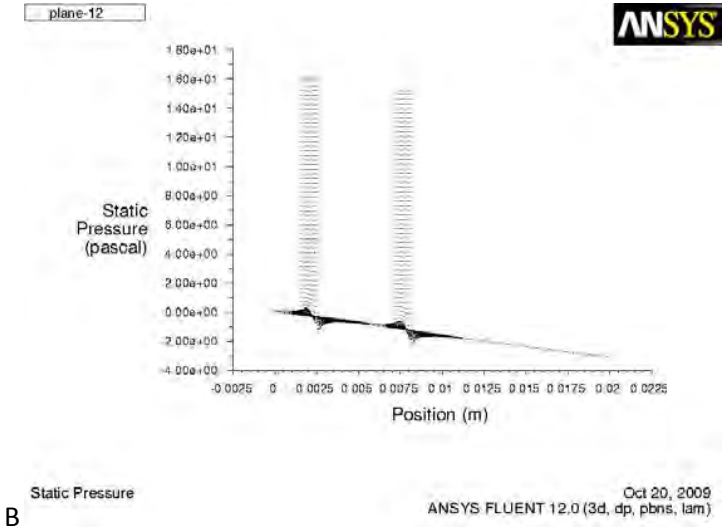

B

Figure C69: Pressure plot (A) and pressure graph (B) for 3_90_0.2

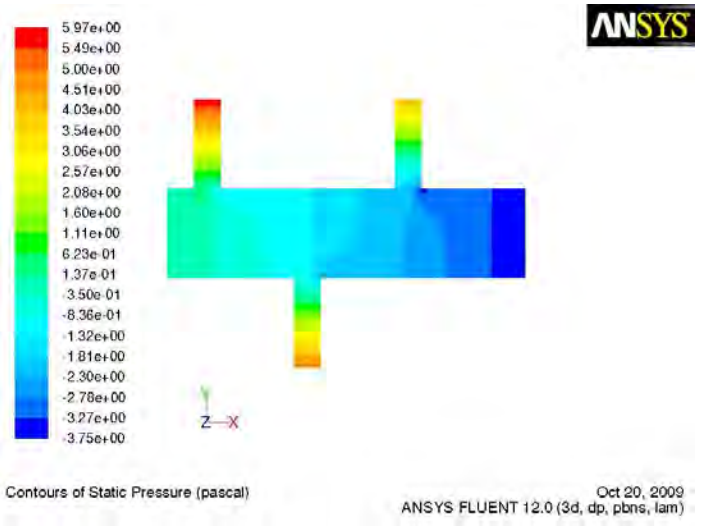

A

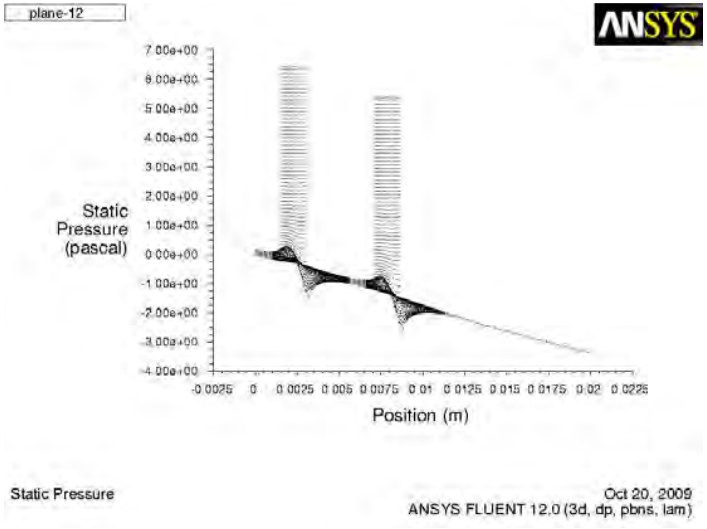

B

Figure C70: Pressure plot (A) and pressure graph (B) for 3_90_0.3

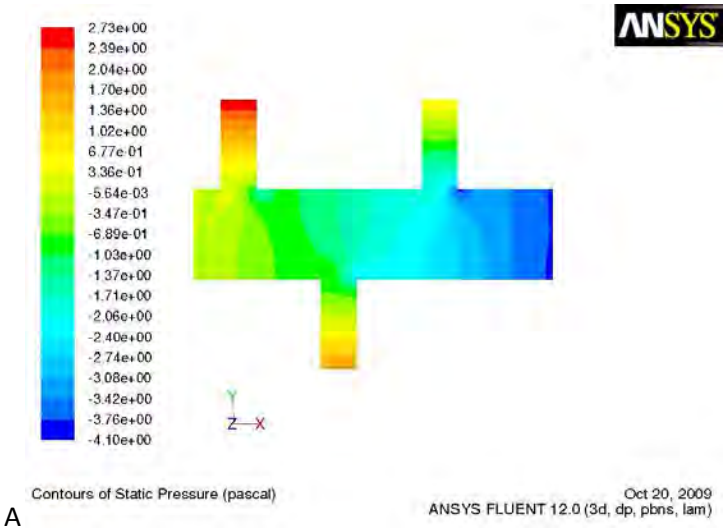

A

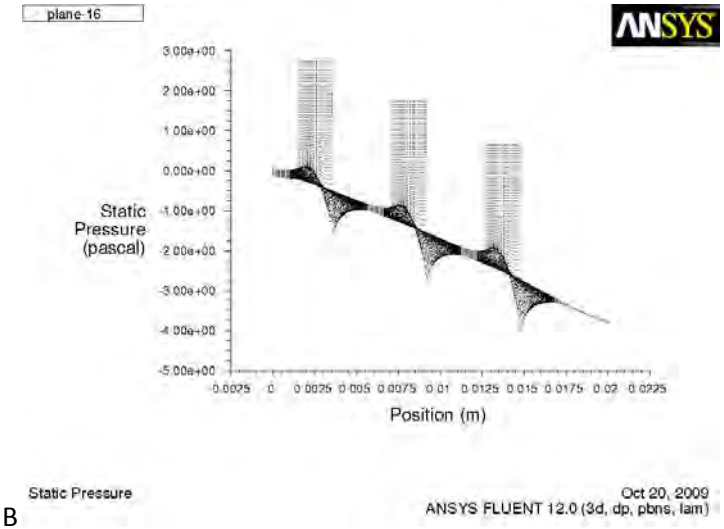

B

Figure C71: Flow pattern(A) and velocity magnitude graph(B) for 3_90_0.4

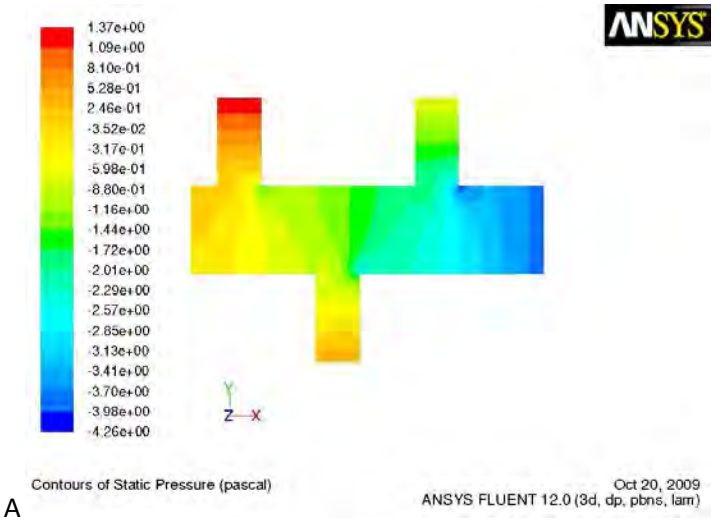

A

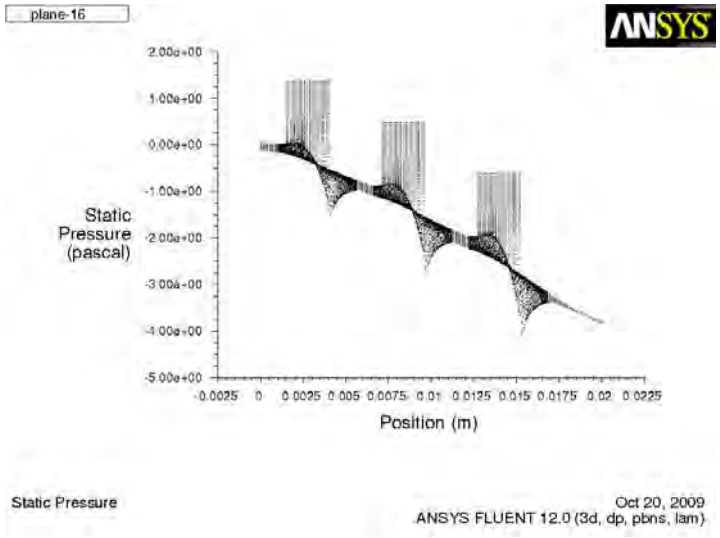

B

Figure C72: Pressure plot (A) and pressure graph(B) for 3_90_0.5